Study and analysis *o*f S*oo*t Filter Regenerati*o*n by using the Lattice B*o*ltzmann *M*eth*o*d

Claudius Stockinger

Normandie Université

INSA INSTITUT NATIONAL DES SCIENCES APPLIQUÉES ROUEN NORMANDIE

THÈSE

Pour obtenir le diplôme de doctorat

Spécialité **MECANIQUE DES FLUIDES, ENERGETIQUE, THERMIQUE, COMBUSTION, ACOUSTIQUE**

Préparée au sein de l'**INSA Rouen Normandie**

Study and analysis of Soot Filter Regeneration by using the Lattice Boltzmann Method

Présentée et soutenue par

CLAUDIUS STOCKINGER

Thèse soutenue le 14/06/2024

devant le jury composé de :

M. HUGO SAFDARI SHADLOO	MAITRE DE CONFERENCES DES UNIVERSITES HDR - INSA Rouen Normandie	Directeur de thèse
MME PASCALE DOMINGO	DIRECTEUR DE RECHERCHE DU CNRS - INSA de Rouen Normandie	Président du jury
M. ABDELLAH HADJADJ	PROFESSEUR DES UNIVERSITÉS - INSA de Rouen Normandie	Co-directeur de thèse
M. JONAS LATT	ASSOCIATE PROFESSOR - Université de Genève	Membre
M. ULRICH NIEKEN	PROFESSEUR - University of Stuttgart	Membre
M. ASHWIN CHINNAYYA	PROFESSEUR DES UNIVERSITÉS - ENSMA	Rapporteur
M. KAMEL HOOMAN	PROFESSEUR - TU Delft	Rapporteur

Thèse dirigée par **HUGO SAFDARI SHADLOO** (COMPLEXE DE RECHERCHE INTERPROFESSIONNEL EN AEROTHERMOCHIMIE) et **ABDELLAH HADJADJ** (COMPLEXE DE RECHERCHE INTERPROFESSIONNEL EN AEROTHERMOCHIMIE)

ED 591 PSIME

CORIA UMR 6614

Normandie Université

DISSERTATION

Submitted in the partial fulfillment for the award of Doctor of Philosophy

Specialized in : MECANIQUE DES FLUIDES, ENERGETIQUE, THERMIQUE, COMBUSTION, ACOUSTIQUE

From CORIA, UMR 6614 CNRS.

Study and analysis of Soot Filter Regeneration by using the Lattice Boltzmann Method

by

Claudius Maximilian Josef STOCKINGER

Thesis defended publicly on June 14^{th}, 2024 in front of the jury comprising of:		
Ashwin CHINNAYYA	Professor, ISAE ENSMA Poitiers	Rapporteur
Kamel HOOMAN	Professor, Technische Universiteit Delft	Rapporteur
Jonas LATT	Associate Professor, Université de Genève	Examinateur
Ulrich NIEKEN	Professor, Universität Stuttgart, Germany	Examinateur
Pascale DOMINGO	CNRS Research Director, Coria, France	Examinatrice
Mostafa S. SHADLOO	Associate Professor, INSA Rouen, France	Dir. Thèse
Abdellah HADJADJ	Professor, INSA Rouen, France	Co-Dir. Thèse

INSA INSTITUT NATIONAL DES SCIENCES APPLIQUÉES ROUEN NORMANDIE

ED 591 PSIME

UMR 6614 CORIA COMPLEXE DE RECHERCHE INTERPROFESSIONNEL EN AEROTHERMOCHIMIE

Acknowledgements

This work has been conducted at complexe de recherche interprofessionnel en aérothermochimie (CORIA), CNRS UMR 6614, and INSA Rouen Normandie, and I am grateful for the enriching experience of working and living in France for three years.
I thank my supervisors Mostafa Safdari Shadloo (HRD) and Prof. Abdellah Hadjadj for their supervision and guidance and the possibility to work on this PhD project. Special thanks goes to Prof. Hadjadj for helping me navigate the french bureaucracy and his continuous support when facing problems. Moreover, I would like to express my thanks to Prof. Dr.-Ing. Ulrich Nieken for the scientific guidance and discussions, as well as for providing me with the possibility of multiple scientific stays at University of Stuttgart. I also thank Antonio Raiolo, my German counterpart in the french-german cooperative project for the scientific exchange, discussions and the good time, which we had as office-mates in Stuttgart. Furthermore, I thank both rapporteurs, Prof. Ashwin Chinnayya and Prof. Kamel Hooman for reviewing my manuscript, their time and the constructive comments. Here, I would also like to thank the other members of my soutenance committee, Prof. Ulrich Nieken, Prof. Jonas Lätt and DR Pascale Domingo.
Also, I would like to thank Muhittin Çelep and Andrei-Silviu Milea for their friendship and assistance with the french language and the other PhD students of our hallway, Chethan Siddappa and Skylar Sawaf for the time spent together.
I also thank my masters students Nikos Alexiadis and Jule Burmeister for their contributions to this work.
Furthermore, I would like to thank my parents for their continuous financial support and their encouragement to pursue an academic career throughout my life. Moreover, I can't thank my wife enough for enduring the last three years, which she had to spend alone in Germany.

Abstract

The control of the emission of carbon black is an important task in many fields of application, with the transport sector being one of the most important domains. Diesel engines, still being extensively used worldwide, are one of the main contributors to the anthropogenic emission of carbon black. In order to counteract the detrimental effect of carbon black on human health, exhaust gas treatment has been the focal point of research for many decades.
State of the art soot filters use a ceramic honey-comb structure, acting as wall flow filters. These filters require periodic regeneration once a critical filter back-pressure is reached. Regeneration is conduced either as active regeneration at elevated temperatures (>600 °C) or continuously, as passive regeneration at temperatures starting from 300 °C. The necessary exhaust gas temperature of active regeneration results in a fuel penalty, making the precise control of the regeneration process imperative. Previous works suggested that the mesoscopic morphology of soot and its evolution during soot combustion influence the reactivity, thus affecting the regeneration process. Hence, the control of the regeneration system requires precise knowledge of the physical and chemical phenomena at hand, necessitating simulations of the regeneration process.
In this thesis, a simulation framework to model gas flow, consisting of the different reactive species, taking into account solid-gas interactions, is created. Furthermore, conjugate heat transfer, heterogeneous reactions and the release of reaction heat at the interface between the solid and gas phases is treated. For this purpose, the lattice Boltzmann method (LBM), due to its mesoscopic nature, is chosen as an excellent tool to model the heterogeneous combustion on the pore scale. Within this thesis, a LBM framework is created and appropriate methods to model soot combustion are chosen and extensively validated. A procedure to use focused ion beam scanning electron microscopy (FIB-SEM) data of realistic soot samples for the combustion simulation is implemented. Furthermore, the combustion regimes are analysed based on variation of Péclet number, Damköhler number, and oxygen mass fraction in the inlet gas stream. Simulations with realistic soot geometries are performed and the results are compared with experimental results. It is found that the evolution of the specific reactive surface, as received from LBM simulations, is not comparable to the experimental results. Transmission electron microscopy (TEM) analysis and Raman spectra of the soot before and after combustion experiments revealed that combustion affects the primary particles on the nano-scale. For this reason, a separate model to describe the heterogeneous primary particles and their combustion was created. Subsequently, first simulations with scale-coupling were conducted, by connecting the mesoscopic LBM simulations with the primary particle design on the nano-scale. It is shown that a more realistic increase in specific surface could be achieved in simulations by coupling the mesoscopic LBM model with a nano-scale primary particle model.

Keywords:

Lattice Boltzmann Method, Heterogeneous Reaction, Soot Combustion, Conjugate Heat Transfer.

Zusammenfassung

Die Reduzierung von Rußemissionen ist von zentraler Bedeutung in vielen Anwendungsbereichen, wobei der Verkehrssektor einer der wichtigsten Bereiche ist. Dieselmotoren, welche weltweit weiterhin breit eingesetzt werden, sind einer der Hauptverursacher von anthropogenen Rußemissionen. Um die schädlichen Auswirkungen von Ruß auf die menschliche Gesundheit zu bekämpfen, steht die Abgasnachbehandlung seit vielen Jahrzehnten im Mittelpunkt der Forschung. Hierbei kommen moderne Wandstromfilter, bestehend aus einer keramischen Wabenstruktur, zum Einsatz. Sobald eine kritische Rußbeladung, welche durch Erreichen eines kritischen Filterstaudruckes indiziert wird, erreicht ist, ist eine periodische Regeneration unumgänglich. Die Regeneration findet sowohl in Form von aktiver Regeneration bei Temperaturen ab 600 °C statt, als auch kontinuierlich in Form von passiver Regeneration bei niedrigeren Temperaturen ab 300 °C. Die hierfür benötigte Temperatur im Abgasstrang schlägt sich in Form eines erhöhten Kraftstoffverbrauches nieder, weshalb die genaue Steuerung des Regenerationsprozesses von Interesse ist. Vorangegangene Veröffentlichungen legten nahe, dass die Rußmorphologie der Mesoskala und deren Veränderung im Verlauf der Rußverbrennung die Reaktionskinetik und damit den Regenerationsprozess beeinflussen. Aus diesem Grund ist die Kenntnis der vorherrschenden physikalischen und chemischen Vorgänge für die Steuerung der Filterregeneration grundlegend. Ziel dieser Dissertationsschrift ist es, ein Framework zur Simulation des Gasflusses, bestehend aus Reaktanden und Produkten sowie inerten Komponenten, in porösen Medien zu erstellen. Zudem soll die Interaktion zwischen der Feststoffphase und der Gasphase, die Energiebilanz, die heterogene Reaktion an der Phasengrenzfläche sowie der konjugierte Wärmeübergang zwischen den Phasen berücksichtigt werden. Aufgrund ihrer mesoskopen Natur ist die Lattice Boltzmann Methode (LBM) ein prädestiniertes Werkzeug für diesen Zweck. Geeignete LBM-Methoden zur Simulation der genannten Phänomene wurden identifiziert und validiert. Des weiteren wurde ein Verfahrensablauf zur Auswertung von focused ion beam scanning electron microscopy (FIB-SEM) Daten realer Rußstrukturen erstellt, der es ermöglicht, reale Rußstrukturen als Basis für LBM Simulationen zu verwenden. Zudem wurde das Abbrandverhalten durch die Variation der Péclet Zahl, der Damköhler Zahl und des Sauerstoffmassenanteils im Einlass analysiert. Daraufhin wurde das Simulationsmodell verwendet, um den Abbrand realer Rußstrukturen zu simulieren und mit experimentellen Daten vom ICVT in Stuttgart abgeglichen. Hierbei wurde eruiert, dass der Anstieg der spezifischen Oberfläche, der in den Abbrandversuchen festgestellt wurde, nicht durch LBM Simulationen abbildbar war. Durch Analyse der Rußproben vor und nach Abbrandversuchen mittels Transmissionselektronenmikroskopie (TEM) und Ramanspektroskopie wurde die Vermutung, dass Veränderungen der Primärpartikelstruktur auf der Nanometerskala für diesen Oberflächenzuwachs verantwortlich sind, bestätigt. Aus diesem Grund wurde ein separates Primärpartikelmodell entworfen, mit dem Ziel, die heterogene Struktur der Primärpartikel und deren Einfluss auf die Oberflächenentwicklung abzubilden. Anschließend wurde was Primärpartikelmodell mit dem Lattice-Boltzmann Modell verknüpft, um Simulationen unter Berücksichtigung der Meso- und Nanoskala durchzuführen. Auf diese Weise war es möglich, den experimentell ermittelten Zuwachs der spezifischen Oberfläche besser abzubilden.

Schlüsselwörter:

LBM, Heterogene Reaktionen, Rußverbrennung, Konjugierter Wärmeübergang.

Résumé

La maîtrise des émissions de noir de carbone est une tâche importante dans de nombreux domaines d'application, le secteur des transports étant l'un des domaines les plus importants. Les moteurs diesel, encore largement utilisés dans le monde entier, sont l'une des principales sources d'émissions anthropiques de noir de carbone. Afin de contrer l'effet néfaste du noir de carbone sur la santé humaine, le traitement des gaz d'échappement est au centre de la recherche depuis de nombreuses décennies. Les filtres à suie de pointe utilisent une structure en nid d'abeille en céramique, agissant comme des filtres à flux mur. Ces filtres nécessitent une régénération périodique une fois qu'une contre-pression de filtre critique est atteinte. La régénération est effectuée soit sous forme de régénération active à des températures élevées (>600 °C), soit en continu, sous forme de régénération passive à des températures à partir de 300 °C. La température nécessaire des gaz d'échappement pour la régénération active entraîne une pénalité en carburant, rendant le contrôle précis du processus de régénération impératif. Des travaux antérieurs ont suggéré que la morphologie mésoscopique de la suie et son évolution pendant la combustion de la suie influencent la réactivité, affectant ainsi le processus de régénération. Par conséquent, le contrôle du système de régénération nécessite une connaissance précise des phénomènes physiques et chimiques en jeu, nécessitant des simulations du processus de régénération. Dans cette thèse, un cadre de simulation pour modéliser l'écoulement de gaz, composé des différentes espèces réactives, en tenant compte des interactions solide-gaz, est créé. De plus, le transfert de chaleur conjugué, les réactions hétérogènes et la libération de chaleur de réaction à l'interface entre les phases solide et gazeuse sont traités. À cette fin, la méthode de Boltzmann sur réseau (LBM), en raison de sa nature mésoscopique, est choisie comme un excellent outil pour modéliser la combustion hétérogène à l'échelle des pores. Dans cette thèse, un cadre LBM est créé et des méthodes appropriées pour modéliser la combustion de la suie sont choisies et largement validées. Une procédure d'utilisation des données de microscopie électronique à balayage par faisceau ionique focalisé (FIB-SEM) de véritables échantillons de suie pour la simulation de combustion est mise en œuvre. De plus, les régimes de combustion sont analysés en fonction de la variation du nombre de Péclet, du nombre de Damköhler et de la fraction molaire d'oxygène dans le flux gazeux d'entrée. Des simulations avec des géométries de suie réalistes sont réalisées et les résultats sont comparés avec des résultats expérimentaux. Il est constaté que l'évolution de la surface réactive spécifique, telle que reçue des simulations LBM, n'est pas comparable aux résultats expérimentaux. L'analyse par microscopie électronique à transmission (TEM) et les spectres Raman de la suie avant et après les expériences de combustion ont révélé que la combustion affecte les particules primaires à l'échelle nanométrique. Pour cette raison, un modèle séparé pour décrire les particules primaires hétérogènes et leur combustion a été créé. Ensuite, les premières simulations avec couplage d'échelle ont été menées, en reliant les simulations LBM mésoscopiques avec la conception des particules primaires à l'échelle nanométrique. Il est démontré qu'une augmentation plus réaliste de la surface spécifique peut être obtenue dans les simulations en couplant le modèle LBM mésoscopique avec un modèle de particules primaires à l'échelle nanométrique.

Mots cles:

LBM, réaction hétérogène, combustion de suie, transfert de chaleur conjugué.

Contents

Glossary

Latin letters

Symbol	Unit	Description
A	m/s	Pre-exponential factor
A_{CO}	m/s	Pre-exponential factor CO
A_{CO2}	m/s	Pre-exponential factor CO_2
A_{BET}	$s-lu^2/m-lu$	Specific BET surface in LBM simulations
BET	m^2	BET surface
c	s-lu/t-lu	Lattice speed
c_s^2	-	Squared lattice speed of sound
c_p	$\frac{kJ}{kg\,K}$	Specific heat capacity
C_m	m-lu/kg	Conversion factor mass
C_{mol}	mol-lu/mol	Conversion factor of the chemical amount
C_s	s-lu/m	Conversion factor length
C_t	t-lu/s	Conversion factor time
C_T	T-lu/K	Conversion factor Temperature
$\vec{c}_i$	-	Lattice velocity vector in direction i
D	-	Dimension
D_n	m^2/s	Diffusion coefficient n^{th} component
Da	-	Damköhler number
E_a	kJ/mol	Activation energy
$E_{a,CO}$	kJ/mol	Activation energy CO
$E_{a,CO2}$	kJ/mol	Activation energy CO_2
F_r	$mol/m^2/s$	Reaction rate
$F_{r,CO}$	$mol/m^2/s$	Reaction rate carbon monoxide
F_{r,CO_2}	$mol/m^2/s$	Reaction rate carbon dioxide
F_n	-	Forcing term n^{th} component
F_T	-	Forcing term temperature

$\vec{f}$	-	Distribution function vector
$\vec{F}$	-	Arbitrary force vector
f	$\rho - lu$	Distribution function
f^{eq}	$\rho - lu$	Equilibrium distribution function
f^{neq}	$\rho - lu$	Non-equilibrium part of the distribution function
f_{coll}	$\rho - lu$	Distribution function f after collision step
f_{corr}	$\rho - lu$	Corrector for distribution function f
g_n	-	Distribution function of n^{th} component
g_n^{eq}	-	Equilibrium distribution function of n^{th} component
h	T-lu	Distribution function temperature field
h^{eq}	T-lu	Equilibrium distribution function temperature field
I	-	Unitary matrix
Kn	-	Knudsen Number
k	m/s	Reaction rate
$\vec{k}$	N	External force vector
Le	-	Lewis number
Ma	-	Mach number
M	-	Transformation matrix
M_{O_2}	g/mol	Molar mass
$\dot{m}_{in}$	kg/s	Inlet mass flow
$\dot{m}_{out}$	kg/s	Outlet mass flow
$\vec{m}$	-	Moment vector
N_g	-	Number of gas lattice nodes
N_s	-	Number of solid lattice nodes
$\vec{n}$	-	Surface normal vector
p	N/m^2	Pressure
Pe	-	Péclet Number
Pr	-	Prandtl number
Q	W	Reaction heat release
Q_{total}	W	Total reaction heat for multiple partial reactions
Q_g	W	Reaction heat for gas phase
Q_s	W	Reaction heat for solid phase
Q_x	-	x component of $\vec{Q}$
Q_y	-	y component of $\vec{Q}$
$\vec{Q}$	-	Correction force vector
R	J/mol K	Ideal gas constant
Re	-	Reynolds number

S	-	Relaxation matrix
S_n	-	Relaxation matrix n^{th} component
S_T	-	Relaxation matrix temperature
T	K	Thermodynamic temperature
T_{eq}	T-lu	Equilibrium temperature
t	s	Time
w_i	-	Lattice weight
$\vec{u}$	m/s	Velocity vector
$\vec{x}$	-	Position
$\vec{x}_b$	-	Position at boundary
X	-	x position after streaming
x_i	-	x position of node with index i
Y	-	y position after streaming
y_i	-	y position of node with index i
$Y_{O_2}^I$	-	Mass fraction of oxygen at the interface
Y_n	-	Mass fraction of component n

Greek letters

Symbol	**Unit**	**Description**
α	m^2/s	Thermal diffusivity
δ_{ij}	-	Kronecker Delta
Δh_r	J/mol	Reaction heat
$\Delta h_{r,CO}$	J/mol	Reaction heat CO
$\Delta h_{r,CO2}$	J/mol	Reaction heat CO_2
$\Delta \dot{m}_{CO_2}$	kg_{CO_2}/s	Reaction turnover CO_2
Δt	t-lu	Time step size
Δx	s-lu	Lattice spacing
$O(\epsilon)$	-	Order of magnitude of epsilon
ϵ	-	Scaling parameter for multiscale expansion
λ	W/(mK)	Thermal conductivity
μ	Pa s	Dynamic viscosity
ν	m^2/s	Kinematic viscosity
ν_n	-	Stoichiometric coefficient component n
ξ	s-lu	Specific length scale
ρ	kg/m^3	Density
σ	-	Ratio of density and specific heat capacity

τ	t-lu	Relaxation time
χ	%	Combustion progress
ω	1/(t-lu)	Collision frequency
Ω	-	Collision operator

Operators

Symbol	**Unit**	**Description**
∇	1/m	Gradient operator
$\vec{}$	-	Vector notation

Subscripts

Symbol	**Description**
α, β, γ, δ	Einstein notation
$+$, $-$	Denoting either side of solid-gas interface
b	Boundary
g	Gas phase
i	Lattice velocity direction i
$\bar{\text{i}}$	Lattice velocity direction in opposite direction of i
n	Component n
s	Solid phase
SI	SI unit
w	Wall

Abbreviations

Symbol	**Description**
BB	Bounce-back
BC	Boundary condition
BET	Brunauer Emmett Teller Methode
C	Carbon
CAST	Combustion aerosol standard
CCD	Charge-coupled device
CO	Carbon monoxide
CO_2	Carbon dioxide
DOC	Diesel oxidation catalyst

DPF	Diesel particle filter
DPM	Diesel particulate matter
FIB-SEM	Focused Ion Beam Scanning Electron Microscopy
GPU	Graphics processing unit - Graphics card
HPC	High performance computer
ICVT	Institute of Chemical Process Engineering
LBM	Lattice Boltzmann Method
LGA	Lattice Gas Automaton
MPI	Message passing interface (for parallel computing)
MRT	Multi relaxation time
N_2	Nitrogen
NO_2	Nitrogen dioxide
O_2	Oxygen
PM	Particle matter
SOA	Structure of arrays
SRT	Single relaxation time
TEM	Transmission electron microscopy
XRD	X-ray diffraction

Chapter 1

Introduction

Context

An increased focus on the environmental impact and efforts to protect nature has lead to an increased interest of both academic research and industry in soot particle filters. Soot filters, primarily used to trap particle matter (PM), are used in a multitude of disciplines and applications, spanning from stationary industrial plants, maritime vehicles [56] as well as the automotive industry, both for heavy duty commercial and personal vehicles [29]. Extensive research has been conducted to investigate the cytotoxicity and health hazards of soot particles, explicitly these emitted from internal combustion engine vehicles using diesel fuel. Early studies investigated the different components of diesel exhaust gases, including soot particles and discussed their potential health risks [127, 88]. In these studies, tests on animals in laboratory scale were conducted and the cytotoxicity of diesel soot was proven, yet the study remained inconclusive about the actual effects on human health outside of the laboratory scale. Newer studies suggested an increased risk of lung cancer among workers with high exposure to diesel engines [140]. Also, it was found that diesel engines of a newer generation, which complied with contemporary political regulations, i.e. Euro-IV, produced soot particles of smaller size. These smaller soot particles exhibited a larger surface area and an abundance of chemically reactive strucutral elements, increasing their cytotoxicity [25]. Furthermore, the organic carbon contend of diesel particulate matter (DPM) was suspected to play an important role regarding their effects on the human respiratory system [107]. These findings resulted in harsher political regulations for the emission of PM of automobiles using diesel internal combustion engines. The evolution of the European emission standards is shown in Figure 1.1, in which it can be seen that the permitted amount of PM per kilometre decreased from an initial value of $180\,\mu g/km$ to $4.5\,\mu g/km$ for the most recent Euro-VI norm.

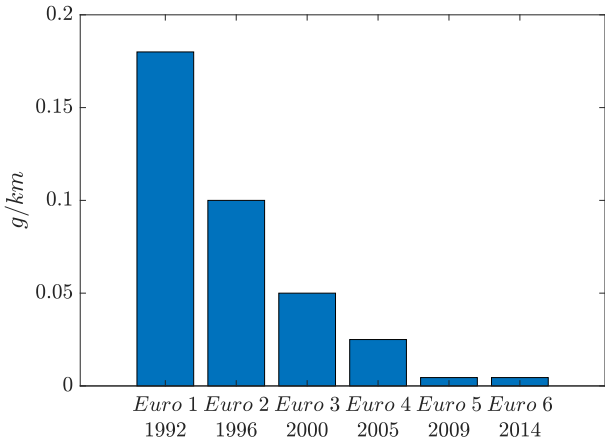

Figure 1.1: Evolution of European emission standards for automobiles up to 3.5 t of weight [135].

Also it is noted that since the introduction of the Euro-VI emission standard, automotive soot filters became mandatory not only in cars relying on diesel fuel, but also for cars using gasoline [141]. Combined with an increase in the consumption of diesel fuel in Germany of around 30 % between 1993 and 2016 [125, 126], this evolution makes efficient soot filtration in the automotive sector increasingly relevant. Current state of the art diesel particle filters (DPF) can reach filtration efficiencies of more than 95 $wt\%$, enabling a drastic reduction of the emission of PM [79]. However, an increasing load of the soot filter then leads to a built-up of filter back pressure. When a critical soot load is reached, the channels are constipated, making periodic regeneration of these diesel particulate filters imperative.

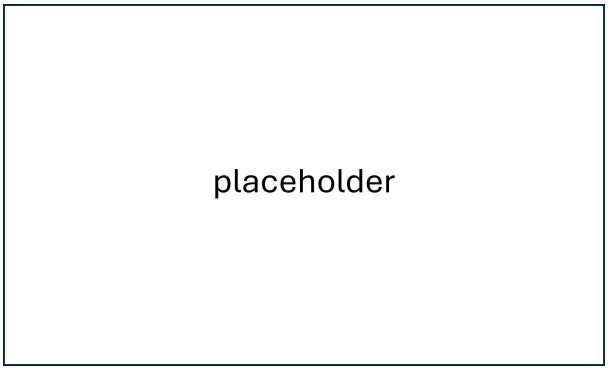

Figure 1.2: Factory new soot filter (right) and fully loaded soot filter requiring regeneration (left) [31].

To illustrate this problem, a factory new filter and a fully loaded filter, which requires regeneration, are shown in Figure 1.2. The honey comb structure and the silver metallic shine of the material are clearly visible on the factory new filter, which is shown on the right-hand side. On the left-hand side, the fully loaded filter is shown, emphasizing the necessity for regeneration. The regeneration of DPFs requires precise control of the

process parameters, i.e. exhaust gas temperature and composition, in order to achieve efficient soot burn off, to prevent thermal runaway of the exothermic reaction and to mitigate the fuel penalty. The control of the regeneration process cannot be achieved by only monitoring the pressure drop of the system. For this reason, precise knowledge of the undertaking process is desired, which can be gained through numerical simulation of the regeneration of DPFs.

In this thesis, the regeneration process of DPFs will be analysed numerically. For this purpose, the lattice Boltzmann method (LBM) will be used to set up a combustion model on the pore scale. The lattice Boltzmann method, being a relatively young method, has received increasing interest in the research community, since it proved to be an efficient tool for effectively characterizing diverse physical phenomena within porous media. Its noteworthy advantages include the capacity to address fluid-solid interactions, particularly in intricate geometries [34], facilitated by its inherent utilization of an equidistant lattice grid. Additionally, due to its explicit temporal discretization and the collision operator being local, parallelization is facilitated.

Previous works at our partner institute suggested that the reactivity of the soot changes with progressing combustion of the soot sample. It was suspected that this was a result of the changing specific reactive surface, induced by the oxidation [116]. Consequently, simulations of the soot combustion on the mesoscopic scale will be performed and the influence of the chemical and morphological properties of the soot onto the reaction kinetics will be investigated. In this scope, soot samples created by our project partner at University of Stuttgart are analysed by FIB-SEM, enabling us to perform combustion simulations while employing the realistic 3D morphology of soot. The LBM model will be extensively validated and the influence of the Péclet and Damköhler numbers as well as the amount of oxygen at the inlet of the reactor onto the combustion regimes will be studied. Subsequently, the evolution of the specific reactive surface is studied and the results are compared with experimental data of our project partner in an effort to determine the dependency of the reaction rate on the soot morphology.

Objectives of the work

As elaborated above, improving the efficiency and designing the regeneration process of soot particle filters necessitates the precise knowledge of the physical and chemical phenomena at hand. In this scope, valuable insights can be gained by numerical simulation of the soot combustion. For this purpose, the lattice Boltzmann method, due to its mesoscopic nature, is chosen as an adequate tool. The objectives of this thesis, which are formulated based on the project with acronyme ASORNE, funded by the ANR under

grant number ANR-20-CE92-0007, are the following:

- Creation of a code, which uses the lattice Boltzmann method for the simulation of single phase flow in porous media. For this purpose, a workflow to use FIB-SEM images of real soot samples as simulation domains should be created.
- Extension of the code to treat flow consisting of multiple components, i.e. N_2, O_2, CO_2 and heterogeneous reactions at the interface between the gas phase and the solid soot phase.
- Addition of solid-gas mass transfer, resulting in the transient evolution of the morphology of the soot phase, which will be consumed by the combustion reaction.
- Validation with and potential adaption of the code to experimental results obtained by the project partners of ICVT, University of Stuttgart.

Structure of the thesis

Here, a brief overview over the structure of the thesis is provided. The thesis is organized into the following six main chapters:

- Chapter 2: In the second chapter, a literature review is presented, encompassing the different soot filter types, the filtration mechanisms as well as regeneration procedures of diesel particulate filters. Furthermore, an overview over the simulation of soot combustion, the lattice Boltzmann method as well as the characterization of soot is given.
- Chapter 3: In this chapter, the theoretical background of this thesis is presented. An extensive overview of the lattice Boltzmann equation and its discretization is presented. Furthermore, this chapter presents the models used for the description of heterogeneous reactions in porous media and connects the LBM expression and continuous expressions. Furthermore, the transformation of all simulation parameters from SI units to lattice units, commonly used in LBM, is derived.
- Chapter 4: This chapter focuses on the implementation techniques, necessary to model all physical phenomena involved in heterogeneous combustion reactions in porous media. The framework developed in this thesis is introduced. Then, the implementation of boundary conditions is described in detail to facilitate reproducibility and the calibration of the simulation model is presented.

- Chapter 5: In chapter five, the results of this thesis are presented in a cumulative manner, based on the publications achieved during the thesis period. First, the proposed lattice Boltzmann model to simulate soot combustion in porous media is validated using a 2D combustion test case found in literature. Subsequently, the model is extended to treat realistic combustion in geometries obtained from FIB-SEM analysis of soot samples generated with a CAST generator at ICVT in Stuttgart. Then, a parametric study is conducted to analyse the combustion behaviour and the phenomena limiting the combustion. For this, the Péclet and Damköhler numbers as well as the inlet mass fraction of oxygen as the main controling parameters in soot regeneration and the geometries are varied. Then, combustion simulations with FIB-SEM geometries are conducted and the evolution of the specific surface is analysed and compared with experimental data. Finally, a scale coupling method for the coupled modelling of mesoscopic combustion in porous media and the evolution of the intrinsic reactive surface of the primary particles on the nano-scale is proposed.

- Chapter 6: Chapter six comprises of a conclusion of the work presented in this thesis and gives an outlook of potential work, which might be conducted based on the findings of this thesis.

Publications

Peer-reviewed journal papers

- R. Alamian, M. Sawaf, C. Stockinger, A. Hadjadj, J. Latt, M. Shadloo, Modeling soot filter regeneration process through surface-reactive flow in porous media using iterative lattice boltzmann method, *Energy* 289 (2024) 129980

- C. Stockinger, A. Raiolo, U. Nieken, R. Alamian, A. Hadjadj, and M. Safdari Shadloo. Lattice Boltzmann Simulations of Heterogeneous Combustion Reactions for Application in Porous Media. *Engineering Analysis with Boundary Elements*, Under Review.

- C. Stockinger, A. Raiolo, A. Hadjadj, U. Nieken, and M. Shadloo. Simulation of Heterogeneous Combustion Reactions in Porous Media for Application in Soot Filter Regeneration Using the Lattice Boltzmann Method. *Journal of Computational Physics*, Under Review.

- A. Raiolo, C. Stockinger, U. Tuttlies, N. Ivleva, M. Safdari Shadloo, and U. Nieken.

Effect of nanostructure and BET surface area on the oxygen reactivity of soot filter cakes. *Carbon*, Under Review.

International conference visits

- ECM2023, Rouen, *France* (April 2023). Poster presentation.
- ICNAAM2023, Heraklion, *Greece* (September 2023). Oral presentation.
- ISCRE28, Turku, *Finland* (June 2024). Poster presentation.

Chapter 2

Literature Review

In this chapter, a concise literature review is given. The literature review aims to provide the reader with all necessary information on the topic of automotive soot filtration as well as the characterization of soot and the computational study of soot filter regeneration. First, application oriented topics, i.e. the different soot filter types, the filtration mechanism and the regeneration of soot filters are presented. Furthermore, the state of the art of the simulation of soot combustion is reviewed. Then, the evolution of the lattice Boltzmann method from the lattice gas automaton is presented. Additionally, its varying capabilities and extensions are introduced. Finally, different methods for the characterization of soot are described. In this context, Raman spectroscopy, FIB-SEM and HRTEM imaging can give insights into the composition and morphology of soot.

2.1 Automotive soot filters

Focusing on the main field of application, the structure and principle of operation of automotive soot filters are discussed in the following. In general, one can differentiate between different principles of soot filtration systems in the automotive sector. However, for cars equipped with a DPF from factory, the concept of wall-flow filters is predominant [65]. These filters are constructed from ceramic material, typically Silicon Carbide (SiC) or Cordierite [30]. Moreover wall-flow filters using aluminum titanate and sintered metal filters exist [35]. Prerequisites of these are a high filtration efficiency, specifically for very small particles, thermal shock resistance, thermal stability, a low filter back pressure and mechanical resistance [35]. They are commonly produced using extrusion and exhibit a typical filtration surface, with respect to the volume of the filter, of $1\,m^2/l$, a thickness of the channel walls of $0.3-0.4\,mm$ as well as a channel density of 300-400 channels per square inch [35].

An exemplary soot filer array is shown in Figure 2.1, in which the ceramic monolith filter is displayed in yellow.

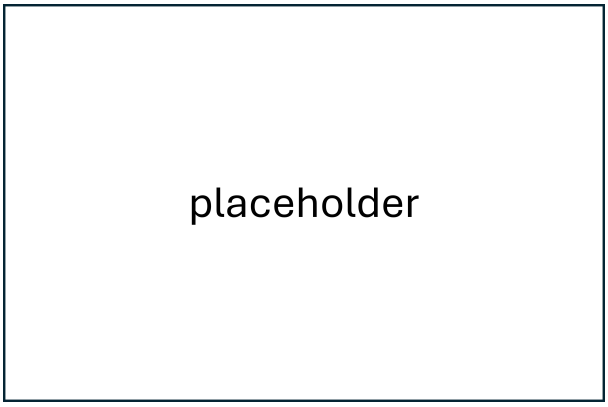

Figure 2.1: Principle of operation of an automotive soot filter [103]. The size of the filter is chosen according to the engine displacement, typically with a filter volume of 1.2-2 times the engine displacement [35].

These filters consist of straight channels, with half of the channels being sealed on the inlet side and the other half being sealed on the outlet side, forming a honeycomb-like structure [1, 52]. The working principle of a wall-flow filter is visualized in Figure 2.2. The dirty exhaust gas, carrying soot particles, enters the array in inlet channels, which are blocked at the outlet. This forces the exhaust gas to flow through the channel walls into the outlet channels, which are blocked at the inlet. Since no bypass exists in this type of filter, high filtration efficiencies are achieved. Inside of the empty filter, the particles are initially filtered by a process known as deep bed filtration.

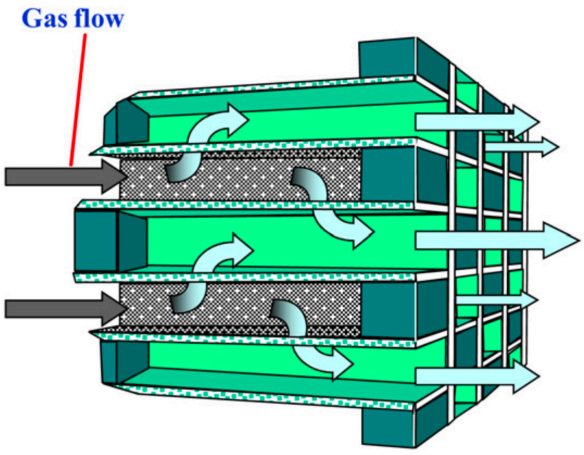

Figure 2.2: Working principle of a wall-flow filter [133].

The main filtration performance is achieved once a soot layer has formed, known as filter cake. Ample publications exist, in which the deposition and formation of soot layers is studied [1, 27, 95, 119], making it possible to improve the filtration efficiency. One possible

method to improve the filter performance is to modify the cross sections of the channels at the inlet and outlet. Specifically, a larger cross section at the inlet in combination with smaller cross sections of outlet channels can reduce the flow resistance and aid with the problem of ash deposition [35]. Another approach is the usage of acicular mullites to improve the overall filter performance, also allowing for the design of their characteristics to meet requirements for special use cases [101]. Also, the influence of the porosity of the filter wall onto its performance was investigated [99]. Regarding the position of the DPF in the exhaust gas system, it was found that the overall size of the filter could be decreased by placing the filter system before the turbo charger [118]. It was argued that this was due to the lower Péclet number for this arrangement and the higher exhaust gas temperatures closer to the engine, facilitating continous passive regeneration.

2.2 Filtration mechanisms

The filtration of solid matter is based on several physical key principles, which can occur separately or in conjunction, depending on the specific case. These principles are the sieve effect, inertia, diffusion, electrostatic attraction and gravity [21]. The sieve effect describes the retention of particles by the filter material, if the particles are larger than the filter channels. Furthermore, particles which are smaller than the filter channels can be separated from the gas flow by different methods, which are visualized in Figure 2.3.

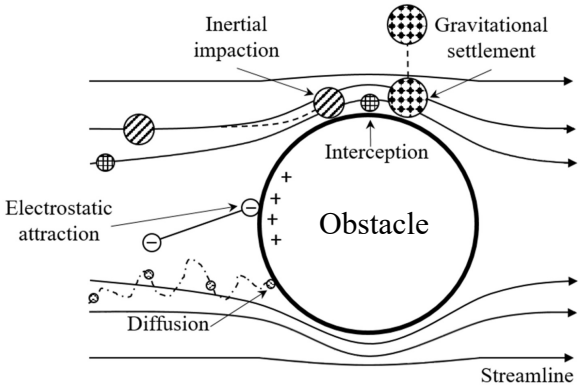

Figure 2.3: Illustration of different physical phenomena inducing separation of a particle from a fluid flow onto an obstacle [13].

In general, particles follow the stream lines of the flow going through the filter channels. If the inertia of a particle is large enough that it is not able to follow the stream line, it collides with the filter material in a process called inertial impaction. A limiting particle path can be calculated for particles by analysing the inertial force of the soot particle and the force, which it receives by the fluid flow. These particles are small enough not to be filtered by impaction. This means that they pass the barrier following the limiting

particle path with subsequent interception at the barrier. Moreover, even smaller particles can be filtered by random Brownian diffusion, meaning collision with the filter material after random motion, or electrostatic attraction. In conclusion, particles, which are much smaller than the channels inside of the filter walls, can be separated from the exhaust gas flow.

Furthermore, the filtration is classified by surface filtration and deep bed filtration [21], as illustrated in Figure 2.4. As described previously, the initial stages of soot filtration by ceramic DPFs is characterized by deep-bed filtration, meaning that particles adsorb inside of the filter material. Over time, a filter cake begins to form, which then provides the main filtration performance [1] but also leads to a buildup of filter back pressure.

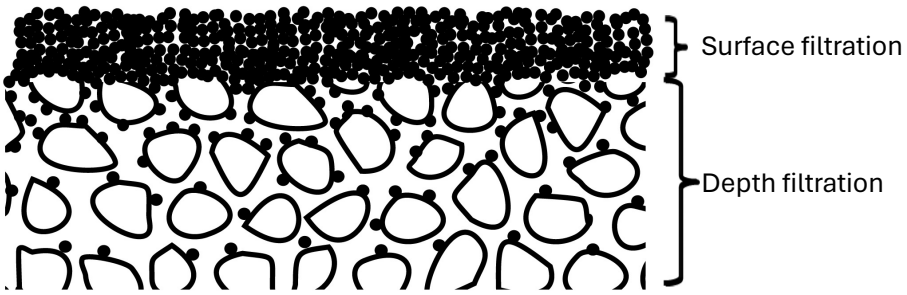

Figure 2.4: Visualization of surface and depth filtration on a filter medium [116].

2.3 Regeneration strategies

As mentioned above, a soot cake is formed inside of the channels of the DPF during operation. An increasing thickness of the filter cake leads to an increase in filter back pressure, resulting in less engine power or higher fuel consumption. Also, if the soot load on a filter is too large, its exothermic combustion during regeneration can lead to temperature peaks, which are detrimental to the filter material [35]. For this reason, the DPFs require periodic regeneration.

The soot filter regeneration can be performed with different mechanisms and operation procedures, all being based on the gasification of the solid soot particles by oxidation. In this context, it is distinguished between active and passive regeneration, depending on the oxidising agent.

Active regeneration, using oxygen as the oxidising agent, follows the chemical equations shown in the equations (2.1) and (2.2) [152] for temperatures in the range of $550\,°C - 650\,°C$ [35]. To reach these temperatures in the particle filter, different methods are used. According to [35], decreasing the efficiency of the engine or combustion of the fuel at an oxidising catalytic converter are possible, both resulting in a fuel penalty. For this reason,

this type of regeneration is only employed actively after a critical soot load is reached. Also, a sufficiently high concentration of oxygen, typically above 5 %, in the exhaust gas stream is necessary [35].

$$C + \frac{1}{2}O_2 \rightarrow CO \tag{2.1}$$

$$C + O_2 \rightarrow CO_2 \tag{2.2}$$

Contrary to active regeneration, passive regeneration uses nitrogen dioxide (NO_2) as oxidising agent for the gasification of soot. The resulting chemical equations are shown in the equations (2.3) and (2.4) [55]:

$$C + 2NO_2 \rightarrow CO_2 + 2NO \tag{2.3}$$

$$C + NO_2 \rightarrow CO + NO \tag{2.4}$$

Passive regeneration occurs for temperatures of $250\,°C - 350\,°C$, which are common in the exhaust gas at the DPF stage. For this reason, the passive regeneration with NO_2 occurs continuously without an additional fuel penalty [153]. In general, the regeneration with NO_2 is slower than the regeneration with oxygen. However, depending on the operating condition of the engine, the passive regeneration is able to oxidise the same amount of soot, which is being deposited, thus increasing the interval until active regeneration becomes necessary [35].
Since the early introduction of ceramic honeycomb DPFs by Corning Glass Works [52], a great effort was made to improve the original design and alternative regeneration methods were introduced. Electrical heating was tested on heavy duty vehicles as a concept to improve regeneration [60]. Furthermore, the regeneration can be improved by lowering the temperature range necessary for oxidation, by the addition of catalysts, either fuel borne or as a coating on the filter material [153, 35]. Another possibility is the use of microwave technology to reduce energy requirements and regeneration time [96]. Moreover, nonthermal plasmas can be used to aid regeneration [123].

2.4 Simulation of soot combustion

Here, a brief overview over the numerical analysis of soot filter regeneration is given. Simulation efforts were made, concerning the different scales of the problem at hand, i.e. the vehicle scale, the channel scale as well as the pore scale in the soot cake. Bissetti et al. [8, 9] introduced a single-inlet, single-outlet model to simulate soot combustion for wall-flow filters. Later, Konstandopoulos et al. [64] extended the model of [8] by

catalyst-assisted soot oxidation. Mitsutani et al. [92] employed a 2D model to study the regeneration of DPFs for different fuels, with and without additives as well as catalysts. Furthermore, Singh et al. developed a integrated system model, which simulates the generation of soot in the cylinders of an internal combustion engine, the diesel oxidation catalyst (DOC), as well as the diesel particle filter [124]. Kostoglou et al. performed early simulations for multi-channel wall flow filters [66], analysing the formation of hot spots during exothermal combustion. Other groups analysed ash deposits during regeneration on the channel scale [17] or the formation of the soot filter cake [119] and the influence of different plugging arrangements [5], both on channel scale. Furthermore, the influence of catalyst activity onto the combustion regime was investigated [112]. Greiner et al. used x-ray tomography to receive a 3D representation of the porous soot structure, which they subsequently used for combustion simulations [41]. Moreover, the flow behaviour and heat transfer of porous media, specifically for the use case of DPFs was studied in [38]. Recently, simulations were performed to evaluate the evolution of the filter back pressure during the filtration and regeneration stages [144]. In the following chapter, the lattice Boltzmann method and its evolution will be introduced. Also, extensions for the simulation of different physical phenomena, as well as for the application in soot combustion, will be presented.

2.5 Lattice Boltzmann method

The lattice Boltzmann method was derived as an evolution of the lattice gas automaton (LGA), which is a cellular automaton based on the principle of particle movement and collision to model fluid flow. The model was introduced by Hardy, Pomeau and De Pazzis in 1973 [46] and is commonly referred to as HPP model. Several rules are the basis of the HPP LGA. The domain is discretized by a lattice and the position of particles is tracked by boolean variables. This means that a particle either exists or does not exist on a given position. The possible directions, in which the particles can move, are discretized orthogonally, meaning that particles can only travel in the horizontal and vertical direction. Furthermore, particles can only exist on lattice nodes, not in between. In each time step, the collision on the lattice nodes according to a predefined collision rule and subsequent propagation of the particles are performed. Particles will only change their velocity and direction by colliding with other particles. This HPP lattice gas automaton was non-isotropic due to its rotational invariance. Later, Frisch, Hasslacher and Pomeau proposed an upgraded model using a hexagonal lattice grid [37]. The main difference was the rotational isotropy due to the hexagonal lattice, resulting in great popularity of the FHP model. In 1988, McNamara and Zanetti proposed a new approach to lattice gas

automata [90]. Instead of using boolean variables to describe the location and velocities of particles, they used the Boltzmann equation and probability distribution functions on a hexagonal lattice. With this approach using ensemble averages, the statistical noise, which LGA exhibit, could be removed. This, in turn, decreased the computational effort of simulations. Only one year later, in 1989, Higuera and Jiménez introduced their version of LBM, also employing a linearized collision operator [50]. Subsequently, both Chen et al. [16] and Koelman et al. [63] used the BGK approximation for the linearized collision operator proposed for lattice gases in [7] for the lattice Boltzmann method. Qian et al. [102] replaced the collision matrix of [50] by a single relaxation time, also utilizing the BGK collision operator [7]. Using multiscale techniques, they showed that their LBM formulation describes the Navier-Stokes equation to second order of approximation. Moreover, in 1997, He & Luo derived the lattice Boltzmann equation as a finite difference discretization of the Boltzmann equation, independently from LGA [48].

Furthermore, the lattice Boltzmann method was extended to treat multi-phase flow problems, for which four differing methods can be distinguished [2].

The Shan-Chen method [121, 122] introduced a pseudo-potential based on the concept of nearest neighbour interaction to model multi-phase flow problems, for which a force term is incorporated into the LBM equation by a shift in the velocity. This method then was extended to model non-ideal fluids by adding realistic equations of state [151]. Furthermore, the biggest limitation of this method, the fact that the equation of state could not independently be chosen from the surface tension, was overcome by tuning of the interparticle potential in [113]. Falcucci et al. [33] showed that the inclusion of soft-core repulsion could prevent droplet coalescence, enabling the simulation of bubble swarms. Viscous coupling effects were studied by [6]. Moreover, the dependency of the surface tension on the relaxation time for a model proposed by [49] was studied by [53], in which this issue could be resolved. Furthermore, the basic Shan-Chen model was extended to control the surface tension independently from the equation of state in [19]. Also, to increase the model stability for high Reynolds numbers, the Shan-Chen model was coupled with a cascaded LBM in [85]. Furthermore, the evolution of spurious currents was studied for the specific case of a rising bubble in [111], in which it was found that spurious currents increase for smaller mesh discretizations.

Contrary to that, the free-energy model proposed by [132] uses a free-energy function to describe the surface tension effects. The second order moments of the equilibrium distribution function are modified to include a non-ideal thermodynamic pressure tensor. Furthermore, correction terms for the equilibrium distribution function are needed to restore galilean invariance. Many studies exist on the reduction of spurious currents. Wagner et al. [137] introduced a body force in order to reduce spurious currents, with

Lee et al. [76] trying to reduce them by using other forcing methods. By applying the scheme proposed in [54], and using a fourth order approximation for the calculation of derivatives in the pressure tensor, the spurious currents were reduced in [120]. Moreover, it was found that a careful choice of the equilibrium distribution function could decrease this problem [100]. Additionally, the model was extended to recover the Cahn-Hilliard equation, which enabled the simulation of higher density ratios [154].

The color-fluid model of [43], which is based on the lattice-gas model of [108], uses red and blue particle distribution functions to allocate lattice nodes to each phase. This model was extended by inserting an interface between the immiscible phases, effectively modelling the surface tension directly at the interface [81]. In [74], the diffusion and phase separation properties were examined and the lattice spinning problem was analysed. Also, Grunau et al. [42] developed a model including the variation of density and viscosity.

The He-Chen-Zhang model [49, 47] uses an index function, similar to the phase field theory, to track the interface and allocate phase space. Due to less discretization errors of the forcing term, this model exhibits enhanced stability. Moreover, it was extended to model high density ratios in [77], which also exactly recovers the phase field equation. Additionally, a MRT variant of this model was introduced in [89]. Mukherjee & Abraham [94] transferred the formulation of [77] from a cartesian coordinate system to an axisymmetric coordinate system and transformed it into a MRT collision model. With these modifications, relatively small viscosities were simulated.

Regarding heterogeneous reactions in porous media, several lattice Boltzmann models have been developed in the past years. Kang et al. [58] introduced a lattice Boltzmann expression for a dissolution model, which was initially presented by [36]. This model treats homogeneous reactions in the fluid phase and a heterogeneous reaction at the solid-fluid interface, incorporating the transport of reactants and products with the fluid flow. Notably, this model is confined to isothermal cases, omitting the simulation of the thermal field. To model non-isothermal heterogeneous reactions effectively, it becomes crucial to consider the temperature field and conjugate heat transfer at the solid-liquid interface. Maintaining continuity of temperature between the fluid and solid phases at the interface, along with conserving the total heat flux on either side, is paramount. Several approaches have been developed for this purpose.

Wang et al. [138] employed the conjugate boundary condition, proposed in [18], and defined a half-way conjugate condition for LB methods. This is the simplest way of describing conjugate heat transfer, as one only needs to take into account the different properties of the phases by employing different relaxation times in the LB method. The advantage of the model is its straight forward implementation and small computational

effort. However, the model is only applicable for cases in which the thermal conductivity ratio and thermal diffusivity ratio match. This becomes apparent by employing the Chapman-Enskog expansion to retrieve the macroscopic transport equation from the LBM. Chen et al. [15] utilized this model to study the thermal processes in a micro-reactor for the catalytic decomposition of ammonia, forming hydrogen. The previously detailed restrictions of the conjugate heat transfer method were resolved by different approaches. Meng et al.'s thermal counter-slip method [91] iteratively computes interface temperatures, particularly suited for high-frequency oscillating flows. Xu et al. [143] extended this method for describing conjugate heat transfer in heterogeneous reactions. Moreover, Karani et al. [59] incorporated the conjugate heat transfer through source terms in the LB equation, eliminating the need for iterative solution of the energy equation at the interface. This is done by comparing the result of the Chapman-Enskog expansion of the LB transport equation with the correct formulation of the energy conservation in continua. The missing terms are then added as a source term to the LBM formulation of the temperature field. Alternatively, Li et al. [80] proposed a bounce-back-like approach to address conjugate heat transfer in an explicit manner. Here, the ratio of the densities and specific heat capacities of the media on either side of the interface is used to calculate the share of a distribution function streaming across the interface, which is reverted (comparable to bounce-back boundary condition), and the share, which is streamed across. For simple geometries, the implementation of this algorithm is straightforward. In case of precise interface tracking in combination with 3D simulations, the method becomes quite complex. Moreover, Lu et al. [84] presented an approach to model conjugate heat transfer by interpolating the exact boundary temperature based on the temperature of the adjacent phases, and using it to calculate the distribution functions at the imaginary node on the boundary by assuming that the non-equilibrium parts of the distribution function are equal to those of the nodes adjacent to the boundary. Another possibility to model conjugate heat transfer was introduced by Pareschi et al. [98], who calculated the temperature at the boundary by interpolation between the two phases. Hereby, they also took into account elaborate interfaces, not restricting themselves onto the half-way method. However, they then employ the so called Grad approximation to calculate the missing distribution functions for either side of the interface. The so-called Grad boundary condition was used by Chikatamarla et al. [20] to calculate the missing distribution functions at the boundaries of the computational domain. It is based on a truncated Hermite polynomial expansion of the Maxwell distribution function, which Harold Grad introduced in an effort to approximate a general solution of the Boltzmann equation [40]. It is noteworthy that only a limited number of publications by a few authors about the specific case of soot combustion exist. Throughout the years, Yamamoto et al. de-

veloped an incompressible LB model for the heterogeneous combustion of diesel soot, gradually extending it to treat realistic soot geometries and simulations on the filter scale [148, 146, 147, 150, 149, 145]. Also, Liu et al. [83] simulated round char particles, considering the formation of a transport-inhibiting ash layer. Xu et al. [143] utilized a single relaxation time (SRT) approach for the combustion of a porous soot structure, albeit without accounting for compressibility effects or thermal expansion, and solving conjugate heat transfer iteratively. In contrast, Lei et al. [78] adopted a multiple relaxation time (MRT) approach for the same soot combustion problem, considering thermal expansion and providing an explicit expression for the conjugate heat transfer. It is important to note that the treatment of conjugate heat transfer in [78] involves calculating spatial derivatives, which include the product of density and specific heat capacity along with temperature. This not only escalates computational costs but also adds complexity to the treatment of boundary conditions.

2.6 Characterization of soot

In the following, different methods for the characterization of soot and relevant literature are presented.

2.6.1 FIB-SEM

In order to allow for the comparison of the experimental data with the results of the simulations, the morphology of the soot is analyzed.

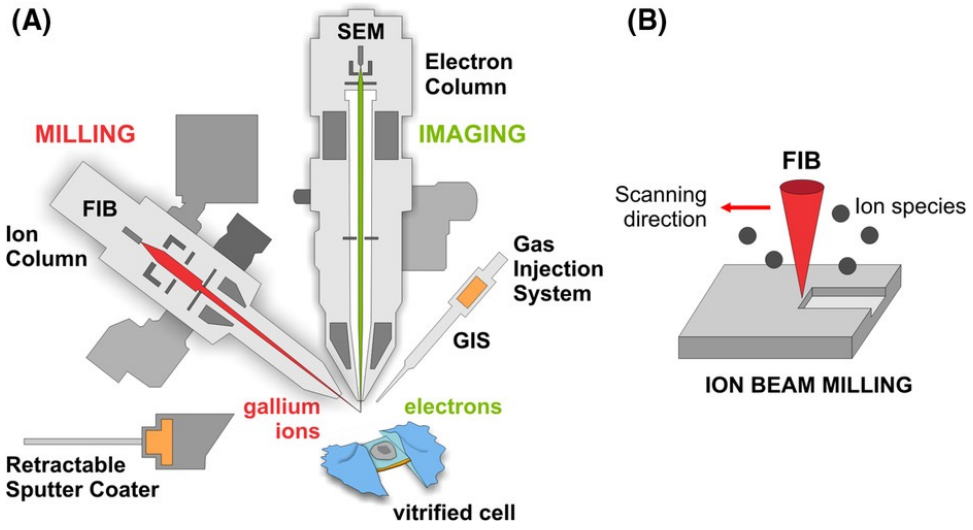

Figure 2.5: Scheme describing the principle of the FIB-SEM method (A) and an enlarged view of the milling process (B). The imaging column is shown in green, with the milling column being shown in red. [68].

The goal is the three-dimensional reconstruction of the soot used for experiments to perform combustion simulations not only with the correct reaction kinetics, but also with the correct mesoscopic structure of the solid domain. This can be achieved by using Focused Ion Beam Scanning Electron Microscopy (FIB-SEM). FIB-SEM differs from classical SEM in the sense that a focused ion beam is used repetitively to remove thin layers of the geometry and analysis of the geometry through SEM imaging. The working principle of FIB-SEM is shown in Figure 2.5. Here, the two main components, i.e. the electron column of the SEM, responsible for the imaging, as well as the ion column of the FIB, responsible for the milling, are shown in green and red, respectively. Furthermore, on the right-hand side of the Figure, a magnified view of the ion beam milling is displayed. With this principle, multiple SEM slices are received. One example of such a SEM slice is shown in Figure 2.6, which visualizes different phases by grey scales. The example shown here only consists of solid soot, displayed in white, and void space, displayed in black. When analyzing other structures, which contain multiple different solid phases, i.e. a substrate and a hydrophobic additive, these would be represented by different shades of grey. This makes it possible to recreate elaborate 3D structures of multiple phases, while not being restricted to only analyze the morphology.

Figure 2.6: FIB-SEM slice of the soot samples of ICVT as received from HZB as .tif file.

With this invasive method, a three-dimensional soot sample is characterized by a set of two-dimensional SEM slices. By reassembling the slices, the original 3D structure can

be reconstructed and the geometry can be utilized for the LBM simulations.

2.6.2 Raman spectroscopy

Raman spectroscopy can be used to analyze the carbon structure of the soot. The method is based on the Raman scattering effect, which describes a form of inelastic photon scattering by the matter, of which information of the structure is to be gained. It was first described by C. Raman in 1928 [105]. In Figure 2.7, the working principle of a Raman spectroscopy setup is shown. The sample is exposed to a monochromatic laser beam, which excites a change of the vibrational energy of the sample. As a result, the a shift in wavenumber of the scattered light occurs. The scattered light is then collected by a lens array and enters the spectrometer, in which a charge-coupled device camera analyses the spectrum.

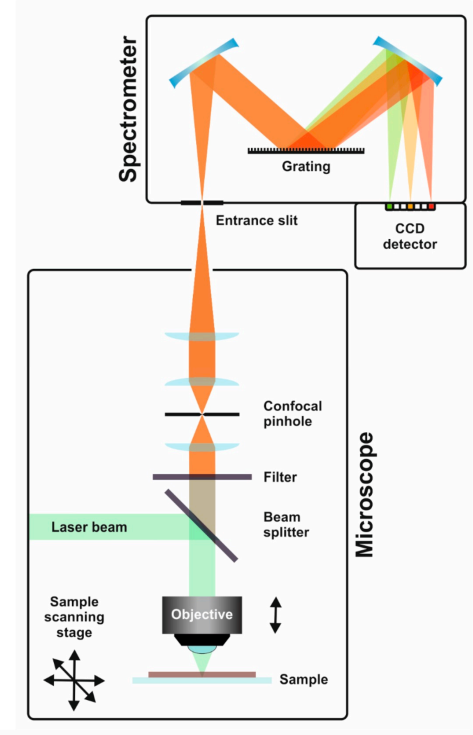

Figure 2.7: Working principle of a Raman spectrometer. A monochromatic laser beam is used to excite Raman scattering on the sample. The scattered light is then collected and enters the spectrometer unit, in which a charge-coupled device (CCD) camera analyses the spectrum. [115]

Tuinstra and Koenig presented the fundamentals regarding the Raman analysis of carbon structures in 1970 [134]. They analysed graphite as well as different, less structured carbon materials and reported the corresponding Raman spectra as well as wavenumbers of the bands. They reported a single characteristic peak at a wavenumber of $1575\,cm^{-1}$

for single crystal graphite. Contrary to that, activated carbon exhibited a second characteristic peak at a wavenumber of $1355\,cm^{-1}$. Both spectra are shown in Figure 2.8. The intensity of the peak at a wavenumber of $1355\,cm^{-1}$ was associated with an increase of less organized carbon and the decrease of the size of the graphite crystals [134].

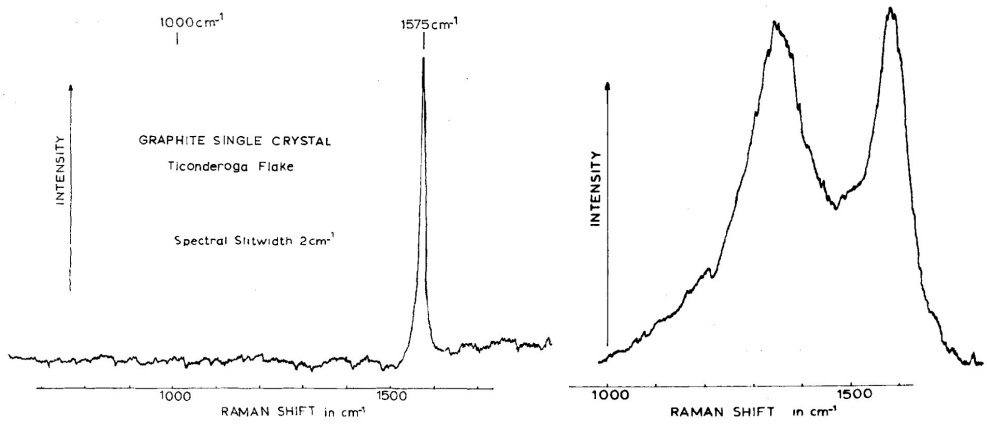

Figure 2.8: Raman spectra of single crystal graphite (left) and activated carbon (right) [134].

In 2005, Sadezky et al. [110] presented important findings for the proper analysis of Raman spectra of soot. They used a five band fit, with a G band and D1-D4 bands. For these bands, Gaussian and Lorentzian functions were used and different combinations of Gaussian and Lorentzian bands were studied. An exemplary Raman spectrum with a five band fit is shown in Figure 2.9, presenting the G band, associated with graphite as well as the D1-D4 bands, which are associated with a disordered graphitic lattice, specifically edges and surface layers for the D1 and D2 bands [139]. The D3 and D4 bands are associated with amorphous carbon and ionic impurities [23].

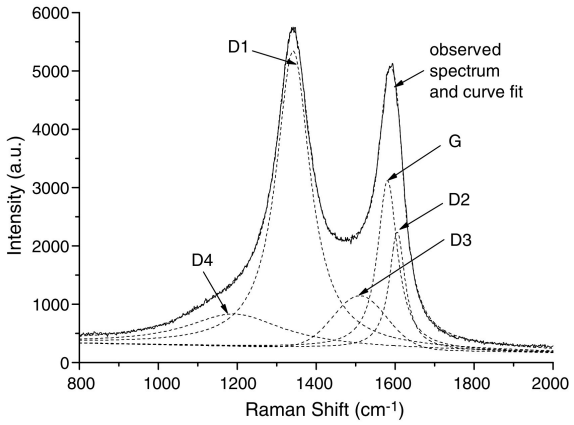

Figure 2.9: Evaluation of a Raman spectrum by applying a five band fit [110].

Furthermore, the change of the structure of different types of soot by oxidation was studied in [62, 61]. It was found that some types of soot exhibit an increase in the degree of

structure throughout oxidation, while others did not show changes in the Raman spectra. Lapuerta et al. [71] presented a study of the effect of laser wavelength, exposure time and power-per-unit surface of incident laser beam onto the raman spectra of diesel soots. As a result, recommendations for the parameters of Raman spectroscopy are given. In [117], different methods for the calculation of the crystallite length based on Raman spectroscopy data were investigated and the results were compared with data obtained from TEM images and X-ray diffraction (XRD) measurements. Le et al. [75] analysed soot generated with a CAST soot generator. It wa shown that heat treatment using an inert atmosphere removed organic compounds from the samples.

2.6.3 Transmission electron microscopy

Utilising high resolution transmission electron microscopy (HRTEM), it is possible to receive structural information of crystalline samples on the atomic scale. In the context of the study of soot, it is possible to investigate the soot morphology on the primary particle scale. A TEM uses a similar structure as a light microscope, with the difference, that electrons are used instead of visible light, necessitating the use of electromagnetic lenses, rather than optical lenses to focus the electron beam. The sample thickness is limited by the fact that the electrons need to be able to pass through the sample. Regarding the application of HRTEM for the study of the morphology of soot, Palotas et al. [97] presented a method to evaluate HRTEM images of diesel soot using computational image analysis techniques. Exemplary, one HRTEM image of diesel soot and the corresponding extracted fringe pattern, are shown in Figure 2.10.

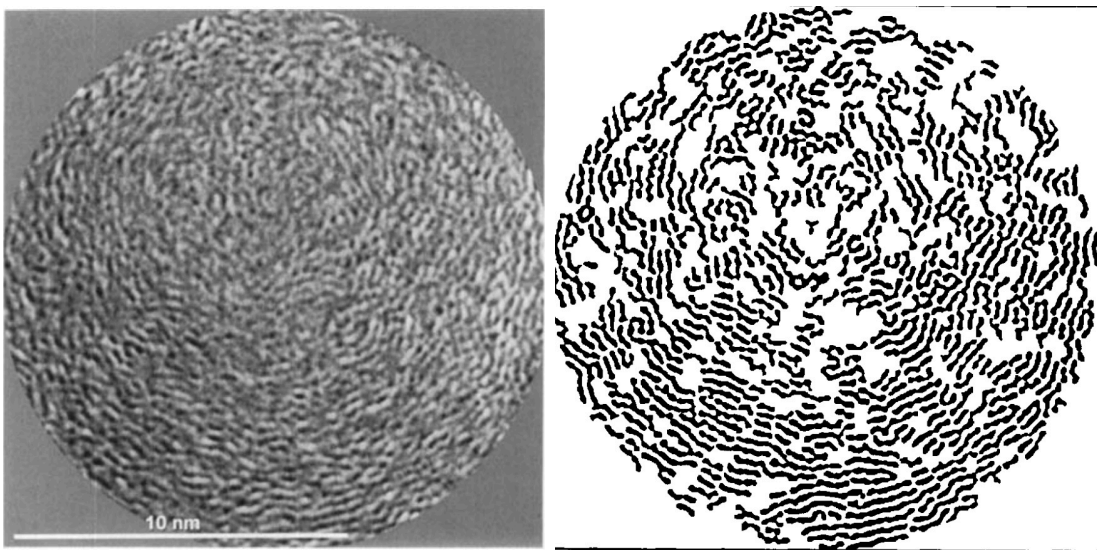

Figure 2.10: HRTEM image of diesel soot (left) and extracted fringe pattern (right) [97].

In 2007, R. Vander Wal et al. [136] investigated the combustion of diesel soot with

HRTEM. It was found that diesel soot would undergo ”densification”, meaning that the particles combust heterogeneously. In this context, the hollowing out of the particles at the core was observed. In the investigation of Euro-IV and Euro-VI diesel soot with HRTEM by Knauer et al. [62], no significant morphological changes before and after oxidation could be observed. Alfè et al. [3] investigated the structures of soot from different fuels regarding their structure on the nanoscale and discussed its influence on the reactivity. Subsequently, Botero et al [10] introduced a method to analyse the HRTEM images and determine the length, tortuosity and spacing of the carbon fringes. This method was then used to investigate the primary soot particles formed in heptane flames and the influence of temperature and fuel type onto the nanostructure was determined. The change in structure throughout the formation process of flame-formed soot particles was studied in [4]. Extending their previous work, Botero et al. [11] extended their investigation and studied the fringe length, their number and tortuosity as a function of the radial position inside of the soot primary particles. In this context, a core-shell structure was observed. This means that the particles consisted of a core, which exhibited larger polycyclic aromatic hydrocarbons when compared with the outer shell of the particle.

Chapter 3

Theoretical Principles

The ability to precisely calculate the fluid flow, depending on the case of application, coupled with other physical phenomena, i.e. surface effects or homogeneous and heterogeneous reactions, is quite important both in the industry for designing and planning of facilities for energy and mass transport as well as material conversion and in the academic world for research and development purposes, respectively. Classical methods are based on describing those phenomena mentioned with homogeneous equations for the macro-scale. I.e., the description of fluid flow is performed by utilising the Navier-Stokes equations, comprised of the continuity equation (equation 3.1) as well as the momentum balance (equation 3.2).

$$\frac{\partial \rho}{\partial t} + \nabla \cdot (\rho \vec{u}) = 0 \tag{3.1}$$

$$\rho \left(\frac{\partial \vec{u}}{\partial t} + (\vec{u} \cdot \nabla)\vec{u} \right) = -\nabla p + \mu \nabla^2 \vec{u} + \vec{k} \tag{3.2}$$

Except for basic problems, like the Poiseuille flow, for which an analytic solution for the Navier-Stokes equations exists, numerical methods must be utilised in order to calculate their solution. Typically, the domain of interest is discretized by a mesh and subsequently the system of differential equations is discretized in space and time and numerically solved at the grid points. The parallelization of this process can be quite difficult to conduct. The lattice Boltzmann method, being a method describing the mesoscopic scale, promises advantages in this regard. In the following, this chapter introduces the lattice Boltzmann method, describes the modelling of heterogeneous reactions in porous media, and finally introduces their LBM expression.

3.1 Lattice Boltzmann method

The lattice Boltzmann method follows a so-called bottom-up strategy, meaning that starting from equations describing the transport on the microscopic scale, i.e. the Boltzmann transport equation, a mesoscopic expression is derived, which can be translated into a macroscopic expression by the means of mathematical up-scaling techniques, i.e. asymptotic analysis or the Chapman-Enskog expansion. It is based on the Boltzmann equation, which describes the statistical distribution of particles (atoms or molecules) on the mesoscopic scale. It can be numerically solved for a given domain by discretising it onto a lattice with equidistant nodes. The transport of the particles is then allowed only in predefined directions and the collision of particles takes place at the lattice nodes. This method is local, denoting that for the evaluation of the collision step at one lattice node, no information of other lattice nodes is necessary. This characteristic makes the parallelisation of the computation straightforward.

3.1.1 Boltzmann equation

For the prediction of macroscopic transport parameters, i.e. the heat conductivity or the diffusion coefficient for the transport of matter, from the microscopic properties of a system, it is necessary to precisely describe and model the microscopic state of the system. Calculating the position and velocities for a set of particles and modelling their dynamics is limited by the computational power available today. With the Boltzmann equation, the transport of particles can be described in a statistical manner. It does not describe the position and velocity of each particle separately, but rather is a model for the transport of a probability distribution function $f(\vec{x},t)$, which describes the probability to meet a particle with a given speed at a distinct point $\vec{x}$ and time t. Consequently, the physical space of the distribution function f is the phase-space, defined by the position $\vec{x}$ and the velocity $\vec{u}$. The Boltzmann equation is depicted in equation (3.3). Here, f is the distribution function and Ω is the collision operator, which describes the interaction between particles.

$$\frac{\partial f}{\partial t} + \vec{u} \cdot \nabla f = \Omega \tag{3.3}$$

As it can be seen, the collision operator Ω contains the whole description of the physical phenomenon of interest and must be known in order to calculate the solution of the Boltzmann equation. Its description is generally rather complicated. The transition from the Boltzmann equation to the lattice Boltzmann equation is done in accordance with [142]. In 1954, Bathnagar, Gross and Krook introduced a simpler description of the collision operator, which allows for the solution of the Boltzmann equation without

significant errors, which is known as BGK approximation [7]. The BGK approximation, shown in equation (3.4), assumes that the collision operator can be approximated as the difference of the distribution function f and its equilibrium value f^{eq}, multiplied by the collision frequency ω.

$$\Omega = \omega(f^{eq} - f) \tag{3.4}$$

Here, the collision frequency ω is the reciprocal of the relaxation time τ. Substituting equation (3.4) into equation (3.3) results in equation (3.5).

$$\frac{\partial f}{\partial t} + \vec{u} \cdot \nabla f = \omega(f^{eq} - f) \tag{3.5}$$

3.1.2 Discretization of the Boltzmann equation

The Boltzmann equation as shown in equation (3.5) is then discretized onto an equidistant lattice with a given set of pre-defined directions, the so-called lattice velocity vectors $\vec{c}_i$. Using a first order finite difference discretization in time and space results in equation (3.6) [114]:

$$\frac{f_i(\vec{x}, t+\Delta t) - f_i(\vec{x}, t)}{\Delta t} + c\,\frac{f_i(\vec{x} + c_i\Delta t, t+\Delta t) - f_i(\vec{x}, t+\Delta t)}{\Delta x} = \Omega \tag{3.6}$$

The subscript i denotes the directions, for which the equation is evaluated, $\vec{c}_i$ describes the lattice velocity vector, $\vec{x}$ stands for the spatial coordinate, t describes the time and Δx and Δt denote the size of the spatial and temporal step. Also, the lattice speed c is defined as the ratio of the size of the spatial and temporal discretization as $c = \frac{\Delta x}{\Delta t}$. Reordering of equation (3.6) then results in the lattice Boltzmann equation, which is shown in equation (3.7).

$$f_i(x + c_i\Delta t, t+\Delta t) - f_i(x,t) = \frac{\Delta t}{\tau}\left[f_i^{eq}(x,t) - f_i(x,t)\right] \tag{3.7}$$

It is important to mention that simulations with the lattice Boltzmann equation are performed in non-dimensional lattice units (lu), and that the conversion factors are usually chosen in such a way that both Δt and Δx assume the value of 1 in lattice units. This results in the lattice speed $c = 1$, which is the reason why c, Δt and Δx are usually omitted from the lattice Boltzmann transport equations in the literature. Nonetheless, this is only valid if the convention for the transformation to lattice units is used, which is not mandatory. As mentioned in the book of Mohammad [93], the left-hand side of the equation describes the streaming step, which is the transport of the distribution function f_i, along the lattice velocity vector $\vec{c}_i$. The right-hand side of the partial differential equation represents the collision step. The explicit nature of the equation has several

advantages, i.e. the property of being effortlessly parallelisable.

Furthermore, the discretized equilibrium distribution function is derived from the Maxwell distribution function, which can be written as equation (3.8):

$$f_i^{eq}(x,t) = \frac{\rho}{(2\pi RT)^{D/2}}\, exp\left(-\frac{(\vec{c}_i\cdot\vec{c}_i - 2\vec{c}_i\cdot\vec{u} + \vec{u}\cdot\vec{u})}{2RT}\right) \tag{3.8}$$

Here, R denotes the ideal gas constant, T stands for the temperature in Kelvin, D represents the dimension of the problem, $\vec{u}$ is the macroscopic velocity vector and ρ is the density. Expanding the exponential function in equation (3.8) with a Taylor series according to [45] results in the following expression (3.9):

$$f_i^{eq}(x,t) = \rho w_i\left(1 + \frac{2\vec{c}_i\cdot\vec{u} - \vec{u}\cdot\vec{u}}{2c_s^2} + \frac{(\vec{c}_i\cdot\vec{u})^2}{2c_s^4}\right) \tag{3.9}$$

In this equation, w_i denotes the lattice weight and c_s^2 is the squared lattice speed of sound. A velocity set is fully defined by a set of lattice velocity vectors $\vec{c}_i$ and the corresponding weighting factors w_i. The lattice weights must satisfy multiple conditions, which then are used for the derivation of their values. This procedure is discussed in detail in the following section.

3.1.3 Discrete lattice velocity models

In the previous section, the discretization of the Boltzmann equation onto a given velocity space was shown, but the specific choice of a velocity discretization scheme remains to be defined. Several different finite discrete velocity models exist, which are commonly used in literature. In general, using a velocity set with a higher count of lattice velocities increases accuracy and ability to resolve different physical phenomena, but also increases the memory requirement and computational cost [67]. Also, it is mentioned that the nomenclature for lattice velocity sets, as proposed in [102], is used here. The velocity sets are named as DdQq, with d and q denoting the spatial dimension of the scheme, i.e. 1D, 2D or 3D, and q referring to the number of discrete directions used in the model. Furthermore, readers need to be cautious since the arrangement of the lattice velocity vectors can vary in different publications, even for the same velocity set. For a given velocity set, the directions of the vectors are defined, but the nomenclature and the numbering from $0\ldots q-1$ or $1\ldots q$ may vary. Throughout this thesis, the nomenclature and numbering will be consistent and follow the convention as provided in this chapter.
The lattice Boltzmann method evolved from the lattice gas automaton, which was based on a two dimensional squared lattice, resulting in each lattice node having four neighbours and four specific lattice velocity directions [46]. This model however was not able

to describe the Navier-Stokes equation due to insufficient lattice isotropy [67]. The first lattice gas automaton, which was able to reproduce the correct behaviour of fluid dynamics, was introduced in 1986 by Frisch et al. [37], and was based on a triangular lattice with hexagonal symmetry. In this way, given the resulting six lattice velocity directions, the lattice discretization exhibited enough isotropy to be able to resolve the Navier-Stokes equation [67]. This type of lattice was then used in other publications, i.e. [22], until it was found that sets of lattice velocities, which are derived by Gauss-Hermite quadratures, exhibit better accuracy and stability properties than models which don't stem from an exact quadrature [109]. For this reason, the most commonly used lattice discretization schemes are derived by using the Gauss-Hermite quadrature, but other schemes exist, which do not need to correspond to an exact quadrature, as shown in [28], which also exhibit isotropy and Galilean invariance. In the following, the rules which a lattice velocity set has to obey in order to satisfy the conditions as mentioned above, are presented, following the works of [72, 131, 114, 45]. These conditions can be derived by evaluating the 0^{th} to 2^{nd} order moments of the equilibrium distribution function (3.9), which represent the mass density, momentum density and momentum flux tensor:

$$\rho = \sum_i f_i^{eq} \tag{3.10}$$

$$\rho u_\alpha = \sum_i c_{i,\alpha} f_i^{eq} \tag{3.11}$$

$$\rho u_\alpha u_\beta + p\delta_{\alpha\beta} = \sum_i c_{i,\alpha} c_{i,\beta} f_i^{eq} \tag{3.12}$$

Inserting the expression (3.9) into equation (3.10) and applying the sum onto each summand of said equation leads to:

$$\rho = \rho \left[\sum_i w_i + \sum_i w_i \left(\frac{\vec{c}_i \cdot \vec{u}}{c_s^2} - \frac{\vec{u} \cdot \vec{u}}{2c_s^2} + \frac{(\vec{c}_i \cdot \vec{u})^2}{2c_s^4} \right) \right] \tag{3.13}$$

Using Einstein notation, equation (3.13) can be reformulated:

$$\rho = \rho \sum_i w_i + \rho \frac{u_\alpha u_\beta}{2c_s^2} \left[\frac{1}{c_s^2} \sum_i \left(w_i c_{i,\alpha} c_{i,\beta} \right) - \delta_{\alpha,\beta} \sum_i w_i \right] + \frac{\rho u_\beta}{c_s^2} \delta_{\alpha,\beta} \sum_i \left(w_i c_{i,\alpha} \right) \tag{3.14}$$

It becomes apparent that the equations with odd exponents regarding the lattice velocities, i.e. $c_{i,\alpha}$, have to equal zero to satisfy the basic condition of symmetry. Applying this constraints to equation (3.14) results in the omission of the last summand, leading

to the following equation:

$$\rho = \rho \sum_i w_i + \rho \frac{u_\alpha u_\beta}{2c_s^2} \left[\frac{1}{c_s^2} \sum_i \left(w_i c_{i,\alpha} c_{i,\beta} \right) - \delta_{\alpha,\beta} \sum_i w_i \right] \tag{3.15}$$

Subsequently, the moment of 1^{st} order, which was shown in equation (3.11), is evaluated.

$$\rho u_\alpha = \rho \sum_i c_{i,\alpha} w_i \left(1 + \frac{2\vec{c}_i \cdot \vec{u} - \vec{u} \cdot \vec{u}}{2c_s^2} + \frac{(\vec{c}_i \cdot \vec{u})^2}{2c_s^4} \right) \tag{3.16}$$

Again applying the Einstein convention to it results in:

$$\rho u_\alpha = \rho \left[\underbrace{\sum_i w_i c_{i,\alpha}}_{=0} + \frac{u_\alpha \delta_\alpha}{c_s^2} \sum_i w_i c_{i,\alpha} c_{i,\beta} - \frac{u_\alpha u_\beta \delta_{\alpha,\beta}}{2c_s^2} \underbrace{\sum_i w_i c_{i,\alpha}}_{=0} + \frac{u_\alpha u_\beta}{2c_s^4} \underbrace{\sum_i w_i c_{i,\alpha} c_{i,\beta} c_{i,\gamma}}_{=0} \right] \tag{3.17}$$

Here, the first, third and fourth summand equal zero, resulting from the necessary condition of rotational isotropy. This results in the final expression given as:

$$\sum_i w_i c_{i,\alpha} c_{i,\beta} = c_s^2 \delta_{\alpha,\beta} \tag{3.18}$$

Inserting equation (3.18) into equation (3.15) results in the omission of the second summand, which gives the following condition for the lattice weights:

$$\sum_i w_i = 1 \tag{3.19}$$

Finally, the 2^{nd} order moment of the equilibrium distribution function is evaluated. Inserting equation (3.9) into equation (3.12) results in:

$$\rho u_\alpha u_\beta + p\delta_{\alpha\beta} = \sum_i c_{i,\alpha} c_{i,\beta} \left[\rho w_i \left(1 + \frac{2\vec{c}_i \cdot \vec{u} - \vec{u} \cdot \vec{u}}{2c_s^2} + \frac{(\vec{c}_i \cdot \vec{u})^2}{2c_s^4} \right) \right] \tag{3.20}$$

Following the same procedure as with the 0^{th} and 1^{st} order moments gives:

$$\rho u_\alpha u_\beta + p\delta_{\alpha\beta} = \rho \sum_i w_i c_{i,\alpha} c_{i,\beta} + \rho \sum_i w_i c_{i,\alpha} c_{i,\beta} \frac{c_{i,\gamma} u_\epsilon \delta_{\gamma,\epsilon}}{c_s^2} \tag{3.21}$$

$$- \frac{\rho}{c_s^2} \sum_i w_i c_{i,\alpha} c_{i,\beta} u_\gamma u_\epsilon \delta_{\gamma,\epsilon} + \frac{\rho}{2c_s^4} \sum_i w_i c_{i,\alpha} c_{i,\beta} c_{i,\gamma} c_{i,\epsilon} u_\alpha u_\beta \tag{3.22}$$

Reordering the terms, omitting terms with odd numbers of lattice velocities for isotropy reasons and using equation (3.18) leads to:

$$\sum_i w_i c_{i,\alpha} c_{i,\beta} c_{i,\gamma} c_{i,\epsilon} = c_s^4 \left(\delta_{\alpha,\beta}\delta_{\gamma,\epsilon} + \delta_{\alpha,\gamma}\delta_{\beta,\epsilon} + \delta_{\alpha,\epsilon}\delta_{\beta,\gamma} \right) \tag{3.23}$$

This results in the full set of all necessary conditions for the discretization of the lattice velocity space, which is shown subsequently:

$$\sum_i w_i = 1 \tag{3.24}$$

$$\sum_i w_i c_{i,\alpha} = 0 \tag{3.25}$$

$$\sum_i w_i c_{i,\alpha} c_{i,\beta} = c_s^2 \delta_{\alpha,\beta} \tag{3.26}$$

$$\sum_i w_i c_{i,\alpha} c_{i,\beta} c_{i,\gamma} = 0 \tag{3.27}$$

$$\sum_i w_i c_{i,\alpha} c_{i,\beta} c_{i,\gamma} c_{i,\epsilon} = c_s^4 \left(\delta_{\alpha,\beta}\delta_{\gamma,\epsilon} + \delta_{\alpha,\gamma}\delta_{\beta,\epsilon} + \delta_{\alpha,\epsilon}\delta_{\beta,\gamma} \right) \tag{3.28}$$

$$\sum_i w_i c_{i,\alpha} c_{i,\beta} c_{i,\gamma} c_{i,\epsilon} c_{i,\zeta} = 0 \tag{3.29}$$

With the conditions for the derivation of the lattice velocity discretizations specified, the most prominent examples for one-, two- and three-dimensional problems are introduced, according to [93]. For one- and two-dimensional problems, the D1Q3, D2Q5 and D2Q9 discretizations are commonly used. As it is shown on the left in Figure 3.1, the D1Q3 discretization consists of two lattice velocities, one streaming in direction +1, the other in direction -1 as well as a stagnant velocity, residing at the lattice node with velocity vector 0.

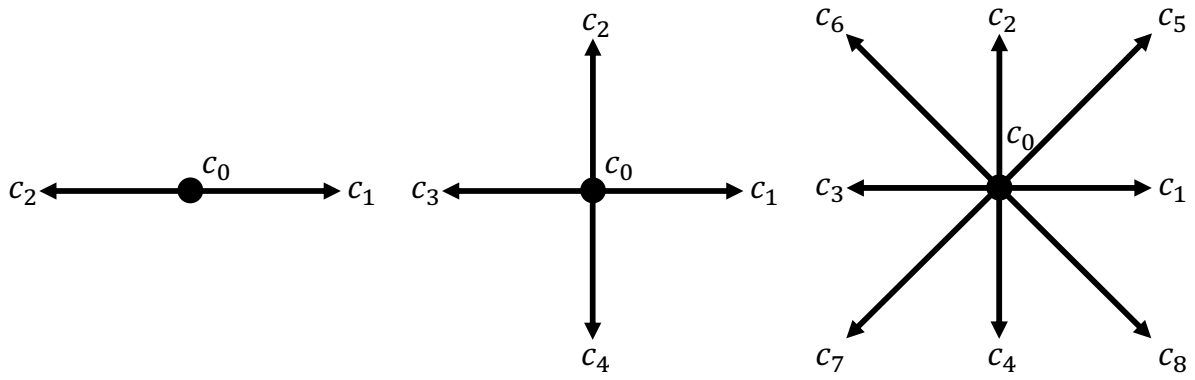

Figure 3.1: 1D and 2D lattice velocity sets. D1Q3 (left), D2Q5 (middle) and D2Q9 (right).

For the D2Q5 discretization, two more lattice velocity vectors are added for streaming in

the second dimension, as shown in the middle of said figure. The D2Q9 velocity set is extended by four velocity vectors in the diagonal directions. For three-dimensional test cases, the D3Q15 and D3Q19 models, which are shown in Figure 3.2, are used extensively.

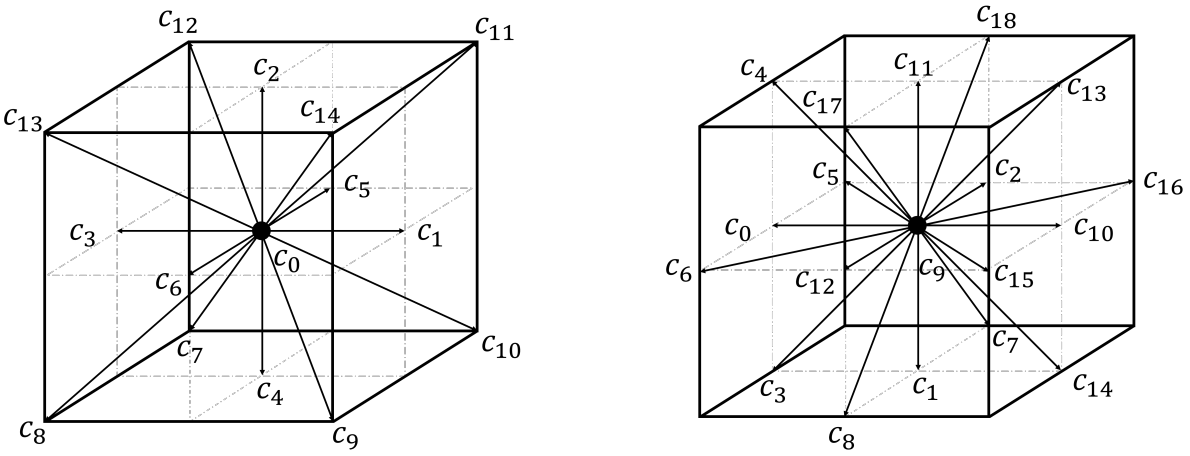

Figure 3.2: 3D lattice velocity sets. D3Q15 (left) and D3Q19 (right).

The D3Q15 model, which is shown on the left, has six face connecting vectors in the three main directions, as well as eight corner connecting vectors and one stagnant velocity. The D3Q19 model (right) has twelve edge connecting velocity vectors in addition to the six face connecting ones. For all mentioned discretizations, the number of lattice velocity vectors, their length, vectoral expression and corresponding weights are summarized in table 3.1. Also, the D3Q27 velocity set exists, combining all face connecting, edge connecting and

Table 3.1: Summary of all characteristic properties of the most common lattice velocity sets in 1D, 2D and 3D.

Notation	Velocity Vectors $\vec{c}_i$	Number	Length $\lvert\vec{c}_i\rvert$	Weight w_i
D1Q3	(0)	1	0	2/3
	(±1)	2	1	1/6
D2Q5	(0,0)	1	0	2/6
	$(\pm1,0)(0,\pm1)$	4	1	1/6
D2Q9	(0,0)	1	0	4/9
	$(\pm1,0)(0,\pm1)$	4	1	1/9
	$(\pm1,\pm1)$	4	$\sqrt{2}$	1/36
D3Q15	(0,0,0)	1	0	2/9
	$(\pm1,0,0)(0,\pm1,0)(0,0,\pm1)$	6	1	1/9
	$(\pm1,\pm1,\pm1)$	8	$\sqrt{3}$	1/72
D3Q19	(0,0,0)	1	0	1/3
	$(\pm1,0,0)(0,\pm1,0)(0,0,\pm1)$	6	1	1/18
	$(\pm1,\pm1,0)(0,\pm1,\pm1)(\pm1,0,\pm1)$	12	$\sqrt{2}$	1/36

corner connecting velocity vectors as a superposition of the D3Q15 and D3Q19 models. In general, one should choose a lattice velocity set with as many velocity directions as necessary and as little vectors as possible to accurately capture the desired physical phenomenon. Using a discretization scheme with more vectors increases the isotropy of the lattice, but in turn increases the computational effort and memory necessary for the code to run since the collision and streaming steps of the LB transport equations need to be performed for q vectors. This makes the D3Q15 more efficient than the D3Q19, which is again more efficient than the D3Q27 [67]. The D2Q9 Model is widely applied for the solution of the Navier Stokes equation [93]. For advection diffusion problems, which describe the transport of a scalar, i.e. a species or temperature, rather than a vector (velocity field), a lattice with lower isotropy is sufficient. Here, the D2Q5 Model can be employed with sufficient precision. In 3D, the D3Q7 exhibits enough isotropy for advection diffusion type problems [67].

3.1.4 Chapman-Enskog expansion

In this section, the connection between the mesoscopic lattice Boltzmann equation and macroscopic transport equations is discussed, based on a multi-scale analysis method. The method used here is the so-called Chapman-Enskog expansion, which is applied following [67].

$$\begin{aligned} f_i(x+c_i\Delta t, t+\Delta t) = f_i(x,t) + \left[\Delta t\frac{\partial}{\partial t}f_i + c_i\Delta t\frac{\partial}{\partial x_\alpha}f_i\right] \\ + \frac{1}{2}\left[\Delta t^2\frac{\partial^2}{\partial t^2}f_i + 2\Delta t c_i\Delta t\frac{\partial}{\partial t}\frac{\partial}{\partial x_\alpha}f_i + (c_i\Delta t)^2\frac{\partial^2}{\partial x_\alpha^2}f_i\right] + \dots \end{aligned} \tag{3.30}$$

The derivation shown here is performed for the standard compressible lattice Boltzmann equation, which is shown in equation (3.7). A taylor-series expansion of the distribution function f with respect to time, shown in equation (3.30), is used and inserted into equation (3.7), giving the following expression:

$$\begin{aligned} \left[\Delta t\frac{\partial}{\partial t}f_i + c_i\Delta t\frac{\partial}{\partial x_\alpha}f_i\right] + \frac{1}{2}\left[\Delta t^2\frac{\partial^2}{\partial t^2}f_i + 2\Delta t c_i\Delta t\frac{\partial}{\partial t}\frac{\partial}{\partial x_\alpha}f_i + (c_i\Delta t)^2\frac{\partial^2}{\partial x_\alpha^2}f_i\right] + \dots \\ = \frac{\Delta t}{\tau}\left[f_i^{eq}(x,t) - f_i(x,t)\right] \end{aligned} \tag{3.31}$$

Using the binomial formula, the operators can be rewritten, as it is shown in expression (3.32):

$$\Delta t\left[\frac{\partial}{\partial t}f_i + c_i\frac{\partial}{\partial x_\alpha}f_i\right] + \frac{\Delta t^2}{2}\left(\frac{\partial}{\partial t} + c_i\frac{\partial}{\partial x_\alpha}\right)^2 f_i + \dots = \frac{\Delta t}{\tau}\left[f_i^{eq}(x,t) - f_i(x,t)\right] \tag{3.32}$$

The second order derivatives in equation (3.32) can be removed by multiplying equation (3.32) with $\frac{\partial t}{2}\left(\frac{\partial}{\partial t}+c_i\frac{\partial}{\partial x_\alpha}\right)$ and subtracting it from itself. The result, while omitting terms of higher order than 2, is shown in equation (3.33):

$$\Delta t\left[\frac{\partial}{\partial t}+c_i\frac{\partial}{\partial x_\alpha}\right]f_i=-\frac{\Delta t}{\tau}[f_i^{neq}]+\frac{\Delta t^2}{2\tau}\left(\frac{\partial}{\partial t}+c_i\frac{\partial}{\partial x_\alpha}\right)f_i^{neq} \tag{3.33}$$

Here, the following expression $f_i^{neq}=f_i(x,t)-f_i^{eq}(x,t)$ is used to simplify the equation. The multi-scale expansion of the distribution function f_i and of the time derivative ∂t are introduced, according to:

$$f_i = f_i^{eq}+\epsilon f_i^{(1)}+\epsilon^2 f_i^{(2)}+\ldots; \tag{3.34}$$

$$\partial_t = \epsilon\partial_t^{(1)}+\epsilon^2\partial_t^{(2)}+\ldots; \tag{3.35}$$

$$\partial_x = \epsilon\partial_x^{(1)}. \tag{3.36}$$

In this equation, the distribution function is expanded around its respective equilibrium value, with $f_i^{(n)}$ denoting dominant terms at scale n. Hereby, the scaling parameter ϵ is given as the ratio of the macroscopic and microscopic length scales. As such, it can be seen as the Knudsen number Kn. With the macroscopic variables ρ and u being defined as the moments of the distribution function f, the following requirements can be derived for the terms $f_i^{(n)}$ at their respective scales:

$$\begin{aligned}\rho&=\sum_{i=1}^{k}f_i=\sum_i\left[f_i^{eq}+\epsilon f_i^{(1)}+\epsilon^2 f_i^{(2)}+\ldots\right]\\&=\underbrace{\sum_i f_i^{eq}}_{\rho}+\underbrace{\left(\sum_i\left[\epsilon f_i^{(1)}+\epsilon^2 f_i^{(2)}+\ldots\right]\right)}_{\lim_{\epsilon\to0}=0}\end{aligned} \tag{3.37}$$

$$\begin{aligned}\rho\vec{u}&=\sum_{i=1}^{k}f_i\vec{c}_i=\sum_i\vec{c}_i\left[f_i^{eq}+\epsilon f_i^{(1)}+\epsilon^2 f_i^{(2)}+\ldots\right]\\&=\underbrace{\sum_i\vec{c}_i f_i^{eq}}_{\rho\vec{u}}+\underbrace{\left(\sum_i\left[\vec{c}_i\epsilon f_i^{(1)}+\vec{c}_i\epsilon^2 f_i^{(2)}+\ldots\right]\right)}_{\lim_{\epsilon\to0}=0}\end{aligned} \tag{3.38}$$

Those relations are strengthened to the following:

$$\sum_i f_i^{(n)}=0\quad\sum_i f_i^{(n)}\vec{c}_i=0\quad\forall n\geq1 \tag{3.39}$$

Inserting the multi-scale expansion shown in equation (3.34)-(3.36) into equation (3.33) gives:

$$\Delta t\left[\epsilon\partial_t^{(1)}+\epsilon^2\partial_t^{(2)}+\ldots+\vec{c}_i\epsilon\partial_\alpha^{(1)}\right]\left(f_i^{eq}+\epsilon f_i^{(1)}+\epsilon^2 f_i^{(2)}+\ldots\right)=-\frac{\Delta t}{\tau}\left[\epsilon f_i^{(1)}+\epsilon^2 f_i^{(2)}+\ldots\right]+\frac{\Delta t^2}{2\tau}\left(\epsilon\partial_t^{(1)}+\epsilon^2\partial_t^{(2)}+\ldots+\vec{c}_{ix}\epsilon\partial_x^{(1)}\right)\left(\epsilon f_i^{(1)}+\epsilon^2 f_i^{(2)}+\ldots\right) \tag{3.40}$$

Dividing the resulting equation by Δt and sorting the terms by its exponent in ϵ leads to:

$$\mathcal{O}(\epsilon) \qquad \partial_t^{(1)} f_i^{eq}+\vec{c}_i\partial_x^{(1)} f_i^{eq}=-\frac{\Delta t}{\tau}f_i^{(1)} \tag{3.41}$$

$$\mathcal{O}(\epsilon^2) \qquad \partial_t^{(2)} f_i^{eq}+(\partial_t^{(1)}+\vec{c}_{ix}\partial_x^{(1)})f_i^{(1)}-\frac{\Delta t}{2\tau}(\partial_t^{(1)}+\vec{c}_{ix}\partial_x^{(1)})f_i^{(1)}=-\frac{1}{\tau}f_i^{(2)} \tag{3.42}$$

Now, the moments of the equations (3.41) and (3.42) are calculated. For the 0^{th} order moment of the $\mathcal{O}(\epsilon)$ stage, the following equation (3.43) is received, which can be simplified, as shown in equation (3.44):

$$\sum_i\left[\partial_t^{(1)} f_i^{eq}+c_i\partial_x^{(1)} f_i^{eq}\right]=-\frac{\Delta t}{\tau}\sum_i f_i^{(1)} \tag{3.43}$$

$$\partial_t^{(1)}\underbrace{\sum_i f_i^{eq}}_{\rho}+\partial_x^{(1)}\underbrace{\sum_i c_i x f_i^{eq}}_{\rho u_x}=-\frac{\Delta t}{\tau}\underbrace{\sum_i f_i^{(1)}}_{=0} \tag{3.44}$$

The 1^{st} order moment of the $\mathcal{O}(\epsilon)$ stage is calculated in a similar fashion, with the simplified equation shown in equation (3.45).

$$\partial_t^{(1)}(\rho u_x)+\partial_y^{(1)}\left(\frac{\rho}{3}\delta_{x,y}+\rho u_x u_{xy}\right)=0 \tag{3.45}$$

In analogy, the 0^{th} and 1^{st} order moments of the $\mathcal{O}(\epsilon^2)$ stage are calculated, and their simplified form is shown here, with $\Pi_{xy}^{(1)}$ being a yet undefined moment:

$$\partial_t^{(2)}(\rho)=0 \tag{3.46}$$

$$\partial_t^{(2)}(\rho u_y)+\partial_x^{(1)}\left(1-\frac{\Delta t}{2\tau}\right)\underbrace{\left(\sum_i c_{ix}c_{iy}f_i^{(1)}\right)}_{\Pi_{xy}^{(1)}}=0 \tag{3.47}$$

Subsequently, the moments of the $\mathcal{O}(\epsilon)$ stage and of the $\mathcal{O}(\epsilon^2)$ need to be recombined in order to receive the correct expression of the moments of equation (3.40). The result for the 0^{th} order moment is displayed in equation (3.48) with the result of the 1^{st} order

moment being displayed in equation (3.49).

$$\epsilon\left[\partial_t^{(1)}\rho+\partial_x^{(1)}(\rho u_x)\right]+\epsilon^2\partial_t^{(2)}\rho=0 \tag{3.48}$$

$$\epsilon\left[\partial_t^{(1)}(\rho u_x)+\partial_y^{(1)}\left(\frac{\rho}{3}\delta_{xy}+\rho u_x u_{xy}\right)\right]+\epsilon^2\left[\partial_t^{(2)}(\rho u_y)+\partial_x^{(1)}\left(1-\frac{\Delta t}{2\tau}\Pi_{xy}^{(1)}\right)\right]=0 \tag{3.49}$$

Rearranging of equation (3.48) and utilising the definition of the asymptotic expansion from the equations (3.34)-(3.36) provides equation (3.50):

$$\underbrace{\epsilon\partial_x^{(1)}}_{\partial_x}(\rho u_x)+\underbrace{\left[\epsilon\partial_t^{(1)}+\epsilon^2\partial_t^{(2)}\right]}_{\partial_t}\rho=0 \tag{3.50}$$

which resembles the mass balance equation. The first order moment in equation (3.49) can be simplified in the same way, resulting in:

$$\underbrace{\left[\epsilon\partial_t^{(1)}+\epsilon^2\partial_t^{(2)}\right]}_{\partial_t}(\rho u_x)+\underbrace{\epsilon\partial_y^{(1)}}_{\partial_y}\underbrace{\left(\frac{\rho}{3}\delta_{xy}+\rho u_x u_y\right)}_{\Pi_{xy}^{eq}}=\underbrace{-\epsilon^2\partial_x^{(1)}\left(1-\frac{\Delta t}{2\tau}\right)\Pi_{xy}^{(1)}}_{\text{unknown}} \tag{3.51}$$

Assuming an isothermal equation of state while only considering terms of $\mathcal{O}(u^2)$ in f_i^{eq} and performing a considerable number of mathematical transformations, the following expression for the unknown moment $\Pi_{xy}^{(1)}$ is received:

$$\Pi_{xy}^{(1)}=-\rho c_s^2\tau\left(\partial_y^{(1)}u_x+\partial_x^{(1)}u_y\right)+\tau\partial_z^{(1)}(\rho u_x u_y u_z) \tag{3.52}$$

The first term on the right-hand side can be seen as a Navier-Stokes like viscous stress-tensor, with the second term being an error term, originating from the lack of terms of $\mathcal{O}(u^3)$ in f_i^{eq}. According to [67], this term can be neglected for the condition of $u^2 \ll c_s^2$, which is equivalent to $Ma \ll 1$. Inserting equation (3.52) into (3.51) and utilizing the definition of $p=\rho c_s^2$ results in:

$$\partial_t(\rho u_x)+\partial_y\left(p\delta_{xy}+\rho u_x u_{xy}\right)=\partial_y\left(\eta(\partial_y u_x+\partial_x u_y)\right) \tag{3.53}$$

after finding the definition of the shear viscosity by comparison with the Navier-Stokes equation as:

$$\eta=\rho c_s^2(\tau-\frac{\Delta t}{2}) \tag{3.54}$$

3.1.5 Multi relaxation time method

In this chapter, an alternative formulation of the collision operator for the lattice Boltzmann equation, shown in equation (3.4), is presented. As described in chapter 4 of Kruger et al. [67], the standard BGK-approximation, which was presented in Chapter 3.1.1, has several disadvantages for a certain choice of the relaxation time, which essentially limits the range of values for the viscosity, respectively. It is stated that, since the discretization error is coupled with the relaxation time, the accuracy of the BGK model is reduced for large values of the viscosity (compare with equation (3.54) in Chapter 3.1.4). Furthermore, through Chapman-Enskog expansion and comparison of the result with the Navier-Stokes equation, the following expression, shown in equation (3.55), can be found for the viscosity. It can be seen that a value of $\tau \geq \frac{\Delta t}{2}$ has to be chosen in order to keep positive values for the viscosity. This results in unstable simulations when the value of the relaxation time is chosen close to the restriction.

$$\eta = \rho c_s^2 \left(\tau - \frac{\Delta t}{2} \right) \tag{3.55}$$

The critical point here is the limit of choice of the relaxation time. Since the relaxation time enters the model only through the collision operator, a more sophisticated choice of the latter promises to improve the lattice Boltzmann method in this regard. The basic idea is the relaxation of different distribution functions with different relaxation times. Several restrictions regarding the relaxation technique have to be met, i.e. mass conservation and momentum conservation. This leads to the basic principle of the multi-relaxation time method, in which not the distribution functions, but moments of the distribution function are relaxed. The derivation of the multi-relaxation time method is done in analogy to chapter 10 in [67]. The multi-relaxation time expression for the collision operator of the lattice Boltzmann equation is derived based on the standard BGK-equation, shown in Chapter 3.1.1, by multiplying the following expression $I = M^{-1}M$ onto the right-hand side of the equation, resulting in equation (3.56). Here, M is the transformation matrix, which will be specified later and $\vec{f}$ is a vector, containing the values of the distribution function f_i for all lattice velocity directions c_i. By multiplying the transformation matrix M as well as its inverse M^{-1} onto the right-hand side, effectively the unitary matrix I is multiplied to it, not changing the expression of the equation.

$$\vec{f}(x + c_i \Delta t, t + \Delta t) - \vec{f}(x,t) = -M^{-1} M \omega \left[\vec{f}(x,t) - \vec{f}^{eq}(x,t) \right] \Delta t \tag{3.56}$$

By rearranging the terms on the right-hand side, the transformation matrix M can be moved into the bracket and multiplied both with the distribution function and its equi-

librium value.

$$\vec{f}(x+c_i\Delta t, t+\Delta t) - \vec{f}(x,t) = -M^{-1}\omega\left[M\vec{f}(x,t) - M\vec{f}^{eq}(x,t)\right]\Delta t \tag{3.57}$$

When defining the moment vector $\vec{m}$ as the matrix-vector multiplication of the transformation matrix M and the distribution function vector $\vec{f}$, then equation (3.57) can be rewritten as shown in equation (3.58).

$$\vec{f}(x+c_i\Delta t, t+\Delta t) - \vec{f}(x,t) = -M^{-1}\omega\left[\vec{m}(x,t) - \vec{m}^{eq}(x,t)\right]\Delta t \tag{3.58}$$

Up to this point, equation (3.58) still expresses the BGK approximation for the lattice Boltzmann equation, with the sole difference that the distribution functions are transformed into moments, the collision is performed with only one relaxation time ω, and the result is transformed back by multiplication with the inverse of the transformation matrix. Now, a second unitary matrix I is introduced, as shown in equation (3.59)

$$\vec{f}(x+c_i\Delta t, t+\Delta t) - \vec{f}(x,t) = -M^{-1}\omega I\left[\vec{m}(x,t) - \vec{m}^{eq}(x,t)\right]\Delta t \tag{3.59}$$

Subsequently, the multiplication of the relaxation rate ω and the unitary matrix is named relaxation matrix S, which is a diagonal matrix with the value of the relaxation rate at each diagonal element. The final equation is shown in (3.60).

$$\vec{f}(x+c_i\Delta t, t+\Delta t) - \vec{f}(x,t) = -M^{-1}S\left[\vec{m}(x,t) - \vec{m}^{eq}(x,t)\right]\Delta t \tag{3.60}$$

As it can be seen in equation (3.60), the collision is performed in the transformed moment space. The exact definition of these moments is not yet defined. What remains to be specified is the choice of the transformation matrix M as well as the relaxation matrix S. In general, the transformation matrix M can be chosen arbitrarily, but choosing it in such a way that the moments m represent hydrodynamic variables, i.e. density and the velocity field, is a smart choice since it enables us to relax them with different relaxation rates ω_i, which can greatly improve the stability of the simulation. Furthermore, M needs to be regular, meaning that its inverse needs to exist. This is obvious since the transformation back from moment space into population space needs to be possible. For the two-dimensional case, the hydrodynamic moments of 0^{th} and 1^{st} order are the density and the velocity in either direction, meaning that six more moments need to be specified. According to literature [67], the two most common methods are using Hermite polynomials to specify the missing moments and the so-called Graham-Schmidt procedure, where orthogonal vectors are being constructed to find the missing entries of

the transformation matrix M. In this work, the Graham-Schmidt procedure is used to find the transformation matrix, which results in equation (3.61) for the D2Q9 discretization for the two-dimensional case:

$$M = \begin{bmatrix} 1 & 1 & 1 & 1 & 1 & 1 & 1 & 1 & 1 \\ -4 & -1 & -1 & -1 & -1 & 2 & 2 & 2 & 2 \\ 4 & -2 & -2 & -2 & -2 & 1 & 1 & 1 & 1 \\ 0 & 1 & 0 & -1 & 0 & 1 & -1 & -1 & 1 \\ 0 & -2 & 0 & 2 & 0 & 1 & -1 & -1 & 1 \\ 0 & 0 & 1 & 0 & -1 & 1 & 1 & -1 & -1 \\ 0 & 0 & -2 & 0 & 2 & 1 & 1 & -1 & -1 \\ 0 & 1 & -1 & 1 & -1 & 0 & 0 & 0 & 0 \\ 0 & 0 & 0 & 0 & 0 & 1 & -1 & 1 & -1 \end{bmatrix} \tag{3.61}$$

It must be noted that the arrangement of the rows and columns of matrix M depends on the type of velocity discretization and the order of the lattice velocity vectors. Here, the set of lattice velocity vectors, displayed in equation (3.62), is used:

$$\vec{c}_i = c \begin{cases} (0,0), & i = 0 \\ (\cos(\alpha), \sin(\alpha)), & \alpha = 0, \frac{\pi}{2}, \pi, \frac{3\pi}{2}, \quad i = 1,2,3,4 \\ (\cos(\alpha), \sin(\alpha)), & \alpha = \frac{\pi}{4}, \frac{3\pi}{4}, \frac{5\pi}{4}, \frac{7\pi}{4}, \quad i = 5,6,7,8 \end{cases} \tag{3.62}$$

As it can be seen, the first row of matrix M represents the moment of 0^{th} order, meaning that all distribution functions f_i are being summed up, resulting in the expression of the density. The 4^{th} row represents the first entry of the 1^{st} order moment, namely the velocity in x-direction with the 6^{th} row being the second entry, namely the velocity in y-direction. Furthermore, the relaxation matrix S needs to be specified, which can be less straight forward than one could assume. In general, the relaxation matrix needs to be a diagonal matrix, with the relaxation time values for the different moments, denoted as $s_0 \dots s_8$, as diagonal elements, as shown in equation (3.63) for the exemplary case of a

D2Q9 discretization scheme.

$$S = \begin{bmatrix} s_0 & 0 & 0 & 0 & 0 & 0 & 0 & 0 & 0 \\ 0 & s_1 & 0 & 0 & 0 & 0 & 0 & 0 & 0 \\ 0 & 0 & s_2 & 0 & 0 & 0 & 0 & 0 & 0 \\ 0 & 0 & 0 & s_3 & 0 & 0 & 0 & 0 & 0 \\ 0 & 0 & 0 & 0 & s_4 & 0 & 0 & 0 & 0 \\ 0 & 0 & 0 & 0 & 0 & s_5 & 0 & 0 & 0 \\ 0 & 0 & 0 & 0 & 0 & 0 & s_6 & 0 & 0 \\ 0 & 0 & 0 & 0 & 0 & 0 & 0 & s_7 & 0 \\ 0 & 0 & 0 & 0 & 0 & 0 & 0 & 0 & s_8 \end{bmatrix} \tag{3.63}$$

The arrangement of the diagonal elements is of course dependent on the nomenclature of the velocity vectors in the lattice scheme. Furthermore, different rules exist for the diagonal elements, depending on which moment is relaxed by the respective relaxation rate. For the conserved, hydrodynamic moments of density and the two velocity components, which are relaxed by the 1^{st}, 4^{th} and 6^{th} entry of the relaxation matrix, arbitrary relaxation rates can be chosen. This is due to these moments being conserved by the collision and streaming method anyways. For the non-conserved, yet macroscopically relevant moment of the strain rate tensor, the relaxation rates are coupled to the bulk and shear viscosities [67]. With our notation, these would be $s_1 = \omega_e$ as well as $s_7 = s_8 = \omega_\nu$, with:

$$\eta = \rho c_s^2 \left(\frac{1}{\omega_\nu} - \frac{1}{2} \right) \tag{3.64}$$

$$\eta_B = \rho c_s^2 \left(\frac{1}{\omega_e} - \frac{1}{2} \right) - \frac{\eta}{3} \tag{3.65}$$

The remaining relaxation rates at position s_2, s_4 and s_6, sometimes referred to as ghost moments, since they don't influence the macroscopic interpretation of the Boltzmann equation, but can affect the numerical properties of the model, are free parameters to tune. This results in the final form for the relaxation matrix S:

$$S = diag(1, \omega_e, s_2, 1, s_4, 1, s_6, \omega_\nu, \omega_\nu) \tag{3.66}$$

3.2 Modelling of heterogeneous reaction in porous media

This section provides a concise overview over the governing equations necessary to describe the physical phenomena of a fluid flow with multiple components while considering the thermal field, solid-fluid interaction as well as heterogeneous reactions. The fluid flow can be described, as mentioned in Chapter 3, by the continuity equation and the momentum balance. These two equations form the well-known Navier-Stokes equation and are shown again, for the sake of readability, in the equations (3.67) and (3.68). The fluid flow, being a gas flow consisting of different reactive species in the specific case of application of soot filter regeneration, needs n additional equations representing the mass conservation for each of the n species. These separate mass conservation equations are shown in equation (3.69), for the n^{th} component. Since an exothermic heterogeneous reaction is to be modeled, the simulation domain cannot be assumed to be isothermal anymore, necessitating the solution of the energy conservation equation, which is shown in equation (3.70). Here, the equations (3.67)-(3.69) are used only in the gas-phase of the domain, since the solid soot is assumed to be homogeneous and not penetrable for the different gaseous species. Contrary to that, equation (3.70) is being applied to both the solid and gas phases, allowing for the calculation of the temporal evolution of the temperature in either phase, while considering the different specific heat capacities, thermal conductivities and densities of both phases.

$$\frac{\partial \rho}{\partial t} + \nabla \cdot (\rho \vec{u}) = 0 \tag{3.67}$$

$$\frac{\partial (\rho \vec{u})}{\partial t} + \nabla \cdot (\rho \vec{u} \vec{u}) = -\nabla p + \nabla \cdot (\nu \rho \nabla \vec{u}) + \vec{F} \tag{3.68}$$

$$\frac{\partial (\rho Y_n)}{\partial t} + \nabla \cdot (\rho Y_n \vec{u}) - \nabla \cdot (D_n \rho \nabla Y_n) = 0 \tag{3.69}$$

$$\frac{\partial (\rho c_p T)}{\partial t} + \nabla \cdot (\rho c_p T \vec{u}) - \nabla \cdot (\alpha \rho c_p \nabla T) = Q \tag{3.70}$$

In the first three equations, ρ denotes the density of the gas phase, $\vec{u}$ is the velocity field vector and t represents the time. The gradient operator is depicted by ∇, with pressure and external forces acting onto the flow field being described by p and $\vec{F}$, respectively. The viscosity of the gas is denoted by ν, with the mass fractions and diffusion coefficient of the n^{th} component being represented by Y_n and D_n. In the energy equation, ρ, c_p and α stand for the density, specific heat capacity and thermal diffusivity of the respective phase (i.e. solid soot or gas phase). Furthermore, T and Q denote the thermodynamic temperature and source-/ sink-term. For the chemical equation at the solid-gas interface,

two different mechanisms are implemented. The first one, which is assumed to be of first order, is shown in equation (3.71) as follows [86]:

$$C + O_2 \rightarrow \mathrm{CO}_2 \tag{3.71}$$

In a first-order reaction, the reaction rate, described by the Arrhenius model, depends only on the concentration of one component. In this case, this holds true because oxygen is the only gaseous reactant, while carbon is in a solid state. Following the Arrhenius formalism, the reaction rate F_r is given by equation (3.72):

$$F_r = Ae^{\left(-\frac{E_a}{RT}\right)} \left(\frac{Y_{O_2}^I \rho}{M_{O_2}} \right) \tag{3.72}$$

In this context, A and E_a describe the two kinetic parameters of the Arrhenius model, which are the pre-exponential factor and the activation energy of the reaction. Also, M_{O_2} and R denote the molecular weight of oxygen and the ideal gas constant. Multiplying the standard enthalpy of the reaction, Δh_r, with the reaction rate gives the reaction heat Q, as shown in equation (3.73):

$$Q = F_r \Delta h_r \tag{3.73}$$

When considering carbon monoxide as a byproduct, the second mechanism can be formulated, resulting in the following chemical equation:

$$C + \frac{1}{2} O_2 \rightarrow CO \tag{3.74}$$

$$C + O_2 \quad \rightarrow CO_2 \tag{3.75}$$

Again, the Arrhenius approach is used to describe the reaction rate for the reaction which produces carbon monoxide:

$$F_{r,CO} = A_{CO} e^{\left(-\frac{E_{a,CO}}{RT}\right)} \left(\frac{Y_{O_2}^I \rho}{M_{O_2}} \right) \tag{3.76}$$

with A_{CO} and $E_{a,CO}$ being the two kinetic parameters. The total reaction heat can then be calculated, utilizing the separate reaction enthalpy values for both reactions.

$$Q_{total} = F_{r,CO} \Delta h_{r,CO} + F_{r,CO_2} \Delta h_{r,CO_2} \tag{3.77}$$

At the solid-gas interface, the following boundary conditions are defined. A no-slip boundary condition is assumed for the flow field, which can be described by equation (3.78). Since the solid domain is assumed to be impenetrable for the different compo-

nents of the gas phase, the mass flux of the n^{th} component normal to the interface $\vec{n}$ and the consumption/production by the chemical reaction have to coincide. Equation (3.79) shows this boundary condition, with both the surface-normal mass flux and the consumption/production of the chemical reaction being shown on the left and on the right-hand side, respectively.

$$\vec{u} = 0 \tag{3.78}$$

$$\vec{n} \cdot \left(\frac{D_{\mathrm{n}} \rho}{M_{\mathrm{n}}} \right) \nabla Y_{\mathrm{n}}^{I} = \nu_{\mathrm{n}} F_r \tag{3.79}$$

In this equation, the stoichiometric coefficient of the n^{th} component in the respective chemical equation is described by ν_n. Furthermore, the continuity of the temperature profile across the interface and the equity of the energy flux on either side of the interface are the boundary conditions for the temperature field. These characteristics can be formulated by the equations (3.80) and (3.81):

$$T\Big|_{-} = T\Big|_{+} \tag{3.80}$$

$$\vec{n} \cdot (\lambda \nabla T + \rho c_p \vec{u} T)\Big|_{-} + Q\Big|_{-} = \vec{n} \cdot (\lambda \nabla T + \rho c_p \vec{u} T)\Big|_{+} + Q\Big|_{+} \tag{3.81}$$

In addition to the parameters previously defined, the symbol λ represents the thermal conductivity, and the subscripts $+$ and $-$ indicate the two sides of the interface. The energy conservation equation presented earlier encompasses not only the diffusive and advective fluxes on each side of the interface but also the heat release resulting from the chemical reaction. The specific lattice Boltzmann method employed in this study assumes interfaces to be situated midway between lattice nodes, ensuring that the interface always exists between lattice nodes assigned to both phases and is never directly positioned on a lattice node. This necessitates to split the heat release of the reaction and to subsequently added it onto either side of the interface. To calculate the respective values to be added to either phase, the condition of the continuity of the temperature profile across the interface (equation (3.80)) has to be considered. Here, the densities and specific heat capacities of the two media on either side of the interface can be used to conserve this condition. For this, the ratio of the specific heat capacities and densities of the solid (subscript s) and gaseous (subscript g) phases σ is written according to equation (3.82):

$$\sigma = \frac{(\rho c_p)_s}{(\rho c_p)_g} \tag{3.82}$$

Subsequently, the respective fraction of the heat, which will be added to both phases, Q_s and Q_g, respectively, is calculated according to equation (3.83):

$$Q_g = \frac{1}{1+\sigma} Q \quad Q_s = \frac{\sigma}{1+\sigma} Q \tag{3.83}$$

3.3 Lattice Boltzmann expression for heterogeneous reactions in porous media

The equations for describing a multi-component flow with heterogeneous reactions and conjugate heat transfer between the solid and gas phases, which were presented in section 3.2, now need to be formulated with lattice Boltzmann type equations. The fundamental transport equations can be formulated following [78], with the equation describing the flow field being shown in equation (3.84) and the transport equations for the components and temperature being shown in equation (3.85) and equation (3.86), respectively.

$$\begin{aligned} \vec{f}(\vec{x}+\vec{c}_i\Delta t, t+\Delta t) - \vec{f}(\vec{x},t) = &- \left(M^{-1}SM\right)\left[\vec{f}(\vec{x},t) - \vec{f}^{\mathrm{eq}}(\vec{x},t)\right] \\ &+ \Delta t \left(M^{-1}(I-0.5S)M\right) F_i \end{aligned} \tag{3.84}$$

$$\begin{aligned} \vec{g}_n(\vec{x}+\vec{c}_i\Delta t, t+\Delta t) - \vec{g}_n(\vec{x},t) = &- \left(M^{-1}S_nM\right)\left[\vec{g}_n(\vec{x},t) - \vec{g}_n^{\mathrm{eq}}(\vec{x},t)\right] \\ &+ \Delta t \bar{F}_{n,j} + 0.5\Delta t^2 \Delta_t \bar{F}_{n,j} \end{aligned} \tag{3.85}$$

$$\begin{aligned} \vec{h}(\vec{x}+\vec{c}_i\Delta t, t+\Delta t) - \vec{h}(\vec{x},t) = &- \left(M^{-1}S_TM\right)\left[\vec{h}(\vec{x},t) - \vec{h}^{\mathrm{eq}}(\vec{x},t)\right] \\ &+ \Delta t \bar{F}_T + 0.5\Delta t^2 \Delta_t \bar{F}_T \end{aligned} \tag{3.86}$$

The distribution functions for the flow field, for the n^{th} component and for the temperature are denoted as $\vec{f}$, $\vec{g}_n$ and $\vec{h}$, respectively. A multi-relaxation time (MRT) method is used, resulting in the distribution functions in the equations (3.84)-(3.86) to be vectors. This is denoted by the arrow used as a superscript. These vectors then contain the distribution functions for all lattice velocity directions $\vec{c}_i$, with $i \in [0, q-1]$ and q depending on the lattice discretization at use. As usual, the spatial coordinates and the time step size are denoted by $\vec{x}$ and Δt. The transformation matrix M is specified according to Chapter 3.1.5. Then, the collision operation is performed in moment-space, utilizing the respective relaxation matrices S, S_n and S_T for the flow field, the n^{th} component and the temperature field. It is noted that, depending on the choice of the relaxation matrices, the MRT method reverts back to the SRT method. In this work, both the MRT and SRT methods are used, and no difference for the given range of values of the parameters, as given in Appendix B, were noted. In the collision operation, each distribution function is relaxed towards its respective equilibrium distribution function, which is given in the

equations (3.87)-(3.89):

$$f_i^{\mathrm{eq}} = w_i \rho \left[1 + \frac{\vec{c}_i \cdot \vec{u}}{c_s^2} + \frac{(\vec{c}_i \cdot \vec{u})^2}{2c_s^4} - \frac{u^2}{2c_s^2}\right] \tag{3.87}$$

$$g_{n,i}^{\mathrm{eq}} = w_i Y_n \left[1 + \frac{\vec{c}_i \cdot \vec{u}}{c_s^2} + \frac{(\vec{c}_i \cdot \vec{u})^2}{2c_s^4} - \frac{u^2}{2c_s^2}\right] \tag{3.88}$$

$$h_i^{\mathrm{eq}} = w_i T \left[1 + \frac{\vec{c}_i \cdot \vec{u}}{c_s^2} + \frac{(\vec{c}_i \cdot \vec{u})^2}{2c_s^4} - \frac{u^2}{2c_s^2}\right] \tag{3.89}$$

The last term in all three equations introduces forcing-terms of diverse origin, which are for example external forces acting onto the flow-field, or source and sink terms in the temperature and component fields. The equilibrium distribution functions f_i^{eq}, $g_{n,i}^{eq}$ and h_i^{eq} for the flow field, the component fields and the temperature fields are received from the Maxwell distribution functions, and the result is shown in the equations (3.87)-(3.89), in analogy to Chapter 3.1.2. As typical, the macroscopic variables of the respective conservation equation are received by evaluation of the according moments of the respective distribution functions. Consequently, the density ρ and the velocity field $\vec{u}$ are defined by the 0^{th} and 1^{st} order moments of the distribution function f. Similarly, the mass fraction of the n^{th} component and the thermodynamic temperature are calculated as the 0^{th} order moment of g_n and of h, respectively. The full set of equations is shown in the equations (3.90)-(3.93).

$$\rho = \sum_i f_i \tag{3.90}$$

$$\rho \vec{u} = \sum_i c_i f_i \tag{3.91}$$

$$Y_n = \sum_i g_{n,i} \tag{3.92}$$

$$T = \sum_i h_i \tag{3.93}$$

In analogy to the standard compressible lattice boltzmann formulation, the pressure and density are coupled according to the following expression (3.94):

$$p = c_s^2 \rho \tag{3.94}$$

For the implementation of external forces, the Guo forcing scheme according to [44] is used, resulting in the expressions shown in the equations (3.95)-(3.97):

$$\bar{F}_i = w_i \left(\frac{\vec{c}_i \cdot \vec{F}}{c_s^2} + \frac{(\vec{c}_i \cdot \vec{u})(\vec{c}_i \cdot \vec{F})}{c_s^4} - \frac{\vec{u} \cdot \vec{F}}{c_s^2} \right) \tag{3.95}$$

$$\bar{F}_{n,i} = w_i F_n \left(1 + \frac{\vec{c}_i \cdot \vec{u}}{c_s^2} \frac{\tau - 0.5}{\tau} \right) \tag{3.96}$$

$$\bar{F}_{T,i} = w_i F_T \left(1 + \frac{\vec{c}_i \cdot \vec{u}}{c_s^2} \frac{\tau - 0.5}{\tau} \right) \tag{3.97}$$

Here, an arbitrary force vector acting onto the flow field is expressed by $\vec{F}$, with the force vectors representing source and sink terms in the component and temperature fields being defined as shown in the equations (3.98) and (3.99), respectively:

$$F_n = \frac{D_n}{\rho} \nabla(Y_n) \cdot \nabla(\rho) + Y_n \nabla \cdot \vec{u} \tag{3.98}$$

$$F_T = \frac{Q}{\rho c_p} \tag{3.99}$$

3.3.1 Modelling of conjugate heat transfer

Conjugate heat transfer describes the temperature boundary conditions between two phases, namely a solid phase and a liquid phase. At the interface between the phases, the boundary condition needs to capture and enforce energy conservation, taking into account both convective and diffusive heat transfer as well as potential souce or sink terms. The homogeneous equations describing this were introduced in the equations (3.80) and (3.81). For the Lattice Boltzmann method, multiple different methods to enforce conjugate heat transfer exist, each with different advantages and drawbacks. In general, one can distinguish between explicit and iterative methods to define the distribution functions at the interface.

Explicit methods

Several ways to effectively model the conjugate heat transfer in an explicit manner exist, with two of which being introduced here. One possibility is to implement a specific boundary condition, taking into account the different heat capacities and thermal conductivities of the phases, according to [80]. This boundary condition can be implemented into the streaming step of the model. Another way is to introduce force terms derived by applying the Chapman-Enskog expansion onto the transport equation, which was shown in equation (3.86), and subsequently comparing it with the homogeneous conservation equation of the energy [59]. The first possible method, which introduces a weight to the streaming step when streaming across the interface between two phases with different

thermal conductivity, specific heat capacity and density, was introduced by Li et al. [80]. For this purpose, the ratio of the densities and specific heat capacities of both phases concerned, denoted as σ, is calculated, according to equation (3.82), which was previously introduced. Then, the post streaming values of the distribution function on both adjacent lattice nodes can be calculated. This algorithm is displayed in the equations (3.100) and (3.101) following [80]:

$$h_{\bar{i}}(\vec{x}_g, t+\Delta t) = \left(\frac{1-\sigma}{1+\sigma}\right)\widehat{h}_i(\vec{x}_g, t) + \left(\frac{2\sigma}{1+\sigma}\right)\widehat{h}_{\bar{i}}(\vec{x}_s, t) \tag{3.100}$$

$$h_i(\vec{x}_s, t+\Delta t) = -\left(\frac{1-\sigma}{1+\sigma}\right)\widehat{h}_{\bar{i}}(\vec{x}_s, t) + \left(\frac{2}{1+\sigma}\right)\widehat{h}_i(\vec{x}_g, t) \tag{3.101}$$

Here, the distribution functions on the right-hand side, which are marked with a hat, *i.e.* $\hat{h}_{\bar{i}}$, represent the post-collision values at time-step t. For a better understanding, the algorithm is visualized in Figure 3.3 and the terms of equation (3.100) and (3.101) are displayed using a colour-coding system consistent with the equations.

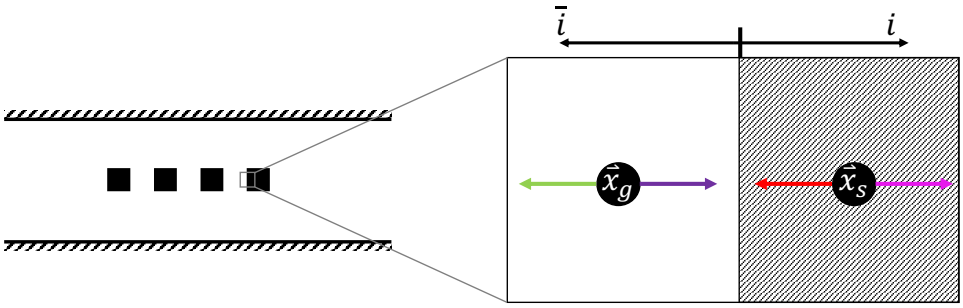

Figure 3.3: Visualization of the distribution functions for the treatment of conjugate heat transfer at the interface between two media. The lattice node in the gas phase adjacent to the interface is denoted by $\vec{x}_g$ with the solid node adjacent to the interface being denoted by $\vec{x}_s$. Also, the direction $\bar{i}$ and i indicate the left and right direction.

In the Figure, an exemplary domain containing four solid obstacles, situated along the centreline of the domain, is shown. For the interface between the gas phase and the fourth solid obstacle, an enlarged view is given, showing the lattice nodes adjacent to the interface. In accordance with the formulas (3.100) and (3.101), direction i points to the right, while direction $\bar{i}$ points to the left. This results in the green and pink distribution functions at the interface being unknown. The algorithm consists of a bounce-back and a corrector term, as it can be seen in the formulas. These additional terms address the thermal flux across the interface. It can be seen that the boundary condition is non-local, meaning that in order to calculate the two distribution functions streamed across the interface ($h_{\bar{i}}(\vec{x}_g, t+\Delta t)$ and $h_i(\vec{x}_s, t+\Delta t)$), knowledge of one post-collision distribution function of a neighbouring node is required. This requires special treatment, if a parallelized code is to be used, since the post-collision information of the neighbouring

nodes needs to be available. Also, this algorithm does not consider thermal sources or sinks, which are present if heterogeneous reactions are treated. In this case, the model is extended by calculating the total reaction heat Q for the node at the interface, according to equation (3.73), multiplying it with the weighting factor σ as presented in equation (3.102) and adding the respective values to both lattice nodes facing the interface.

$$Q_g = \frac{1}{1+\sigma} Q \quad Q_s = \frac{\sigma}{1+\sigma} Q \tag{3.102}$$

The second approach is based on the comparison of the lattice Boltzmann transport equation for the temperature field and its macroscopic, homogeneous expression. Following [59], applying the Chapman-Enskog expansion onto equation (3.86) results in

$$\frac{\partial T}{\partial t} + \nabla \cdot (T\mathbf{u}) - \nabla \cdot (\alpha \nabla T) = F_T \tag{3.103}$$

This equation, compared with the transport equation of energy, as given in equation (3.70), does not satisfy energy conservation, if spatial gradients of the density and specific heat capacity are present, which is the case for domains with multiple phases. This results in an error in energy conservation at the interfaces in the simulation domain, meaning that the standard lattice Boltzmann equation is not able to capture the conjugate heat transfer effect between phases with different physical properties. This can be circumvented by comparing equation (3.70) with equation (3.103). For this, the terms in equation (3.70) are split by applying the Leibnitz product rule, resulting in:

$$\rho c_p \frac{\partial T}{\partial t} + T \frac{\partial (\rho c_p)}{\partial t} + \rho c_p \nabla \cdot (T\vec{u}) + T\vec{u} \cdot \nabla(\rho c_p) - \rho c_p \nabla \cdot (\alpha \nabla T) - \alpha \nabla T \cdot \nabla(\rho c_p) = Q \tag{3.104}$$

Now, equation (3.104) is divided by ρc_p and the result is reordered in such a way that the left side resembles equation (3.103):

$$\frac{\partial T}{\partial t} + \nabla \cdot (T\vec{u}) - \nabla \cdot (\alpha \nabla T) = Q - \frac{T}{\rho c_p} \frac{\partial (\rho c_p)}{\partial t} - \frac{T\vec{u}}{\rho c_p} \cdot \nabla(\rho c_p) + \frac{\alpha \nabla T}{\rho c_p} \cdot \nabla(\rho c_p) \tag{3.105}$$

By comparison of equation (3.103) with equation (3.105), it can be concluded that by inclusion of an extra force term, which comprises of the additional terms on the right-hand side of equation (3.105), the correct energy conservation equation can be recovered by the lattice Boltzmann method. The resulting force term is displayed in the following:

$$F_{extra} = \frac{T}{\rho c_p} \partial(\rho c_p) \left(\alpha \nabla T - T\vec{u}\right) - \frac{T}{\rho c_p} \frac{\partial (\rho c_p)}{\partial t} \tag{3.106}$$

Iterative method

While iterative methods are not used in this thesis, they are mentioned briefly for the sake of completeness. One example of an iterative method for the treatment of conjugate heat transfer is the coupling of the thermal counter slip scheme, proposed in [91] with the wet node scheme for the surface reaction, proposed in [57]. One distinct difference is the fact that, unlike the half-way models used in this thesis, lattice nodes are placed right on the interface. These lattice nodes are called wet nodes and contain distribution functions for both the solid and liquid phases. Then, the thermal counter slip scheme is used to calculate the missing solid and fluid distribution functions for the wet node. With these values calculated, the temperature on the boundary node is defined. This temperature is subsequently used for the calculation of the mass fractions of the educt and product at the interface utilizing the scheme presented in [57]. Since the educt concentration at the interface affects the reaction rate of the heterogeneous reaction, thus affecting the temperature field, the thermal counter slip scheme and the wet node scheme for the mass fractions at the interface have to be solved iteratively, until a converged solution is found. As it becomes obvious, this method has several drawbacks. On one hand, the method requires iterative solution, resulting in additional computational effort. Furthermore, the method needs precise identification of the orientation of the boundary condition, complicating the implementation [143] as well as the adaption for 3D simulations.

3.3.2 Reactive boundary condition

The reactive boundary condition for the component fields was shown in equation (3.79) in section 3.2. The equation describes the continuity of the transport of the components to/from the interface and their respective consumption and generation at the interface. To implement this boundary condition into the lattice Boltzmann model, the equation is rearranged in the following [78]. For clarity, equation (3.79) is repeated here.

$$\vec{n} \cdot \left(\frac{D_\mathrm{n} \rho}{M_\mathrm{n}} \right) \nabla Y_\mathrm{n}^I = \nu_\mathrm{n} F_r \tag{3.107}$$

In this equation, $\vec{n}$ denotes the surface normal vector, with the other parameters already being defined previously. The gradient of the mass fraction of the n^{th} component of the left-hand side of the equation can be expressed by a difference quotient, as shown in the following:

$$\vec{n} \cdot \nabla Y_{O_2}^I = \frac{Y_{O_2}^I - Y_{O_2}^g}{0.5\, \vec{n} \cdot \vec{c}_i\, \Delta x} \tag{3.108}$$

Inserting equation (3.108) into equation (3.107) results in the following expression:

$$\left(\frac{D_{O_2}\rho}{M_{O_2}}\right)\frac{Y^I_{O_2}-Y^g_{O_2}}{0.5\,\vec{n}\cdot\vec{c}_i\,\Delta x}=\nu_{O_2}F_r \tag{3.109}$$

Now, the expression of the reaction rate, which was defined in equation (3.72), is inserted, resulting in:

$$\left(\frac{D_{O_2}\rho}{M_{O_2}}\right)\frac{Y^I_{O_2}-Y^g_{O_2}}{0.5\,\vec{n}\cdot\vec{c}_i\,\Delta x}=\nu_{O_2}\,A\,e^{(-\frac{E_a}{RT})}\left(\frac{Y^I_{O_2}\rho}{M_{O_2}}\right) \tag{3.110}$$

This equation can be solved for the mass fraction of oxygen at the interface, $Y^I_{O_2}$, resulting in:

$$Y^I_{O_2}=\frac{D_{O_2}Y^g_{O_2}}{D_{O_2}+0.5\,\vec{n}\cdot\vec{c}_i\,\Delta x\left(\nu_{O_2,r1}\,Ae^{(-E_a/RT)}+\nu_{O_2,r2}\,A_{CO}e^{\left(-E_{a,CO}/RT\right)}\right)} \tag{3.111}$$

Here, $\nu_{O_2,r1}$ and $\nu_{O_2,r2}$ represent the stoichiometric coefficient of oxygen in both reactions, denoted by $r1$ and $r2$. Similarly, the mass fractions of CO_2 and CO at the interface can be determined, resulting in:

$$Y^I_{CO_2}=Y^g_{CO_2}-\frac{0.5\,\vec{n}\cdot\vec{c}_i\,\Delta x\,\nu_{CO_2}\,Ae^{(-E_a/RT)}M_{CO_2}Y^I_{O_2}}{D_{CO_2}M_{O_2}} \tag{3.112}$$

and:

$$Y^I_{CO}=Y^g_{CO}-\frac{0.5\,\vec{n}\cdot\vec{c}_i\,\Delta x\,\nu_{CO}\,Ae^{(-E_a/RT)}M_{CO}Y^I_{O_2}}{D_{CO}M_{O_2}} \tag{3.113}$$

Concluding, this chapter introduced the lattice Boltzmann method to the reader, describing its derivation from the Boltzmann equation, specifying the most common lattice velocity models and introducing the concept of the multi relaxation time method. Furthermore, the partial differential equations to describe all necessary physical phenomena for the simulation of soot combustion as well as the corresponding boundary conditions were proposed. Finally, the LBM expression of said equations were described.

Chapter 4

Technical and numerical methods

This chapter provides the reader with a brief overview of the COLBM framework, which has been developed during the work on this dissertation. The architecture and the implemented features are described. Furthermore, the different methods to impose boundary conditions are presented and formulations for all boundaries, as implemented in the framework, are given with the goal to facilitate reproducibility. Moreover, the breadth-first search algorithm for the calculation of the realistic reactive surface and the treatment of elaborate geometries are described. Finally, the calibration of the model, which connects the simulations to the experimental data, is introduced.

4.1 COLBM framework

In this chapter, the COLBM framework, which has been created for this dissertation, is described. The single phase self-contained STLBM code of the university of Geneva was used as a basis [73], which was extended extensively. In this context, the first section describes the basic architecture and structure of the code. In the second section the usage and features implemented into the code are described in detail.

4.1.1 Architecture overview

In this section, the code framework, is described. The code is split into different files, which are organized according to their functionality. All code files are contained in a separate ”apps” folder. The text files containing the test case configurations and the files containing the geometry data are stored in the ”Config_Files” and the ”Geometry_Files” folder, respectively. Inside of the main folder, which contains all previously mentioned folders, a shell file named ”compile.sh” is located, which needs to be executed in order to compile the code. Inside of the ”apps” folder, the file ”CMakeLists.txt” is located,

containing the information about the files, which are specified for the compilation process. The LBM code is written in C++, enabling the usage of structs to organize the code. Three main structures are used throughout the code. The structure "LBM" contains all LBM related functions, i.e. the collision and streaming functions, boundary conditions, forcing functions as well as the calculation of the macroscopic variables. Furthermore, the functions responsible for accessing the memory of the lattice vector are located here. The "Dim" structure contains the information about the dimensions of the problem, i.e. the number of lattice nodes in each direction as well as routines to calculate the total number of lattice nodes and the total length of the storage vectors necessary to store the information for all lattice velocity directions per lattice node. The last main structure is called "functions", containing the post-processing functions, functions to read in data as well as functions to store data.
The "COLBM.cpp" file is the main source file of the code, including all necessary header files as well as containing the "int main()" function, in which the choice of the test cases for the user is located. The "Utility.h" file contains the "functions" structure. The "LBM.h" files contains the LBM struct as well as the DIM struct and the definition of the cell-types.
Each pre-defined test case is located in a separate header file, named according to the test case. These header files contain one function, in which the configuration of the test case as well as the execution of the LBM model is performed for the specified number of time steps. The overall organization of these files is shown in the subsequent pseudo-code.

Algorithm 1 Basic code structure

```
1: function LBM_Simulation
2:     Read_Simulation_Parameters(input_file)
3:     initialize DIM struct
4:     allocate lattice vector with known dimensions
5:     initialize LBM struct
6:     initialize lattice vector with initial conditions
7:     set geometry                    ▷ Allocate respective phases to lattice nodes
8:     for each time step do
9:         perform collision step
10:        perform streaming step
11:        perform data storage
12:    end for
13: end function
```

The collision and streaming steps inside of the time stepping loop are described in more detail in appendix A. It is noted that for the lattice vector, a vector twice the necessary size to store all distribution functions for each lattice node is allocated. This is due to the reason that the two-populations model is used, meaning that pre and post

streaming distribution functions are stored in separate vectors. Inherent to this procedure is the advantage that implementation and parallelization are straight forward, since no special streaming order or routine has to be followed. A disadvantage, especially for the potential of simulations on GPUs, which tend to be more memory restrictive, is the increased memory cost. Furthermore, the structure-of-arrays (SOA) approach is used for storing the distribution functions in the lattice vector. This means that the distribution functions of each lattice node, corresponding to one specific lattice velocity direction, are stored together inside of the lattice vector. In other words, all values of a single attribute are stored together. This facilitates better memory access patterns, which is especially needed for GPU optimization [87].

4.1.2 Usage and features

In this sub-section, the features and abilities of the code as well as the interface for interaction with the code are elaborated. Based on the LBM equations, namely the equations (3.84)-(3.86), which were presented in Chapter 3.3, the code is able to simulate fluid flow with wall interactions, while considering different components of the fluid, the temperature field as well as conjugate heat transfer between different phases and heterogeneous reactions at the solid-gas interface. These capabilities are displayed in a graphical way in Figure 4.1, in which a 2D domain with an inlet on the left, an outlet on the right and two adiabatic no-slip walls are shown on the top and bottom. Furthermore, the domain is filled with porous solid particles, displayed in blue. Four magnified views are displayed, representing the different physical phenomena, which are treated by the employed model. Along the cross section, the velocity profile, which resembles a Poiseuille type flow, is visualized, resulting from the interaction of the flow with the no-slip walls. Moreover, exemplary profiles of the mass fractions of O_2 and CO_2 in flow direction are depicted, in which both the advective and diffusive transport as well as the consumption and production, resulting from the heterogeneous reaction at the soot particles are visualized. Also, the conjugate heat transfer at the interface between the gas and solid domains is illustrated on the top right magnified view, in which the result of a heat conduction test case across the interface of two phases is shown. Lastly, the increase in temperature caused by the release of the enthalpy of reaction is shown in the magnified view on the bottom right. The code contains multiple preset test cases for 2D and 3D simulations. More specifically, in 2D, calculations of the flow field for the initialization of combustion simulations are preset for the combustion validation test case of [143], for a porous geometry specified by ordered round particles and for FIB-SEM geometries. For these geometries, combustion test cases are also prepared.

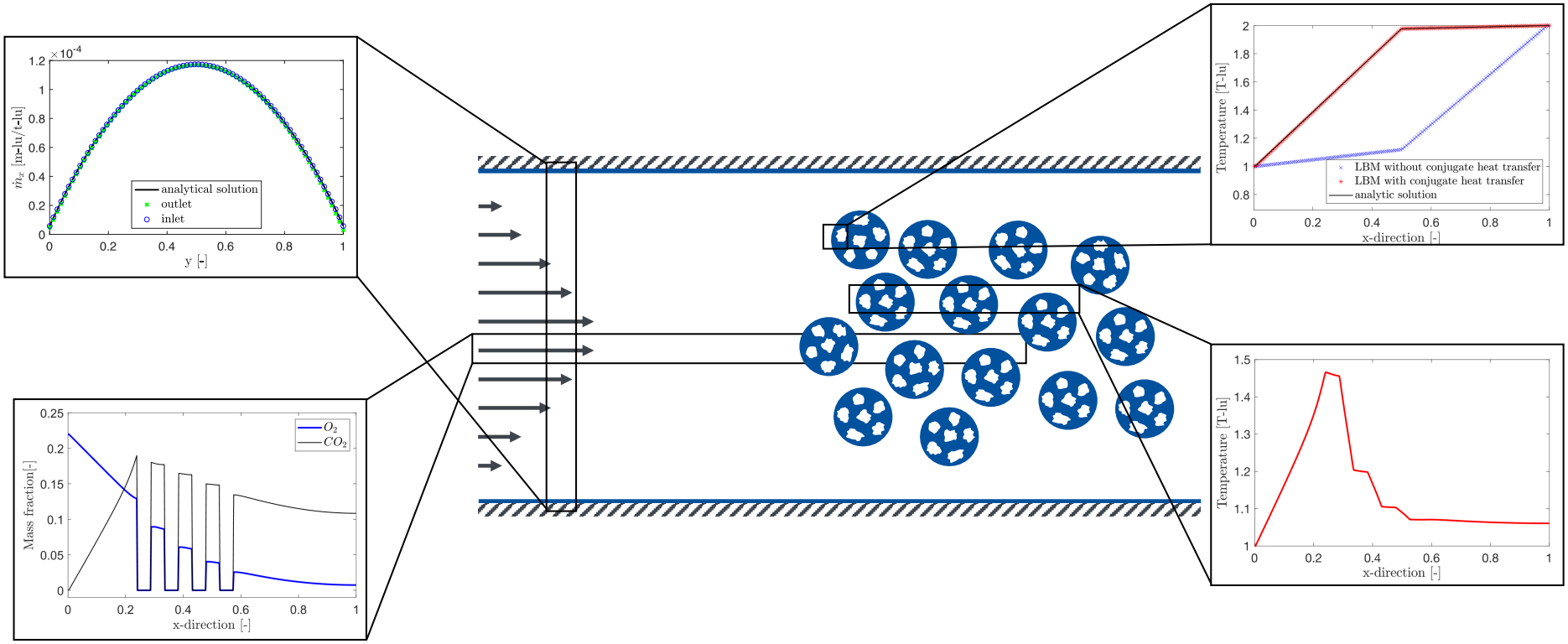

Figure 4.1: Abilities of the code displayed schematically for a simulation domain consisting of porous particles, with the fluid-wall interaction leading to the evolution of a parabolic velocity profile in the cross section (top left), the consumption and production of various components of the gas phase (bottom left), the conjugate heat transfer (top right) and the release of energy caused by the heterogeneous reaction (bottom right) being shown.

For the 3D case, presets for determining the stationary flow field for the combustion test case of [143], for FIB-SEM geometries as well as for the combustion simulation with said geometries exist. Furthermore, the heat conduction test case and the temperature relaxation test case have presets. The user can specify all relevant input parameters through .txt files. In this context, the parameters to specify the condition of the inlet flow, i.e. velocity profile, temperature and composition, as well as the initial condition for the computational domain, can be set. Additionally, the time step size and the number of time steps can be specified. Also, the relevant parameters of the phases, i.e. densities, specific heat capacities, diffusion coefficients etc. can be set. Additionally, the values of the reaction kinetics and the stoichiometric coefficients are chosen. Lastly, boolean variables, which enable a choice of the type of velocity profile, or input and output options, as well as the name of the geometry file, are set. For all aforementioned test cases, preset .txt input files exist. Then, when executing the COLBM file, the program lets the user choose from the pre-defined test cases. The results of the simulation are then saved in .vtk files for visualization in Paraview. Furthermore, for 2D and 3D simulations, 2D slice data is saved in .txt files, enabling the automated visualization of the data in Matlab. Moreover, the code performs the calculation of the current soot mass and the total accessible reactive surface and saves the information in .txt files for Matlab visualization. The geometry data is read-in from .txt files. For this purpose, a Matlab routine exists, which reads in the .tif files of the FIB-SEM images, analyses the grey scales, allocates the pixels to their respective phases, and produces a readable .txt file for the C++ LBM code.

4.2 Boundary conditions

In this section, different boundary conditions for the lattice Boltzmann model are discussed. First, different methods for the derivation of the missing distribution functions at boundary nodes are presented in section 4.2.1. Subsequently, the complete set of boundary conditions is given in the sections 4.2.2 and 4.2.3 for 2D and 3D simulations.

4.2.1 Theory of boundary conditions

In general,multiple different types of boundary conditions can be distinguished when performing a lattice Boltzmann simulation, depending on the physical phenomenon which is to be modelled and the resulting type of equation. The Dirichlet-type boundary condition imposes a fixed value for a physical variable, which then has to be translated into values for the distribution functions f. The second type is called the Neumann boundary

condition, which describes a fixed value for the gradient of a physical variable. In general, for both boundary conditions, a multitude of algorithms for their translation to the values of the distribution functions and implementation techniques exist. These methods can be classified into methods which only impose values onto the distribution functions, which are unknown on the boundary, and those, where all distribution functions of a boundary node are set. Furthermore, periodic and symmetry boundary conditions can be imposed. These differ from Dirichlet and Neumann boundary conditions, since no specific value of a macroscopic variable is imposed. Rather, these boundary conditions modify the streaming directions of outgoing distribution functions to achieve periodicity or symmetry within the simulation.

No-slip boundary condition

This section describes the most prominent boundary condition in the LBM. The no-slip boundary condition for a stationary wall is implemented by the so-called bounce-back algorithm, which originated from lattice gas automata [46, 22] and was first described in [155] for lattice Boltzmann simulations. The process of determination of the missing distribution functions for the no-slip boundary condition is shown in Figure 4.2, where a lattice node adjacent to the no-slip wall boundary condition is shown.

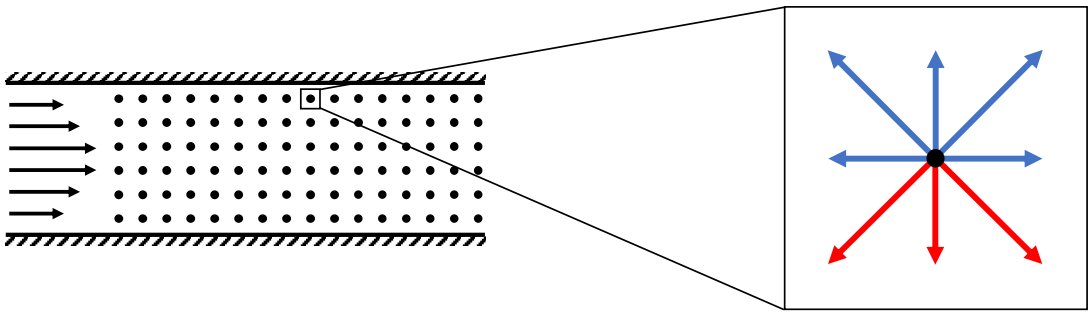

Figure 4.2: Node at wall boundary with lattice velocity vectors in magnified view. The known and unknown lattice velocities are marked in blue and red, respectively.

For this node, the lattice velocity vectors for the two-dimensional D2Q9 discretization model are displayed, with the three directions for which the value of the distribution function f_i is unknown after the streaming step being displayed in red. These are unknown since the lattice nodes, from which these distribution functions would have originated, would lay outside of the simulation domain. First, the unknown values for the distribution functions need to be determined. Several different bounce-back algorithms exist, which allow for the precise calculation of no-slip walls at any point between lattice nodes. Here, the half-way bounce-back is used. This means that the no-slip wall is assumed to be at half-way (exactly in the middle) between the wall node and the last fluid node. The distribution functions which move towards the wall in the streaming step, are "bounced back", which means that they are retro-reflected, according to equation (4.1), with x_b

being the node at the boundary, i being the index of the lattice velocity vector and $\bar{i}$ being the index of the lattice velocity in the opposite direction of i.

$$f_{\bar{i}}(x_b, t + \Delta t) = f_i(x_b, t) \tag{4.1}$$

With this scheme, the values of the unknown distribution functions can be determined in a fully local way, meaning that for the determination of the values of the missing distribution functions, no information from the neighbouring nodes needs to be known. This is advantageous if the code is written in a parallelized manner since no synchronization between the calculation of different lattice nodes is necessary.

Free-slip boundary condition

For dynamic multi-phase test cases, the free-slip wall boundary condition is employed. Here, the normal component of the fluid velocity is assumed to be zero at the wall with the tangential component not being influenced. Essentially, the boundary is assumed to be non-penetrable with no shear stress being imposed. The algorithm to determine the missing values of the distribution functions with the free-slip boundary condition is shown in Figure 4.3, where an exemplary domain with a free-slip boundary at the top is shown on the left and a magnified view of three boundary-adjacent lattice nodes on the right.

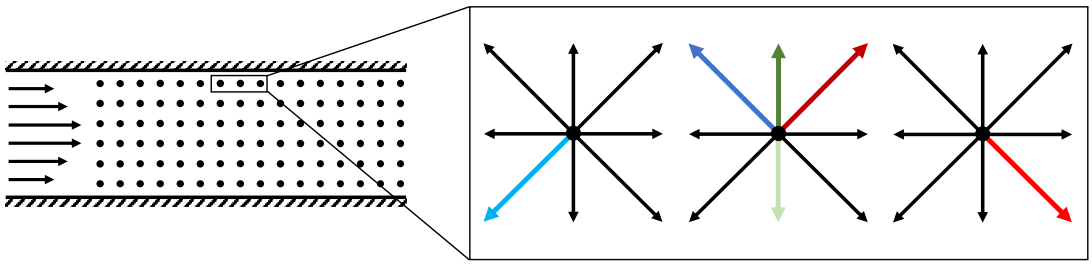

Figure 4.3: 2D simulation domain with a free-slip boundary condition on the top (left) and a magnified view of the boundary-adjacent nodes (right) for the non-local free-slip BC. The pre-streaming velocity vectors are displayed in dark blue, red and green, with the post-streaming vectors are displayed in the respective brighter colour.

The lattice nodes are displayed in black and the free-slip streaming convention is performed on the middle lattice node. Lattice velocity vectors which are not related to the boundary condition are displayed in black, with the pre-streaming velocity vectors being displayed in darker shades of blue, green and red. The lattice velocity vectors after the streaming step are displayed in brighter colours. As it can be seen in Figure 4.3, the distribution function, whose lattice velocity vector is perpendicular to the boundary condition (displayed in dark green), is retro reflected, similar to the classical bounce-back algorithm. The distribution functions, which intersect the boundary condition at an angle, are being mirrored at the boundary condition. Figure 4.4 shows the local free-slip

method, where all values of the missing distribution functions can be calculated based on other distribution functions at the same lattice node. Small differences regarding the accuracy of both methods with varying relaxation time exist, with a good analysis being provided in [39].

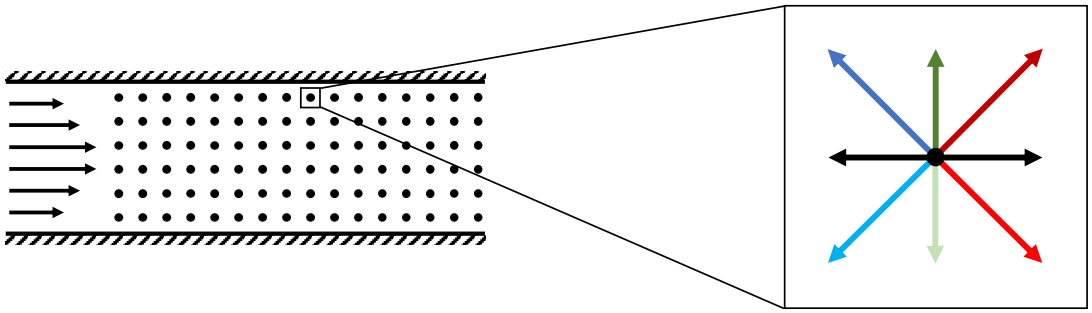

Figure 4.4: 2D simulation domain with a free-slip boundary condition on the top (left) and a magnified view of the boundary-adjacent nodes (right) for the local free-slip BC. The pre-streaming velocity vectors are displayed in dark blue, red and green, with the post-streaming vectors are displayed in the respective brighter colour.

Periodic boundary condition

Next, the periodic boundary condition, with which a large domain with periodic structure can be treated in a computationally efficient way, is presented. With this boundary condition, i.e. fully developed pipe flows or flows with a large domain perpendicular to the flow direction, can be modelled.

The schematic of the determination of the unknown values for the distribution function on the lattice nodes at the edge of the simulation domain are shown in Figure 4.5. On each node at the boundary, the values of the incoming distribution functions are unknown. The periodic boundary condition assumes that the distribution functions travel through the boundary condition and re-enter the domain at the opposite side. This can conveniently be implemented into the algorithm in the streaming step, where the outgoing distributions are ”streamed” through the boundary and re-enter the domain. This process is shown for the example of one node at the top boundary of the domain, where the red distributions re-enter the domain on the bottom at the respective lattice nodes.

Diriclet-type boundary condition for velocity

In the following, the implementation of inflow and outflow boundary conditions is discussed, which are needed in addition to the chosen wall boundary condition, to set up the flow in a domain. In Figure 4.6, the inlet of a domain with solid no-slip walls at the top and bottom is shown. At the inlet node, the known and unknown distribution functions are depicted in blue and red, respectively. Two different ways for the derivation of the values of the missing distribution functions will be presented. The first method is based on the implementation of a moving no-slip wall with momentum exchange.

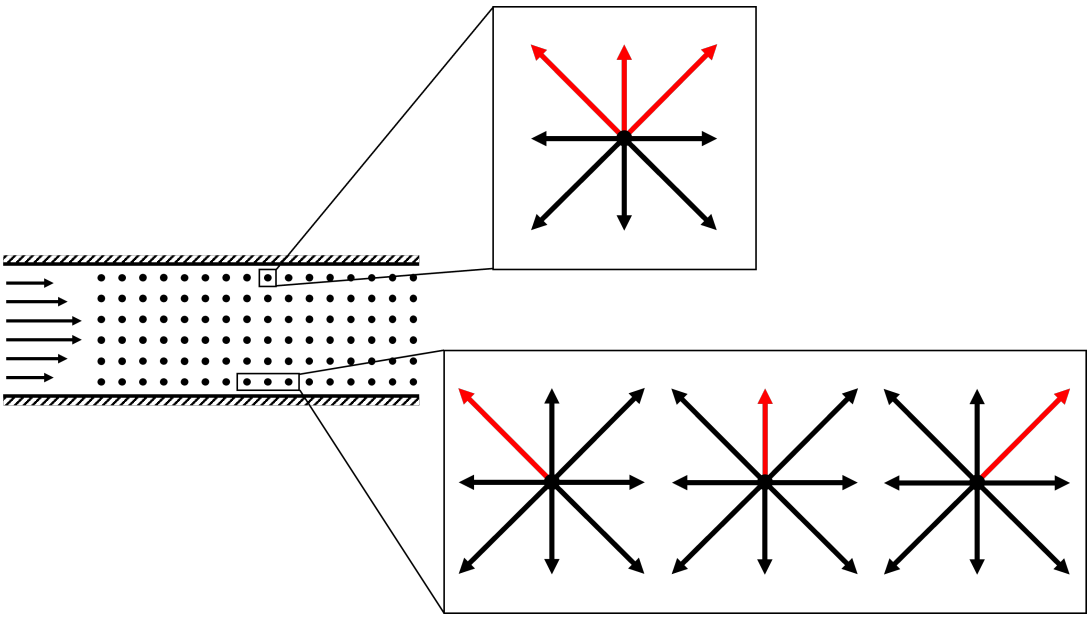

Figure 4.5: 2D simulation domain with a periodic boundary condition at the top and bottom shown on the left. On the right, a magnified view of lattice nodes at the top and bottom boundary of the domain is shown, visualizing the schematic of the streaming step across the periodic boundary condition. The lattice velocity vectors streaming out of the domain on the top will re-enter the domain at the bottom at the corresponding wall nodes.

With the no-slip wall with momentum exchange, a Dirichlet-type boundary condition for the velocity can be imposed, for example for a lid-driven Couette flow, where the moving wall drives the fluid flow through shear-stress parallel to itself. Although not possible for a wall at a specific point in space in reality, this type of boundary condition can also be used to impose a fixed velocity perpendicular to the wall at a stationary point of the domain. The second method is based on [156] and gives an expression for the calculation of the missing values of the distribution function at the inlet-boundary based on a local value (equilibrium, bounceback, pre-collision) and a corrector. It will be presented for the outlet boundary condition.

Implementation by momentum exchange bounce back

In this subsection, the previously mentioned implementation based on the bounce-back with momentum exchange is discussed in detail. If the code in use is capable of choosing the bounce-back boundary condition for selective lattice nodes, specifically the bounce-back with momentum exchange (i.e. if the lid-driven cavity test case is implemented), then this method of implementation can be used to impose the inlet boundary condition in a quick and straightforward way. If the code is not capable of the BB with momentum exchange, this formalism first needs to be implemented. The bounce-back boundary condition with momentum exchange for the lattice Boltzmann method [70] originated from the lattice gas automaton [69] and a good explanation can be found in section 5 of [67].

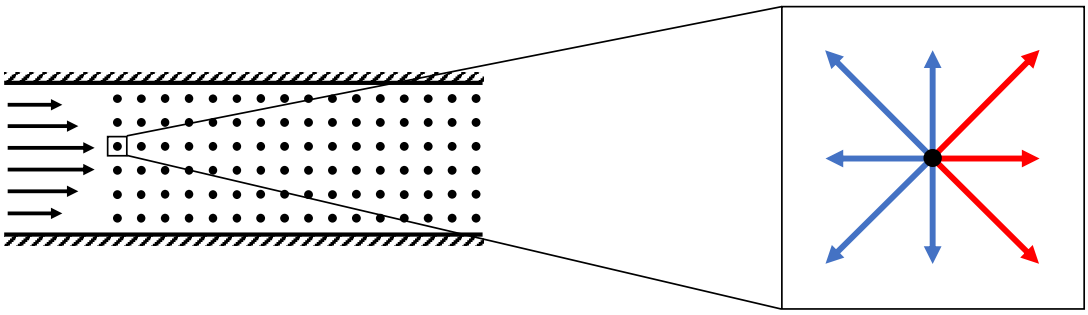

Figure 4.6: Scheme of a 2D simulation domain, with the known and unknown distribution functions at the inlet depicted in blue and red, respectively.

The final equation is shown in equation (4.2):

$$f_{\bar{i}}(x_b, t+\Delta t) = f_i(x_b, t) - 2t_i \frac{\rho_w(\vec{c}_i \cdot \vec{u}_w)}{c_s^2} \tag{4.2}$$

Here, $f_{\bar{i}}(x_b, t+\Delta t)$ is the value of the distribution function f in the direction $\bar{i}$ which is the inverse of the direction i, at lattice position x_b, which is the lattice node adjacent to the solid wall. The location of the wall is, since it is based on the half-way bounce back method, in-between the lattice node at position x_b and the "wall-node". The velocity of the wall is denoted by $\vec{u}_w$ and the density of the fluid at the wall ρ_w can be set to either the local density or the system-averaged density, according to [67]. The lattice weight t_i and the lattice speed of sound c_s are variables dependent on the chosen lattice. The values of these two parameters are provided for the most common lattice discretizations in Chapter 3.1.3. As it can be seen in equation (4.2) on the right-hand side, the algorithm consists of a bounce-back term (first summand) and a correction term for the momentum exchange (second summand). This can be conveniently implemented into the streaming-step. In order to stream the distribution functions after the collision step, the position of the node, to which it is streamed, is given by the tuple (X, Y), and can be expressed based on the coordinates of the lattice node with index i, (x_i, y_i), and the lattice velocity vector by:

$$\begin{pmatrix} X \\ Y \end{pmatrix} = \begin{pmatrix} x_i \\ y_i \end{pmatrix} + \begin{pmatrix} c_{i,x} \\ c_{i,y} \end{pmatrix} \tag{4.3}$$

If the node at (X, Y) is of cell type bounce-back, a solid wall is adjacent to the current lattice node and the bounce-back algorithm is performed. It is implemented in a straightforward way since the position of the cell which it will be streamed to stays constant (x_i, y_i) with just the lattice velocity vector being inverted. The information about the inverse lattice velocity vectors is stored in a vector called "opp". The streaming thus is performed

according to:

$$f_{out}(i, \text{opp}[k]) = f_{coll}(i, k) + f_{corr} \tag{4.4}$$

The correction term f_{corr} is given by the last summand in equation (4.2). Since the expression in equation (4.4) is fully local and no information of adjacent nodes is needed, the streaming step can be implemented in a parallelized manner without further effort. Furthermore, this method is based on the bounce-back boundary implementation, making it possible to include it without changing the general structure of the used template, if it already comes with the general bounce-back implementation.

Neumann-Type boundary condition (outflow)

The outflow boundary condition for a flow driven by a given velocity profile at the inlet is of Neumann type. This means macroscopically that instead of imposing a certain value of the velocity at the outlet, a certain value of the velocity gradient is imposed. In contrast to the boundary conditions of a common partial differential equation, the gradient cannot be directly imposed but values for the missing distribution functions have to be set in such a way that the desired gradient of the macroscopic variable is achieved. In Figure 4.7, the sector of the computational domain containing the outlet boundary condition is shown. At the top and bottom, a wall boundary condition is specified with the outlet at the right-hand side of the domain. The lattice velocity vectors are shown exemplary for one lattice node with the known and unknown values being denoted in blue and red, respectively. For the outlet, the distribution functions 3, 6 and 7 are unknown.

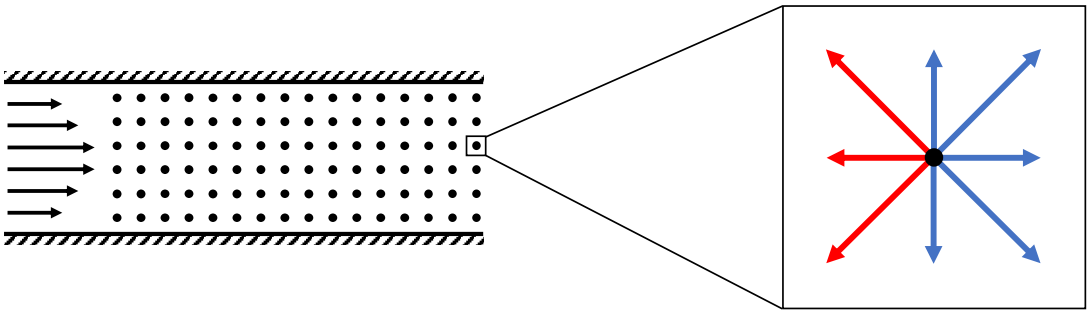

Figure 4.7: Lattice scheme at the outlet with unknown distribution functions marked in red.

Again, several different methods for the implementation are possible. It is possible to extrapolate the value of the missing distribution functions based on the value of the distribution functions of adjacent nodes with different order, thus having different orders of precision. Another possible option is to calculate the value of the macroscopic variable, i.e. the velocity, which is necessary to meet the Neumann-type boundary condition, and subsequently calculating the corresponding values of the distribution functions according

to the Zou-He Boundary condition, which will be introduced subsequently.

Extrapolation of distribution functions based on adjacent nodes

In this section, the calculation of the values of the missing distribution functions by extrapolation from the adjacent nodes upstream in the computational domain is discussed. The formulas for the calculation are derived based on the Taylor expansion of the distribution function, through which approximations with different order of precision can be achieved. The simplest approximation is achieved by using the Taylor expansion of first order for the calculation of f, as shown in equation (4.5), with x being the x-coordinate of the lattice node and Δx being the lattice spacing:

$$f(x) = f(x-\Delta x) + \Delta x \left.\frac{\partial f}{\partial x}\right|_x - \mathcal{O}(x^2) \tag{4.5}$$

Assuming the derivative of f to be zero in order to achieve a zero derivative of the macroscopic velocity results in the expression $f(x) = f(x-\Delta x)$. This means, that the values of the distribution functions are copied from the upstream cell to the boundary cell, as elucidated in Figure 4.8, where the three missing distribution functions and their corresponding ones at the upstream node are represented by a green, red and purple arrows.

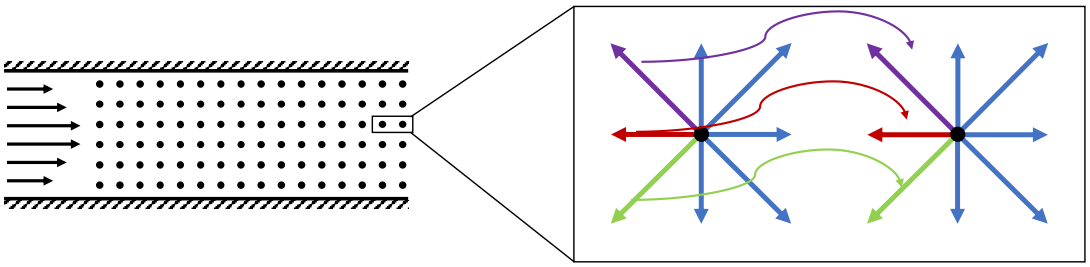

Figure 4.8: Neumann boundary condition by first order extrapolation resulting in mere copying of the distribution functions towards the boundary nodes.

A higher order expression can be derived by utilising more lattice nodes upstream for the calculation of the extrapolation. In the equations (4.6) and (4.7), the Taylor series expansion for the first and second neighbors of the boundary node are shown.

$$f(x-\Delta x) = f(x) - \Delta x \left.\frac{\partial f}{\partial x}\right|_x + \frac{\Delta x^2}{2!}\left.\frac{\partial^2 f}{\partial x^2}\right|_x + \cdots \tag{4.6}$$

$$f(x-2\Delta x) = f(x) - 2\Delta x \left.\frac{\partial f}{\partial x}\right|_x + \frac{4\Delta x^2}{2!}\left.\frac{\partial^2 f}{\partial x^2}\right|_x + \cdots \tag{4.7}$$

Taking equation (4.7) and subtracting equation (4.6) four times to eliminate the terms of the second order derivative results in the following expression for the extrapolation of the value of the distribution function f at the lattice position x, with the gradient of f

again being of value zero:

$$f(x) = \frac{1}{3}\left(4f(x-\Delta x) - f(x-2\Delta x)\right) \tag{4.8}$$

Both the first order extrapolation and the second order extrapolation can be implemented in the same way. Since the calculation of the missing distribution functions at the boundary node is performed through extrapolation, it requires information from adjacent lattice nodes. In a parallelized code, this would make the synchronization and tracking of the calculations, which are performed by different CPUs in parallel, necessary, if the extrapolation would be performed after the collision step and in the stream function. This can be circumvented by implementing the boundary condition before the collision and streaming steps.

Transformation to Dirichlet-type - extrapolation of macroscopic variables

The methods described in the previous section only took into account the distribution functions corresponding to the missing ones from the cells adjacent to the boundary node. Here, the calculation of the missing values for the boundary node is based on the macroscopic variables of the system, i.e. the velocity, thus taking into account all 9 (for the 2D model) distribution functions. In a first step, the necessary value of the velocity for the boundary node to enforce the Neumann-type boundary condition needs to be calculated. This is done in analogy to the methods of extrapolation, which were discussed in the previous section. For a zero-gradient boundary condition, the resulting extrapolation for first and second order are shown in equation (4.9) and (4.10).

$$\vec{u}(x) = \vec{u}(x-\Delta x) \tag{4.9}$$

$$\vec{u}(x) = \frac{4}{3}\left(\vec{u}(x-\Delta x) - \vec{u}(x-2\Delta x)\right) \tag{4.10}$$

Zou-He Boundary Condition

Now, the direct implementation of a Dirichlet-type boundary condition, proposed in [156], is discussed according to [14, 51]. Based on the nomenclature defined previously, the values of the distribution function for the lattice velocity vectors 3, 6 and 7 need to be determined. Here, the missing values are again calculated from the known values of the local distribution functions f_i^* and a corrector term (second summand on the right-hand side), as shown in equation (4.11):

$$f_i(\vec{x},t) = f_i^*(\vec{x},t) + \frac{w_i}{c}\vec{c}_i \cdot \vec{Q} \tag{4.11}$$

Here, w_i as usual represents the lattice weight, $\vec{c}_i$ the lattice velocity vector, $\vec{Q}$ being the correction force vector and c being the lattice speed, defined as the quotient of spatial and temporal discretization length. Evaluating this equation for the missing distribution functions at the outlet leads to the following expressions:

$$f_3(\mathbf{x},t) = f_3^*(\mathbf{x},t) - w_3 \cdot Q_x \tag{4.12}$$

$$f_6(\mathbf{x},t) = f_6^*(\mathbf{x},t) - w_6 \cdot (Q_x - Q_y) \tag{4.13}$$

$$f_7(\mathbf{x},t) = f_7^*(\mathbf{x},t) - w_7 \cdot (Q_x + Q_y) \tag{4.14}$$

Inserting these into the equations for calculating the macroscopic variables of density and velocity, we receive three equations in the 2D case. For a given velocity at the boundary (this is what we want to impose), those three equations can be transformed to solve for the three unknowns Q_x, Q_y and ρ after which an expression for the three distribution functions 3, 6 and 7 is received. The calculation is done in analogy to [51] and in accordance to the nomenclature of the lattice velocities in this paper, with u and v being the x and y components of the velocity vector. The resulting expressions are shown in the equations (4.15)-(4.17).

$$f_3 = f_3^* \quad -\frac{2}{3}\rho u + \frac{2}{3}(f_1 - f_3^*) + \frac{2}{3}(f_5 - f_7^*) + \frac{2}{3}(f_8 - f_6^*) \tag{4.15}$$

$$f_6 = f_6^* + \frac{1}{2}\rho v - \frac{1}{6}\rho u + \frac{1}{6}(f_1 - f_3^*) - \frac{1}{3}(f_5 - f_7^*) + \frac{2}{3}(f_8 - f_6^*) + \frac{1}{2}(f_4 - f_2) \tag{4.16}$$

$$f_7 = f_7^* - \frac{1}{2}\rho v - \frac{1}{6}\rho u + \frac{1}{6}(f_1 - f_3^*) + \frac{2}{3}(f_5 - f_7^*) - \frac{1}{3}(f_8 - f_6^*) - \frac{1}{2}(f_4 - f_2) \tag{4.17}$$

Subsequently, the values for the local part of the expressions in equation (4.12), denoted by an asterisk, need to be chosen. According to the literature, the following three common choices exist: (i) $f_i^*(x,t) = f_{\bar{i}}(x,t)$, (ii) $f_i^*(x,t) = f_i(x,t-\Delta t)$, (iii) $f_i^*(x,t) = f_i^{eq}(x,t)$. Here, the first choice again resembles the bounce-back rule. According to [51] and [82], the different choices produce equivalent results, which is suggested to origin from the momentum conservation, which all three choices satisfy. Also, the value of the density at the boundary node is received as:

$$\rho = \frac{1}{1+u}\left(f_0 + f_2 + f_4 + 2(f_1 + f_5 + f_8)\right) \tag{4.18}$$

The equations (4.15)-(4.17) are then again applied in the "Boundary" function, which calculates the missing distribution functions for boundary nodes before the calculation of the collision and the streaming step, as previously discussed. This way, no special treatment or alterations of the collision and of the streaming functions need to be conducted. Also, specific treatment is required for the corners at the outlet, as multiple distribution

functions remain undefined. To illustrate this, consider the top-right corner of the domain as depicted in Figure 4.9.

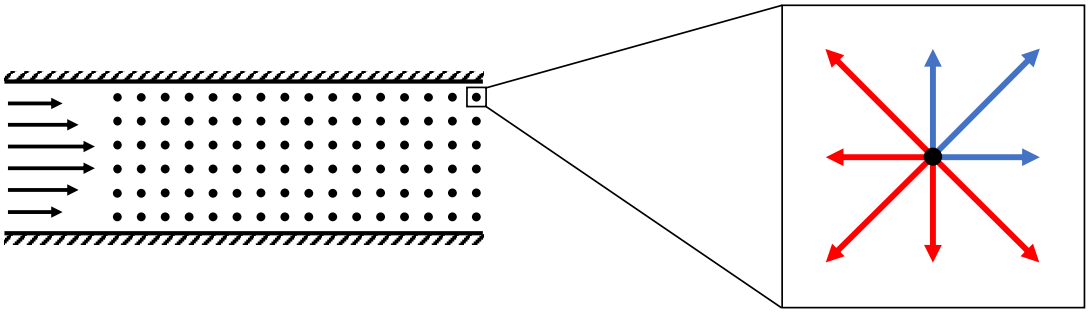

Figure 4.9: 2D Domain with known and unknown distribution functions for a corner node marked in blue and red, respectively.

The distribution functions number 1, 2 and 5 are known from streaming within the domain, whereas the distribution functions 3, 4, 6, 7 and 8 are unknown in the corner. Although vectors 6 and 8 stream out of the domain, their values influence the density at the corner node. Consequently, it is imperative to specify the density at the corner. The approach outlined in this paper aligns with the principles presented in reference [82], utilizing the nomenclature of the distribution functions introduced earlier. The missing distribution functions are determined as shown in equation (4.19):

$$\begin{aligned} f_3(\vec{x},t) &= f_1(\vec{x},t) - w_3 \cdot Q_x \quad & f_6(\vec{x},t) &= f_8(\vec{x},t) - w_6 \cdot (Q_x - Q_y) \\ f_4(\vec{x},t) &= f_2(\vec{x},t) - w_4 \cdot Q_y \quad & f_7(\vec{x},t) &= f_5(\vec{x},t) - w_7 \cdot (Q_x + Q_y) \end{aligned} \tag{4.19}$$

Subsequently, the values are incorporated into the equations used to calculate the macroscopic density and the two velocity components, following the determination of the three unknown variables Q_x, Q_y and f_8. The resulting expressions are shown in equation (4.20):

$$\begin{aligned} f_8(\vec{x},t) &= \frac{1}{2}\left[\rho - f_0(\vec{x},t) - 2(f_1(\vec{x},t) + f_2(\vec{x},t) + f_5(\vec{x},t)) + \rho u + \frac{2}{3}\rho v\right] \\ f_6(\vec{x},t) &= f_8(\vec{x},t) - \frac{1}{6}\rho u + \frac{1}{6}\rho v, \quad & f_3(\vec{x},t) &= f_1(\vec{x},t) - \frac{2}{3}\rho u \\ f_7(\vec{x},t) &= f_5(\vec{x},t) - \frac{1}{6}\rho u + \frac{1}{6}\rho v, \quad & f_4(\vec{x},t) &= f_2(\vec{x},t) - \frac{2}{3}\rho v \end{aligned} \tag{4.20}$$

The process is repeated in a similar manner for the lower corner at the outlet of the domain, leading to the determination of the missing distribution functions, as illustrated

in equation (4.21):

$$\begin{aligned} f_5(\vec{x},t) &= \frac{1}{2}\left[\rho - f_0(\vec{x},t) - 2(f_1(\vec{x},t) + f_4(\vec{x},t) + f_8(\vec{x},t)) + \rho u - \frac{2}{3}\rho v\right] \\ f_6(\vec{x},t) &= f_8(\vec{x},t) - \frac{1}{6}\rho u + \frac{1}{6}\rho v, \quad f_3(\vec{x},t) = f_1(\vec{x},t) - \frac{2}{3}\rho u \\ f_7(\vec{x},t) &= f_5(\vec{x},t) - \frac{1}{6}\rho u + \frac{1}{6}\rho v, \quad f_2(\vec{x},t) = f_4(\vec{x},t) + \frac{2}{3}\rho v \end{aligned} \tag{4.21}$$

4.2.2 2D formulation

In this section, the formulations for all boundary conditions (BC) for the 2D case as subsequently used in this thesis are summarized.

Flow BC

- Outlet-centre

$$\begin{aligned} f_3 =& f_3^{eq} - \frac{2}{3}\rho u + \frac{2}{3}(f_1 - f_3^{eq}) + \frac{2}{3}(f_5 - f_7^{eq}) + \frac{2}{3}(f_8 - f_6^{eq}) \\ f_6 =& f_6^{eq} + \frac{1}{2}\rho v - \frac{1}{6}\rho u + \frac{1}{6}(f_1 - f_3^{eq}) - \frac{1}{3}(f_5 - f_7^{eq}) + \frac{2}{3}(f_8 - f_6^{eq}) + \frac{1}{2}(f_4 - f_2) \\ f_7 =& f_7^{eq} - \frac{1}{2}\rho v - \frac{1}{6}\rho u + \frac{1}{6}(f_1 - f_3^{eq}) + \frac{2}{3}(f_5 - f_7^{eq}) - \frac{1}{3}(f_8 - f_6^{eq}) - \frac{1}{2}(f_4 - f_2) \end{aligned} \tag{4.22}$$

- Outlet top corner

$$\begin{aligned} f_8(x,t) &= \frac{1}{2}\left[\rho - f_0(\vec{x},t) - 2(f_1(\vec{x},t) + f_2(\vec{x},t) + f_5(\vec{x},t)) + \rho u + \frac{2}{3}\rho v\right] \\ f_6(\vec{x},t) &= f_8(\vec{x},t) - \frac{1}{6}\rho u + \frac{1}{6}\rho v, \quad f_3(\vec{x},t) = f_1(\vec{x},t) - \frac{2}{3}\rho u \\ f_7(\vec{x},t) &= f_5(\vec{x},t) - \frac{1}{6}\rho u + \frac{1}{6}\rho v, \quad f_4(\vec{x},t) = f_2(\vec{x},t) - \frac{2}{3}\rho v \end{aligned} \tag{4.23}$$

- Outlet bottom corner

$$\begin{aligned} f_5(\vec{x},t) &= \frac{1}{2}\left[\rho - f_0(\vec{x},t) - 2(f_1(\vec{x},t) + f_4(\vec{x},t) + f_8(\vec{x},t)) + \rho u - \frac{2}{3}\rho v\right] \\ f_6(\vec{x},t) &= f_8(\vec{x},t) - \frac{1}{6}\rho u + \frac{1}{6}\rho v, \quad f_3(\vec{x},t) = f_1(\vec{x},t) - \frac{2}{3}\rho u \\ f_7(\vec{x},t) &= f_5(\vec{x},t) - \frac{1}{6}\rho u + \frac{1}{6}\rho v, \quad f_2(\vec{x},t) = f_4(\vec{x},t) + \frac{2}{3}\rho v \end{aligned} \tag{4.24}$$

Components

- Inlet

$$\begin{aligned} g_{5,O_2}(\vec{x},t) &= -g_{7,O_2}(\vec{x},t) + 2\,t[5]\,Y_{O_2,in} \\ g_{1,O_2}(\vec{x},t) &= -g_{3,O_2}(\vec{x},t) + 2\,t[1]\,Y_{O_2,in} \\ g_{8,O_2}(\vec{x},t) &= -g_{6,O_2}(\vec{x},t) + 2\,t[8]\,Y_{O_2,in} \end{aligned} \tag{4.25}$$

- Outlet center

$$\begin{aligned} g_{6,O_2}(\vec{x},t) &= -g_{8,O_2}(\vec{x},t) + 2\,t[6]\,Y_{O_2,out} \\ g_{3,O_2}(\vec{x},t) &= -g_{1,O_2}(\vec{x},t) + 2\,t[3]\,Y_{O_2,out} \\ g_{7,O_2}(\vec{x},t) &= -g_{5,O_2}(\vec{x},t) + 2\,t[7]\,Y_{O_2,out} \end{aligned} \tag{4.26}$$

- Outlet bottom corner

$$\begin{aligned} g_{2,O_2}(\vec{x},t) &= g^{eq}_{2,O_2}(\vec{x},t) + t[2]\,GC_{O_2} \\ g_{3,O_2}(\vec{x},t) &= g^{eq}_{3,O_2}(\vec{x},t) + t[3]\,GC_{O_2} \\ g_{5,O_2}(\vec{x},t) &= g^{eq}_{5,O_2}(\vec{x},t) + t[5]\,GC_{O_2} \\ g_{6,O_2}(\vec{x},t) &= g^{eq}_{6,O_2}(\vec{x},t) + t[6]\,GC_{O_2} \\ g_{7,O_2}(\vec{x},t) &= g^{eq}_{7,O_2}(\vec{x},t) + t[7]\,GC_{O_2} \end{aligned} \tag{4.27}$$

$$\begin{aligned} GC_{O_2} &= \frac{(Y_{O_2} - Y_{O_2,\epsilon})}{t[2]+t[3]+t[5]+t[6]+t[7]} \\ Y_{O_2} &= \sum_i g_{i,O_2} \\ Y_{O_2,\epsilon} &= g_{0,O_2} + g_{1,O_2} + g^{eq}_{2,O_2} + g^{eq}_{3,O_2} + g_{4,O_2} + g^{eq}_{5,O_2} + g^{eq}_{6,O_2} + g^{eq}_{7,O_2} + g_{8,O_2} \end{aligned} \tag{4.28}$$

- Outlet top corner

$$\begin{aligned} g_{3,O_2}(\vec{x},t) &= g^{eq}_{3,O_2}(\vec{x},t) + t[3]\,GC_{O_2} \\ g_{4,O_2}(\vec{x},t) &= g^{eq}_{4,O_2}(\vec{x},t) + t[4]\,GC_{O_2} \\ g_{6,O_2}(\vec{x},t) &= g^{eq}_{6,O_2}(\vec{x},t) + t[6]\,GC_{O_2} \\ g_{7,O_2}(\vec{x},t) &= g^{eq}_{7,O_2}(\vec{x},t) + t[7]\,GC_{O_2} \\ g_{8,O_2}(\vec{x},t) &= g^{eq}_{8,O_2}(\vec{x},t) + t[8]\,GC_{O_2} \end{aligned} \tag{4.29}$$

$$\begin{aligned} GC_{O_2} &= \frac{(Y_{O_2} - Y_{O_2,\epsilon})}{t[3]+t[4]+t[6]+t[7]+t[8]} \\ Y_{O_2} &= \sum_i g_{i,O_2} \\ Y_{O_2,\epsilon} &= g_{0,O_2} + g_{1,O_2} + g_{2,O_2} + g^{eq}_{3,O_2} + g^{eq}_{4,O_2} + g_{5,O_2} + g^{eq}_{6,O_2} + g^{eq}_{7,O_2} + g^{eq}_{8,O_2} \end{aligned} \tag{4.30}$$

temperature field

- inlet

$$\begin{aligned} g_{5,T}(\vec{x},t) &= -g_{7,T}(\vec{x},t) + 2\,t[5]\,T_{in} \\ g_{1,T}(\vec{x},t) &= -g_{3,T}(\vec{x},t) + 2\,t[1]\,T_{in} \\ g_{8,T}(\vec{x},t) &= -g_{6,T}(\vec{x},t) + 2\,t[8]\,T_{in} \end{aligned} \tag{4.31}$$

- outlet

$$\begin{aligned} g_{6,T}(\vec{x},t) &= -g_{8,T}(\vec{x},t) + 2\,t[6]\,T_{out} \\ g_{3,T}(\vec{x},t) &= -g_{1,T}(\vec{x},t) + 2\,t[3]\,T_{out} \\ g_{7,T}(\vec{x},t) &= -g_{5,T}(\vec{x},t) + 2\,t[7]\,T_{out} \end{aligned} \tag{4.32}$$

4.2.3 3D formulation

For three dimensional simulations using the D3Q19 lattice discretization, the methods to derive the boundary conditions, which were presented in section 4.2.1 for the 2D case, are applied to receive the 3D expressions of the boundary conditions, as shown in the following:

Flow Boundary Condition

- Outlet

$$f_0 = f_0^* - \frac{1}{3}\rho u_x + \frac{1}{3}(f_{10} + f_{13} + f_{14} + f_{15} + f_{16} - f_0^* - f_3^* - f_4^* - f_5^* - f_6^*) \tag{4.33}$$

$$\begin{aligned} f_3 = f_3^* &- \frac{1}{6}\rho u_x - \frac{1}{2}\rho u_y + \frac{1}{6}\left[(f_{10} - f_0^*) + (f_{15} - f_5^*) + (f_{16} - f_6^*)\right] \\ &+ \frac{1}{2}\left[(f_{11} - f_1) + (f_{18} - f_8) + (f_{17} - f_7)\right] + \frac{1}{3}(f_4^* - f_{14}) + \frac{2}{3}(f_{13} - f_3^*) \end{aligned} \tag{4.34}$$

$$\begin{aligned} f_4 = f_4^* &- \frac{1}{6}\rho u_x + \frac{1}{2}\rho u_y + \frac{1}{6}\left[(f_{10} - f_0^*) + (f_{15} - f_5^*) + (f_{16} - f_6^*)\right] \\ &+ \frac{1}{2}\left[(f_1 - f_{11}) + (f_8 - f_{18}) + (f_7 - f_{17})\right] + \frac{1}{3}(f_3^* - f_{13}) + \frac{2}{3}(f_{14} - f_4^*) \end{aligned} \tag{4.35}$$

$$\begin{aligned} f_5 = f_5^* &- \frac{1}{6}\rho u_x - \frac{1}{2}\rho u_z + \frac{1}{6}\left[(f_{10} - f_0^*) + (f_{14} - f_4^*) + (f_{13} - f_3^*)\right] \\ &+ \frac{1}{2}\left[(f_{17} - f_7) + (f_{12} - f_2) + (f_8 - f_{18})\right] + \frac{1}{3}(f_6^* - f_{16}) + \frac{2}{3}(f_{15} - f_5^*) \end{aligned} \tag{4.36}$$

$$\begin{aligned} f_6 = f_6^* &- \frac{1}{6}\rho u_x + \frac{1}{2}\rho u_z + \frac{1}{6}\left[(f_{10} - f_0^*) + (f_{13} - f_3^*) + (f_{14} - f_4^*)\right] \\ &+ \frac{1}{2}\left[(f_{18} - f_8) + (f_7 - f_{17}) + (f_2 - f_{12})\right] + \frac{1}{3}(f_5^* - f_{15}) + \frac{2}{3}(f_{16} - f_6^*) \end{aligned} \tag{4.37}$$

- Outlet upper edge

$$
\begin{aligned}
f_{14}(\vec{x},t) &= \frac{1}{2}\left[\rho+\rho u_x+\frac{2}{3}\rho u_y - f_9 - f_2 - f_{12} - 2(f_{10}+f_{11}+f_{13}+f_{15}+f_{16}+f_{17}+f_{18})\right]\\
f_1(\vec{x},t) &= f_{11}(\vec{x},t) - \frac{1}{3}\rho u_y\\
f_7(\vec{x},t) &= f_{17}(\vec{x},t) - \frac{1}{6}\rho u_y - \frac{1}{4}\rho u_z - \frac{1}{4}(f_2 - f_{12})\\
f_8(\vec{x},t) &= f_{18}(\vec{x},t) - \frac{1}{6}\rho u_y + \frac{1}{4}\rho u_z + \frac{1}{4}(f_2 - f_{12})\\
f_3(\vec{x},t) &= f_{13}(\vec{x},t) - \frac{1}{6}\rho u_x - \frac{1}{6}\rho u_y\\
f_0(\vec{x},t) &= f_{10}(\vec{x},t) - \frac{1}{3}\rho u_x\\
f_5(\vec{x},t) &= f_{15}(\vec{x},t) - \frac{1}{6}\rho u_x - \frac{1}{4}\rho u_z - \frac{1}{4}(f_2 - f_{12})\\
f_6(\vec{x},t) &= f_{16}(\vec{x},t) - \frac{1}{6}\rho u_x + \frac{1}{4}\rho u_z + \frac{1}{4}(f_2 - f_{12})\\
f_4(\vec{x},t) &= f_{14}(\vec{x},t) - \frac{1}{6}\rho u_x + \frac{1}{6}\rho u_y
\end{aligned}
\tag{4.38}
$$

- Outlet lower edge

$$
\begin{aligned}
f_{13}(\vec{x},t) &= \frac{1}{2}\left[\rho+\rho u_x-\frac{2}{3}\rho u_y - f_9 - f_2 - f_{12} - 2(f_{10}+f_{15}+f_{16}+f_1+f_7+f_8+f_{14})\right]\\
f_{11}(\vec{x},t) &= f_1(\vec{x},t) + \frac{1}{3}\rho u_y\\
f_{17}(\vec{x},t) &= f_7(\vec{x},t) + \frac{1}{6}\rho u_y + \frac{1}{4}\rho u_z + \frac{1}{4}(f_2 - f_{12})\\
f_{18}(\vec{x},t) &= f_8(\vec{x},t) + \frac{1}{6}\rho u_y - \frac{1}{4}\rho u_z - \frac{1}{4}(f_2 - f_{12})\\
f_3(\vec{x},t) &= f_{13}(\vec{x},t) - \frac{1}{6}\rho u_x - \frac{1}{6}\rho u_y\\
f_0(\vec{x},t) &= f_{10}(\vec{x},t) - \frac{1}{3}\rho u_x\\
f_5(\vec{x},t) &= f_{15}(\vec{x},t) - \frac{1}{6}\rho u_x - \frac{1}{4}\rho u_z - \frac{1}{4}(f_2 - f_{12})\\
f_6(\vec{x},t) &= f_{16}(\vec{x},t) - \frac{1}{6}\rho u_x + \frac{1}{4}\rho u_z + \frac{1}{4}(f_2 - f_{12})\\
f_4(\vec{x},t) &= f_{14}(\vec{x},t) - \frac{1}{6}\rho u_x + \frac{1}{6}\rho u_y
\end{aligned}
\tag{4.39}
$$

Temperature

- Inlet

$$\begin{aligned} g_{10,T}(\vec{x},t) &= -g_{0,T}(\vec{x},t) + 2\,t[0]\,T_{in} \\ g_{13,T}(\vec{x},t) &= -g_{3,T}(\vec{x},t) + 2\,t[3]\,T_{in} \\ g_{14,T}(\vec{x},t) &= -g_{4,T}(\vec{x},t) + 2\,t[4]\,T_{in} \\ g_{15,T}(\vec{x},t) &= -g_{5,T}(\vec{x},t) + 2\,t[5]\,T_{in} \\ g_{16,T}(\vec{x},t) &= -g_{6,T}(\vec{x},t) + 2\,t[6]\,T_{in} \end{aligned} \tag{4.40}$$

- Outlet

$$\begin{aligned} g_{0,T}(\vec{x},t) &= -g_{10,T}(\vec{x},t) + 2\,t[10]\,T_{out} \\ g_{3,T}(\vec{x},t) &= -g_{13,T}(\vec{x},t) + 2\,t[13]\,T_{out} \\ g_{4,T}(\vec{x},t) &= -g_{14,T}(\vec{x},t) + 2\,t[14]\,T_{out} \\ g_{5,T}(\vec{x},t) &= -g_{15,T}(\vec{x},t) + 2\,t[15]\,T_{out} \\ g_{6,T}(\vec{x},t) &= -g_{16,T}(\vec{x},t) + 2\,t[16]\,T_{out} \end{aligned} \tag{4.41}$$

Components

- Inlet

$$\begin{aligned} g_{10,O_2}(\vec{x},t) &= -g_{0,O_2}(\vec{x},t) + 2\,t[0]\,Y_{O_2,in} \\ g_{13,O_2}(\vec{x},t) &= -g_{3,O_2}(\vec{x},t) + 2\,t[3]\,Y_{O_2,in} \\ g_{14,O_2}(\vec{x},t) &= -g_{4,O_2}(\vec{x},t) + 2\,t[4]\,Y_{O_2,in} \\ g_{15,O_2}(\vec{x},t) &= -g_{5,O_2}(\vec{x},t) + 2\,t[5]\,Y_{O_2,in} \\ g_{16,O_2}(\vec{x},t) &= -g_{6,O_2}(\vec{x},t) + 2\,t[6]\,Y_{O_2,in} \end{aligned} \tag{4.42}$$

- Outlet center

$$\begin{aligned} g_{0,O_2}(\vec{x},t) &= -g_{10,O_2}(\vec{x},t) + 2\,t[10]\,Y_{O_2,out} \\ g_{3,O_2}(\vec{x},t) &= -g_{13,O_2}(\vec{x},t) + 2\,t[13]\,Y_{O_2,out} \\ g_{4,O_2}(\vec{x},t) &= -g_{14,O_2}(\vec{x},t) + 2\,t[14]\,Y_{O_2,out} \\ g_{5,O_2}(\vec{x},t) &= -g_{15,O_2}(\vec{x},t) + 2\,t[15]\,Y_{O_2,out} \\ g_{6,O_2}(\vec{x},t) &= -g_{16,O_2}(\vec{x},t) + 2\,t[16]\,Y_{O_2,out} \end{aligned} \tag{4.43}$$

- Outlet Top Edge

$$
\begin{aligned}
g_{0,O_2}(\vec{x},t) &= g^{eq}_{0,O_2}(\vec{x},t) + t[0]\, GC_{O_2} \\
g_{1,O_2}(\vec{x},t) &= g^{eq}_{1,O_2}(\vec{x},t) + t[1]\, GC_{O_2} \\
g_{3,O_2}(\vec{x},t) &= g^{eq}_{3,O_2}(\vec{x},t) + t[3]\, GC_{O_2} \\
g_{4,O_2}(\vec{x},t) &= g^{eq}_{4,O_2}(\vec{x},t) + t[4]\, GC_{O_2} \\
g_{5,O_2}(\vec{x},t) &= g^{eq}_{5,O_2}(\vec{x},t) + t[5]\, GC_{O_2} \\
g_{6,O_2}(\vec{x},t) &= g^{eq}_{6,O_2}(\vec{x},t) + t[6]\, GC_{O_2} \\
g_{7,O_2}(\vec{x},t) &= g^{eq}_{7,O_2}(\vec{x},t) + t[7]\, GC_{O_2} \\
g_{8,O_2}(\vec{x},t) &= g^{eq}_{8,O_2}(\vec{x},t) + t[8]\, GC_{O_2} \\
g_{14,O_2}(\vec{x},t) &= g^{eq}_{14,O_2}(\vec{x},t) + t[14]\, GC_{O_2}
\end{aligned}
\tag{4.44}
$$

$$
\begin{aligned}
GC_{O_2} &= \frac{(Y_{O_2} - Y_{O_2,\epsilon})}{t[0]+t[1]+t[3]+t[4]+t[5]+t[6]+t[7]+t[8]+t[14]} \\
Y_{O_2} &= \sum_i g_{i,O_2} \\
Y_{O_2,\epsilon} &= g^{eq}_{0,O_2} + g^{eq}_{1,O_2} + g_{2,O_2} + g^{eq}_{3,O_2} + g^{eq}_{4,O_2} + g^{eq}_{5,O_2} + g^{eq}_{6,O_2} + g^{eq}_{7,O_2} + g^{eq}_{8,O_2} + g_{9,O_2} \\
&+ g_{10,O_2} + g_{11,O_2} + g_{12,O_2} + g_{13,O_2} + g^{eq}_{14,O_2} + g_{15,O_2} + g_{16,O_2} + g_{17,O_2} + g_{18,O_2}
\end{aligned}
\tag{4.45}
$$

- Outlet Bottom Edge

$$
\begin{aligned}
g_{0,O_2}(\vec{x},t) &= g^{eq}_{0,O_2}(\vec{x},t) + t[0]\, GC_{O_2} \\
g_{3,O_2}(\vec{x},t) &= g^{eq}_{3,O_2}(\vec{x},t) + t[3]\, GC_{O_2} \\
g_{4,O_2}(\vec{x},t) &= g^{eq}_{4,O_2}(\vec{x},t) + t[4]\, GC_{O_2} \\
g_{5,O_2}(\vec{x},t) &= g^{eq}_{5,O_2}(\vec{x},t) + t[5]\, GC_{O_2} \\
g_{6,O_2}(\vec{x},t) &= g^{eq}_{6,O_2}(\vec{x},t) + t[6]\, GC_{O_2} \\
g_{11,O_2}(\vec{x},t) &= g^{eq}_{1,O_2}(\vec{x},t) + t[11]\, GC_{O_2} \\
g_{13,O_2}(\vec{x},t) &= g^{eq}_{13,O_2}(\vec{x},t) + t[13]\, GC_{O_2} \\
g_{17,O_2}(\vec{x},t) &= g^{eq}_{17,O_2}(\vec{x},t) + t[17]\, GC_{O_2} \\
g_{18,O_2}(\vec{x},t) &= g^{eq}_{18,O_2}(\vec{x},t) + t[18]\, GC_{O_2}
\end{aligned}
\tag{4.46}
$$

$$
\begin{aligned}
GC_{O_2} &= \frac{(Y_{O_2} - Y_{O_2,\epsilon})}{t[0]+t[3]+t[4]+t[5]+t[6]+t[11]+t[13]+t[17]+t[18]} \\
Y_{O_2} &= \sum_i g_{i,O_2} \\
Y_{O_2,\epsilon} &= g^{eq}_{0,O_2} + g_{1,O_2} + g_{2,O_2} + g^{eq}_{3,O_2} + g^{eq}_{4,O_2} + g^{eq}_{5,O_2} + g^{eq}_{6,O_2} + g_{7,O_2} + g_{8,O_2} + g_{9,O_2} \\
&+ g_{10,O_2} + g^{eq}_{11,O_2} + g_{12,O_2} + g^{eq}_{13,O_2} + g_{14,O_2} + g_{15,O_2} + g_{16,O_2} + g^{eq}_{17,O_2} + g^{eq}_{18,O_2}
\end{aligned} \tag{4.47}
$$

- Outlet Front Edge

$$
\begin{aligned}
g_{0,O_2}(\vec{x},t) &= g^{eq}_{0,O_2}(\vec{x},t) + t[0]\, GC_{O_2} \\
g_{2,O_2}(\vec{x},t) &= g^{eq}_{2,O_2}(\vec{x},t) + t[2]\, GC_{O_2} \\
g_{3,O_2}(\vec{x},t) &= g^{eq}_{3,O_2}(\vec{x},t) + t[3]\, GC_{O_2} \\
g_{4,O_2}(\vec{x},t) &= g^{eq}_{4,O_2}(\vec{x},t) + t[4]\, GC_{O_2} \\
g_{5,O_2}(\vec{x},t) &= g^{eq}_{5,O_2}(\vec{x},t) + t[5]\, GC_{O_2} \\
g_{6,O_2}(\vec{x},t) &= g^{eq}_{6,O_2}(\vec{x},t) + t[6]\, GC_{O_2} \\
g_{7,O_2}(\vec{x},t) &= g^{eq}_{7,O_2}(\vec{x},t) + t[7]\, GC_{O_2} \\
g_{16,O_2}(\vec{x},t) &= g^{eq}_{16,O_2}(\vec{x},t) + t[16]\, GC_{O_2} \\
g_{18,O_2}(\vec{x},t) &= g^{eq}_{18,O_2}(\vec{x},t) + t[18]\, GC_{O_2}
\end{aligned} \tag{4.48}
$$

$$
\begin{aligned}
GC_{O_2} &= \frac{(Y_{O_2} - Y_{O_2,\epsilon})}{t[0]+t[3]+t[4]+t[5]+t[6]+t[2]+t[7]+t[16]+t[18]} \\
Y_{O_2} &= \sum_i g_{i,O_2} \\
Y_{O_2,\epsilon} &= g^{eq}_{0,O_2} + g_{1,O_2} + g^{eq}_{2,O_2} + g^{eq}_{3,O_2} + g^{eq}_{4,O_2} + g^{eq}_{5,O_2} + g^{eq}_{6,O_2} + g^{eq}_{7,O_2} + g_{8,O_2} + g_{9,O_2} \\
&+ g_{10,O_2} + g_{11,O_2} + g_{12,O_2} + g_{13,O_2} + g_{14,O_2} + g_{15,O_2} + g^{eq}_{16,O_2} + g_{17,O_2} + g^{eq}_{18,O_2}
\end{aligned} \tag{4.49}
$$

- Outlet Back Edge

$$
\begin{aligned}
g_{0,O_2}(\vec{x},t) &= g^{eq}_{0,O_2}(\vec{x},t) + t[0]\, GC_{O_2} \\
g_{3,O_2}(\vec{x},t) &= g^{eq}_{3,O_2}(\vec{x},t) + t[3]\, GC_{O_2} \\
g_{4,O_2}(\vec{x},t) &= g^{eq}_{4,O_2}(\vec{x},t) + t[4]\, GC_{O_2} \\
g_{5,O_2}(\vec{x},t) &= g^{eq}_{5,O_2}(\vec{x},t) + t[5]\, GC_{O_2} \\
g_{6,O_2}(\vec{x},t) &= g^{eq}_{6,O_2}(\vec{x},t) + t[6]\, GC_{O_2} \\
g_{8,O_2}(\vec{x},t) &= g^{eq}_{8,O_2}(\vec{x},t) + t[8]\, GC_{O_2} \\
g_{12,O_2}(\vec{x},t) &= g^{eq}_{12,O_2}(\vec{x},t) + t[12]\, GC_{O_2} \\
g_{15,O_2}(\vec{x},t) &= g^{eq}_{15,O_2}(\vec{x},t) + t[15]\, GC_{O_2} \\
g_{17,O_2}(\vec{x},t) &= g^{eq}_{17,O_2}(\vec{x},t) + t[17]\, GC_{O_2}
\end{aligned}
\tag{4.50}
$$

$$
\begin{aligned}
GC_{O_2} &= \frac{(Y_{O_2} - Y_{O_2,\epsilon})}{t[0]+t[3]+t[4]+t[5]+t[6]+t[8]+t[12]+t[15]+t[17]} \\
Y_{O_2} &= \sum_i g_{i,O_2} \\
Y_{O_2,\epsilon} &= g^{eq}_{0,O_2} + g_{1,O_2} + g_{2,O_2} + g^{eq}_{3,O_2} + g^{eq}_{4,O_2} + g^{eq}_{5,O_2} + g^{eq}_{6,O_2} + g_{7,O_2} + g^{eq}_{8,O_2} + g_{9,O_2} \\
&\quad + g_{10,O_2} + g_{11,O_2} + g^{eq}_{12,O_2} + g_{13,O_2} + g_{14,O_2} + g^{eq}_{15,O_2} + g_{16,O_2} + g^{eq}_{17,O_2} + g_{18,O_2}
\end{aligned}
\tag{4.51}
$$

4.3 Calculation of reactive surfaces

As described earlier, the main parameter for the comparison between experimental and computational soot combustion will be the temporal evolution of the reactive surface of the soot geometry as a result of combustion. Therefore, an algorithm for the calculation of the reactive surface at each time step is needed.

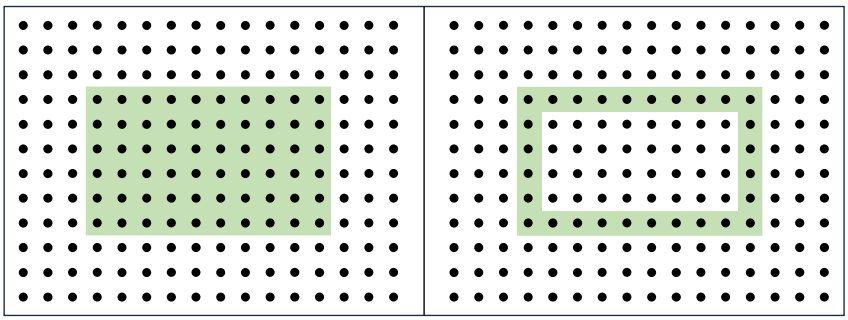

Figure 4.10: Solid obstacle displayed in green without (left) and with (right) cavity, resulting in different values for the reactive surface, as calculated by the rudimentary algorithm.

A trivial idea would be to iterate over all lattice nodes associated with the solid domain, to compare its property with the properties of all neighbouring nodes, and to sum up

all interfaces by means of multiples of the lattice distance Δx. This, however, does not result in the correct value of the accessible reactive surface, as it is demonstrated by Figure 4.10. When iterating over all solid nodes (depicted in red) and summing up the interfaces, the rudimentary way to calculate the accessible reactive surface will result in the value of 32 for the case of a solid obstacle without cavities (left case). For the case of a solid obstacle with cavities, which are not connected to the surrounding gas phase (right case), the algorithm would wrongfully conclude that the inner surface is "accessible reactive surface", resulting in a value of 56. It becomes apparent that cavities with no connection to the surrounding gas phase have to be excluded from the calculation of the effective, accessible reactive surface. This can be achieved by using the "Breitensuche (engl. breadth-first search)" algorithm, originally invented by Konrad Zuse in 1945 [157]. With this algorithm, the lattice can be systematically propagated through from a given starting point, and the information of all nodes which are accessed throughout the propagation, is stored in a tree-like data structure. The implementation is subsequently explained in detail. The algorithm is implemented by utilizing two vectors, one of type "std::vector< *bool* > visited", in which the information, if a cell has been "visited" by the algorithm, is stored as a Boolean variable (true or false). The second vector is of type "std::queue< *int* > q", which saves the index of the visited cells. The algorithm starts by assigning the outermost nodes of the domain to the queue-vector by utilizing the C++ command "push". This adds the pushed cell to the top of the queue. Also, the cells are marked as "true" in the Boolean vector. This is done because the outermost nodes are used as a starting point to propagate through the domain and to find all accessible gaseous nodes. Then, a while-loop is performed with the condition "!q.empty", which means that the following operators will be executed as long as there are cells left inside of the queue-vector q. Inside of the while-loop, the uppermost index stored in vector q is taken. Subsequently, its four neighbouring nodes are being examined according to "celltype::bulk" && "!visited", which means that they are assigned to the gas phase and have not yet been visited. If this condition is true, the neighbouring node is added to the list q and its Boolean value is set to "true". Since a while-loop is used, the algorithm will propagate through the part of the domain, which is of type gas-phase and connected with the outer flow. Explicitly it would mean that the inner cavity, as shown in Figure 4.10, would be excluded by the algorithm. Finally, after the code leaves the while-loop, a for-loop is executed, which runs over all cells of the domain. Inside, with an if-condition, the cells assigned to the solid-domain are taken and their neighbours are examined. If the neighbour is of type "gas-phase" and has been "visited" by the previous search algorithm, then the value of the surface is increased by the value of 1 lattice spacing.

Algorithm 2 Breadth-First Search Algorithm for surface calculation

```
1: Input: lbm, q, visited, surface
2:                                          ▷ Initialize the queue with boundary nodes
3: for iX ← 0 to lbm.dim.nx do
4:     for iY ← 0 to lbm.dim.ny do
5:         i ← lbm.xyz_to_i(iX,iY)
6:         if lbm.flag[i] = bulk and node on Boundary then
7:             q.push(i)
8:             visited[i] ← true
9:         end if
10:    end for
11: end for
12:                                                  ▷ Breadth-First Search
13: while not q.empty() do
14:    i ← q.front()
15:    (iX,iY) ← lbm.i_to_xyz(i)
16:    q.pop()
17:    for k ← 0 to 3 do
18:        XX ← iX + lbm.c[k+1][0]
19:        YY ← iY + lbm.c[k+1][1]
20:        nb ← lbm.xyz_to_i(XX,YY)
21:        if XX within domain and YY within domain then
22:            if lbm.flag[nb] = CellType::bulk and not visited[nb] then
23:                q.push(nb)
24:                visited[nb] ← true
25:            end if
26:        end if
27:    end for
28: end while
29:                          ▷ Sum up the surface of the solid obstacle with the outer flow
30: for iX ← 0 to lbm.dim.nx do
31:    for iY ← 0 to lbm.dim.ny do
32:        i ← lbm.xyz_to_i(iX,iY)
33:        if lbm.flag[i] = CellType::reactive_obstacle and not visited[i] then
34:            for k ← 0 to 3 do
35:                XX ← iX + lbm.c[k+1][0]
36:                YY ← iY + lbm.c[k+1][1]
37:                nb ← lbm.xyz_to_i(XX,YY)
38:                if XX within domain and YY within domain then
39:                    if lbm.flag[nb] = CellType::bulk and visited[nb] then
40:                        surface ← surface + 1
41:                    end if
42:                end if
43:            end for
44:        end if
45:    end for
46: end for
[1]
```

4.4 Combustion with elaborate geometries - calculation of normal vectors

For the calculation of the interface mass fractions of the reactive species, the surface normal vectors are needed, as it was shown in the equations (3.111)-(3.113). The calculation is performed based on the flag properties of the neighbouring nodes. For this, a loop is executed over all lattice velocity directions with index k∈[0,9] in the 2D case, in which the flag property is verified. If a neighbouring node is of type "reactive_obstacle", the value of k gets added up. This is demonstrated on one exemplary case, as shown in Figure 4.11. Here, the surface normal vector calculated based on the lattice node indicated in red, will be shown. The lattice nodes to its north, west and north-west direction are assumed to be solid, with the other nodes being assigned to the gas-phase. The sum of all directions, in which a solid-node is found, is given as 11=2+3+6. After the sum to distinguish between the different solid configurations has been calculated, the surface normal for each streaming direction has to be determined. Since the half-way bounce-back method is used throughout the model, the interface is always assumed to be in the centre between two lattice nodes, creating a step-like shape with either horizontal or vertical interfaces. This leads to the surface normal vector for streaming in the direction of the main axes being always the vector with opposite orientation. Only the surface normal vectors for the streaming in the diagonal directions vary with different surface geometries and thus have to be calculated based on the aforementioned sum of the lattice velocity vectors. For this, every possible orientation is examined and the corresponding sum is saved in order to determine all surface normal vectors.

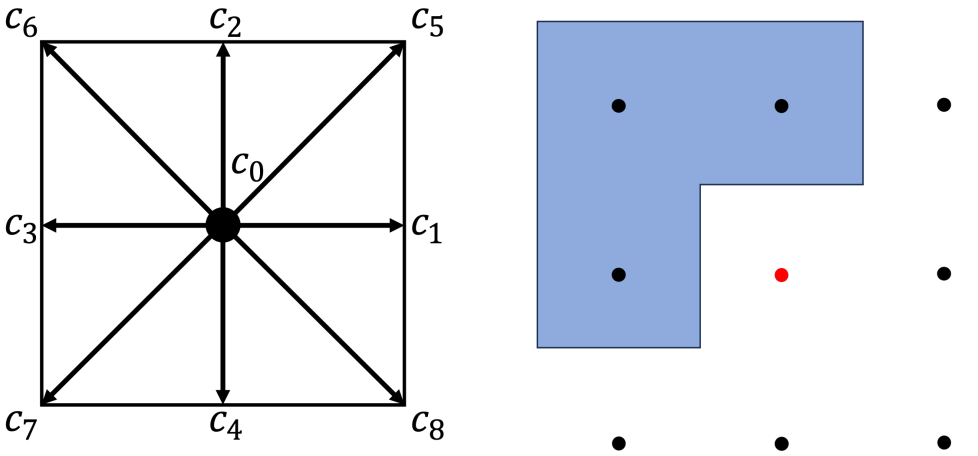

Figure 4.11: D2Q9 lattice (left) and example of a interface morphology for the calculation of surface normal vectors (right).

4.5 Calibration of the model

The lattice Boltzmann model, which is used for the simulation of heterogeneous combustion reactions in porous media, requires and enables calibration on multiple fronts. First, correct values for the parameters describing the properties of the phases, i.e. the solid soot phase and the gas phase consisting of O_2 and CO_2 need to be known. Additionally, the model requires information about the reaction equation as well as a reaction kinetics. Finally, a realistic soot geometry, given by FIB-SEM images, needs to be provided.
The parameters of the material properties are chosen as described in Appendix B and the determination of the geometry by FIB-SEM analysis was introduced in section 2.6.1. In order to describe the heterogeneous reaction, occurring at the interface between the solid soot phase and the educts in the gas phase, a chemical reaction and a corresponding reaction kinetics need to be defined. In this thesis, kinetics parameters are used, which are calculated based on data of soot combustion experiments provided by the ICVT. At ICVT, facilities exist to conduct soot combustion experiments while measuring the turnover. The turnover $\Delta\dot{m}_{CO_2}$ is calculated based on an inlet mass flow $\dot{m}_{in}$ with defined composition $Y_{CO_2,in}$, and analysis of the flow composition at the outlet $Y_{CO_2,out}$ using mass spectroscopy. This calculation is performed in the following equation:

$$\Delta\dot{m}_{CO_2} = \dot{m}_{out}\, Y_{CO_2,out} - \dot{m}_{in}\, Y_{CO_2,in} \tag{4.52}$$

Moreover, the combustion is conducted step-wise, enabling for the measurement of the reactive surface between the combustion cycles. This is achieved by cooling down the reactor using liquid nitrogen and subsequent adsorption of inert gas (i.e. nitrogen) to the porous media. After heating up the reactor to ambient temperature, the adsorbate is removed from the surface and the amount can be measured. By utilizing the Brunauer–Emmett–Teller (BET) method, the total surface of the porous soot structure can be calculated. Then, the surface specific reaction rate F_R, given in $\left[mol\, m^{-2}\, s^{-1}\right]$ can be calculated according to the following equation:

$$F_R = \frac{\Delta\dot{m}_{CO_2}}{M_{CO_2} \cdot BET} \tag{4.53}$$

The expression to describe the reaction kinetics, which was shown in equation (3.72), contains two parameters, which are to be determined. These are the pre-exponential factor A and the activation energy E_a. In order to calculate these parameters from experimental data, combustion experiments at multiple temperatures need to be conducted. Then, both missing parameters can be determined by reordering the reaction kinetics equation

according to equation (4.54) and drawing the following graph, as shown in Figure 4.12:

$$ln\left[\frac{F_r}{\frac{Y_{O_2}^I \rho}{M_{O_2}}}\right] = ln(A) - \frac{E_a}{RT} \tag{4.54}$$

Using this graph, the activation energy can be determined as the gradient of the line, with the pre-exponential factor being determined by the y-intercept.

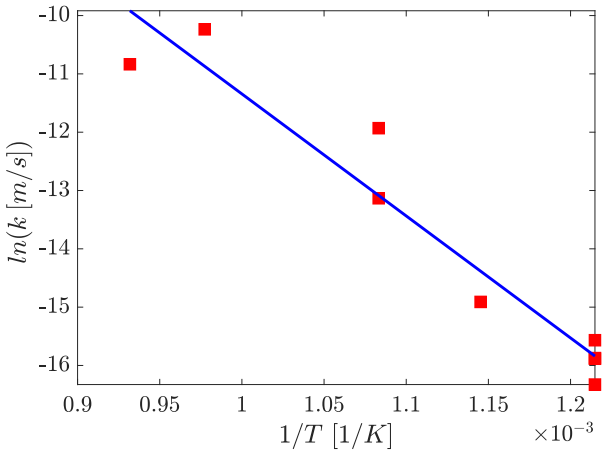

Figure 4.12: Arrhenius plot for the calculation of the parameters E_a and A of the reaction kinetics.

Concluding, this chapter presented the reader with an overview of the COLBM framework developed during this dissertation and its features. Furthermore, the implementation of all relevant boundary conditions in 2D and 3D was elaborated in detail. Moreover, the breadth-first search algorithm for the calculation of the specific reactive surface and the treatment of elaborate geometries was discussed. Finally, the calibration of the model with the experiments was introduced. The connection is facilitated by implementing the reaction kinetics, determined from experimental data, and usage of the soot structure, determined by FIB-SEM analysis of soot samples.

Chapter 5

Results and Discussion

In this chapter, the results of the doctoral work are presented. The main objective was to find means to study the influence of the morphology, and with it the surface area of soot onto the regeneration process of soot filters. For this purpose, a C++ code was developed and a multi-physics lattice Boltzmann model was implemented. The model encompasses LB expressions to describe a multi-component gas flow, consisting of the reactants, reaction products and inert components. Furthermore, a LB expression to describe the energy balance was implemented and a specific, explicit treatment for conjugate heat transfer at the interface between the solid soot and gas phase was added. In Chapter 5.1, the 2D LB model as described above, is validated thoroughly. It is a quote based on my recent publication [129]. Subsequently, the extension of the model to 3D as well as additional boundary conditions necessary to perform large-scale simulations, are presented in Chapter 5.2. In Chapter 5.3, an extensive parametric study, employing a realistic combustion test case, encompassing the consumption and temporal evolution of the soot structure, is performed. It is a quote based on a manuscript prepared for publication [128]. With this knowledge, simulations using the FIB-SEM geometry obtained from the experimental work, are performed and the results of the simulations are then compared with experimental data in Chapter 5.4. The main focus here was the study of the evolution of the specific surface with progressing combustion. Furthermore, the CO/CO_2 ratio was compared with experiments. Finally, a brief introduction into the primary particle design on the nano-scale is given in Chapter 5.5 in an effort to reproduce the tremendous increase in specific surface, which was found in the combustion experiments.

5.1 Validation of the combustion model in 2D

In this section, the *in-house* code will be systematically validated. Initially, its ability to accurately resolve fluid flow will be validated, employing the test case depicted in Figure 5.1. The flow will be driven by the velocity boundary condition at the inlet (left-hand side), where both a parabolic and a plug flow velocity profile will be applied. The ensuing flow will be examined with regard to mass and momentum conservation. Subsequently, the energy conservation is verified by performing a temperature relaxation test case, consisting of two media with different specific heat capacities, thermal conductivities and densities. Consequently, a stationary heat conduction test case is performed to examine the proper treatment of conjugate heat transfer. Finally, the ability of the code to encompass all physical phenomena in a combustion scenario will be examined.

5.1.1 Validation of the flow field

The validation of the lattice Boltzmann model for the velocity field is conducted through the following test case, illustrated in Figure 5.1.

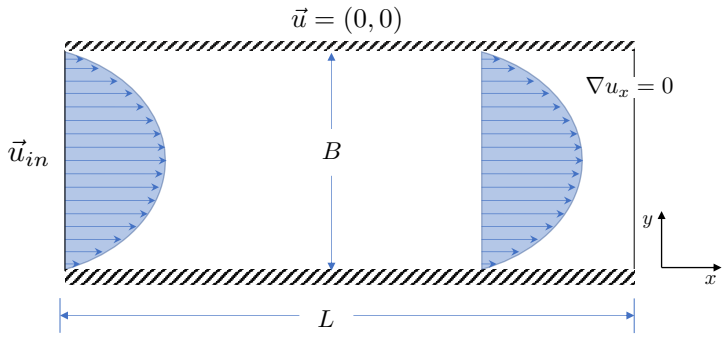

Figure 5.1: Test case for the validation of the flow field regarding mass and momentum conservation with L=210 and B=80.

This test case consists of a rectangular domain with no-slip walls at the top and bottom. At the inlet, a Dirichlet-type boundary condition is applied to impose a parabolic profile while a zero-gradient Neumann-type boundary condition is set at the outlet (right side), implying a fully developed flow. These boundary conditions lead to the simulation of a Poiseuille-type flow. The simulations are carried out in two dimensions with a lattice resolution of 210 by 80 nodes and the time step size is determined as per Table B.2. The flow-field is validated regarding the conservation of mass and momentum, where the mass-flux ($\dot{m}$) and momentum-flux ($\dot{p}$) across the inlet and outlet are computed using equation (5.1):

$$\dot{m} = \mathbf{n} \cdot (\rho \mathbf{u}), \quad \dot{p} = \mathbf{n} \cdot (\rho \, \mathbf{u} \, \mathbf{u}) \tag{5.1}$$

The result is presented in Figure 5.2, showing the mass-flow profiles along the cross section at both the inlet and at the outlet. It is important to note that ensuing the convergence of the solution is crucial, considering both the lattice configuration and time. To assess temporal convergence, a crucial parameter, such as the total kinetic energy of the system, can be employed.

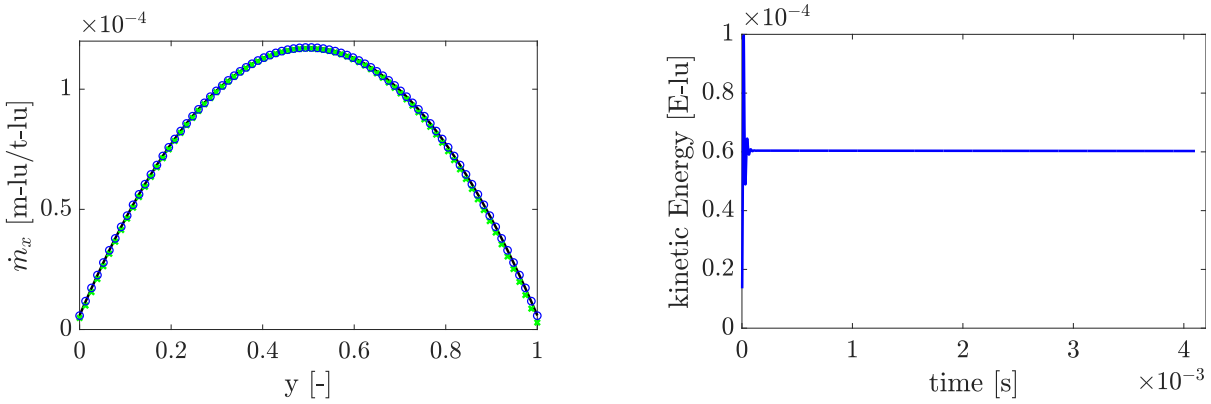

Figure 5.2: Mass-flow profiles at the inlet (○) and the outlet (×) shown over analytical solution (−) on the left and total kinetic energy of the system as a reference for solution convergence on the right.

On the right side of the figure, the total kinetic energy of the system is displayed, indicating the temporal convergence of the solution by converging towards an asymptotic value. The results show a good accordance between the mass flow profiles at the inlet and outlet, with a calculated total error in mass conservation of approximately 1.4 %.

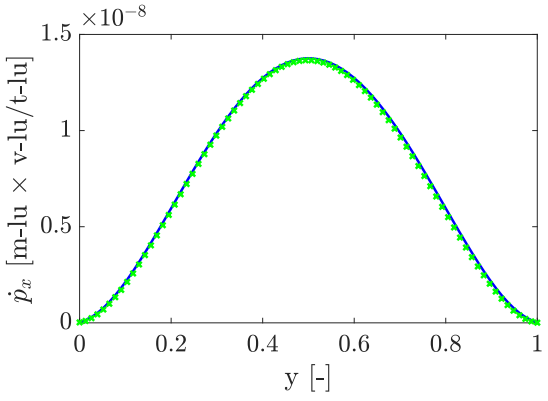

Relaxation time τ_ν	error [%]
0.7	1.22
0.8	0.022
0.9	0.83
1.0	1.45
1.2	5.02

Figure 5.3: Profile of the momentum flow at the inlet (−) and outlet (×) cross-section (left) and error in mass conservation for different relaxation times (right).

Furthermore, the temporal evolution of the total kinetic energy suggests a converged solution. Additionally, on the left side of Figure 5.3, the profiles of the momentum flow in lattice units are displayed for both the inlet and outlet, with the deviation between these two being calculated to be approximately 0.019 %. Overall, the model exhibits the capability to simulate Poiseuille-flow driven by the inlet velocity boundary condition

with an acceptable margin of error in mass conservation and excellent conservation of momentum. It is worth noting that the error in mass conservation was observed to be influenced by the relaxation time used in the simulation. This observation implies that better results may be achievable if the simulations are conducted with a parameter set which deviates from the one recommended in [143]. These results are displayed on the right side of Figure 5.3. For a relaxation time of 0.8, the error in mass conservation could be reduced to approximately 0.022 %, while the simulation diverged for relaxation times exceeding 1.2 and falling below 0.7.

5.1.2 Validation of energy conservation

The verification of energy conservation and conjugate heat transfer at the interface between the gas and solid domains is established through two specific test cases. The first case as depicted in Figure 5.4 involves a squared domain of phase 1 with side length of B, alongside another squared domain representing phase 2, and a length $b = 0.2B$ at its centre:

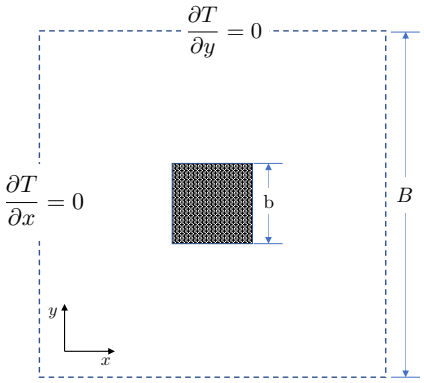

Figure 5.4: Test case for the verification of the conservation of energy and conjugate heat transfer, consisting of a squared domain with a squared, solid block centered inside of the domain. The edge lengths are related as b=0.2B.

The external boundaries of the entire domain are assumed to be adiabatic, ensuring the conservation of the total thermal energy within the system. Both phases are initialized with different temperatures and the relaxation of the temperature towards an equilibrium value is examined. This equilibrium value can be calculated based on the masses of both phases, their specific heat capacities as well as their initial temperatures. This test case allows for the study of the influence of the conjugate heat transfer on the conservation of thermal energy, since the only source/sink-term in the lattice Boltzmann equation for the temperature originates at the interface between the two phases as a result of the conjugate heat transfer algorithm. The solid obstacle is initialized with a temperature of 2.0 in lattice units while the gas phase is set to a temperature of 1.0, both corresponding

to a reference temperature of 773 K. The simulation is run for 40000 time-steps, which corresponds to approximately 0.8 milliseconds, which provides ample time for the temperature within the domain to relax towards its equilibrium value. The outcome of this temperature relaxation process towards the equilibrium state is visualized on the left side of Figure 5.5. The initial condition in blue and the fully relaxed profile after 0.8 ms (red) as well as several intermediate steps are shown.

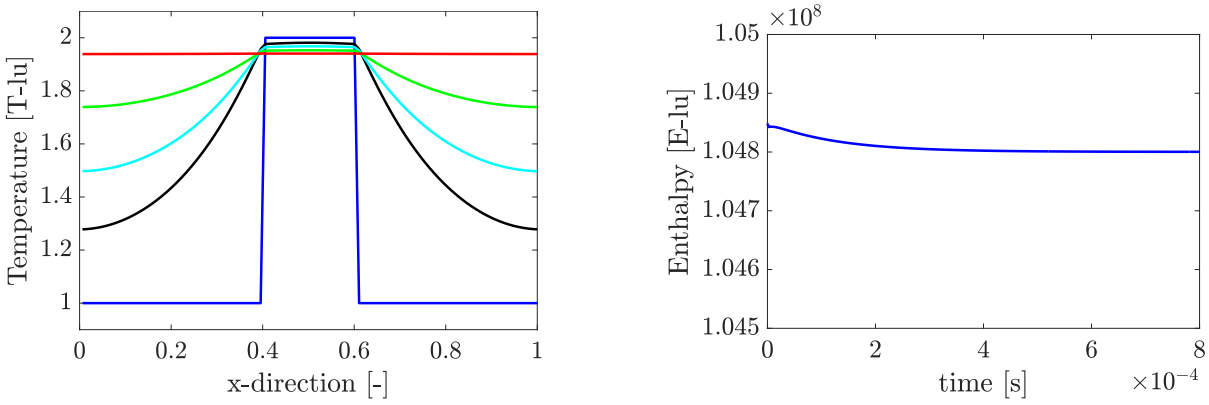

Figure 5.5: Temperature profile along the centre-line of the domain at different points in time (initial condition (−), 0.05 ms (−), 0.1 ms (−), 0.2 ms (−), 0.8 ms (−) (left) and temporal evolution of the total enthalpy of the system (right).

The system progressively reaches the equilibrium temperature $\overline{T}$, which can be calculated according to equation (5.2):

$$\overline{T} = \frac{N_g \rho_g c_{p,g} T_{ini,g} + N_s \rho_s c_{p,s} T_{ini,s}}{N_g \rho_g c_{p,g} + N_s \rho_s c_{p,s}} \tag{5.2}$$

where N_g represents the number of lattice nodes associated to the gaseous phase, ρ_g and $c_{p,g}$ denote the density and specific heat capacity of the gas, and $T_{ini,g}$ is the initial temperature of the gas phase. The parameters marked with the subscript "s" correspond to the respective values of the solid phase. In this simulation, the parameters outlined in Table B.2 are utilized. The simulation converges towards a temperature of 1.9403, with the analytically derived value being 1.9411. To elucidate the error in energy conservation, the temporal evolution of the total enthalpy of the system is presented on the right side of Figure 5.5. Notably, the total enthalpy of the system, which is determined based on the local temperature and heat capacities, exhibits a slight decrease, resulting in an error of approximately 0.046 %.

Furthermore, a two-dimensional heat conduction test case is employed, as illustrated in Figure 5.6. The domain is defined with a lattice resolution of 150×5 cells and is bounded by adiabatic walls on the top and bottom. Meanwhile, Dirichlet-type temperature boundary conditions are imposed on the left and right sides, imposing a temperature of T_1 at

the left boundary and T_2 at the right boundary. The left half of the domain consists of medium 1, characterized by a specific heat capacity and thermal diffusivity, while the right half is occupied by medium 2, which is characterized by a different thermal diffusivity and heat capacity, respectively.

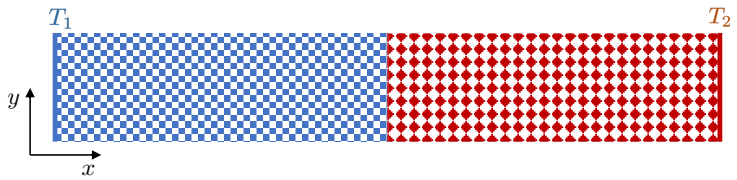

Figure 5.6: 2-D heat conduction test case for the validation of conjugate heat transfer consisting of a domain filled with medium 1 on the left and medium 2 on the right. Both media have different densities, specific heat capacities and thermal conductivities.

With the domain and boundary conditions defined in this manner, a quasi-one-dimensional heat conduction test case is formulated, for which an analytical solution exists. This analytical solution will then be used as means to validate the simulation results. It is worth noting that to ensure the successful implementation of conjugate heat transfer for the D2Q9 lattice, a minimum of five lattice nodes in the y-direction must be employed. This is because a fully one dimensional test case would not incorporate lattice velocities with vectors diagonal to the principal axes. Consequently, the analytical solution of this test case along with the results of the LBM simulation with and without the conjugate heat transfer treatment are presented in Figure 5.7.

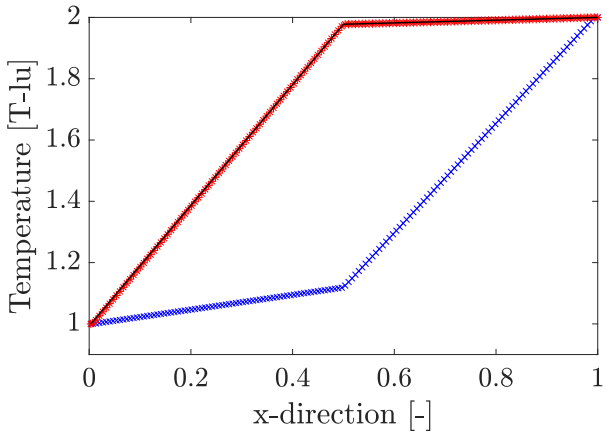

Figure 5.7: Analytical solution of the stationary heat conduction test case (-) as well as LBM simulation with (∗) and without (×) treatment of conjugate heat transfer.

For medium 1 and medium 2, a thermal conductivity ratio (λ_1/λ_2) of 0.228 and a thermal diffusivity ratio (α_1/α_2) of 8.4 are selected. The analytical solution of the energy conservation equation, with the boundaries defined as described above, thus leads to the black curve, with an almost horizontal temperature profile in medium 2, given its significantly higher thermal conductivity compared to medium 1. However, when using the standard

lattice Boltzmann model, the temperature profile exhibits a steep temperature gradient in medium 2, despite its higher thermal conductivity. This discrepancy arises because the LB-model only resolves the conservative diffusive form of the energy equation, as described in equation (3.103). Consequently, for cases with unequal thermal conductivity and thermal diffusivity ratios, the standard LB-model deviates from the correct solution of the energy conservation equation. As observed, the implementation of the conjugate heat transfer treatment, following [80], enables the correct solution of the heat conduction problem by LBM, with a normalized root mean square (RMS) error of 0.2 %.

5.1.3 Validation of combustion test case

The validation of the combustion model is performed using the test case depicted in Figure 5.8 [143]. This test case consists of a two-dimensional domain, containing four solid coke obstacles, which will react with the oxygen supplied by the gas flow at the inlet. The resolution of the domain is set to include 80 lattice nodes for the height (B), with a total length of 420 lattice nodes. The inlet length (l_{in}) is set to 100 lattice nodes and the four square obstacles are each represented with a resolution of 20×20 nodes and are separated by 20 nodes, respectively. The domain is bounded by solid walls at the top and bottom boundaries, treated as adiabatic surfaces, imposing no-slip boundary conditions for the velocity and zero-gradient Neumann-type boundary conditions for the components and the temperature. At the inlet, a parabolic velocity profile is imposed, with (u_0) representing the average velocity. Furthermore, the inlet-temperature and the mass fractions of the components are set by Dirichlet-type boundary conditions.

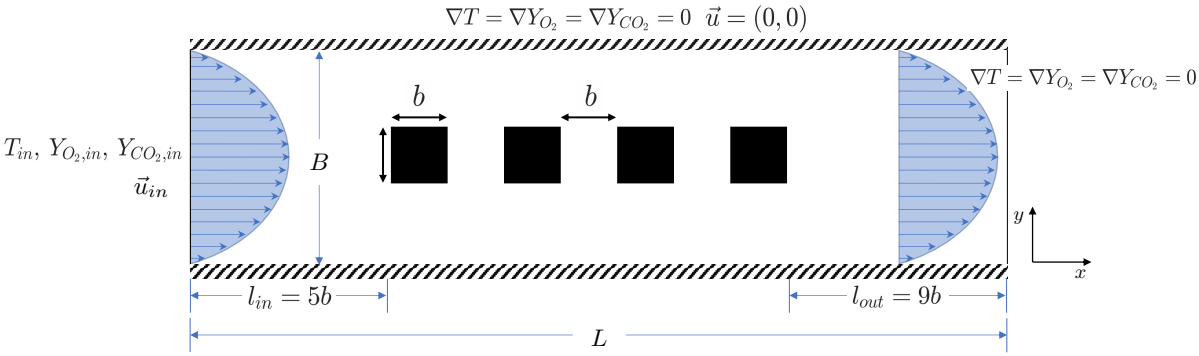

Figure 5.8: two-dimensional domain for the test case consisting of an inlet (left), outlet (right), no-slip walls at the top and bottom side of the domain and four solid obstacles (coke, displayed in black).

The flow is considered to be fully developed at the right boundary of the domain, resulting in zero-gradient boundary conditions for the velocity field, the temperature and the mass fractions of the components at the outlet. This test case serves as means to validate

the code, aligning the results with those from [78] and [143]. Notably in this scenario, the solid is assumed to have infinite mass, implying that despite the combustion reaction consuming carbon, the morphology of the coke obstacle remains unchanged over time. The model validation primarily concerns its ability to accurately represent the continuity of the conjugate heat transport at the interface between solid and gas phases. The specific values of the inlet boundary conditions as well as the definition of all physical parameters in SI units and lattice units is given in appendix B. In Figure 5.9, a velocity contour plot is depicted for $Pe = 10^{-2}$, corresponding to the test case presented in [143]. In SI units, this corresponds to an average inlet velocity $\overline{u}_{in}$ of $3.82 \times 10^{-3}\, m/s$, which is equivalent to an average inlet velocity of 0.000078 and a maximum inlet velocity of 0.0001174 in lattice units. This value in combination with the relaxation time for the flow with the value of 1.0 is significantly below the threshold value suggested by [67] for the velocity in lattice units, ensuring the stability of the method.

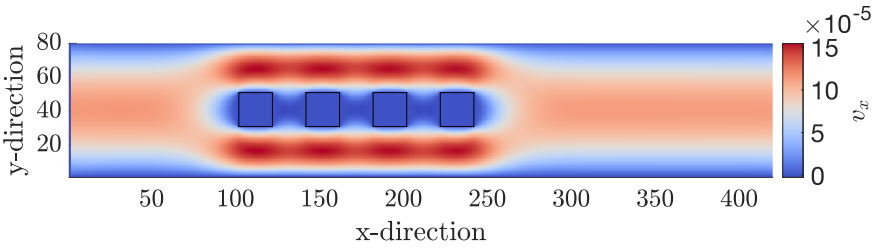

Figure 5.9: Velocity contour for the combustion test case for $Pe = 0.01$.

The figure illustrates the parabolic velocity profile at the inlet, which is altered by the presence of the four obstacles located in the centre line of the domain. Subsequently, the flow regains a parabolic velocity profile in the outflow region of the domain. The simulation reveals an overall maximum velocity within the domain of 0.00016 in lattice units adjacent to the obstacles, which constrict the cross-section of the domain.

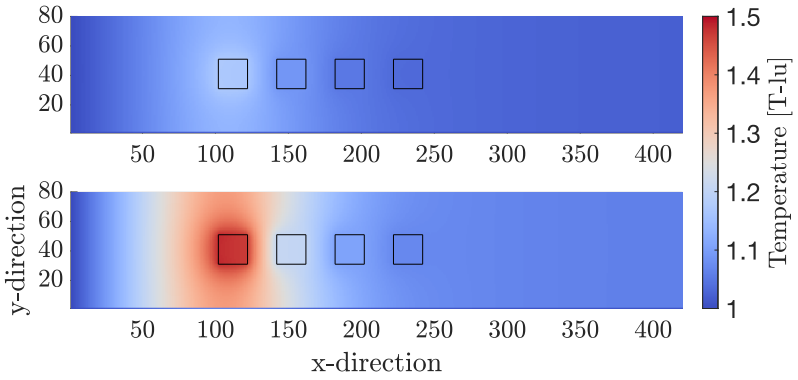

Figure 5.10: Temperature contour at 6 ms (top) and 10 ms (bottom).

In Figure 5.10, the temperature contours for the combustion process at $t = 6 \times 10^{-3}\, s$ and

$t = 1 \times 10^{-2}\, s$ are presented, normalized with respect to an inlet temperature of 773 K. After 6 milliseconds, the first obstacle exhibits a temperature increase to approximately 1.15 due to the release of reaction heat at the interface. After 10 ms, the temperature of the first obstacle rises to 1.4, primarily dissipating energy through heat conduction in the gas. This is attributed to the diffusion-dominated regime, as indicated by a Péclet-number less than 1.0. Moreover, the temperature of the gas upstream of the first obstacle begins to rise. It becomes evident that the majority of the reaction occurs at the first obstacle, indicating that the limiting factor for the reaction rate is the supply of oxygen. The corresponding contours of the mass-fraction of oxygen (educt) are presented in Figure 5.11 at 2 ms (top), 6 ms (middle) and at 10 ms (bottom).

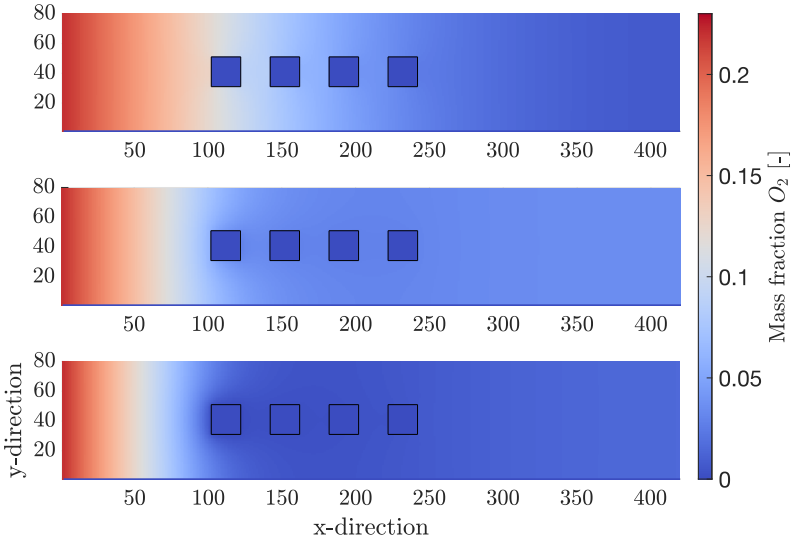

Figure 5.11: Contours of the mass-fraction of oxygen at 2 ms, 6 ms and 10 ms.

Notably, the diffusive component of the transport of oxygen is more significant than the advective flux, as the oxygen spreads uniformly across the domain rather than following the velocity contour. Additionally, the mass fraction at the outlet rises from 0 to approximately 0.04 at 6 ms. Over time, the reaction is accelerated by the released heat, leading to an increased consumption at the first obstacle. This results in the depletion of oxygen in the outlet of the domain to a value of approximately 0.01 at 10 ms. The corresponding contours of the mass fractions of carbon dioxide (product) are shown in Figure 5.12. As it can be seen, the release of CO_2 increases over time, given the strong coupling between the reaction rate and temperature. The dominant mode of transport phenomenon for carbon dioxide is diffusion, demonstrated by the transport of CO_2 upstream towards the inlet and its accumulation around the obstacles. Furthermore, following the complete turnover of O_2 at the interface of the first obstacle at 10 ms, the mass fraction of CO_2 reaches 0.28. This consistency between both components in terms of the molarity and

the resulting mass fractions, considering the different molecular weights of the two components.

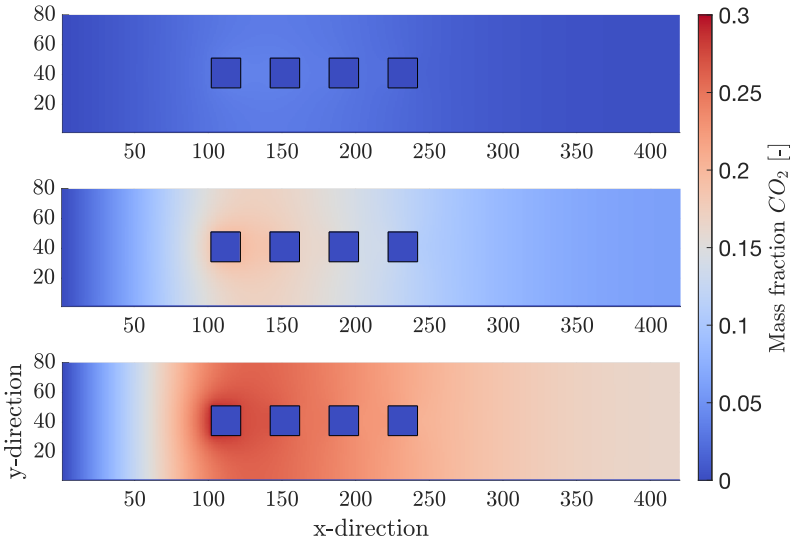

Figure 5.12: Contours of the mass-fraction of carbon dioxide at 2 ms, 6 ms and 10 ms.

Furthermore, the model results are compared to those of a COMSOL simulation [143], which simulates the same test case using the identical parameter set as presented in Table B.2. The comparison of the velocity profile along the centre line symmetry within the domain obtained from the LBM simulation with the result from the literature is shown in Figure 5.13. The velocity is standardized by the average velocity at the inlet and the variable at the abscissa is standardized by the domain length. Given this normalization, the maximum velocity at the inlet reaches 1.5 for the 2D Poiseuille flow between two plates.

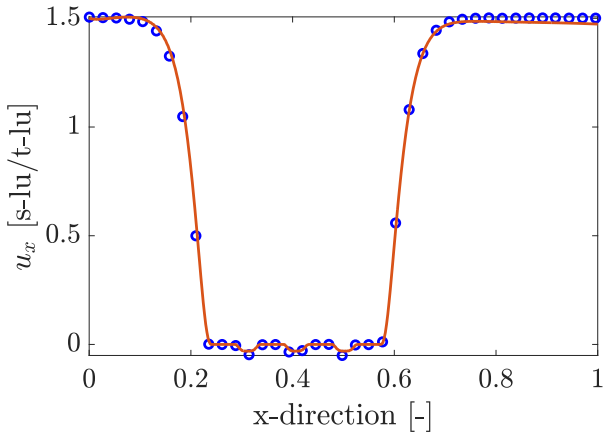

Figure 5.13: Comparison of the velocity profiles of the current LB-model (–) and a COMSOL simulation from the literature (○) [143] along the symmetry line of the domain.

As expected, the velocity reduces to zero at the four obstacles, with small recirculation

zones forming between them. Overall, the comparison reveals a very close agreement between the two. In addition, Figure 5.14 presents a comparison of the profiles along the centre line for the educt (oxygen) and the product (carbon dioxide) with the literature values.

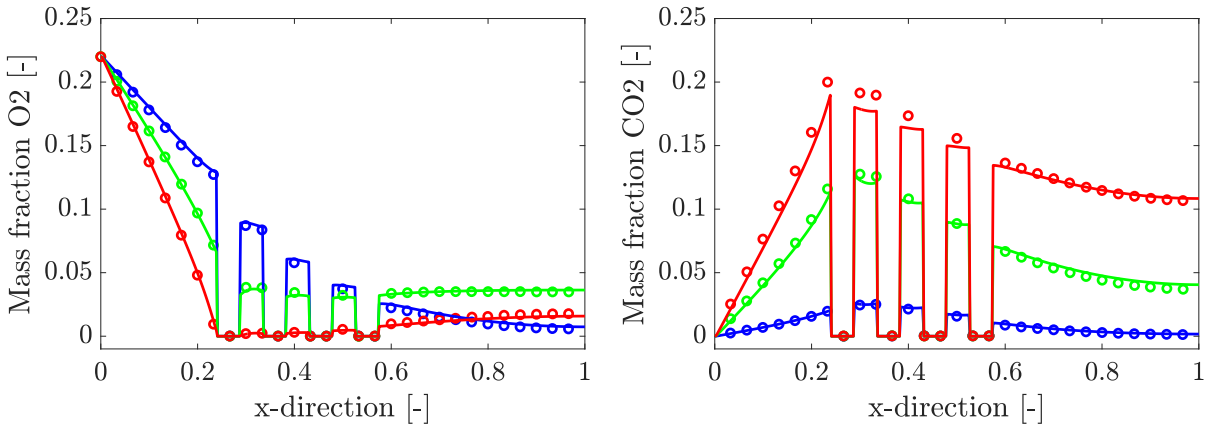

Figure 5.14: Comparison of the simulation results with results of a COMSOL simulation conducted in [143] In each graphic, (∘) and (−) represent the literature data and the LBM results at 2 ms, (∘) and (−) at 6 ms and (∘) and (−) at 10 ms for the mass fractions of oxygen (left) and carbon dioxide (right).

The results are depicted at 2 ms, at 6 ms and at 10 ms with oxygen on the left-hand side of the figure and for carbon dioxide on the right. It is evident that the initially oxygen-depleted domain gradually fills with oxygen, thanks to the oxygen supplied at the inlet via the Dirichlet boundary condition. Oxygen is uniformly distributed, primarily driven by the dominant diffusive mass transport. At 2 ms, there is minimal to no reaction taking place at the solid-gas interface, evident by the near-zero gradient of the mass fraction at the solid-gas interface. The outlet concentration of oxygen rises through mass diffusion up until 6 ms. Then, the reaction rate increases, which is caused by the increase in temperature at the solid obstacles. At 10 ms, the oxygen mass fraction reaches zero at the side of the first obstacle facing the inlet, signifying the complete consumption of the educt through chemical reaction with the reaction rate being limited by mass diffusion. On the right-hand side of Figure 5.14, the mass fraction of carbon dioxide is shown at 2 ms, displaying a slight increase around the first obstacle. With progressing time, the reaction rate accelerates, leading to the full conversion of the existing educt at the first obstacle. This is evident by the mass fraction of CO_2 almost reaching the value of the inlet mass fraction of O_2. It is worth noting that the literature source [143] uses a non-consistent naming scheme, interchanging the terms “fraction”, “species concentration” and “concentration fraction” for the variable representing the composition of the gas. Here, the model employs mass fractions for the species transport equations, considering both O_2 and CO_2 with different molecular weights. To facilitate comparison with the literature,

the ratio of the average molecular weight of the gas at the inlet and the molecular weight of CO_2 is used, assuming that the results in the literature are presented in molar fractions. As demonstrated, the results for the mass-fractions of O_2 and CO_2 exhibit a good agreement with the COMSOL simulation from the literature source, closely matching the values at the face of the first obstacle at each point in time with minor deviations toward the outlet. Furthermore, the temperature profile along the centre line is compared. Here, the two approaches for incorporating conjugate heat transfer, as detailed in section 3.3.1, are compared. Specifically, we contrast the second method, which relies on a bounce-back algorithm with a correction term. Both the implementation of the heat released by the reaction in the gas phase, following the approach proposed in [78], and the implementation in corresponding proportions in the gas- and solid domain, as suggested in this thesis, are compared. In the initial attempt, the method, which is consistent with [78], is employed. The results are shown in Figure 5.15.

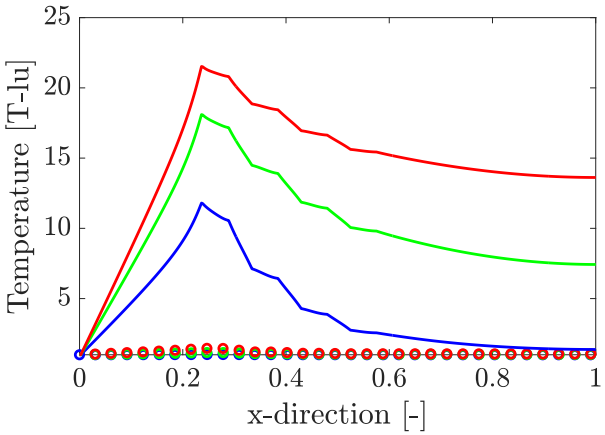

Figure 5.15: Comparison of the temperature profiles of the LBM simulation using the conjugate heat transfer method of [78] with the results of [143]. In the graphic, (∘) and (−) represent the literature data and the LBM results at 2 ms, (∘) and (−) at 6 ms and (∘) and (−) at 10 ms for the mass fractions of oxygen (left) and carbon dioxide (right).

Evidently, the results obtained by this method clearly deviated from the simulation outcomes of the COMSOL software. The maximum the temperature in lattice units peaked at approximately 20 while the temperature at the outlet of the domain reached approximately 11 T-lu. This discrepancy stems from the inability of our code to effectively represent conjugate heat transfer at the interface between two domains with different heat capacities, thermal conductivities and thermal diffusivities. In this method, the reaction heat is incorporated in the lattice nodes of the gas-phase, adjacent to the interface, following the approach in [78]. When the treatment of conjugate heat transfer fails to function correctly, the dampening effects of the solid domain, which has a high density and specific heat capacity, are no longer effective. As a result, the domain experiences uncontrollable heating, further amplifying the reaction rate. The method used in [78] and

shown in equation (3.106) with term F_{extra}, involves spatial derivatives. This method is originally detailed in [59], which also provides guidance on calculating these spatial derivatives. In this context, a forward difference scheme is used for their computation, introducing inherent errors and asymmetries. This occurs because the forward difference scheme makes the source term for the energy equation non-invariant concerning the orientation of the interface. For this reason, simulations were conducted using the forward-difference scheme, a central difference scheme and a scheme, which dynamically verifies the orientation and location of the interface, switching adaptively between forward and backward difference schemes. The source of the error remains uncertain, as it is unclear whether the issue lies in the method of implementation within the code, or if the method itself contains inherent errors. As a result, the method for the implementation of conjugate heat transfer, as described by [80], was employed. Initially, this method incorporated the reaction heat in the fluid domain. The temperature profiles, shown in Figure 5.16, demonstrate an excellent math for small temperature increases, such as those occurring at 2 ms.

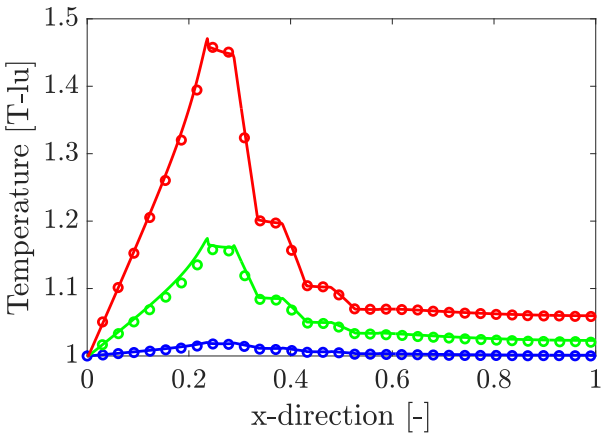

Figure 5.16: Comparison of the temperature profiles for the LBM simulation conducted in this thesis and the results from the literature. In the graphic, (○) and (−) represent the literature data and the LBM results at 2 ms, (○) and (−) at 6 ms and (○) and (−) at 10 ms for the mass fractions of oxygen (left) and carbon dioxide (right).

However, for longer simulation times, the heat release due to the reaction intensifies as temperature rises, further increasing the reaction rate. In this scenario, the model still proves its ability to correctly resolve the conjugate heat transfer problem, resulting in a very good accordance between the LBM simulation and the COMSOL simulation. Nonetheless, the model exhibits a minor issue in resolving the local heat release at the interface nodes, which is indicated by the discontinuities in the temperature profile at the solid-gas interface, where the reaction heat is released. This limitation arises from the model being primarily developed for heat conduction problems, as evidenced in [80], without the inclusion of external source or sink terms. The results of the simulation can

be improved by adapting the method of the implementation of the reaction heat to the conjugate heat transfer algorithm by implementing it as illustrated in equation (3.102). The computational results using this adapted model are presented in Figure 5.17. It is evident that the minor temperature jump, observed in previous simulations, has been reduced, improving the overall consistency of the simulation and the continuity of the temperature profile could be improved.

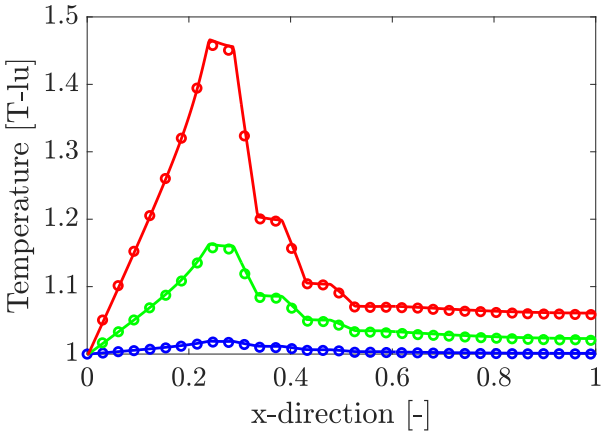

Figure 5.17: Resulting temperature profile of the LBM model with adapted implementation of the reactive heat release. In the graphic, (○) and (−) represent the literature data and the LBM results at 2 ms, (○) and (−) at 6 ms and (○) and (−) at 10 ms for the mass fractions of oxygen (left) and carbon dioxide (right).

Having validated the model against literature data, a parametric study is conducted to identify different combustion regimes and the dominant physical phenomena influencing the reaction rate in each regime. Additionally, the parametric study aims to provide a general understanding of the range of values feasible for the inlet parameters, namely velocity and temperature. These are the process variables that can be adjusted by engineers in real-life applications, ensuring the stability of the model. Initially, the inlet temperature is varied between 500 K and 1100 K, while keeping the remaining parameters consistent with those used in the model validation test case. This temperature range corresponds to Damköhler numbers between 5.13×10^{-7} and 15.16 across seven orders of magnitude. The resulting temperature and educt mass-fraction profiles are shown in Figure 5.18.

It is evident that the temperature profile remains almost flat and unaltered throughout the domain for inlet-temperatures of 700 K and below. This indicates minimal to negligible reaction activity, which is further supported by the mass fraction profiles shown at the right-hand side of the figure. These profiles exhibit the typical pattern of a component being transported through the domain by diffusion, with a slight reduction in the oxygen mass fraction at an inlet temperature T_{in} of 700 K. The profiles presented here, for an inlet temperature of 773 K, are identical to those obtained during the model val-

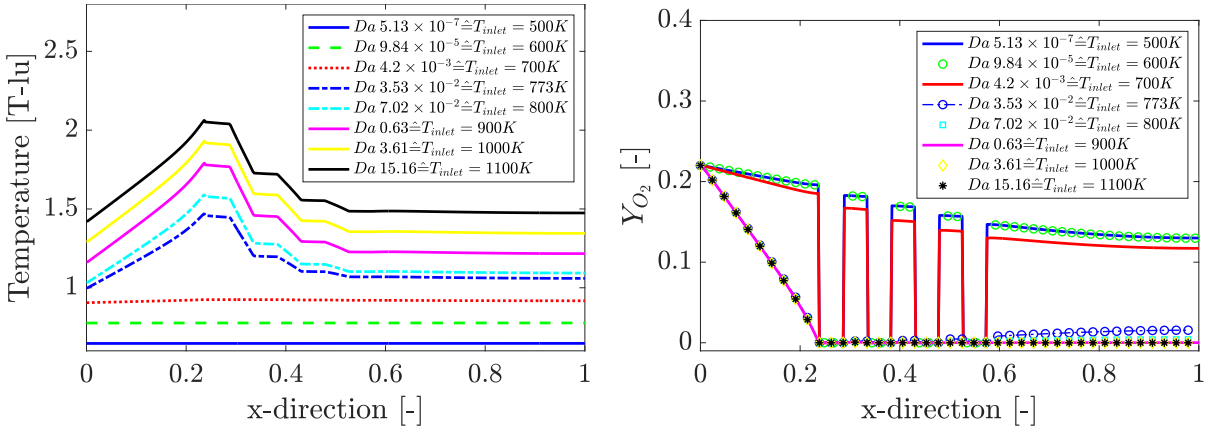

Figure 5.18: Temperature profiles (left) and mass fraction Y_{O_2} profiles (right) for different Damköhler-numbers.

idation. A notable temperature increase is observed near the first soot-obstacle, which, coupled with the complete depletion of the educt, indicates strong reactive activity. The profiles exhibit little change for higher inlet-temperatures, implying the full conversion of reactants. This suggests that the overall reaction takes place under transport limited conditions. It is worth mentioning that while the inlet temperature usually serves as the reference for the conversion to lattice units, here, a constant reference temperature of 773 K was opted for. Consequently, the baseline for the temperature profile graphs varies for different inlet temperatures to enhance graph readability. Furthermore, the effect of the inlet velocity on the reaction regime was investigated. The "base-simulation" employing the parameters used for the model validation indicates a predominance of diffusion driven component transport, as indicated by a Péclet number of 0.01, which is several orders of magnitude smaller than 1. Simulations were carried out across a range of Péclet numbers spanning from 0.0001 to 0.5. The resulting temperature and educt-mass-fraction profiles are shown in Figure 5.19.

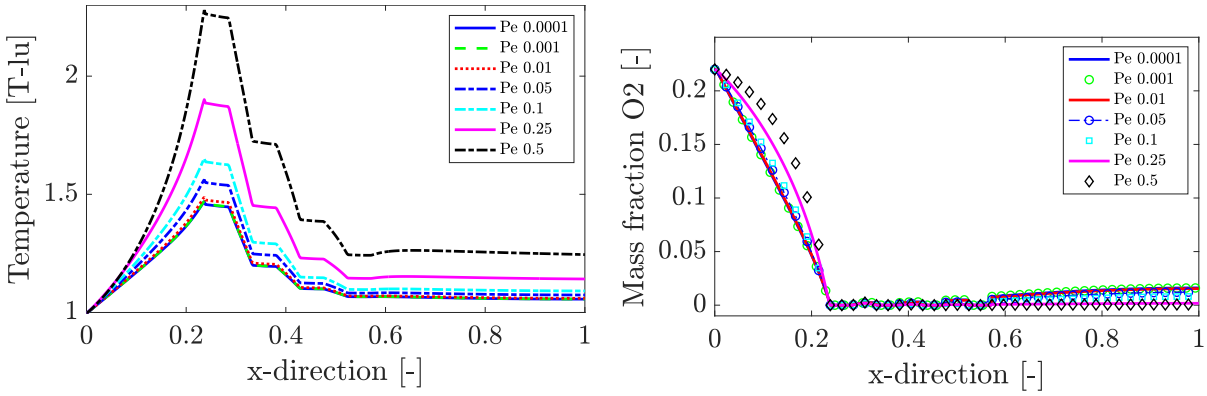

Figure 5.19: Temperature profiles (left) and educt mass fraction profiles (right) for varying Peclet-numbers.

The findings indicate that with an increase in Péclet number, the maximum temperature

at the initial obstacle, as well as the temperature distribution throughout the domain, rises due to the enhanced supply of educts to the reactive interface. Moreover, the educt-profile between the inlet and the first reactive obstacle undergoes a change from a linear profile, denoting diffusive transport, to a convex profile, indicating convective transport. However, despite the increased component transport via advection, the overall reaction rate remains constrained. This limitation persists because the Péclet number, at which the temperature ceases to change, has not yet been reached.

5.1.4 Conclusion

In this part, we implemented a multi-relaxation-time lattice Boltzmann model, using the multi-distribution function approach (MDF) within an in-house-code. The purpose was to simulate heterogeneous reactions. Specifically, distinct distribution functions were used to represent the fluid flow, the different reactive species within the fluid and the thermal field across both the fluid and solid domains. The treatment of the heterogeneous reaction at the fluid-solid interface was implemented in an explicit way, offering several advantages. Firstly, no iterative method is necessary to ensure the continuity of the temperature across the interface. Furthermore, our explicit approach eliminated the requirement to compute derivatives of certain macroscopic variables at the interface, resulting in improved computational efficiency and greater versatility in handling different interface geometries. Our approach demonstrated excellent performance in modeling flow, component transport and the consumption and release of components via heterogeneous surface reaction. Additionally, we compared and validated various methods for the energy conservation and the ability to address conjugate heat transfer issues using analytical solutions and results from existing literature. The method based on a bounce-back like approach from [80] was adapted to treat conjugate heat transfer with heat sources. This resulted in an excellent agreement compared to the literature data. Subsequently, we conducted a parametric study to analyse different combustion regimes and to highlight the capability of the code across a range of values for simulations. In summary, the developed LBM model shows great promise for simulating heterogeneous reactions in 2D porous media.

5.2 Extension of the model to 3D and validation of additional boundary conditions

In this chapter, the 3D implementation of the model, as described in the Chapters 3.3 and 4.2.3, is validated. For the validation, similar test cases as for the validation of the 2D

model are used. These are comprised of a flow validation case for examining the mass conservation, a heat conduction test case and a temperature relaxation test case to validate the conjugate heat transfer implementation and its effects on the energy conservation, as well as the full combustion test case, which is adapted to be used for 3D validation. Furthermore, the combustion test case is used to validate additional boundary conditions, namely the periodic boundary condition and the symmetry boundary condition.

Mass conservation - Flow field

For the validation of the flow field, a squared tube with no-slip walls at the top and bottom as well as in the back and front is set up. The cross section has a lattice resolution of 40×40 lattice nodes and the domain has a length of 100 lattice nodes. At the inlet, a plug flow profile is imposed and the outflow is defined by a zero-gradient Neumann boundary condition. Furthermore, the domain is filled with a three dimensional porous strucutre, which is received by extracting a part of the full-size FIB-SEM geometry. The cubic porous medium has an edge length of 40 lattice nodes and is located 10 lattice nodes downstream from the inlet. The stationary solution of the velocity magnitude is shown in Figure 5.20, exhibiting the uniform velocity of the imposed plug flow at the inlet, subsequently describing a strongly disturbed velocity field inside of the porous structure and forming the parabolic velocity profile of a fully developed flow in the outlet region of the domain.

Figure 5.20: Solid soot domain (left) and stationary solution of the velocity magnitude (right) for the mass conservation test case.

At the inlet and outlet, the mass flow is calculated by multiplying the density with the velocity component perpendicular to the interface and integrating the mass flow over the inlet and outlet surfaces. As the stationary solution is reached, the deviation between inlet and outlet mass fluxes reaches 0.03262 %.

Heat Conduction

The heat conduction test case is set up in a similar manner to the one used for the two dimensional validation. This results in a rectangular cross section with a lattice resolution of 100×10 and three lattice nodes in the third dimension. On the short faces of

the cross section, Dirichlet temperature boundary conditions are set. The long faces of the cross section are assumed to be adiabatic and the third dimension is assumed to be periodic. For the imposed temperatures on the left and right side, the values of 1 and 2 in temperature lattice units are chosen. The stationary solution of the simulation as well as the analytic solution for the given heat conduction test case are shown in Figure 5.21. As it can be seen, the LBM simulation perfectly resembles the analytic solution.

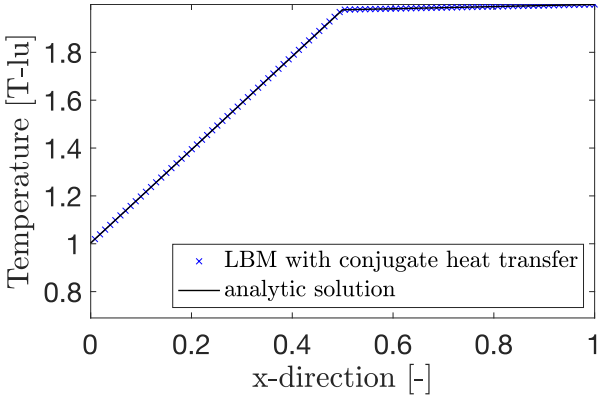

Figure 5.21: Analytic solution and results of the LBM simulation for the 3D heat conduction test case.

Temperature Relaxation

The test case used for the validation of the energy conservation in 3D is shown in Figure 5.22. It consists of a cubic domain with a resolution of $100 \times 100 \times 100$ lattice nodes. A second cube with edge length of 20 lattice nodes, here displayed in blue, is located in its centre. With the outer boundaries of the domain being assumed to be adiabatic, the energy within the system should be conserved.

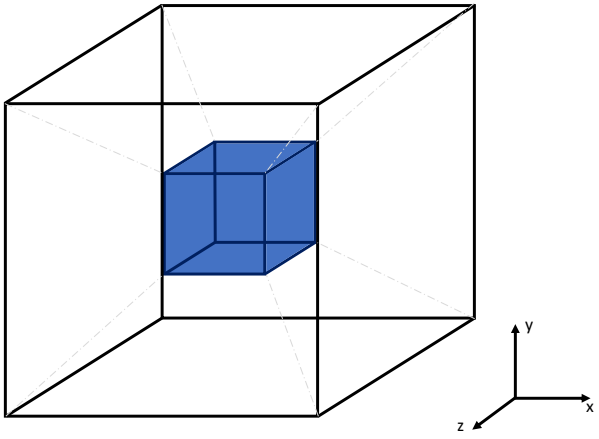

Figure 5.22: Domain for the 3D temperature relaxation test case consisting of a cubic domain, with a second cube centered in the middle of the domain. The inner cube is allocated with the properties of coke, while the outer cube is assumed to be air. All six outer boundaries are set to be adiabatic.

This is investigated by imposing a temperature profile onto the domain in such a way

that the inner cube has an initial temperature of $T_0 = 2.0$ [T-lu], with the surrounding phase having an initial temperature of $T_0 = 1.0$ [T-lu]. This temperature profile will relax to a certain equilibrium value, which can be calculated based on the densities and specific heat capacities of the two domains as well as the number of lattice nodes allocated to each domain. The resulting temporal evolution of the total enthalpy of the system as well as the temperature profiles along the centre line in x direction are shown in Figure 5.23.

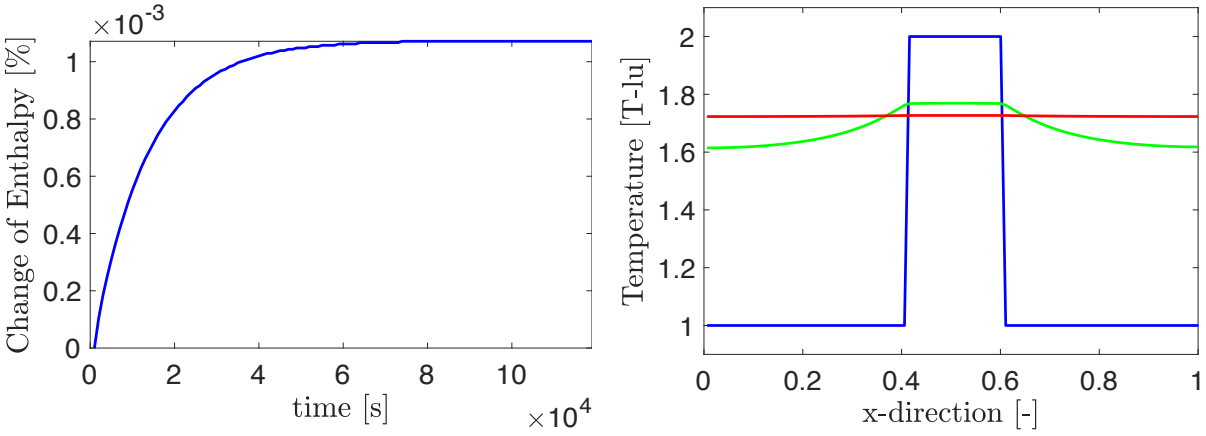

Figure 5.23: Total thermal energy of the system over time (left) and resulting temperature profiles along the centre line in x direction (right).

It can be seen that the total thermal energy of the system increases slightly throughout the relaxation process, exhibiting an error of approximately 0.001 %. The analytical solution of the equilibrium temperature is calculated to be $T_{eq} = 1.7258$ [T-lu], with the LBM simulation relaxing towards an equilibrium value of $T_{eq,LBM} = 1.72579$ [T-lu].

Symmetry boundary condition

For the simulation of repetitive domains, which exhibit a symmetry line, it is possible to save computational resources by defining a symmetry boundary condition for the LB method, enabling the simulation of the full test case by performing the LB algorithm on just half of the domain. Figure 5.24 shows an example of the combustion test case, which was presented by [143] and which was used in our previous work to validate our LB model [129]. Contrary to the depiction in the mentioned literature, a symmetry line is added in blue and the top half of the domain is removed.

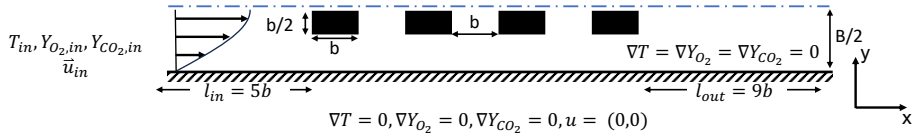

Figure 5.24: Combustion test case as presented in [143], with symmetry line.

If a symmetric boundary condition is imposed in a proper manner, the computational

cost of the domain can be split in half. In order for the boundary condition to be symmetric, it has to satisfy multiple conditions. The boundary condition has to impose a zero gradient of all scalar variables as well as of the components of the velocity field perpendicular to the symmetric boundary. Furthermore, the transport of scalar variables as well as a boundary velocity parallel to the symmetric boundary has to be possible. These conditions are satisfied by the so-called specular reflection boundary condition [37], which is typically used to impose free-slip boundaries. Here, the normal component of the fluid velocity is assumed to be zero at the wall with the tangential component not being influenced. Essentially, the boundary is assumed to be non-penetrable with no shear-stress being imposed. This results in the distribution functions, whose lattice velocity vectors are perpendicular to the boundary, to be reflected, similar to the classical bounce-back algorithm. The distribution functions, which intersect the boundary condition at an angle, are being mirrored at the boundary condition. This process can be performed both in a local and non-local manner, as subsequently shown:

Local Expression	**Non-local expression**
$f_4(x_b, t+\Delta t) = f_2(x_b, t)$	$f_4(x_b, t+\Delta t) = f_2(x_b, t)$
$f_7(x_b, t+\Delta t) = f_6(x_b, t)$	$f_7(x_b-\Delta x, t+\Delta t) = f_6(x_b, t)$
$f_8(x_b, t+\Delta t) = f_5(x_b, t)$	$f_8(x_b+\Delta x, t+\Delta t) = f_5(x_b, t)$

(5.3)

For an extensive comparison of both methods regarding convergence and accuracy, the reader is referred to [39]. Subsequently, the symmetry boundary condition is validated. For this, the combustion test case of [143], which has been used previously for the validation of the 2D model in section 5.1, is applied again.

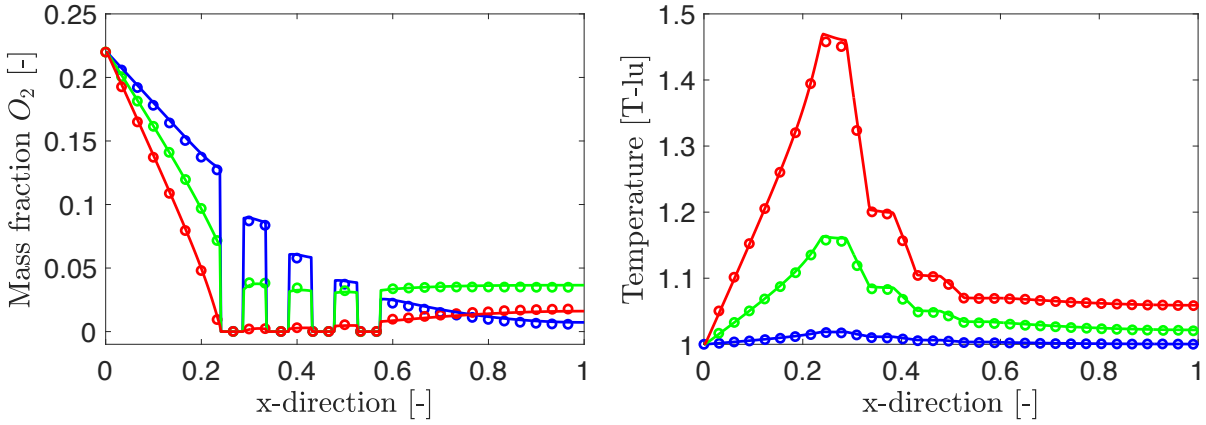

Figure 5.25: Validation of the symmetry boundary condition by comparison of the results with literature data [143]. In the graphic, (∘) and (−) represent the literature data and the LBM results at 2 ms, (∘) and (−) at 6 ms and (∘) and (−) at 10 ms for the mass fractions of oxygen (left) and temperature (right).

As shown in Figure 5.24, the domain of the combustion test case is symmetric, enabling

the calculation to be restricted to half of the domain. This results in a resolution of 420 × 41 lattice nodes, with all parameters being chosen according to Table B.2. The resulting profiles of the mass fraction of O_2 and the temperature at the symmetry line are shown in Figure 5.25. It can be seen that the results agree very well with the literature data for all three displayed times. The direct comparison of the simulation with the full domain and with the reduced domain is shown in Figure 5.26. The profiles along the symmetry line of the mass fraction of O_2 and CO_2 as well as the temperature and the RMS errors between are shown. It becomes apparent that the implementation of the symmetry boundary condition marginally affects the results, with the largest RMS error being 0.17 % for the temperature field after 10 ms. For the profiles of O_2 and CO_2, RMS errors smaller than 0.027 % and 0.0654 % are reported.

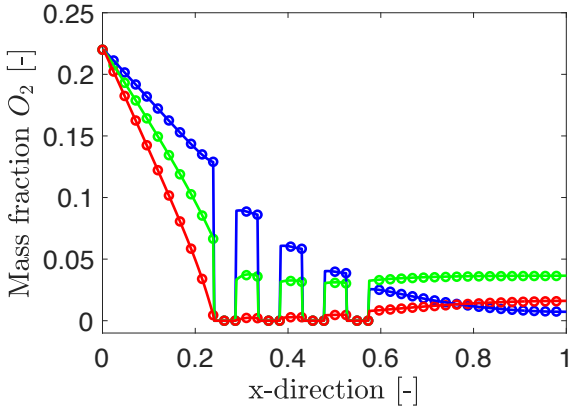

(a)

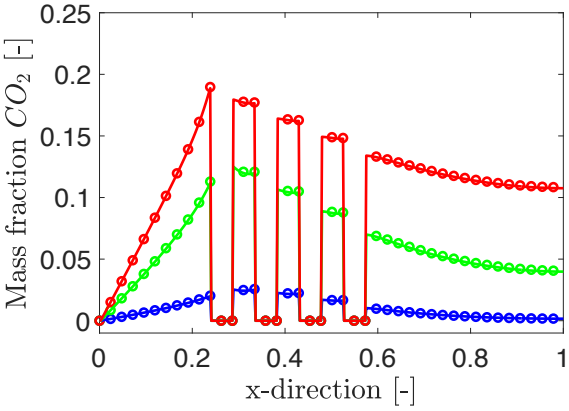

(b)

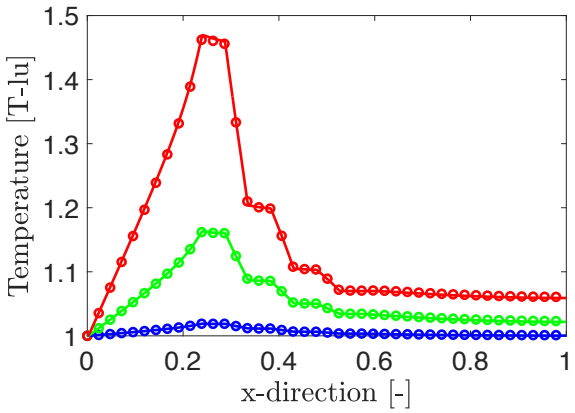

(c)

time points	error [%]		
	T	O_2	CO_2
2 ms	0.0374	0.0108	0.022
6 ms	0.0686	0.0269	0.0654
10 ms	0.17	0.0159	0.0553

(d)

Figure 5.26: Comparison of the LBM results with and without symmetry boundary condition. Shown are the mass fraction of O_2 5.26a, the mass fraction of CO_2 5.26b, the temperature profile 5.26c as well as the RMS error values 5.26d . In the graphic, (○), (○) and (○) represent the LBM simulation with the full domain at 2 ms, 6 ms and 10 ms, while (–), (–) and (–) represent results of the simulation with the symmetry boundary condition.

5.3 Analysis of combustion regimes with realistic mass consumption

In this section, the existing two dimensional LBM model, which was validated in the previous section, is extended by realistic mass consumption, by allocating the respective mass according to the density of soot, to each solid node. Subsequently, combustion simulations are performed in a two dimensional domain consisting of regularly ordered round solid obstacles, consisting of an inert core, which is covered with a reactive layer of soot. This domain is used for an extensive parametric study, in which the Péclet number, the Damköhler number, the inlet mass fraction of oxygen as well as the thickness of the reactive soot layer are varied. With this parameterization, the influence of convective and diffusive educt transport as well as of the reactivity of the soot onto the combustion regime is analysed. Furthermore, first 3D simulations are introduced. This section is a quote of the results section of a paper prepared for publication [128].
Here, a two-dimensional test case is created to assess different combustion regimes depending on the Péclet number, the Damköhler number and the inlet mass fraction of oxygen, Y_{O_2}. Subsequently, the information gained from this academic test case is used to define and analyse the simulation with realistic geometries, obtained from FIB-SEM images of soot samples, provided by the ICVT at University of Stuttgart. The test case used to analyse the combustion regimes is shown in Figure 5.27.

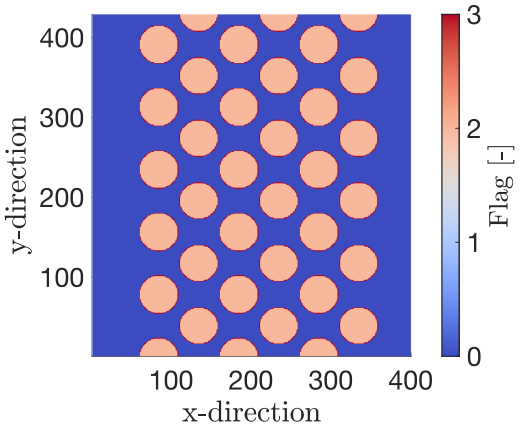

Figure 5.27: 2D Test case consisting of round inert substrate particles, which are ordered in a regular manner and covered by a reactive soot layer (red).

A square domain with the length of 400 μm in both x and y directions is set up. Inside, round particles are arranged in a regular manner. The affiliation of a lattice node to a phase is indexed by a specific value, stored in the so-called flag matrix. The particles with a radius of 25 μm consist of an inert substrate carrier, depicted in orange (corresponding

to a flag value of 2), which is coated with a reactive layer of soot of the thickness of 1 μm, depicted in red (corresponding to a flag value of 3), with the pore space, filled with gas, being depicted in blue (eq. flag value 0). The distance between the centres of the particles in the x and y direction are 100 μm and 78 μm, respectively, with the smallest distance between particle centres being 63.4 μm in diagonal direction. This results in an initial porosity of 51.6 % before combustion. After confirming grid convergence, a lattice width of 1 μm per is chosen.

At the top and bottom of the computational domain, periodic boundary conditions are assumed, with the inlet and outlet being on its left and right sides, respectively. At the inlet, a velocity profile as well as a static value for the temperature and the mass fractions of all components, are defined. At the outlet, a zero gradient boundary condition is assumed. The domain is assumed to be filled with pure nitrogen gas of the temperature T_0 and the stationary solution for the velocity field corresponding to the mentioned boundary condition is used as initial condition. For the values of the pre-exponential factor A and the activation energy E_a of the reaction, which was shown in equation (3.72), the values of $A = 9.717 \times 10^6 \, \frac{m}{s}$ and $E_a = 131.09 \, \frac{kJ}{mol}$ are used [106]. The enthalpy of the reaction is defined according to [143] as $\Delta h_r = 431.3 \, \frac{kJ}{mol}$. For the chemical properties of soot, the following values of the density $\rho_s = 2505.123 \, \frac{kg}{m^3}$, the specific heat capacity $c_{p,s} = 0.7244 \, \frac{kJ}{kg\,K}$ and thermal diffusivity $\alpha_s = 1.357 \times 10^{-6} \, \frac{m^2}{s}$ are assumed. For the gas phase, the density of $\rho = 4.5 \, \frac{kg}{m^3}$, a specific heat capacity of $c_{p,g} = 1.096 \, \frac{kJ}{kg\,K}$, a thermal diffusivity of $\alpha_g = 1.14 \times 10^{-5} \, \frac{m^2}{s}$ and a viscosity of $\mu_g = 3.673 \times 10^{-5} \, Pas$ are used [143].

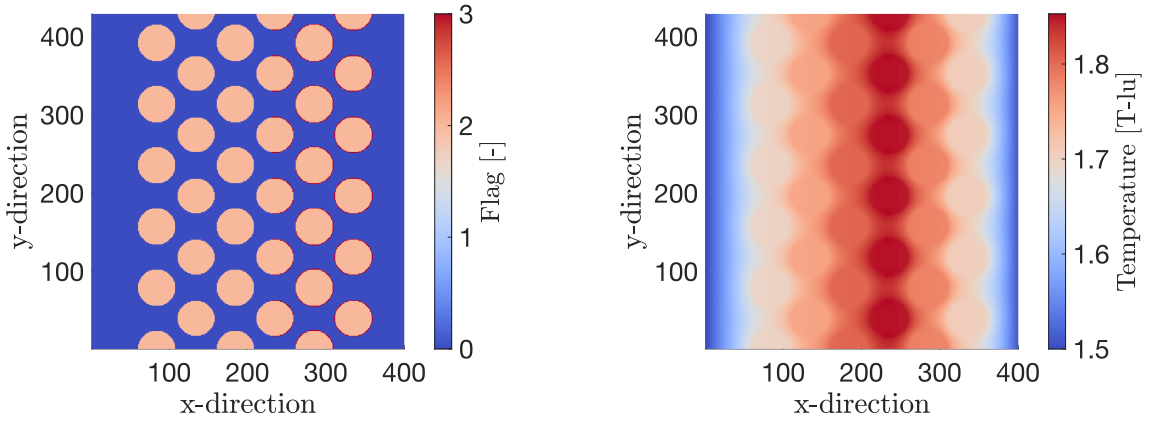

Figure 5.28: Exemplary test case for 2D combustion with simulation domain (left) and temperature field (right) at t=1.2 s.

The diffusivities of O_2 and CO_2 are given as $D_{O_2} = 1.76 \times 10^{-5} \, \frac{m^2}{s}$ and $D_{CO_2} = 1.6 \times 10^{-5} \, \frac{m^2}{s}$ [24]. Combustion simulations are performed for varying inlet temperatures between 500 $°C$ and 900 $°C$, for inlet mass fractions of oxygen between 5 % and

25 % and for different inlet velocities, corresponding to Péclet numbers of 0.001 and 1, respectively. The result of one exemplary simulation is shown in Figure 5.28, in which the composition of the domain, displayed by the flag, denoting the different phases (left) and the temperature field (right) are shown. Furthermore, the mass fraction of oxygen (left) and carbon dioxide (right) are shown in Figure 5.29 at $t = 1.2\,s$. The exemplary simulation was conducted with an inlet temperature of 1.5 T-lu, corresponding to a Temperature of around $T = 1159\,K$, with $Pe = 0.01$ and an inlet mass fraction of oxygen of $Y_{O_2} = 0.22$. It can be seen on the left of Figure 5.28 that the reactive carbon layer has been burnt off completely on the first three columns of particles. Combined with the fact that the mass fraction of oxygen on the left sub-figure in Figure 5.29 fully depletes in the middle of the particles of the fourth column, and a temperature spike at the same position, it can be concluded that the combustion is limited by the mass transport of the educt. This leads to a combustion front propagating through the domain from inlet to outlet, meaning that the reactive carbon layer on the particles is not consumed simultaneously throughout the domain.

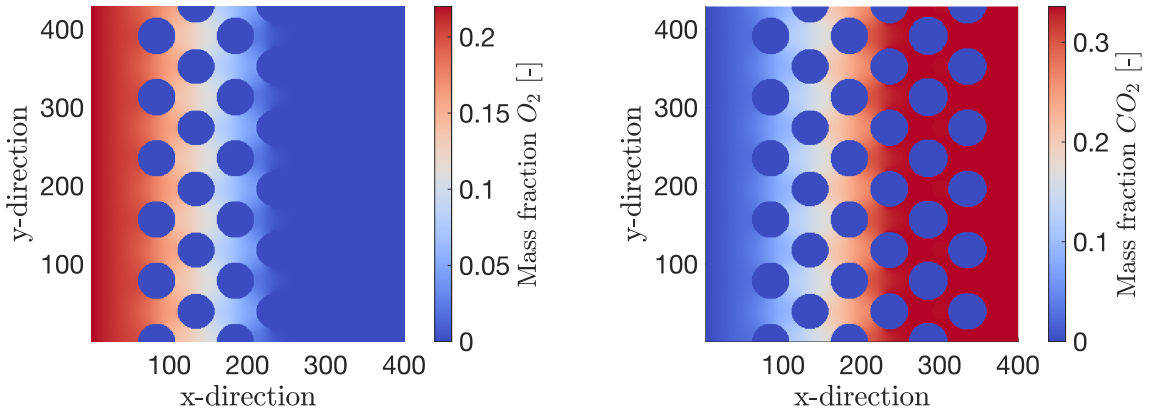

Figure 5.29: Exemplary test case for 2D combustion with mass fraction of oxygen Y_{O_2} (left) and mass fraction of carbon dioxide Y_{CO_2} (right) at t=1.2 s.

In the following, the combustion behaviour is analysed by variation of Péclet number, Damköhler number and mass fraction of educt at the inlet. The temporal evolution of the front position, the burning rate and the residual coke mass are used as characteristic parameters for the evaluation of the results. Furthermore, the maximum temperature of the combustion front over time will be analysed.

First, the Damköhler number, which is a measure for the ratio of the chemical reaction rate to the diffusive transport of the educt, is varied. Since the initial simulation, which was shown in the Figures 5.28 and 5.29 exhibited a transport limited reaction for an inlet temperature of 1.5 T-lu, the range of values for the parametric study is chosen to be $T_{in} = [1.1, 1.5174]$, corresponding to SI-unit values between 577 $°C$ and 900 $°C$. The

results of the parametric study of the Damköhler number are shown in Figure 5.30, in which the position and maximum temperature of the combustion front over time are shown. Based on the position of the front, the time averaged propagation velocity is calculated for each Damköhler number and displayed in Figure 5.30c. Furthermore, the temporal evolution of the residual coke mass is shown in Figure 5.30d. It can be seen that the profiles of the maximum temperature of the combustion front are similar, just being offset by the different values of the initial temperature. This indicates a transport limited combustion regime with total turnover of the educt provided at the inlet, even for inlet temperatures as low as 1.1 T-lu, corresponding to 577.3 $°C$. Also, this results in congruent profiles for the residual coke mass, position and propagation velocity of the front, since a higher temperature, resulting in higher reaction rates, can not result in a higher release of reaction heat.

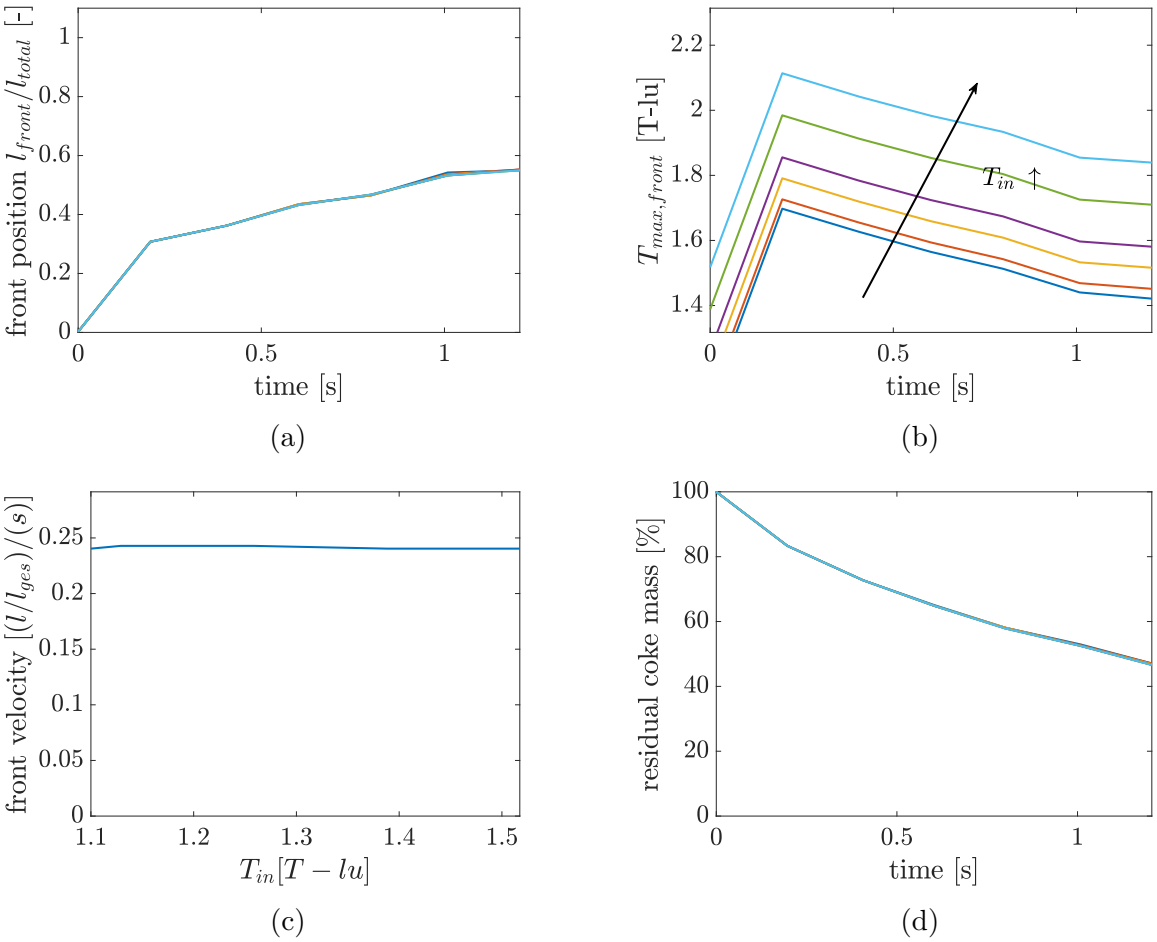

Figure 5.30: Parametric study of Damköhler number: Temporal evolution of the position of the combustion front (a), maximum temperature (b) and residual coke (d) as well as propagation velocity of the combustion front for different inlet temperatures (c). In the graphs, the colors represent the following values of the inlet temperature T_{in}: $T_{in} = 1.1$, $T_{in} = 1.129$, $T_{in} = 1.19$, $T_{in} = 1.2587$, $T_{in} = 1.388$, $T_{in} = 1.5174$.

Subsequently, the influence of $Y_{O_2,in}$ is investigated, to assess its influence on the reaction regime. Since a transport limited combustion regime is identified for the given range of parameters, an increase in inlet mass fraction of oxygen, resulting in higher gradients, thus a higher mass transport, will have a greater effect on the combustion properties. Simulations are performed with a constant inlet temperature of 650 $°C$ and $Pe = 0.01$ for a range of $Y_{O_2,in} \in [5\%, 50\%]$ and the results are shown in Figure 5.31.

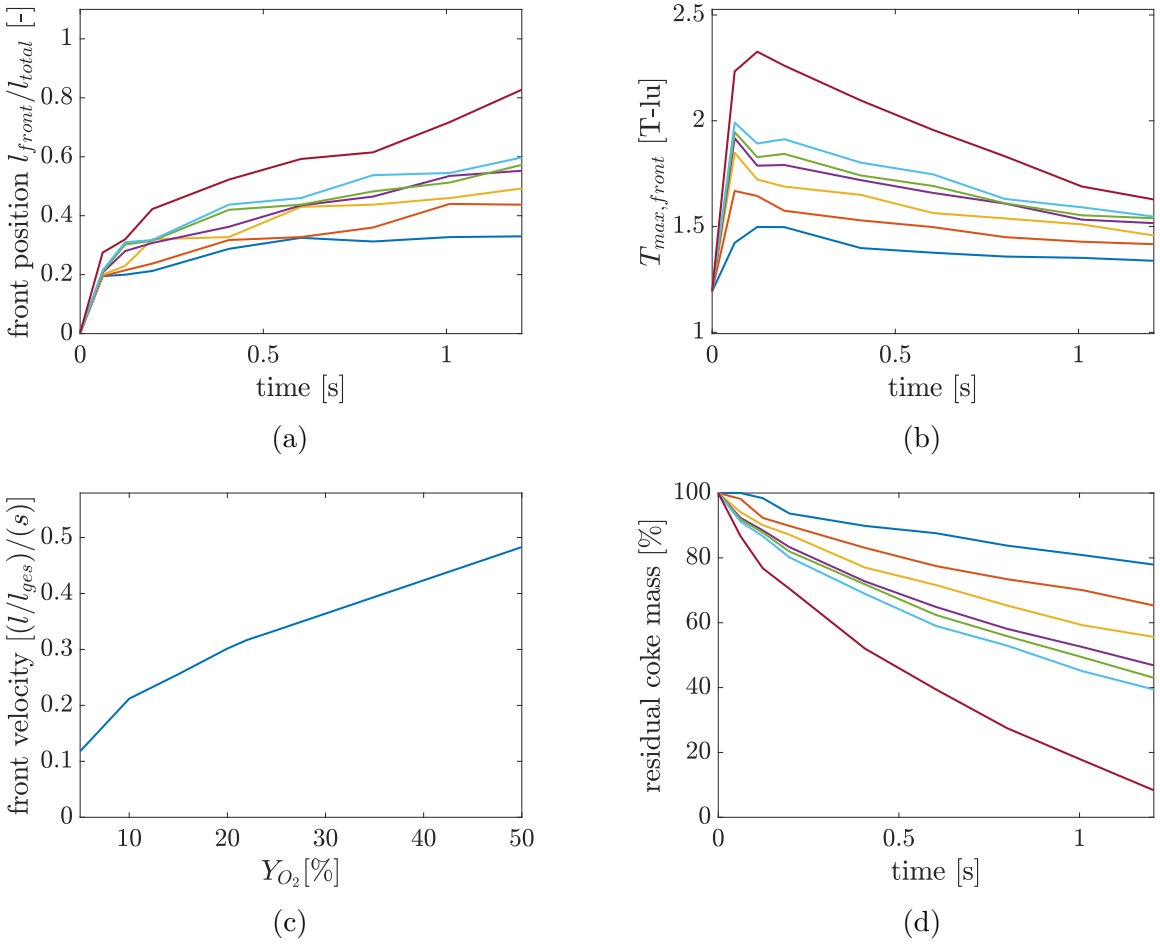

Figure 5.31: Parametric study of Y_{O_2}: Temporal evolution of the position of the combustion front (a), maximum temperature (b) and residual coke (d) as well as propagation velocity of the combustion front for different inlet mass fractions of oxygen (c). In the graphs, the colors denote the following values of the inlet mass fraction of oxygen: $Y_{O_2} = 5\,\%$, $Y_{O_2} = 10\,\%$, $Y_{O_2} = 15\,\%$, $Y_{O_2} = 20\,\%$, $Y_{O_2} = 22\,\%$, $Y_{O_2} = 25\,\%$, $Y_{O_2} = 50\,\%$.

The temporal evolution of the combustion front position describes a similar course throughout the range of values of $Y_{O_2,in}$, with an almost linear increase in propagation speed, as it can be seen in Figure 5.31c. The maximum front temperatures also exhibit similar profiles, with a maximum at 0.2 seconds, as shown in Figure 5.31b. This maximum is prominent for all values of $Y_{O_2,in}$. As expected for a transport limited combustion regime, an increase in the provided educt leads to a higher burn rate, resulting

in a steeper drop of the residual coke mass. A value of $Y_{O_2,in} = 5\,\%$ results in approximately 20 % of the original coke mass being burned after 1.2 seconds, with $Y_{O_2,in} = 25\,\%$ resulting in a consumption of around 60 % and $Y_{O_2,in} = 50\,\%$ leading to a consumption of more than 90 % of the initial soot mass, as shown in Figure 5.31d. Since all characteristic values, i.e. the velocity of the combustion front, the maximum front temperature and the consumption rate of coke still change with an increase of $Y_{O_2,in}$, the combustion can still be assumed to take place in a transport limited regime, even at inlet mass fractions of oxygen of 50 %.

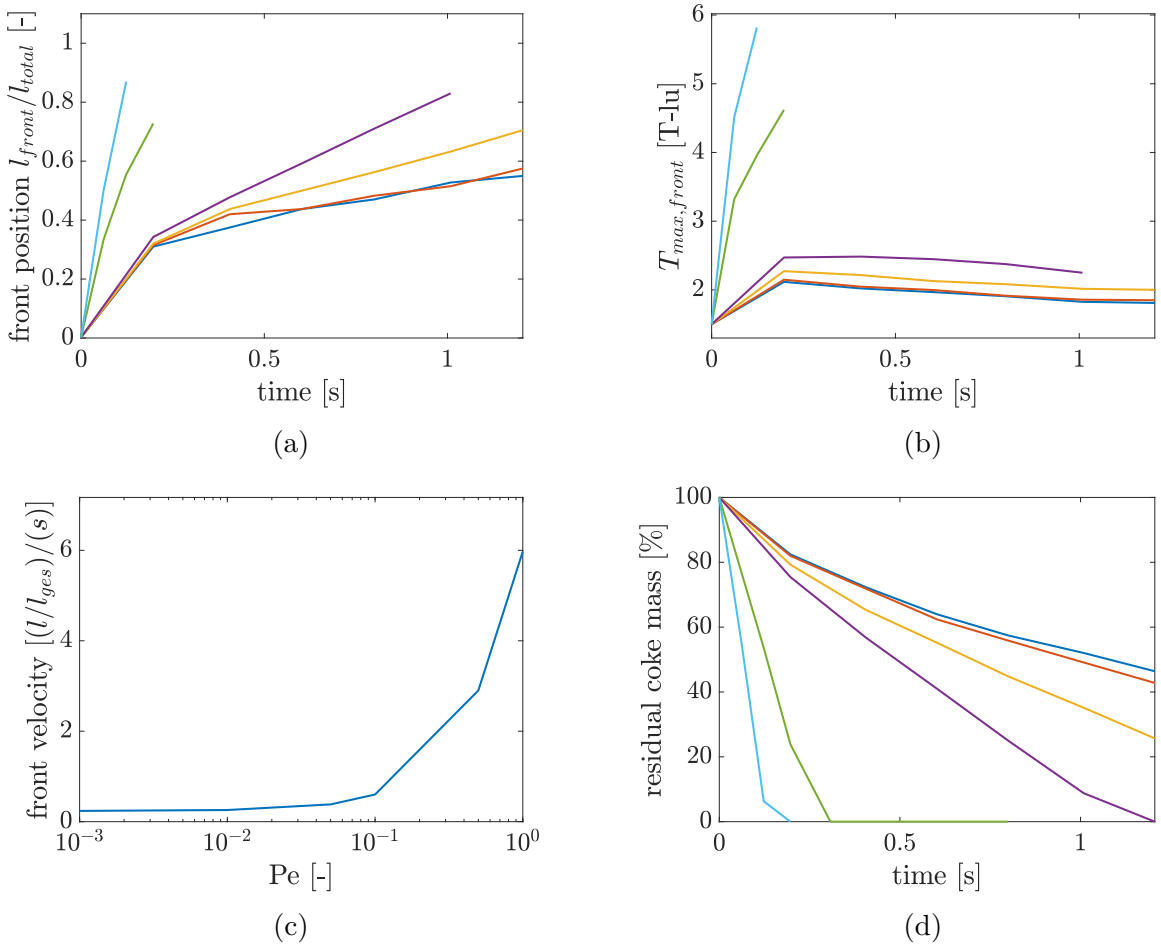

Figure 5.32: Parametric study of Péclet number: Temporal evolution of the position of the combustion front (a), maximum temperature (b) and residual coke (d) as well as propagation velocity of the combustion front for different inlet mass fractions of oxygen (c). Here, the colors represent the following Péclet numbers: $Pe = 0.001$, $Pe = 0.01$, $Pe = 0.05$, $Pe = 0.1$, $Pe = 0.5$, $Pe = 1$.

Since an increase in the educt mass fraction linearly increases the gradient of the mass fraction along the direction of the flow, which is the main driving force for mass transfer at $Pe = 0.01$, a linear dependency of the front velocity from the inlet educt mass fraction should be presumed. As it can be seen in Figure 5.31c, this assumption is fulfilled to a

good degree. Subsequently, the influence of the Péclet number onto the combustion mode is investigated. The Péclet number is varied by means of changing the inlet velocity and the results are shown in Figure 5.32, again with the front position, its propagation velocity and maximum temperature as well as the residual coke mass being displayed. More time steps are used for the evaluation of the simulation with $Pe = 1$ since full conversion of the initial soot mass is achieved at $t = 0.2\,s$. For a Péclet number of $Pe = 0.1$, the simulation reaches total conversion of soot after around $t = 1.2\,s$. Further decreasing the Péclet number results in smaller changes of the temporal evolution of the residual coke mass in accordance with the fact that the advective transport becomes irrelevant. Furthermore, the propagation speed, displayed in the bottom left of Figure 5.32c, exhibits an exponential dependency of the Péclet number and the maximum temperature of the combustion front shows a drastic increase to approximately 5.7 T-lu, compared to the range of 2 - 2.5 T-lu for $Pe \in [0.001, 0.1]$. Both Pe and $Y_{O_2,in}$ have an influence on the mass transport in the simulation. When comparing the propagation velocity for a change of Pe and of $Y_{O_2,in}$ in the Figures 5.31c and 5.32c, a different behaviour can be noted. The propagation velocity for a change in $Y_{O_2,in}$ shows a nearly linear dependency, also hinting an asymptotic behaviour. This results from the driving force of mass transfer, in this specific case the gradient of Y_{O_2}, declining with propagation of the combustion front, dampening the effect of higher inlet mass fractions of oxygen. For $Pe \ll 1$, diffusion is the dominating phenomenon of mass transport. This results in an almost constant propagation velocity of the combustion front, since the overall mass transport remains almost unchanged. For Péclet numbers approaching 1, the convective mass transport becomes relevant. This results in a steep incline in the front velocity due to the fact that the total mass transport drastically increases with further increases of the inlet velocity. Furthermore, the influence of the thickness of the reactive soot layer is investigated. For this purpose, the simulation domain is altered in such a way that the overall diameter of the round particles is kept constant, with the thickness of the outer reactive layer being altered. This leads to a change in the ratio of the reactive and inert solid masses while keeping the porosity of the system constant. Simulations are conducted with a layer thickness of one, two and five lattice nodes, with the first one being the standard case used in the previous parametric study. The results of the study are shown in Figure 5.33, in which the maximum front temperature, the front velocity, the residual coke mass and the axial temperature profiles are shown. It can be seen that the maximum front temperature increases with increasing soot layer thickness. This results from the higher ratio of reactive to inert solid mass, which leads to a higher release of reactive energy compared to a smaller amount of inert, temperature dampening mass. Furthermore, the higher amount of reactive mass per particle in conjunction with the transport limited

combustion regime results in a smaller front velocity for an increasing soot layer thickness.

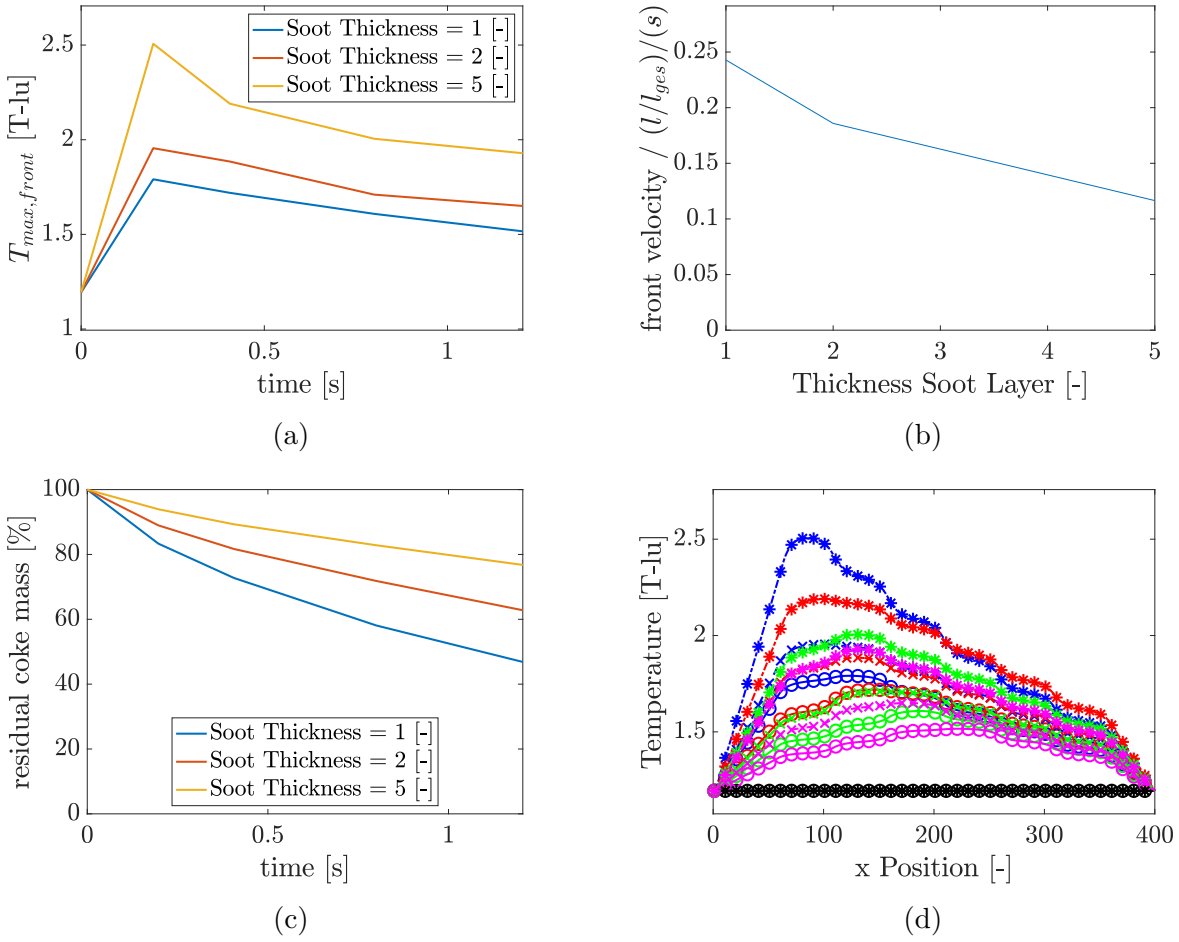

Figure 5.33: Results of simulations with different thickness of reactive soot layer. Shown are the maximum front temperature (a) and front velocity (b) as well as the residual coke mass (c) and the temperature profiles at different time steps for the three geometric configurations. In Figure 5.33d, $\circ$, $\times$ and $*$ denote the thickness of 1, 2 and 5 lattice nodes. The colors represent the simulation time, with -, -,- and - denoting 0.2 s, 0.4 s, 0.8 s and 1.2 s.

The transport limited regime also equates to a different residual coke mass after a combustion simulation of $t = 1.2\,s$. The oxygen provided at the inlet dictates the maximum reaction rate possible within the boundaries of the simulation. With more reactive soot initially present for higher soot layer thicknesses, the residual coke for a specific combustion time will increase accordingly.

In a final step, a combustion simulation is performed using a realistic soot geometry. This geometry is obtained by Focused Ion Beam Scanning Electron Microscopy (FIB-SEM) analysis of real soot samples generated by a combustion aerosol standard (CAST) generator at ICVT in Stuttgart. With the FIB-SEM method, the three dimensional structure of soot samples can be analysed and reconstructed for 2D and subsequent 3D simulations.

This is achieved by repeatedly taking a SEM image and subsequent removal of the top layer of the structure by a focused ion beam (FIB). One exemplary 2D slice is shown in Figure 5.34, which will be used for the first realistic combustion simulation. Also, the steady state velocity profile for this porous geometry is shown on the right of Figure 5.34 as the velocity magnitude. By analysing the velocity magnitude, the main flow paths through the porous domain can be visualized.

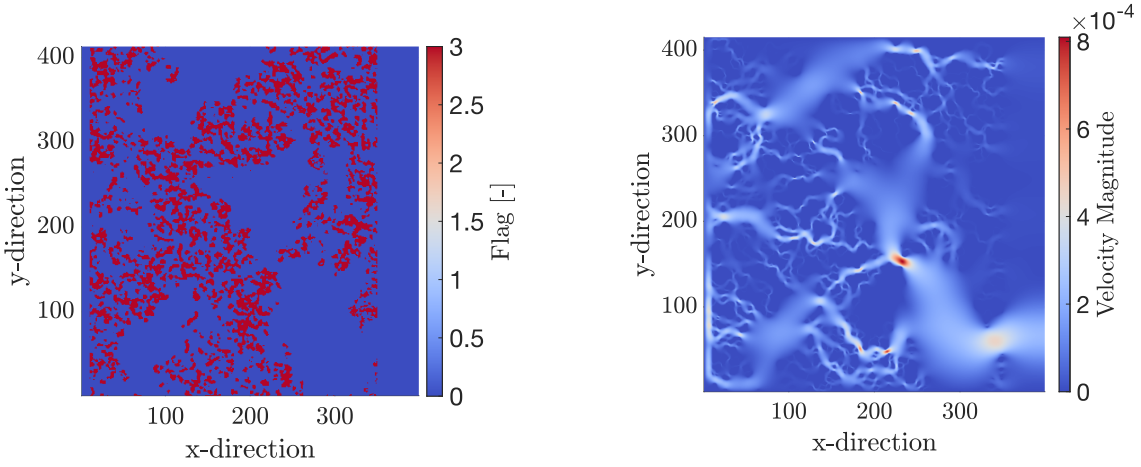

Figure 5.34: Realistic soot geometry used for combustion simulations obtained by FIB-SEM imaging (performed at HZB) of CAST soot generated at ICVT in Stuttgart (left) and stationary solution of the velocity magnitude (right).

The FIB-SEM resolution is 339×415 pixels, with a pixel size of 10 nm. As it can be seen, the domain is extended by 10 lattice nodes at the inlet and 50 lattice nodes at the outlet for a total domain size of 399×415 pixels. This measure is necessary to guarantee a stable steady state solution of the flow field in conjunction with the boundary conditions. Not extending the domain at the inlet and outlet would lead to instabilities induced by the incompatibility of the velocity boundary conditions with the domain. Also, this smaller discretization requires the parameters in lattice units to be rescaled. Following the relationship between the relaxation time and viscosity, which is received from the Chapman-Enskog analysis, the following relationship between the size of the spatial and temporal steps is received:

$$\frac{\Delta t/\Delta x^2}{\nu} = c_s^2 \left(\tau_f - 0.5\right) \tag{5.4}$$

With this expression, the change in the temporal step size can be calculated. For the lattice width of 10 nm, given by the FIB-SEM resolution, the time step size results in $\Delta t = 2.04 \times 10^{-12} s$. With these parameters, simulations with 20 million time steps are performed, resulting in a simulation time of approximately $40\,\mu s$. For the temperature and inlet velocity, values corresponding to real world scenarios are chosen. This results in an inlet temperature of $600\,°C$ and an inlet velocity of $0.2\,m/s$. The temporal evolution

of the soot geometry is shown in Figure 5.35a and 5.35b for 20 μs and 40 μs.

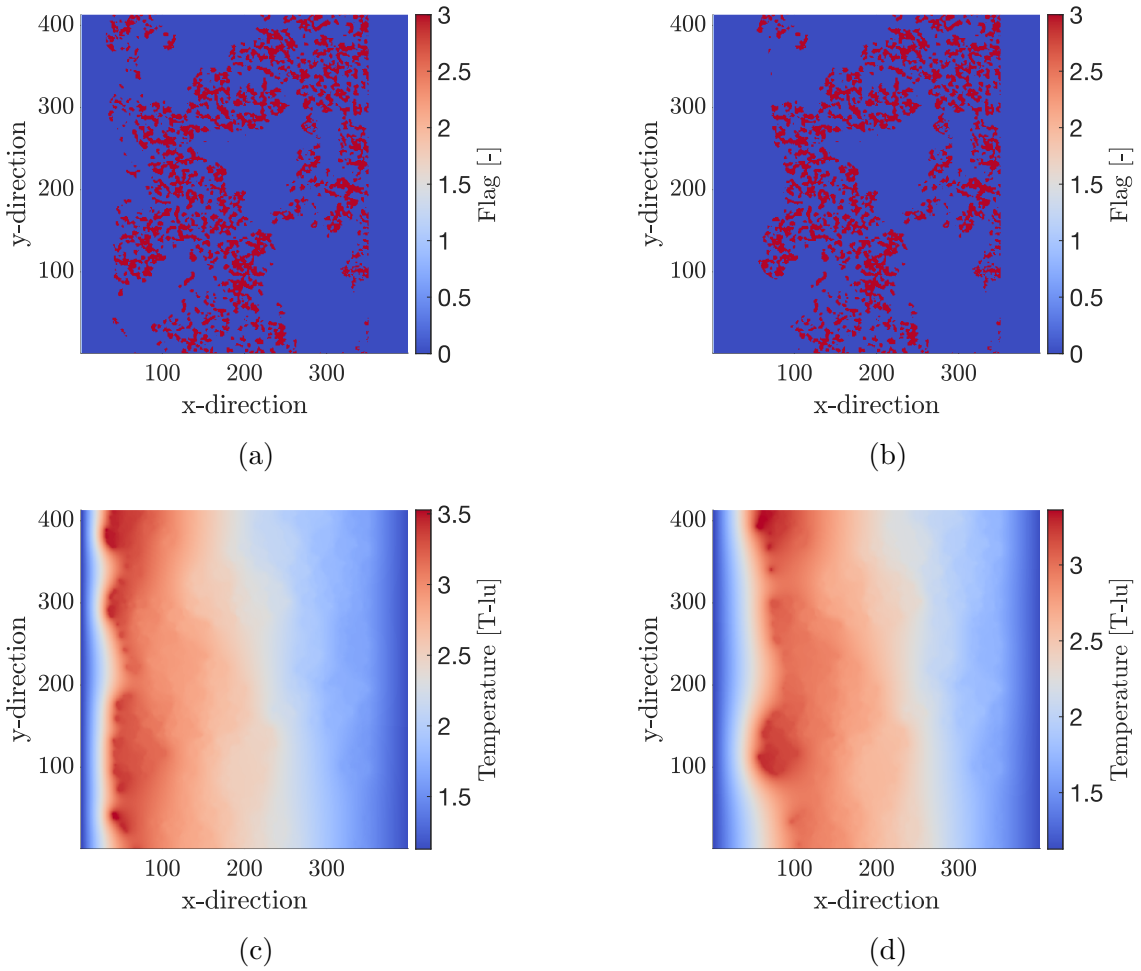

Figure 5.35: Consumption of the soot geometry by combustion, shown at 20 μs (a) and 40 μs (b) as well as the corresponding temperature profiles shown at 20 μs (c) and 40 μs (d).

It can be seen that a combustion front is propagating in downstream direction, resulting in the geometry being consumed homogeneously from the left. This behaviour is to be expected, since the inlet parameters correspond to a Péclet number of $Pe = 3 \times 10^{-3}$ and a Damköhler number of $Da = 1.759 \times 10^{-4}$. As it is shown in the parametric study above, these values correspond to a mass transfer limited combustion regime, resulting in a propagating combustion front. This combustion front can also be observed in Figure 5.35c and 5.35d, which shows the temperature profiles at $t = 20\,\mu s$ and $t = 40\,\mu s$. In this context, the change of specific surface with propagating combustion is of interest. For more elaborate geometries with potentially enclosed cavities, a Breadth-first search algorithm can be used to accurately calculate the effective reactive surface, omitting any enclosed spaces from the calculation, which are not accessible by the educt-rich gas entering the simulation domain at the inlet. The resulting surface is related to the total

mass of soot, resulting in the specific reactive surface. The change of the specific reactive surface as well as its relative change are shown in Figure 5.36 on the left side, with the total reactive surface being shown on the right. Since the consumption is characterized by a propagating combustion front, the specific reactive surface shows marginal changes. This is expected since a combustion progress of approximately 20 % means that the first fifth of the domain, as seen from the inlet, is consumed, leaving 80 % of the domain virtually untouched. If the simulation domain, as defined by the FIB-SEM images, covers an area large enough to describe the characteristics of the morphology, suppressing statistical deviations, the remaining 80 % of the domain will approximately show the same mass specific reactive surface.

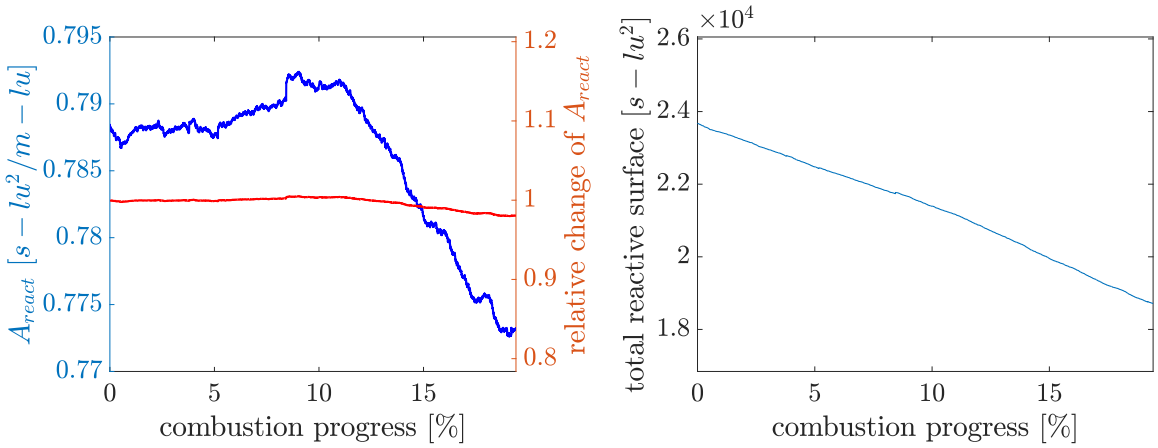

Figure 5.36: Specific reactive surface shown with propagating combustion (blue) and change relative to the initial value (red).

This combustion behaviour, which is characterized by a moving combustion front and stepwise oxidation from inlet towards the outlet direction, enables a possibility to study the change of the specific reactive surface while saving computational resources. Since this combustion regime exhibits educt mass transport limitations, it is possible to reduce the allocated mass of the lattice nodes which are allocated to be solid soot. This leads to a faster propagation of the combustion front with less time steps necessary while preserving the characteristic evolution of the specific reactive surface, since this is a parameter intrinsic to the morphology of the domain. To validate this assumption, the same 2D combustion simulation is performed, while only allocating 1 % of the real solid mass to each soot lattice node. The results are displayed in Figure 5.37, in which the evolution of the specific reactive surface and the relative changes are displayed with progressing combustion. It can be seen that both simulations with the full density and with the reduced density exhibit a qualitatively similar behaviour, with the reduced density leading to only small deviations. This proves that the evolution of the specific surface is morphology intrinsic and does not change as long as the combustion regime remains unaltered. With

this knowledge, combustion simulations in 3D can be performed in a computationally more feasible manner.

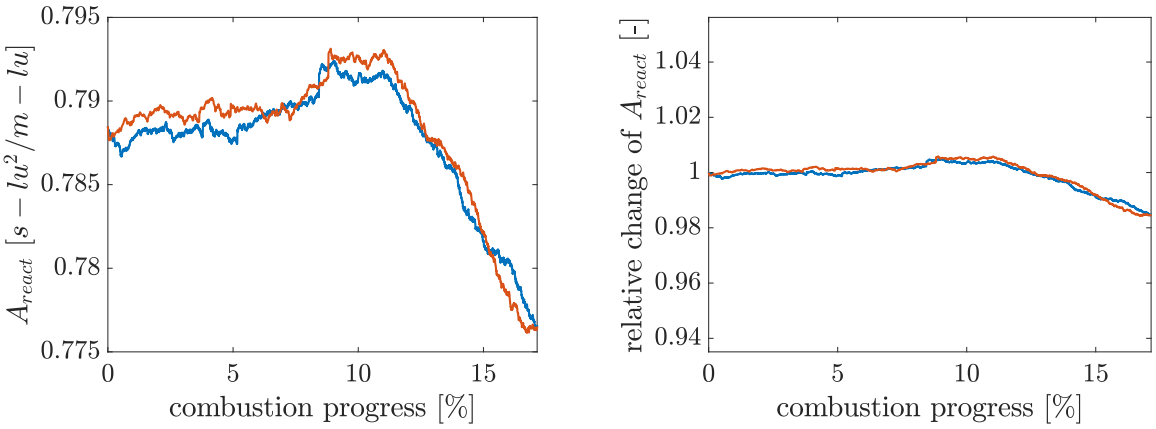

Figure 5.37: Evolution of the specific surface over the combustion progress (left) and relative change of the specific surface (right) for the full solid density (–) and reduced solid density (–).

These are imperative in order to investigate possible 3D effects on the combustion behaviour and to ensure that the 2D slice accurately represents the 3D domain. The 3D model is validated in analogy to the 2D validation, which was shown in [129], using the 2D test case presented first in [143], which is set up in 3D. For this purpose, a domain size of $420 \times 80 \times 20$ is chosen and the geometry and boundary conditions are the same as in the 2D case, with the difference that the z-direction is assumed to be periodic.

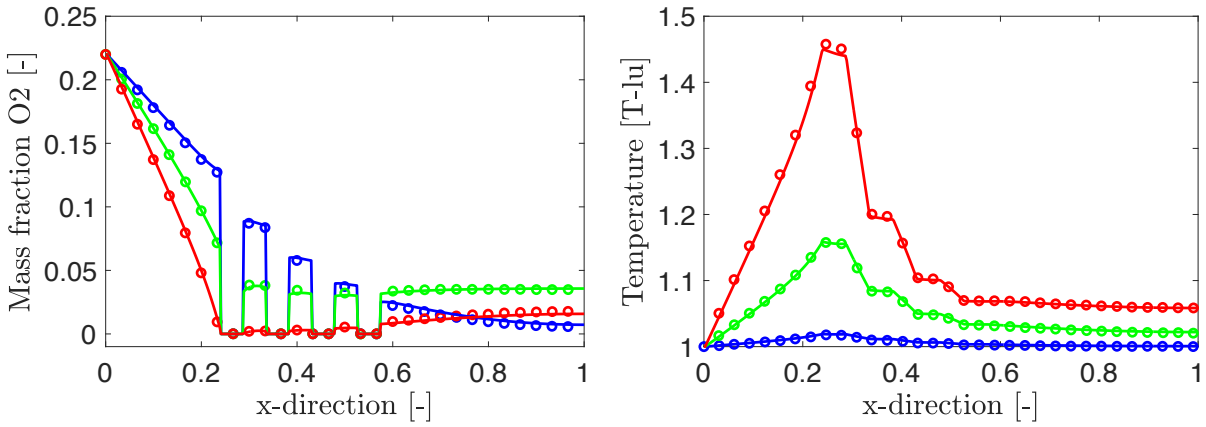

Figure 5.38: Validation of the 3D model by comparison of the results with literature data [143]. In the graphic, (○) and (–) represent the literature data and the LBM results at 2 ms, (○) and (–) at 6 ms and (○) and (–) at 10 ms for the mass fractions of oxygen (left) and temperature (right).

With this setup, the literature data of the 2D case can be used to validate the 3D model. The resulting temperature and O_2 profiles are shown in Figure 5.38. As it can be seen, both temperature and O_2 profiles exhibit excellent accordance with the literature

data. With the 3D model being validated, a combustion simulation based on the realistic soot morphology of the 3D FIB-SEM data is conducted. The domain has a size of $100 \times 121 \times 111$ lattices. The evolution of the geometry is displayed in Figure 5.39.

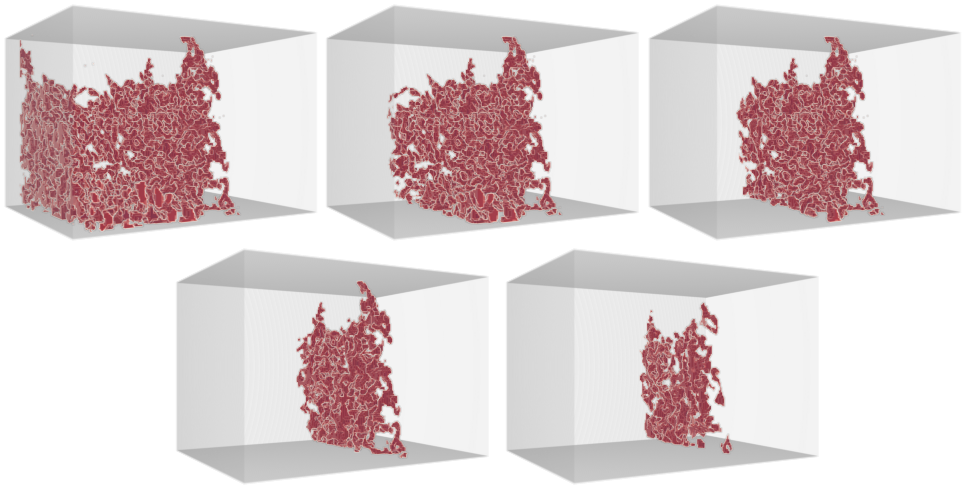

Figure 5.39: Evolution of the 3D geometry with a lattice resolution of size of $100 \times 121 \times 111$ over time at approximately 0 %, 15 %, 35 %, 60 % and 80 % combustion progress.

Since the computational effort for 3D simulations is exceedingly high, the previously discussed method of reducing the density of the solid domain is used again. This means that the solution of the temperature field and of the component fields is wrong, but the evolution of the specific surface is still usable since the overall combustion regime remains unchanged by the density scaling. Furthermore, the temporal evolution of the specific and total surface is displayed in Figure 5.40.

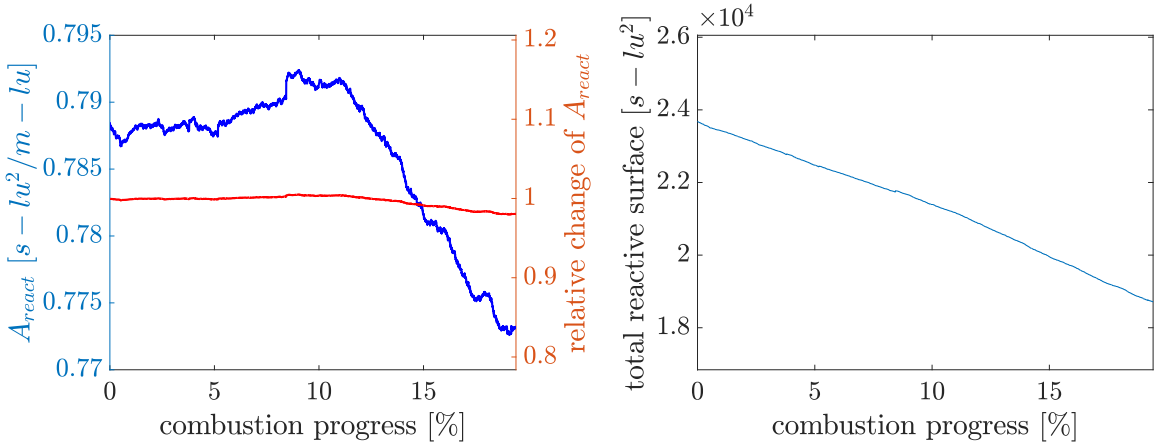

Figure 5.40: Temporal evolution of the specific reactive surface (left) and total reactive surface (right) over the combustion progress.

It can be seen that the soot is consumed in the downstream direction as the combustion front progresses which results in a mostly constant specific reactive surface. It becomes

apparent that the specific surface evolution in 2D and 3D is similar, since again only slight changes in the specific surface with progressing combustion state can be found.

5.4 Comparison of simulation data with experiments conducted at ICVT Stuttgart

In the ASORNE project proposal, it was suggested that FIB-SEM pictures will be taken to analyse the morphology of the soot structure before and after combustion and to be able to conduct numerical simulations with the exact structures. This was suggested since the main change of the reactive surface was assumed to happen on the mesoscopic scale of the soot structure, which can be analysed with FIB-SEM. Multiple findings of this thesis and the related PhD-thesis at ICVT by Antonio Raiolo lead to a shift in the focus for the continuation of this thesis. Firstly, both the Helmholtz-Zentrum in Berlin (HZB) as well as the Institute of Materials Science of the University of Stuttgart were contracted to conduct the FIB-SEM analysis of the soot samples. However, both institutions faced difficulties in analysing the provided soot samples as a result of their brittle structure. It is suspected to result from the preparation of the soot samples for FIB-SEM imaging. Before conducting the FIB-SEM analysis, it is necessary to embed the porous structure by penetrating it with a stabilizing agent. During this process, a vacuum is used to extract the remaining air from within the structure.

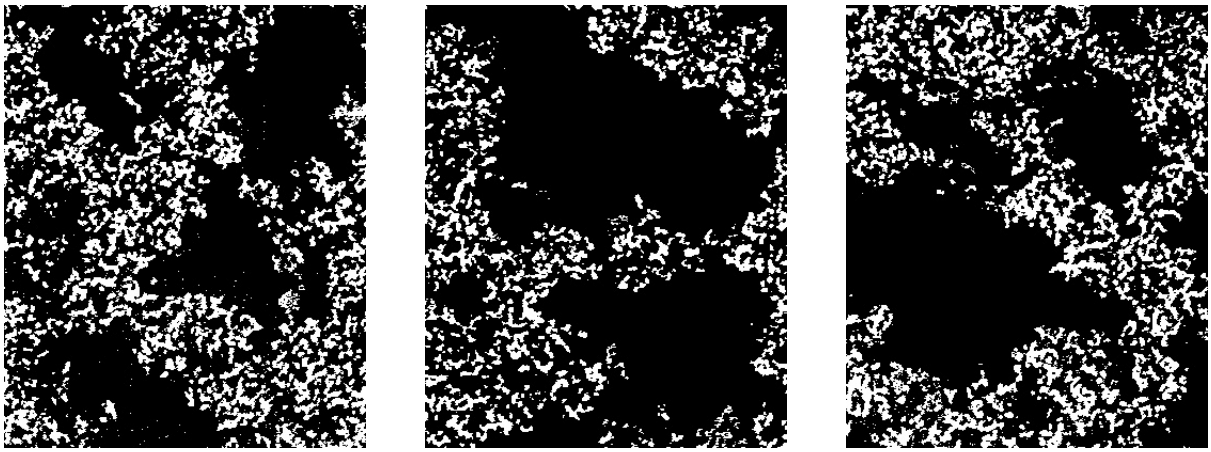

Figure 5.41: FIB-SEM slices number 1 (left), number 250 (middle) and number 500 (right), with the soot and void space being shown in white and black, respectively. The images exhibit large cavities resulting from the sample preparation.

It is suggested that during this process, the structure is damaged as a result of its weak stability. For this reason, up until the submission of this thesis, only one FIB-SEM image set of one soot sample was received. These pictures were taken at HZB and they exhibit a resolution per slice of 339 $\times$ 415 pixels, with a pixel size of 10 nm. Furthermore, the

distance between each slice is 10 nm and 500 slices are taken, resulting in a total domain size of 3.39 μm × 4.15 μm × 5 μm. In Figure 5.41, exemplary, the 1^{st}, 250^{th} and 500^{th} slices are shown. Here, the solid soot is displayed in white, with the pore space being displayed in black. As it can be seen, the homogeneous porous structure is interrupted by large cavities. The visibility of these cavities is enhanced once the three-dimensional structure is recreated, as shown in Figure 5.42.

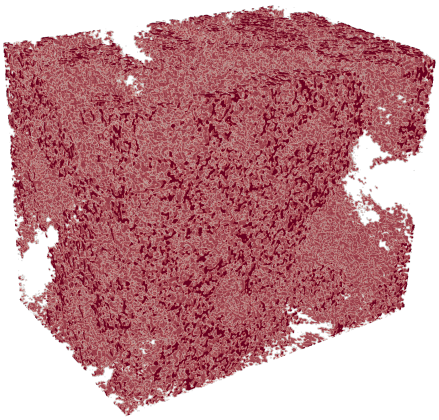

Figure 5.42: 3D reconstruction of the realistic soot structure based on the 2D FIB-SEM slices with a domain size of 3.39 μm × 4.15 μm × 5 μm.

Furthermore, extensive shifting of the geometry, meaning that the FIB exerts force onto the carbon structure, rearranging it in the process, could be observed. Subsequently, combustion simulations both in 2D as well as 3D were conducted by utilizing the only FIB-SEM data, which was available. Analysis of the two-dimensional FIB-SEM slices results in a mean porosity of 79.87 % with a standard deviation of 3.89 %, which is equivalent to the 3D volume analysis. As described in the beginning of the chapter, the main assumption of the project was that the mesoscopic morphology of the soot provides the main reactive surface. Thus, changes in the morphology of the soot would influence the reactivity, which should be measurable by changes in the BET-surface during combustion experiments. This assumption was based on the findings of a PhD thesis conducted at ICVT in Stuttgart by Simone Seher [116]. For this reason, the main parameter of interest for the comparison between the combustion experiments at ICVT and the LBM simulations is the evolution of the specific surface with progressing combustion. Eight randomly chosen excerpts of the FIB-SEM slices are used and combustion simulations are performed. The eight geometries are displayed in Figure 5.43, with a flag value of 3, displayed in red, indicating the reactive soot and a value of 0, displayed in blue, indicating the gas phase. Combustion simulations are performed with a resolution of the computational domain of 100 × 160 lattice nodes, resulting in a total domain size of

$1\,\mu m \times 1.6\,\mu m$, with a lattice spacing of $10\,nm$ after confirming grid convergence. The inlet temperature and velocity are set to $600\,°C$ and $0.2\,m/s$, similar to the values set in the combustion experiments.

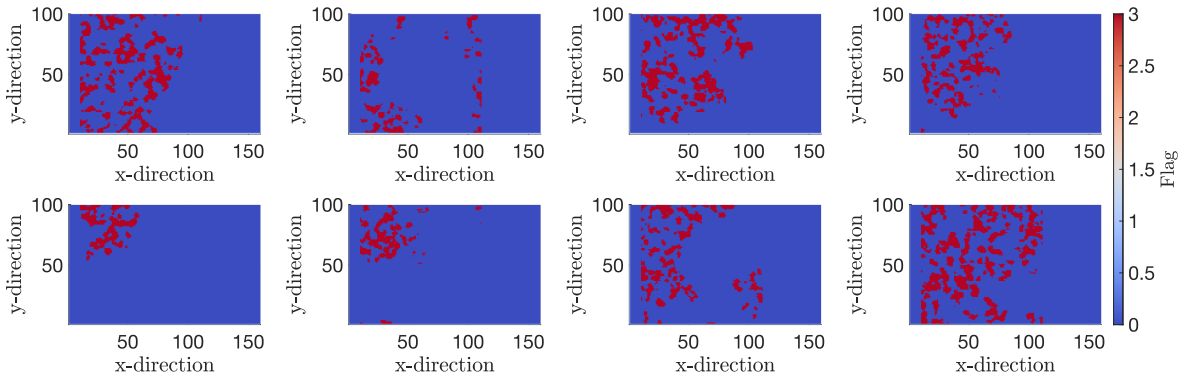

Figure 5.43: 2D simulation domains obtained from randomly chosen FIB-SEM slices, cropped to a 100 × 100 domain size.

These parameters lead to a educt mass transport limited regime based on the parametric study, which was performed in Chapter 5.3. The simulations are run for $20{\times}10^6$ time steps, resulting in a total simulation time of around $40.8\,\mu s$. The resulting evolution of the specific reactive surface with progressing combustion is shown in Figure 5.44.

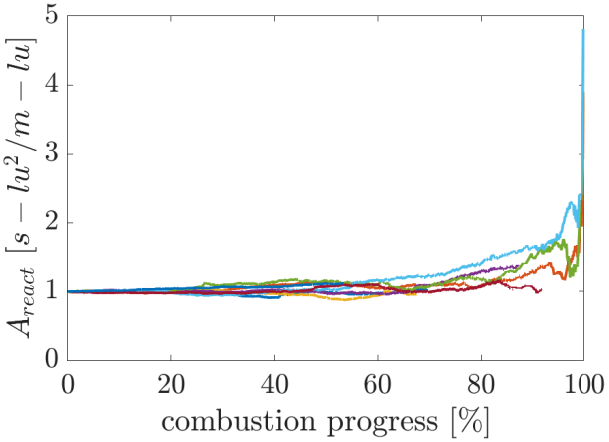

Figure 5.44: Evolution of the specific surface with progressing combustion for the domains shown in Figure 5.43.

It can be seen that the evolution of the specific surface is largely unaffected by the geometry chosen. Furthermore, it is noted that the course of all eight graphs follows the so-called shrinking core model. The shrinking core model describes the dynamics of a round particle, which is consumed homogeneously in radial direction and the resulting evolution of the specific surface. This results in an almost constant specific surface with progressing combustion followed by an exponential increase, once total consumption is approached. Subsequently, the influence of the inlet mass fraction of oxygen onto the

evolution of the specific surface is investigated. The same simulation parameters as before are chosen, with the exception that the inlet mass fraction of oxygen is reduced to 5 %. The reduced inlet mass fraction of the educt leads to an even higher limitation in educt mass transport, thus decreasing the overall reaction rate and heat release inside of the soot domain. Due to the decreased reaction rate, the simulation had to be run for 50×10^6 time steps (102.1 μs) for a total combustion of 25 % of the initial soot mass. The evolution of the solid soot domains of the simulation with 5 % oxygen and with 22 % oxygen are shown on the left and right of Figure 5.45, respectively.

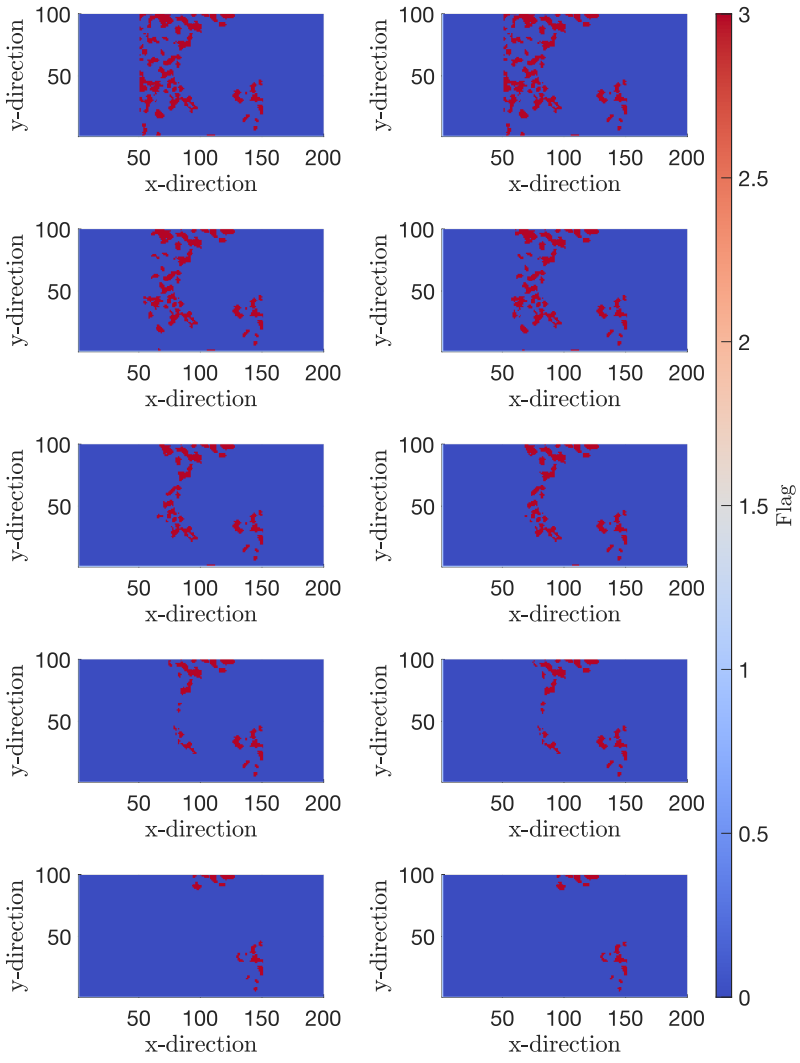

Figure 5.45: Evolution of the soot structure for $Y_{O_2,in} = 5\,\%$ (left) and $Y_{O_2,in} = 22\,\%$ (right) at combustion progresses of 0 %, 20 %, 40 %, 60 % and 80 % in the rows 1-5.

The first row shows the initial morphology of the soot, as taken from the FIB-SEM, with the domain at combustion progresses of 20 %, 40 %, 60 % and 80 % being shown in

the rows 2-5. For the simulation with 22 % oxygen, around 31×10^6 time steps (63.3 μs) were necessary to reach a combustion progress of 80 %, while around 121×10^6 time steps (247.1 μs) were necessary for the simulation with 5 % oxygen at the inlet due to the reduced mass transport. This is a result of the mass transport limited reaction regime, leading to the reaction rate being directly proportional to the mass transport.

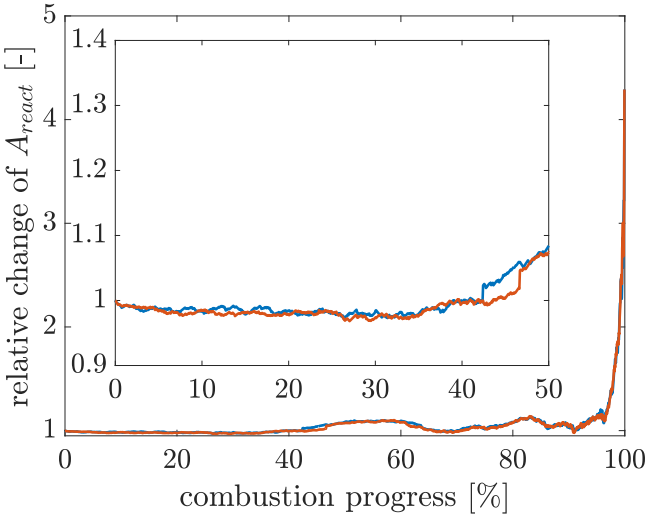

Figure 5.46: 2D Simulation with inlet mass fraction of O_2 of 5% and of 22%. The lower inlet mass fraction results in an even higher restricting in educt mass transport and slower reaction rate.

Furthermore, it can be seen that the evolution of the soot structure during the combustion is similar, with only minuscule differences in the structure being visible. This is due to the combustion being limited by the diffusive mass transport of oxygen in both cases. The resulting evolution of the specific surface is shown in Figure 5.46 and compared with the simulation with an inlet mass fraction of 22 %. As expected from the previous analysis of the change of the geometry with progressing combustion, only marginal changes in the evolution of the specific surface occur when altering the inlet mass fraction of oxygen. This is also in accordance with the findings of the experimental part of the ASORNE project, as it is shown in [104]. For both inlet mass fractions, the evolution of the specific surface follows the course described by the shrinking core model. In addition to the 3D simulation with reduced solid density, which was performed in Chapter 5.3, a 3D simulation with correct density and reduced domain size is performed to validate the evolution of the specific surface. Reducing the domain size is necessary for simulations with the correct solid density values in order to reduce the computational effort. The simulation was conducted with an inlet temperature of 880 °C and an inlet mass fraction of oxygen of 22 %. The reduced soot domain size resulted in a total domain resolution of $40\times40\times100$ lattice nodes, equating to 160000 lattice nodes in total. For the total consumption of

the soot, the simulation was run for $10{\times}10^6$ time steps, resulting in a simulation time of around 20 μs. The domain, which was used for the simulation as well as the evolution of the specific surface are shown in Figure 5.47.

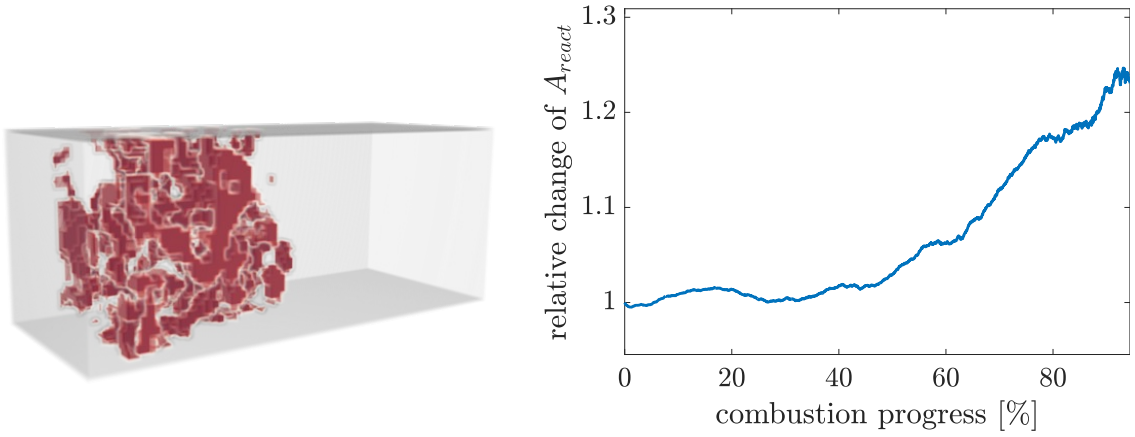

Figure 5.47: Computational domain with resolution of 40×40×100 lattice nodes (left) and result of the evolution of the specific surface with progressing combustion (right).

In Figure 5.48, the mass fraction fields of CO_2 and O_2 in conjunction with the soot structure (black) are displayed on the left and right, respectively. The mass transport limited combustion regime, resulting in a progressing combustion front, can be observed on the right. The oxygen is fully depleted at the position of the combustion front, resulting in the soot being consumed progressively. These results are compared with the experimental data acquired by Antonio Raiolo at ICVT. In Figure 5.49, the evolution of the specific surface of a soot sample with a diameter of the soot agglomerates of 156 nm, similar to the sample used for the only existing FIB-SEM geometry, is shown. This means that the parameters of the CAST generator were set in such a way that soot particles with a diameter of 156 nm are generated. Shown are the simulation data in blue as well as a polynomial fit in black. The data is evaluated only up to a combustion progress of around 90 %. This is due to the fact that the measurement errors are increasing for smaller remaining soot masses on the filter. It can be seen that the evolution of the specific surface greatly differs from the shrinking core model, as it described a steep incline for small combustion progresses. For higher combustion progresses, an asymptotic behaviour is noted. Similar results were found for different diameters of the generated soot, for varying inlet temperatures and inlet mass fractions of oxygen, as shown in [104]. This large increase in specific surface cannot be reproduced by LBM simulations on the meso-scale, as shown above. 2D and 3D simulations with realistic geometries obtained from FIB-SEM analysis of the soot used in combustion experiments were conducted for varying inlet temperature and mass fractions of oxygen. It was shown that, while only capturing the accessible surface on the mesoscopic scale, the evolution of the specific

surface always follows to good agreement the shrinking core model. For this reason, it is suspected that the primary particles, of which the mesoscopic structure of the soot consists, are responsible for the increase in specific surface.

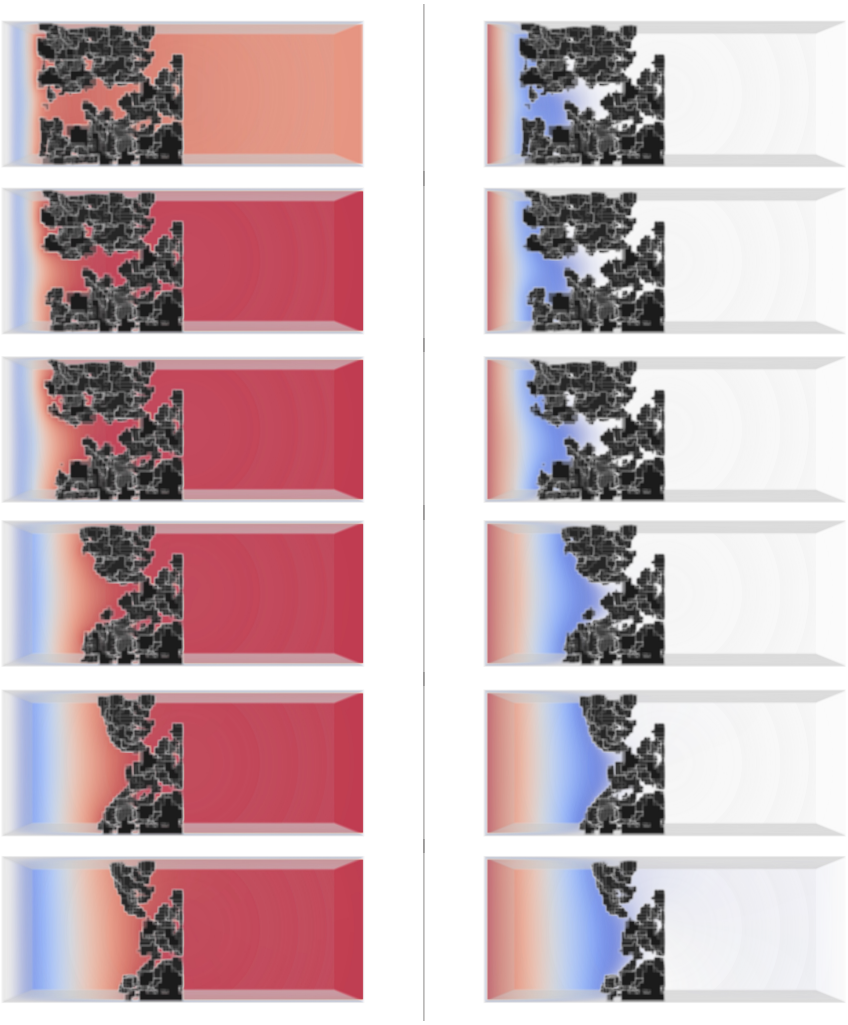

Figure 5.48: Mass fractions of CO_2 (left) and O_2 (right), each with soot structure being displayed in black at time step 6×10^4, 3×10^5, 6×10^5, 1.8×10^6, 3×10^6 and 4.5×10^6 from top to bottom.

The FIB-SEM resolution is, as specified previously, limited to a pixel size of 10 nm. This means that, for the LBM simulations with realistic soot geometries, entities smaller than 10 nm are treated as homogeneous soot, without accounting for heterogeneities on the nano-scale of the primary particles. There exist ample studies describing the layered structure of primary particle in the range of 4-10 nm [11, 3]. Specifically, Alfè et al. [3] discuss the evolution of the primary particle structure during their formation in the flame generator. The mature soot particles are described as concentric shell nanostructures, consisting of an quasi-amorphous, about 1-2 nm large core, surrounded by graphene layers. In both publications, TEM imaging is used to investigate the structure of the primary particles. For this reason, TEM was chosen as a valid method to analyse the soot samples

before and after the combustion experiments.

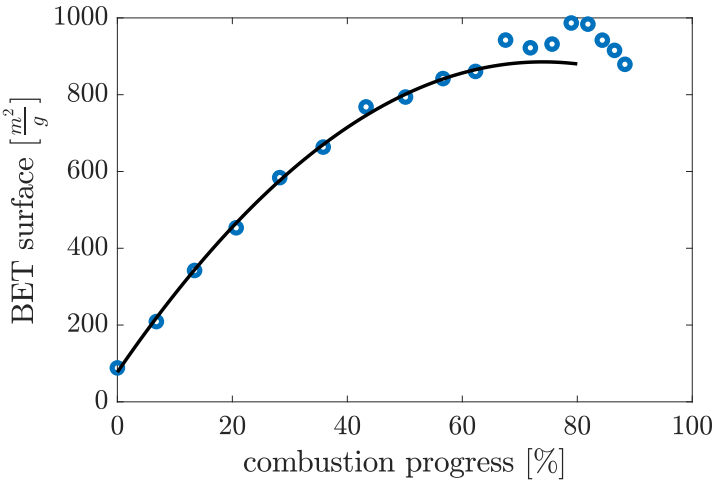

Figure 5.49: Evolution of the specific surface of a combustion experiment conducted at ICVT.

With this procedure, the primary particle structure and their potential evolution during the oxidation process is studied. The TEM images of soot samples before the combustion reaction are shown in Figure 5.50. Here, primary particles with a magnification of 720×10^3 are displayed. The inner structure of the primary particles and the so-called fringes, can clearly be seen. Fringes are the planar polyaromatic hydrocarbons, which are characterized by their length and tortuosity, i.e. their length divided by the closest distance between their ends. It becomes obvious from the two TEMs shown that the primary particles consist of an amorphous core, with a layered, more structures outer shell.

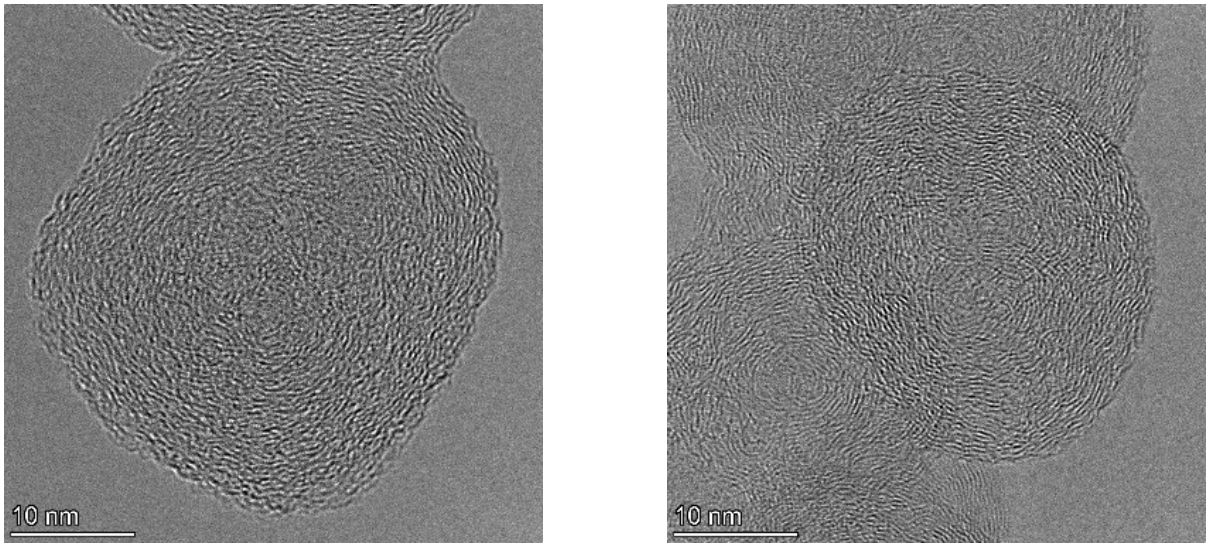

Figure 5.50: TEM images of the primary particles at 0% combustion progress.

This observation implies the potential for varying reactivities of the different sections

of the primary particles. For this reason, soot samples of particles with a diameter of 156 nm, corresponding to the sample FIB-SEM shown in Figure 5.42, at 0 % and at 75 % combustion progress are analysed. The resulting TEM images are shown in Figure 5.51. The sample at 0 % combustion progress is shown in the first row at 380×10^3 (left) and 720×10^3 magnification, with the sample at 75 % being shown in the second row, respectively. It can be seen that the non-combusted samples exhibit the previously described core-shell structure, with the whole particle being of uniform grey-scale. The different grey scales in the left picture are a result of overlapping primary particles. Moreover, it is evident that the images of the samples at 75 % combustion progress exhibit an increase in brightness towards the core-regions of the primary particle.

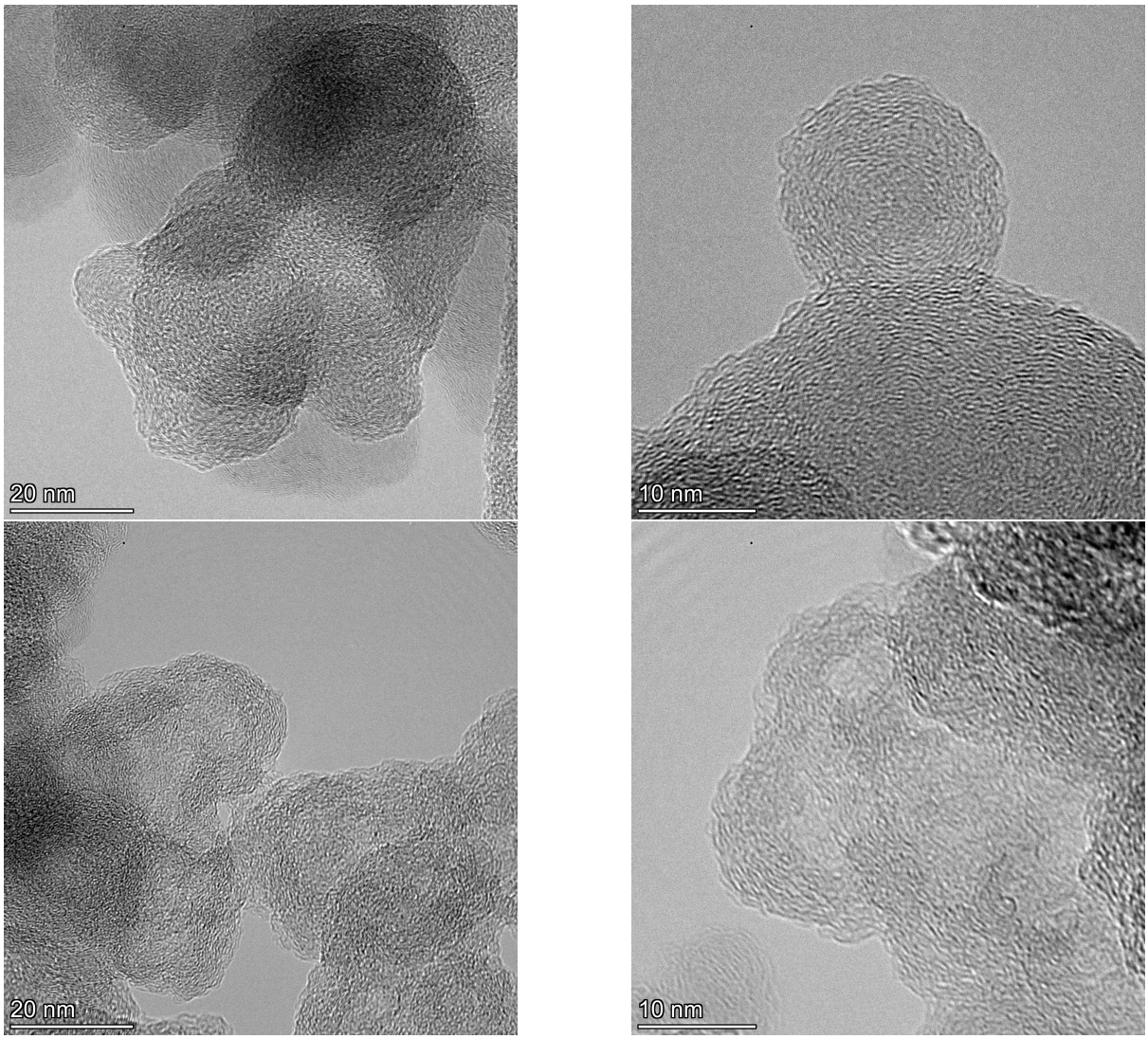

Figure 5.51: TEM pictures of soot with a CAST diameter of 156 nm at 0 % combustion progress in the first row and at 75 % combustion progress in the second row. Magnifications of 380×10^3 (left) and 720×10^3 (right) are shown.

This suggests the presumed heterogeneous consumption of the primary particles in amor-

phous regions, which exhibit a higher chemical reactivity due to the weaker structure of the carbon as a result of a lower binding energy in amorphous regions. For an in-depth analysis of the soot structure and primary particles, the reader is referred to the joint publication with Antonio Raiolo [104]. Furthermore, Raman spectroscopy was chosen to analyse the soot samples before and after the combustion experiments. With Raman spectroscopy, it is possible to determine the fraction of crystalline and amorphous parts of the primary particles. For this purpose, Raman-spectra of the same soot particles at 0 % and at 75 % combustion progress were taken, with the results being shown in Figure 5.52. For the evaluation of the spectra, the D and G bands are fitted by using Gaussian functions, with the resulting band fits also being displayed in Figure 5.52. Knauer et al. [62] report the D and G bands at approximately 1350 cm^{-1} and at 1580 cm^{-1}, respectively. For the soot samples at 0 % and at 75 % combustion progress, the band fitting is performed for three spectra, with the average D and G bands being at 1338 cm^{-1} and at 1595 cm^{-1}.

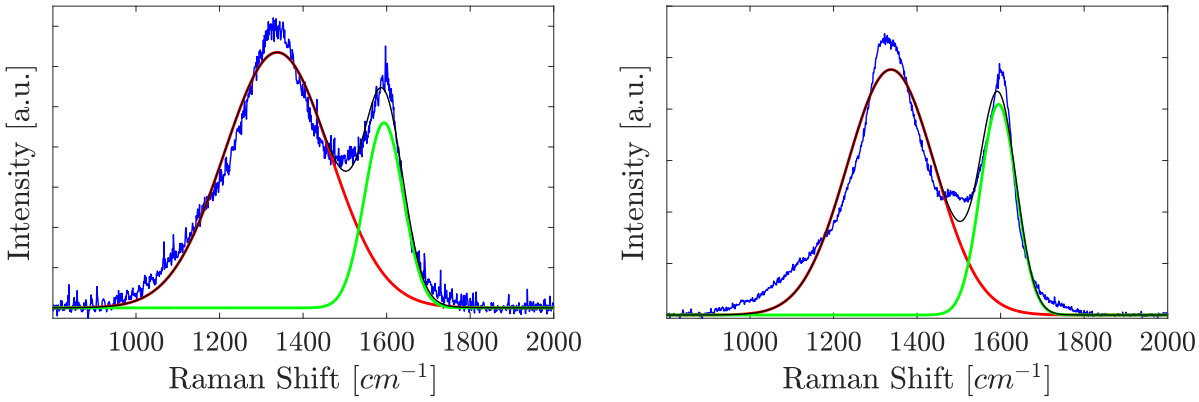

Figure 5.52: Raman Spectra with D and G band fit for soot particles of 156 nm CAST diameter at 0 % (left) and at 75 % (right) combustion progress.

According to the literature, the ratio of the intensities of the D and G bands indicates the degree of graphitization, with the intensity of the D peak relative to the intensity of the G peak decreasing for increasing order in the graphite strucutre [110, 134]. As it is shown in Figure 5.52, the intensity of the D and G bands relative to each other changes with progressing combustion. Initially, the intensity ratio of 1.38 was calculated. At 75 % combustion progress, the intensity ratio decreased to 1.16. In accordance with the mentioned literature, this suggests a higher order of graphitization with progressing combustion. Combined with the TEM analysis, it is presumed that the increased crystallinity is a result of the preferred combustion of the amorphous cores of the primary particle, rather than a structural reordering. For an in-depth analysis of the Raman spectra of soot samples with different agglomerate diameters, at different combustion progresses and with varied combustion parameters, the reader is referred to the publication of Raiolo et

al. [104]. Moreover, the comparison of the simulation data with the experimental results is not restricted to the comparison of the evolution of the specific reactive surface with progressing combustion. Another parameter to compare is the composition of the gas at the outlet. In the combustion experiments, the two components of CO and CO_2 in the outlet gas stream are quantified using a mass spectrometer. According to the procedure described in Chapter 4.5, the reaction kinetics for the separate oxidation of solid carbon to CO and to CO_2 are determined. For reaction (5.5), an activation energy of $151.79\,kJ/mol$ is found, with the activation energy of reaction (5.6) being $197.51\,kJ/mol$.

$$C + O_2 \rightarrow CO_2 \tag{5.5}$$

$$C + \frac{1}{2}O_2 \rightarrow CO \tag{5.6}$$

The parameters of the two reaction kinetics are then inserted into the combustion model and the corresponding reactive boundary condition, which was shown in the equations (3.112) and (3.113). Then, combustion simulations at different temperatures are performed. Since the ratio of CO/CO_2 is temperature dependent, the combustion simulations are set up with non-adiabatic walls at the top and bottom to mitigate the influence of the reaction heat, which is released during the simulation. Furthermore, small inlet mass fractions of O_2 are used to further decrease the influence of the reaction heat. The simulations are conducted in the same geometry, which was shown in Figure 5.45. The resulting steady state solution for an inlet temperature of $750\,°C$ with an inlet velocity of $0.2\,m/s$, similar to the parameters used in the experiments and with an inlet mass fraction of O_2 of $1\,\%$ is shown in Figure 5.53.

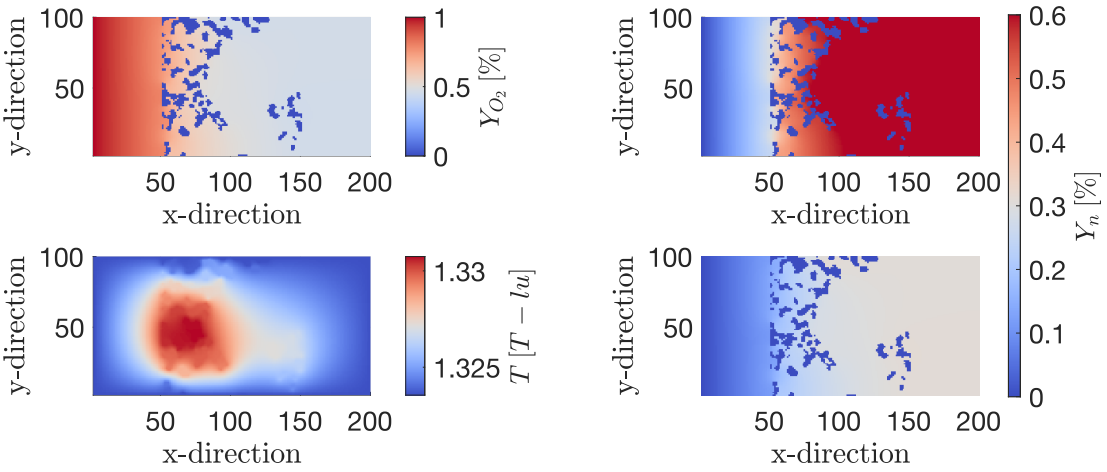

Figure 5.53: Steady state solution of the mass fraction of oxygen (top left), CO (top right), temperature (bottom left) and CO_2 (bottom right) for an inlet temperature of $750\,°C$ and $Y_{O_2,in} = 1\%$.

On the left, the mass fraction of the educt O_2 and the temperature in lattice units, are shown. On the right, the mass fractions of CO and CO_2 are shown on the top and bottom, respectively. A slight temperature increase can be observed in the centre of the domain, equating to approximately $4\,°C$. The temperature profile reaches a steady state when the reaction heat, produced by the combustion reaction, and the heat flux through the boundaries, which are kept at a constant temperature, are equivalent. With this steady state temperature profile, the combustion consumes approximately half of the oxygen, which is provided to the computational domain at the inlet. Furthermore, it can be observed that around 80 % of the total consumed oxygen is consumed by the partial reaction forming CO, as seen on the right. Further simulations are performed for inlet temperatures between $600\,°C$ and $750\,°C$ in accordance with the experimental investigation. The resulting mass fractions of CO and CO_2 at the outlet are converted to molar fractions for comparison with the measurements of the mass spectrometer. The resulting molar fraction of CO, with reference to the total molarity of CO and CO_2, is shown in Figure 5.54. Since the activation energy of the partial oxidation reaction of carbon is higher than the activation energy for the full oxidation to CO_2, it is expected that the molar fraction of CO increases for increasing temperatures [32]. This behaviour is reproduced by both the experimental data, shown in red and the results of the simulation, shown in blue. At $600\,°C$, the combustion experiment shows a molar $CO/(CO+CO_2)$ ratio of 63 %, with the LBM simulation resulting in 61.6 %. The difference between the experimental data and the LBM simulations remains mostly constant with deviations between $2-4\,\%pt$. At $750\,°C$, the LBM and experimental data result in 80.14 % and 81.5 %, respectively.

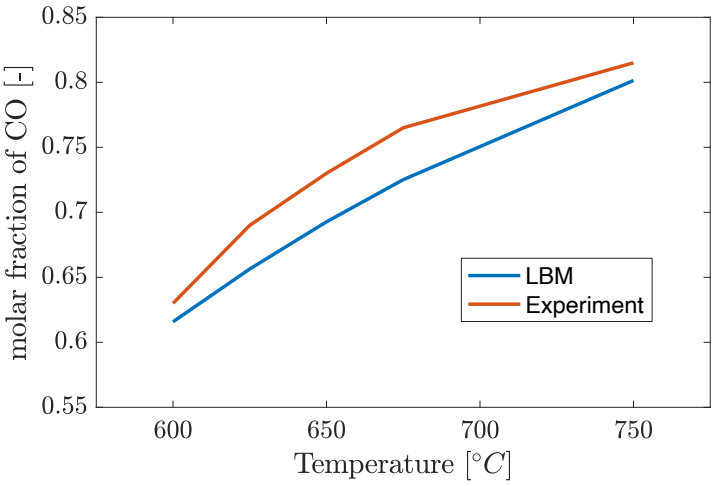

Figure 5.54: Molar fraction of CO with respect to the molarity of CO and CO_2

Moreover, it is mentioned that both reaction rates, for reaction (5.5) and (5.6), were observed to be miniscule. The reaction kinetics, using an Arrhenius type equation, is

characterized by a pre-exponential factor and an activation energy. The activation energies, which were obtained by evaluating the results of the experimental work done at ICVT, are in good accordance with literature data [130]. However, the determination of the values of the pre-exponential factors bears great potential for errors. The procedure for determining the parameters of the kinetics were described in section 4.5, specifically in equation 4.54. When calculating the reaction rate, the total mass balance of the reactor is divided by the surface concentration of oxygen. This value cannot be obtained in the experiments. For this reason, the bulk concentration of oxygen is used. This assumption differs greatly from the real surface concentration for significant reaction rates. Consequently, assuming a surface concentration value too large by multiple orders of magnitude results in a deviation of the same order of magnitude of the pre-exponential factor. However, this error results only in an offset in the Arrhenius-plot while not affecting its slope. Thus, the values of the activation energy remain valid, with the pre-exponential factor being too small compared to literature data [143]. Moreover, since the values of the activation energies remain valid, the ratio of CO/CO_2 is not affected. Consequently, for the simulation shown in Figure 5.53, the pre-exponential factor of the CO_2 reaction was chosen based on literature values and the pre-exponential factor of the CO reaction was calculated based on the ratio of the pre-exponential factors, as determined by the evaluation of the experimental data.
Summarizing this chapter, it was found, that the nanoscale combustion on the primary particle scale is responsible for the drastic increase of the specific surface, making extensive simulations on the mesoscopic scale, which is resolved by the FIB-SEM, obsolete, since the scale, which influences the evolution of the specific surface and thus the reaction, can not be resolved. For this reason, a separate nanoscale model for the purpose of designing the primary particles was created. With this model, the heterogeneity of the primary particles, their heterogeneous reactivity and the resulting increase in specific surface, will be described. Furthermore, simulations with CO and CO_2 as products were conducted at different temperatures and their ratio in the outlet gas stream was compared to experimental results, for which a good congruence was found.

5.5 Primary particle design - scale coupling

As elaborated in the previous chapter, it is not possible to recreate the increase in specific surface over the combustion progress, which is measured by the experimental group at the ICVT in Stuttgart, by assuming a homogeneous soot structure on the primary particle scale. It was shown through TEM analyis and Raman spectroscopy of soot samples before and after combustion experiments, that:

- Primary particles exhibit an inhomogeneous structure.
- Combustion happens on primary particle scale.
- Inner surface generated on primary particle scale influences combustion.

In order to study the effect of the microscopic morphology of the primary particles of the soot onto the combustion, two separate steps are necessary. First, the structure of the primary particles and their influence on the evolution of the specific surface needs to be studied. For this purpose, an algorithm for the generation of homogeneous as well as heterogeneous particles with random cavities was developed in MATLAB. Furthermore, the MATLAB code can progressively remove outer lattice nodes of the soot particle, emulating a combustion reaction limited by the educt mass transport. This study provides us with a function, which assigns an internal surface to a primary particle at different combustion progresses. Here, combustion progress refers to the combustion progress of one single primary particle rather than the global combustion progress of the mesoscopic structure. Furthermore, with this function received, the LBM code has to be coupled to the primary particle scale. For this purpose, a new flag index is implemented, treating partially burned pixels and allocating their internal surface.
In a first instance, the evolution of the specific surface shown in Figure 5.49, which was received from the experimental data, is used to calculate a function for the evolution. For this purpose, a polynomial of second order is applied, resulting in the following expression of the specific surface A_{BET} as a function of the combustion progress χ:

$$A_{BET} = -0.1476\chi^2 + 21.8439\chi + 77.1807 \tag{5.7}$$

This expression for the specific surface change of a primary particle is received from the evaluation of the change of specific surface of the global soot structure. It is used in a first instance to evaluate if the LBM code is able to reproduce such an evolution if the primary particles exhibit an inner surface. In a next step, the expression in equation (5.7) is substituted based on the consumption simulations of primary particles. The LBM code then performs the combustion simulation, with the difference that particles, which exhibit a combustion progress of 80 %, are switched to the newly added flag index, indicating that their amorphous part has been consumed, leaving behind the graphitic skeleton. A 2D combustion simulation is performed, using the FIB-SEM geometry, which was shown in Figure 5.45. Since the inlet temperature and mass fraction of oxygen don't influence the evolution of the specific surface, as shown in the previous chapter, sufficiently high values are chosen to guarantee a swift consumption of the soot. This results in the inlet values of $T_{in} = 1.5\,[T-lu]$ and $Y_{O_2,in} = 0.22$ being chosen. The evolution of the specific

surface, when using equation (5.7) as a factor to model the inner surface of partially burned particles, is shown in Figure 5.55.

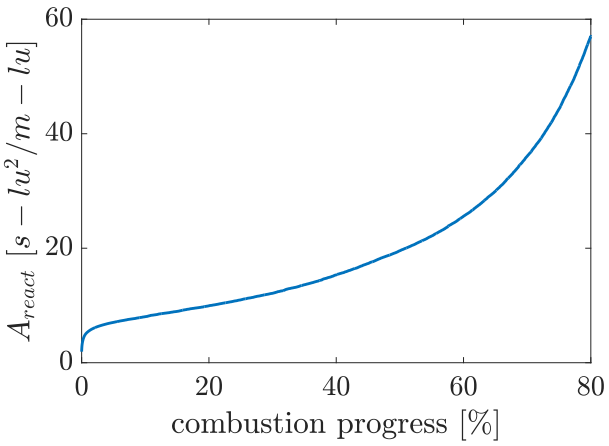

Figure 5.55: Evolution of the specific surface of the mesoscopic soot structure with progressing combustion, accounting for the inner surface of primary particles.

As it is shown, the mass specific surface, including the inner surface of the primary particles, which is estimated based on its outer surface and the relation, which was shown in equation (5.7), increases exponentially with progressing combustion. A steep increase is observed initially, which then exhibits an asymptotic behaviour and finally follows the exponential evolution towards the end of the combustion. The increase is steeper compared to the shrinking core model, however, this model is not capable of reproducing the experimental data. For this reason, the structure of primary particles and their influence onto the surface evolution is studied in the following.

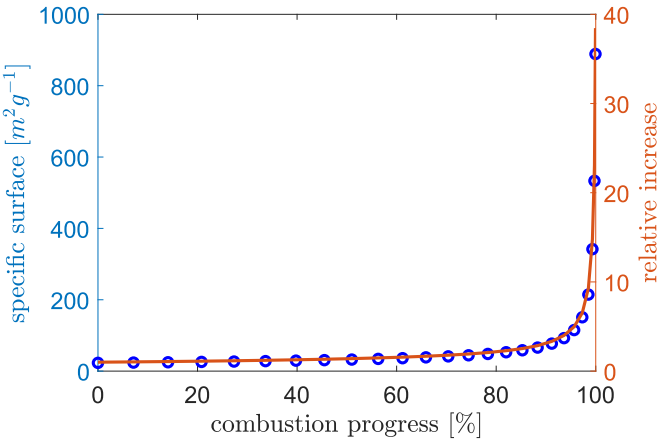

Figure 5.56: Course of the specific surface over the combustion progress for consumption of a homogeneous soot particle, conducted by the Matlab consumption algorithm.

For this purpose, the previously mentioned MATLAB code is used and layered primary particles with random cavities, are generated. The MATLAB code can generate random particles and perform the combustion reaction multiple times consecutively and calculate

the average surface increase as well as the standard deviation, and display the results graphically. Thus, the code allows for the study of different primary particles, with different numbers and sizes of cavities, different layer thicknesses and outer shells. In a first instance, the consumption of a homogeneous soot particle, calculated with said MATLAB code, is studied. As expected, this results in the following course of the specific surface, as shown in Figure 5.56, which follows the "shrinking core" model. The model exhibits a slow increase of the specific surface up to a combustion progress of around 90 %, when the soot mass reaches zero, thus leading to the relative surface approaching infinity. Subsequently, the consumption of heterogeneous particles is studied. With the code, particles resembling the core-shell structure, which was discussed in the previous chapter, can be created. Moreover, the different reactivities attributed to amorphous and crystalline soot are mimicked by assigning parts of the particle as being inert. With these boundaries, layered particles including randomly distributed cavities can be created. The size of these cavities varies according to a Gaussian distribution function, with the average size being specified in the code. One example of the generated geometry is shown in Figure 5.57. Initially, a layered particle without cavities or other additional heterogeneities is studied. A domain size of 200 × 200 pixels is chosen, with a particle radius of 50 pixels, consisting of 10 layers.

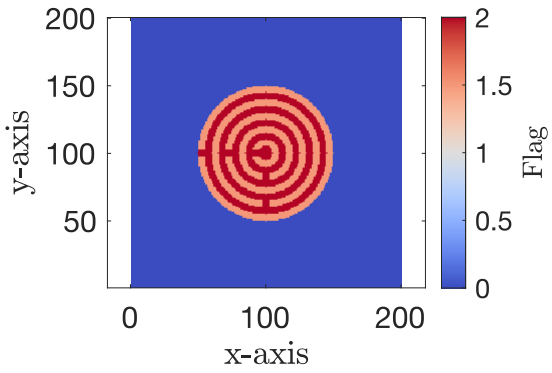

Figure 5.57: Example of a randomly generated heterogeneous domain with reactive soot (red), inert solid (orange).

With these constraints, the consumption of this particle would results in the orange skeleton to remain, leading to a drastic increase in specific surface. The resulting surface evolution is shown in Figure 5.58. Furthermore, the influence of cavities in the primary particles is studied. A similar particle is set up, with the addition of randomly distributed cavities. The radius, number and thickness of the layers is kept constant. Since randomly distributed cavities are used, the generation and consumption is performed ten times and the average surface increase and the standard deviation are calculated. The results are shown in Figure 5.59, with the course of the specific surface for each run (in total 5 runs)

being shown on the left and the averaged increase of the surface being shown on the right.

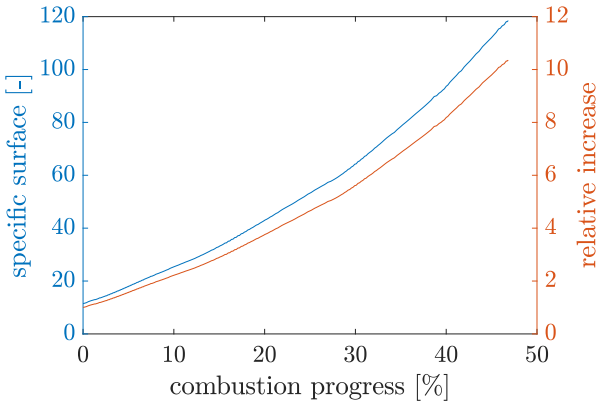

Figure 5.58: Absolute and relative increase of the specific surface of a layered particle.

It can be seen that the addition of cavities in the primary particles leads to a large spread in the evolution of the inner surface. This results from the design of the particles in inert and reactive layers and the fact that a consumption algorithm is used, which removes the outer accessible layer of reactive soot. Random cavities can lead to a bypass of inert layers, thus an altered combustion behaviour. Furthermore, primary particles, resembling the already described core-shell structure, were created.

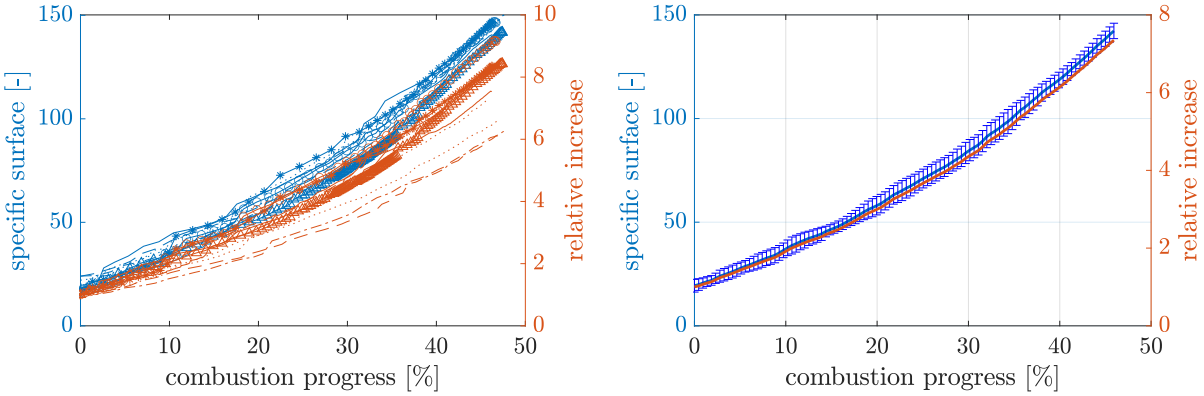

Figure 5.59: Absolute and relative increase of the specific surface for each simulation run (left) as well as average values with markers for the standard deviation (right) for a layered particle with random cavities.

The domain size was kept at 200 × 200 pixels, with an outer particle radius of 50 pixels, and a radius of the homogeneous core of 25 pixels. The results of the consumption simulation are shown in Figure 5.60. The specific surface initially follows the shrinking core model, meaning that only small increases are shown for a combustion progresses until approximately 30 % consumption. Here, the homogeneous core starts to be consumed, resulting in a steep rise of the specific reactive surface. Concluding, it was shown that the course of the mesoscopic evolution of the specific surface with progressing combustion,

when used to describe the inner surface of the primary particles, is not sufficient to reproduce the experimental results. Furthermore, it was shown that the inner surface evolution of the primary particles can be altered based on the microscopic structure of the primary soot particles. However, this small study is only of academic nature.

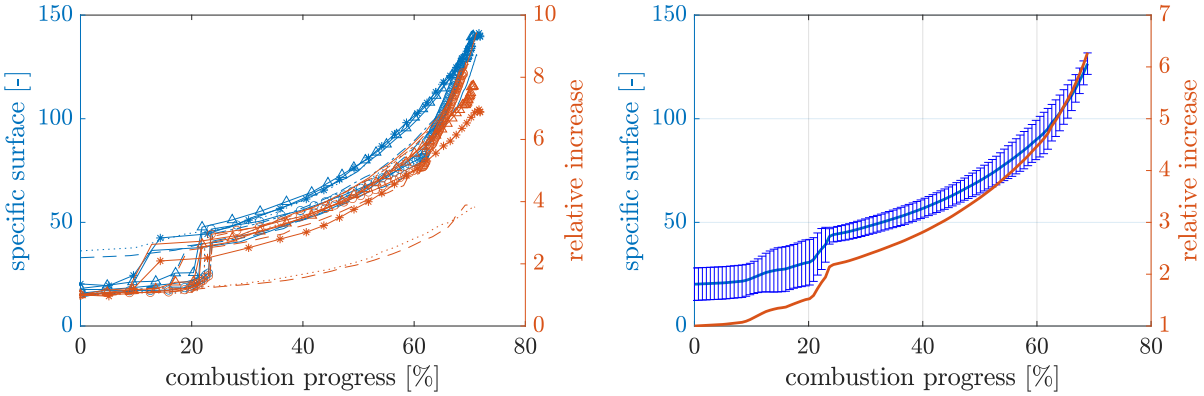

Figure 5.60: Absolute and relative increase of the specific surface for each simulation run (left) as well as average values with markers for the standard deviation (right) for a primary particle with layered shell and homogeneous core.

The primary particle design should be based on scientific data, for which an extensive data set of TEM pictures of soot samples at different combustion progresses would be necessary. Rigorously evaluating the TEM figures regarding fringe length, their distance and tortuosity could allow for a data-based recreation of the primary particle structure.

Chapter 6

Conclusions and Outlook

6.1 Conclusions

A LBM method was found, which was capable of simulating multi-component flow in porous media, while also incorporating conjugate heat transfer as well as heterogeneous reactions. O_2, CO and CO_2 were implemented as components of the gas phase. This method was used for a C++ in-house code, which was written during the work for this thesis. The code uses C++ standard library parallelization as well as a breath-first search algorithm for the calculation of the accessible reactive surface. The code was validated extensively with analytical solutions for the mass conservation of the flow field, for the energy conservation and conjugate heat transfer. Furthermore, a combustion test case found in the literature [143] was employed to validate the full combustion model. The code showed great capabilities to simulate accurate heterogeneous combustion in porous media.

Based on this combustion test case, the code was extended to account for the temporal evolution of the solid domain. Furthermore, the model was extended to 3D and additional symmetry and periodic boundary conditions were implemented to facilitate large-scale simulations with minimal computational effort. The additional boundary conditions and the 3D implementation were validated with the same rigor as the 2D model.

A combustion test case consisting of round, inert particles, coated with reactive soot, arranged in an ordered manner, was used to analyze combustion regimes and the propagation of a combustion front. For this purpose, a parametric study was conduced by variation of the Péclet number, Damköhler number, inlet mass fraction of oxygen and the thickness of the reactive soot layer. The model was extended by a second combustion product, namely carbon monoxide. Reaction kinetics obtained from the

experimental results of ICVT were implemented and combustion simulations at different temperatures were conducted. The resulting product ratio CO/CO_2 was compared with the experimental data and a very good congruence was found.
Furthermore, simulations in 2D and 3D using realistic soot structures, obtained by FIB-SEM imaging of soot samples provided by our project partners at ICVT, were conducted. The main parameter of interest was the evolution of the specific surface, which was compared with the experimental results of the PhD candidate at the partner university. Combustion simulations and experiments were conducted with varying inlet temperature and mass fraction of oxygen. The evolution of the specific surface with progressing combustion obtained from combustion experiments showed a drastic increase. This finding could not be reproduced by the LBM simulations.
It was shown by utilizing transmission electron microscopy and Raman spectroscopy that the combustion occurs on the primary particle scale. This suggests that the heterogeneous consumption of the primary particles is responsible for the large increase in specific surface, rather than the change of the mesoscopic morphology. Unfortunately, the Helmholtz Zentrum in Berlin and the institute of material science in Stuttgart faced difficulties in FIB-SEM analysis of the soot structure. For this reason, it was not possible to analyze and compare the evolution of the mesoscopic structure with the LBM simulations.
Furthermore, a small analysis of the primary particle consumption was conducted. For this purpose, a method was set-up to generate layered particle containing random cavities. Furthermore, a method to consume the particles progressively was added, enabling the determination of the evolution of the specific surface as an ensemble average. It was shown that heterogeneous particles with cavities could help in reproducing the drastic increase of the specific surface. Although, an extensive data set of TEM images of soot samples at different states of consumption would be necessary to thoroughly analyse the structure of the primary particles, enabling their accurate design and possibly the reproduction of the experimental results regarding the increase in BET surface.

6.2 Future works

Based on the findings presented in this dissertation, the work could be advanced in several different directions.

- A new LBM in-house code was generated by the author, able to simulate heterogeneous reactions in porous media. However, the code only used the parallelization routine inherent to the C++ standard library. This makes parallelization straight-

forward, yet limits the usage to all CPU cores of one node. This is not a restriction when running the code on a desktop PC. However, for utilizing more than one node on a high performance computer (HPC), MPI should be implemented into the code for parallelization. This would be necessary to simulate larger test cases with extended simulation times for realistic applications.

- Furthermore, it was shown that the combustion on the primary particle scale is responsible for the drastic increase in specific surface. The primary particle design presented here is just a method to show its effectiveness. However, it should be extended in future studies and be based on extensive TEM analysis of soot samples before and after combustion. The fringe length, fringe tortuosity and fringe distance should be parameters taken into account when designing the primary particles to model the evolution of the specific surface on the nano-scale.

- Furthermore, the LBM model could be expanded to account for the thermal expansion of the gas phase and additional components and chemical reactions for the oxidation with NO_2 should be added.

List of Figures

List of Tables

Appendix

A Code structure.

The code starts with reading in the parameters for the given test case as well as the corresponding geometry from data files. Then, the populations of the flow-field, the thermal field as well as of the component fields, respectively, are initialized. Subsequently, the geometry data is used to allocate each lattice node to a phase, and the outer boundary conditions are defined. Following this step, the code proceeds with the time progression loop. Inside, the code follows a defined procedure, depending on the phase, to which each lattice node belongs. For gaseous lattice nodes, the code imposes the external boundary conditions of the domain and subsequently performs the collision and streaming algorithm for the calculation of the flow field. Then, the boundary conditions of the scalar fields, i.e. the temperature and component fields, are imposed. Following this step, the collision and streaming step of the component fields are executed. In this step, the surface mass fractions of the educt are calculated, which are necessary for the calculation of the reactive heat release inside of the collision step of the thermal field. Then, the collision and streaming step for the temperature field are executed and the correct reactive heat release is inserted.

For lattice nodes allocated to the solid phase, the calculation of the flow field and component fields are omitted, since the solid domain is assumed to be impenetrable. For this reason, the code only proceeds to impose the temperature boundary condition, inserts the reaction heat and proceeds with the calculation of the collision and streaming step of the temperature field.

After the code performed the collision and streaming steps for the whole domain, the solid structure is updated, and fully consumed soot lattice nodes are converted to the gas phase.

Algorithm 3 Combustion Simulation

```
1: procedure COMBUSTION SIMULATION
2:     Initialization Phase:
3:     Read Parameters from Data-file
4:     Read Geometry file
5:     Initialize distribution functions flow-field
6:     Initialize distribution functions thermal field
7:     Initialize distribution functions component fields
8:
9:     Initialise Domain:
10:    Call SetGeometry
11:    Call SetBoundaryConditions(flow-field, thermal-field, component-fields)
12:
13:    Simulation Loop:
14:
15:    while not ReachedMaxTime do
16:
17:        Gas-Phase Calculations:
18:        if phase == "gas-phase" then
19:            Execute Collide and Stream Functions for Flow-Field:
20:            Call BoundaryCondition(flow-field)
21:            Call CollideAndStream(flow-field)
22:
23:            Calculate Scalar Fields:
24:            Call BoundaryCondition(thermal-field, component-fields)
25:            Call CollideAndStream(component-fields)
26:            Call CalculateSurfaceMassFraction(component-fields)
27:            Call CollideAndStream(thermal-field)
28:        end if
29:
30:        Solid-Phase Calculations:
31:        if phase == "solid soot" then
32:            Calculate Temperature Field for Solid Phase:
33:            Call InsertReactionHeat()
34:            Call CalculateTemperatureField(thermal-field)
35:            Call ConjugateHeatTransfer()
36:            Call CollideAndStream(thermal-field)
37:        end if
38:
39:        Update solid structure
40:
41:    end while
42: end procedure
```

B Transformation from SI units to Lattice units

As mentioned previously in Chapter 3.1.2, simulations utilizing the lattice Boltzmann method are commonly performed in lattice units, meaning that a transformation from SI-units to lattice units is necessary. Here, the Buckingham π-Theorem [12] is used to identify the independent characteristic dimensionless parameters, which are relevant for the description of multi-component flow with heterogeneous reactions. Then, the transformation of all parameters included in the system of equations given in the equations (3.84)-(3.86) into a dimensionless form in analogy to [114] and [26], is performed.
Fundamentally, the conversion between unit systems, in the given case between the SI-unit and the non-dimensional lattice-unit system, is nothing else but a mere scaling operation, relating each parameter to a reference value in a consistent manner. However, intrinsic restrictions of the lattice Boltzmann method have to be considered when choosing the reference values, since accuracy, stability and efficiency of the simulation have to be taken into account [67]. Fundamentally, a set of physical base quantities exists for any simulation. When considering fluid flow, consisting of different components, while also taking into account the temperature field, the following physical base quantities of [m], [s], [kg], [mol] and [K] can be identified. These stand for the length scale, the time scale, the weight scale, the molar amount of a substance and for the thermodynamic temperature. Conversion factors for these five base quantities for the transition from SI-units to lattice units have to be defined. With these conversion factors acquired, the conversion of any physical quantity is possible. For the comparison of simulations with different parameters, dimensionless characteristic parameters are commonly used. For the model at hand, these comprise the Péclet-number Pe, the Prandtl-number Pr, the Lewis-number for both the gas- and solid phase Le_g and Le_s, the Damköhler-number Da and the Reynolds-number Re, which are defined in equation (1):

$$\mathrm{Pe} = \frac{u\xi}{D_{\mathrm{O_2}}}, \quad \mathrm{Pr} = \frac{\nu}{\alpha_g}, \quad \mathrm{Le}_g = \frac{\alpha_g}{D_{\mathrm{O_2}}}, \quad \mathrm{Le}_s = \frac{\alpha_s}{D_{\mathrm{O_2}}}, \quad \mathrm{Da} = \frac{k\xi}{D_{\mathrm{O_2}}}, \quad \mathrm{Re} = \frac{\rho u}{\nu} \tag{1}$$

The basis for the conversion is the set of given characteristic numbers and specifications of the reaction, as shown in Table B.1. Exemplary, the values of [143] are used. The value of the Reynolds number is not specified as it would be redundant, with both Pe and Pr being given. Furthermore, values for the kinetic parameters of the reaction need to be specified. They depend on the reaction present and the specific kinetic model which is used. Here, literature values are used, but later on, values obtained by experimental work conducted at ICVT in Stuttgart will be utilized. Such a parameter set is sufficient to determine all other parameters of the simulation consistently.

Table B.1: Initial set of parameters for the validation case.

Parameter	**Symbol**	**Value**	**Unit**
Characteristic numbers			
Péclet number	Pe	0.01	-
Prandtl number	Pr	0.716	-
Lewis number (gas phase)	Le_g	1.49	-
Lewis number (solid phase)	Le_s	0.177	-
Damköhler number	Da	0.03525	-
Reaction kinetics			
Activation energy	E_a	131.09	kJ/mol
Pre-exponential factor	A_0	9.717×10^6	m/s
Standard enthalpy of reaction	Δh_r	431.303	kJ/mol
Reference Temperature	T_{ref}	773	K
Ratios of physical properties			
Ratio of density	$\kappa_1 = \rho_s/\rho_g$	556.694	-
Ratio of specific heat capacities	$\kappa_2 = c_{p,s}/c_{p,g}$	0.661	-
Ratio of thermal diffusivities	$\kappa_3 = \alpha_s/\alpha_g$	0.119	-
Ratio of diffusion coefficients	$\kappa_4 = D_{\mathrm{CO_2}}/D_{\mathrm{O_2}}$	0.909	-
Inlet parameters			
Mass fraction oxygen	$Y_{\mathrm{O_2}}$	0.22	-
Mass fraction carbon dioxide	$Y_{\mathrm{CO_2}}$	0.0	-
Temperature	T_{in}	773	K
Physical properties			
Specific heat capacity gas	$c_{p,g}$	1.096	kJ/(kg K)
Density gas	ρ_g	4.5	kg/m^3
Thermal diffusivity gas	α_g	1.14×10^{-5}	m^2/s
Molecular weight oxygen	$M_{\mathrm{O_2}}$	32	g/mol
Molecular weight Carbon dioxide	$M_{\mathrm{CO_2}}$	44	g/mol

In a first step, the remaining chemical properties, namely the density, the specific heat capacity and the thermal diffusivity of the solid phase can be calculated, as shown in equation (2):

$$\rho_s = \rho_g \cdot \kappa_1 \quad = 2505.123 \text{ kg/m}^3 \tag{2}$$

$$c_{p,s} = c_{p,g} \cdot \kappa_2 = 0.724456 \text{ kJ/(kg K)} \tag{3}$$

$$\alpha_s = \alpha_g \cdot \kappa_3 \quad = 1.357 \times 10^{-6} \text{ m}^2/\text{s} \tag{4}$$

By utilizing the Prandtl-number, the dynamic viscosity of the gas can be calculated, as given in equation (5):

$$\mu_g = \mathrm{Pr} \cdot \alpha_g \cdot \rho_g = 0.716 \times 1.14 \times 10^{-5} \times 4.5 = 3.673 \text{ Pa s} \tag{5}$$

Furthermore, the mass diffusivity of oxygen is calculated based on the Lewis-number, as depicted in equation (6):

$$D_{O2} = \frac{\alpha_g}{\mathrm{Le}_g} = \frac{1.14 \times 10^{-5}}{1.49} = 7.651 \times 10^{-6}\ \mathrm{m}^2/\mathrm{s} \tag{6}$$

By utilising the given ratio κ_4, the diffusion coefficient of carbon dioxide can be calculated:

$$D_{CO2} = \kappa_4 \cdot D_{O2} = 0.909 \cdot 7.651 \times 10^{-6} = 6.955 \times 10^{-6}\ \mathrm{m}^2/\mathrm{s} \tag{7}$$

Then, the Damköhler-number can be used to calculate the characteristic length scale of the problem, with the rate constant of the chemical reaction k also given as in equation (8):

$$k = A_0 \cdot e^{-\frac{E_a}{R \cdot T}} = 1.346 \times 10^{-2}\,\mathrm{m/s} \quad \text{and} \quad \xi = \frac{Da \cdot D_{O2}}{k} = 20.04\ \mu\mathrm{m} \tag{8}$$

Now, the average velocity at the inlet $\bar{u}_{x,\mathrm{inlet}}$ can be calculated based on the Péclet-number according to:

$$\bar{u}_{x,\mathrm{inlet}} = \frac{\mathrm{Pe} \cdot D_{O2}}{\xi} = 3.818 \times 10^{-3}\,\mathrm{m/s} \tag{9}$$

Then, by utilizing the specific length scale ξ, the resolution can be defined. Exemplary, the given characteristic length is assumed to have a resolution of 20 lattice-nodes, resulting in the lattice spacing in SI-units Δx_{SI} to be given as:

$$\Delta x_{\mathrm{SI}} = \frac{\xi}{20} = 1.002\,\mu\mathrm{m} \tag{10}$$

Following equation (11), the time step size Δt_{SI} can be determined:

$$\Delta t_{\mathrm{SI}} = c_s^2 \cdot (\tau_f - 0.5) \cdot \Delta x_{\mathrm{SI}}^2 / \nu = 2.05 \times 10^{-8}\,\mathrm{s} \tag{11}$$

Here, the value of the kinematic viscosity ν was calculated based on the dynamic viscosity and the density of the gas, which resulted in $\nu = 8.162 \times 10^{-6} m^2/s$ and the relaxation time for the fluid flow τ_f was chosen as 1.0, according to [143]. The transformation from SI-units to lattice-units will be described subsequently, now that a full set of all necessary parameters for the description of a flow, consisting of multiple components with interaction with a solid phase and heterogeneous reaction at its interface, in SI-units is given. As mentioned previously, conversion factors need to be introduced for the physical base quantities of [m], [s], [K], [mol] and [kg]. In current scientific literature, lattice-unit parameters are often referred to simply as "variable x in lattice units," potentially causing confusion due to the generic use of lattice units across various physical base quantities.

To address this, we propose a specific set of lattice units. For instance, [s-lu] (spatial lattice unit) combines the SI symbol for space [s] with the lattice unit abbreviation [lu]. Similarly, [t-lu] is introduced for time, [T-lu] for thermodynamic temperature, [m-lu] for mass, and [mol-lu] for chemical amount. This naming convention aims to enhance clarity in discussions involving lattice-based parameterization. Fundamentally, the choice of conversion factors is arbitrary. However, as mentioned in section 3.1.2, certain conventions are common, involving the choice of the time step Δt and the size of one lattice Δx, which are both chosen as 1.0 in the respective lattice units. This leads to the definition of the conversion factors for the temporal scale C_t and spatial scale C_s as shown in equation (12):

$$C_t = \frac{\Delta t}{\Delta t_{\mathrm{SI}}} = 48771706.22\,\mathrm{t\text{-}lu/s} \quad C_s = \frac{\Delta x}{\Delta x_{\mathrm{SI}}} = 1.00 \times 10^6\,\mathrm{s\text{-}lu/m} \tag{12}$$

Furthermore, the conversion factor for the temperature is chosen based on the reference temperature, which is set to 1.0 in lattice units, and defined in SI-units according to Table B.1 as:

$$C_T = \frac{T_{\mathrm{ref,lu}}}{T_{\mathrm{ref}}} = \frac{1}{773}\,\mathrm{T\text{-}lu/K} \tag{13}$$

The conversion factor for the mass is calculated based on the density in lattice units, which is set to 1.0, according to equation (14):

$$C_m = \frac{\rho_{\mathrm{lu}}}{\rho_g} \cdot C_s^3 = 2.\overline{22} \times 10^{17}\,\mathrm{m\text{-}lu/kg} \tag{14}$$

Finally, the conversion factor for the chemical amount has to be chosen. It is arbitrary and follows no convention, thus being chosen by the reference of $M_{O2,lu} = 32\frac{m-lu}{mol-lu}$, resulting in the conversion factor as:

$$C_{mol} = \frac{M_{O2}}{M_{O2,lu}} \cdot \frac{C_m}{1000\,\mathrm{g/kg}} = 2.\overline{22} \times 10^{14}\,\mathrm{mol\text{-}lu/mol} \tag{15}$$

Using these conversion factors, all simulation parameters and physical properties can be converted from SI-units to their respective lattice-units. The full set of parameters in lattice-units, and for better comprehension again in SI-units, is given in Table B.2: The parameters shown in Table B.2 are subsequently used for all simulations regarding the validation of the model, which is conducted in Chapter 5.1.

Table B.2: Full set of parameters in SI-units and in lu.

Parameter	**Symbol**	**Value (SI)**	**Value (lu)**
Reaction kinetics			
Activation energy	E_a	131.09 kJ/mol	5.511×10^4
Preexponential factor	A_0	9.717×10^6 m/s	1.9923×10^5
Standard enthalpy of reaction	Δh_r	431.303 kJ/mol	1.813×10^5
Reference Temperature	T_{ref}	773 K	1.0
Inlet parameters			
Mass fraction oxygen	Y_{O2}	0.22	0.22
Mass fraction carbon dioxide	Y_{CO2}	0.0	0.0
Inlet temperature	T_{in}	773 K	1.0
Inlet velocity x-direction	u_{in}	3.818×10^{-3} m/s	7.827×10^{-5}
Inlet density	ρ_{in}	4.5 kg/m^3	1.0
Physical properties			
Ideal gas constant	R	8.314 J/(mol K)	2701.802603
Dynamic viscosity gas	μ_g	3.673×10^{-5} Pa s	0.167359328
Kinematic viscosity gas	ν_g	8.162×10^{-6} m^2/s	0.167359328
Specific heat capacity gas	$c_{p,g}$	1.096 kJ/(kg K)	356.1673867
Density gas	ρ_g	4.5 kg/m^3	1.0
Thermal diffusivity gas	α_g	1.14×10^{-5} m^2/s	0.233742079
Specific heat capacity solid	$c_{p,s}$	0.724456 kJ/(kg K)	235.4266426
Density solid	ρ_s	2505.123 kg/m^3	556.694
Thermal diffusivity solid	α_s	1.357×10^{-6} m^2/s	0.027815307
Molecular weight oxygen	M_{O2}	32 g/mol	32
Molecular weight Carbon dioxide	M_{CO2}	44 g/mol	44
Diffusion coefficient O2	D_{O2}	7.651×10^{-6} m^2/s	0.156873878
Diffusion coefficient CO2	D_{CO2}	6.955×10^{-6} m^2/s	0.142598355

Bibliography

[1] J. Adler. Ceramic diesel particulate filters. International Journal of Applied Ceramic Technology, 2(6):429–439, 2005. (Cited on pages 8 & 10).

[2] C. K. Aidun and J. R. Clausen. Lattice-boltzmann method for complex flows. Annual Review of Fluid Mechanics, 42:439–472, 2010. (Cited on page 13).

[3] M. Alfè, B. Apicella, R. Barbella, J. N. Rouzaud, A. Tregrossi, and A. Ciajolo. Structure-property relationship in nanostructures of young and mature soot in premixed flames. Proceedings of the Combustion Institute, 32 I(1):697–704, 2009. (Cited on pages 21 & 117).

[4] B. Apicella, A. Ciajolo, A. Tregrossi, J. Abrahamson, R. L. Vander Wal, and C. Russo. HRTEM and EELS investigations of flame-formed soot nanostructure. Fuel, 225(February):218–224, 2018. (Cited on page 21).

[5] S. Basu, M. Henrichsen, P. Tandon, S. He, and A. Heibel. Filtration efficiency and pressure drop performance of ceramic partial wall flow diesel particulate filters. International Journal of Fuels and Lubricants, 6:877–893, 2013. (Cited on page 12).

[6] Y. Bazilevs, M. Hsu, J. Kiendl, R. Wüchner, and K. Bletzinger. 3D Simulation of Wind Turbine Rotors at Full Scale. Part II: Fluid – Structure Interaction Modeling with Composite Blades. International Journal for Numerical Methods in Fluids, 65(October 2010):236–253, 2011. (Cited on page 13).

[7] P. L. Bhatnagar, E. P. Gross, and M. Krook. A model for collision processes in gases. I. Small amplitude processes in charged and neutral one-component systems. Physical Review, 94(3):511–525, 1954. (Cited on pages 13 & 25).

[8] E. J. Bissett. Mathematical model of the thermal regeneration of a wall-flow monolith diesel particulate filter. Chemical Engineering Science, 39(7):1233–1244, 1984. (Cited on page 11).

[9] E. J. Bissett. Thermal regeneration of particle filters with large conduction. Mathematical Modelling, 6(1):1–18, 1985. (Cited on page 11).

[10] M. L. Botero, D. Chen, S. González-Calera, D. Jefferson, and M. Kraft. HRTEM evaluation of soot particles produced by the non-premixed combustion of liquid fuels. Carbon, 96:459–473, 2016. (Cited on page 21).

[11] M. L. Botero, Y. Sheng, J. Akroyd, J. Martin, J. A. Dreyer, W. Yang, and M. Kraft. Internal structure of soot particles in a diffusion flame. Carbon, 141:635–642, 2019. (Cited on pages 21 & 117).

[12] E. Buckingham. On physically similar Systems, 1914. (Cited on page 145).

[13] C. Chang, Y. Chen, L. Sheng, and S.-S. Hsiau. A New Approach of Dedusting for IGCC by a Two-Stage Moving Granular Bed Filter. Energies, 14:2534, 2021. (Cited on pages 9 & 133).

[14] C. Chang, C. H. Liu, and C. A. Lin. Boundary conditions for lattice Boltzmann simulations with complex geometry flows. Computers and Mathematics with Applications, 58(5):940–949, 2009. (Cited on page 61).

[15] L. Chen, Q. Kang, Y. L. He, and W. Q. Tao. Pore-scale simulation of coupled multiple physicochemical thermal processes in micro reactor for hydrogen production using lattice Boltzmann method. International Journal of Hydrogen Energy, 37(19):13943–13957, 2012. (Cited on page 15).

[16] S. Chen, H. Chen, D. Martnez, and W. Matthaeus. Lattice Boltzmann model for simulation of magnetohydrodynamics. Physical Review Letters, 67(27):3776–3779, 1991. (Cited on page 13).

[17] T. Chen, Z. Wu, J. Gong, and E. Jia-qiang. Numerical simulation of diesel particulate filter regeneration considering ash deposit. Flow, Turbulence and Combustion, 97:849–864, 10 2016. (Cited on page 12).

[18] X. Chen and P. Han. A note on the solution of conjugate heat transfer problems using SIMPLE-like algorithms. International Journal of Heat and Fluid Flow, 21(4):463–467, 2000. (Cited on page 14).

[19] S. Chibbaro, G. Falcucci, G. Chiatti, H. Chen, X. Shan, and S. Succi. Lattice Boltzmann models for nonideal fluids with arrested phase-separation. Physical Review E - Statistical, Nonlinear, and Soft Matter Physics, 77(3), 2008. (Cited on page 13).

[20] S. S. Chikatamarla, S. Ansumali, and I. V. Karlin. Grad's approximation for missing data in lattice Boltzmann simulations. Europhysics Letters, 74(2):215–221, 2006. (Cited on page 15).

[21] D. S. Christen. Praxiswissen der chemischen Verfahrenstechnik. Springer, Berlin, Heidelberg, 2 edition, 2009. (Cited on pages 9 & 10).

[22] R. Cornubert, D. D'Humières, and D. Levermore. A Knudsen layer theory for lattice gases. Physica D: Nonlinear Phenomena, 47(1-2):241–259, 1991. (Cited on pages 27 & 54).

[23] A. Cuesta, P. Dhamelincourt, J. Laureyns, A. Martínez-Alonso, and J. M. Tascón. Raman microprobe studies on carbon materials. Carbon, 32(8):1523–1532, 1994. (Cited on page 19).

[24] E. L. Cussler. Diffusion Mass Transfer in Fluid Systems. Cambridge University Press, third edit edition, 2007. (Cited on page 99).

[25] S. S. Dang, A. Serafino, J. O. Müller, R. E. Jentoft, R. Schlögl, and S. Fiorito. Cytotoxicity and inflammatory potential of soot particles of low-emission diesel engines. Environmental Science and Technology, 42(5):1761–1765, mar 2008. (Cited on page 1).

[26] J. J. Derksen. Lecture 3. Practical aspects of lattice-Boltzmann simulations. Lecture Notes - PGR Course UAberdeen 2018, pages 1–10, 2018. (Cited on page 145).

[27] T. Deuschle and M. Piesche. Modellierung und simulation von filtrations-, regenerations- und umlagerungseffekten in gasfiltersystemen am beispiel eines dieselruß- partikelfilters. Chemie-Ingenieur-Technik, 82(12):2151–2160, dec 2010. (Cited on page 8).

[28] D. D'Humières, M. Bouzidi, and P. Lallemand. Thirteen-velocity three-dimensional lattice Boltzmann model. Physical Review E - Statistical, Nonlinear, and Soft Matter Physics, 63(6):1–7, 2001. (Cited on page 27).

[29] A. Dittler. The application of diesel particle filters—from past to present and beyond. Topics in Catalysis, 60:342–347, 3 2017. (Cited on page 1).

[30] R. Dong, Z. Zhang, Y. Ye, H. Huang, and C. Cao. Review of Particle Filters for Internal Combustion Engines. Processes, 10(5), 2022. (Cited on page 7).

[31] DPF, OWL. Reinigung und Regeneration von Dieselpartikelfiltern. https://dieselpartikelfilter-owl.de/dpf-reinigung. Accessed: 2024-01-07. (Cited on pages 2 & 133).

[32] Z. Du, A. F. Sarofim, J. P. Longwell, and L. Tognotti. The CO/CO2 Ratio in the Products of the Carbon-Oxygen Reaction. In Fundamental Issues in Control of Carbon Gasification Reactivity, pages 91–106. Springer Netherlands, 1991. (Cited on page 122).

[33] G. Falcucci, G. Bella, G. Chiatti, S. Chibbaro, M. Sbragaglia, and S. Succi. Lattice Boltzmann models with mid-range interactions. Communications in Computational Physics, 2(6):1071–1084, 2007. (Cited on page 13).

[34] E. Fattahi, C. Waluga, B. Wohlmuth, U. Rüde, M. Manhart, and R. Helmig. Lattice Boltzmann methods in porous media simulations: From laminar to turbulent flow. Computers and Fluids, 140:247–259, 2016. (Cited on page 3).

[35] S. Fischer, M. Krüger, U. Projahn, H. Lüders, and F. Dittrich. Abgasnachbehandlung, pages 206–254. Springer Fachmedien Wiesbaden, Wiesbaden, 2020. (Cited on pages 7, 8, 9, 10, 11 & 133).

[36] C. N. Fredd and H. S. Fogler. Influence of Transport and Reaction on Wormhole Formation in Porous Media. Fluid Mechanics and Transport Phenomena, 44(9):1933–1949, sep 1998. (Cited on page 14).

[37] U. Frisch, B. Hasslacher, and Y. Pomeau. Lattice-gas automata for the Navier-Stokes equation. Physical Review Letters, 56(14):1505–1508, 1986. (Cited on pages 12, 27 & 96).

[38] J. Fu, T. Zhang, M. Li, S. Li, X. Zhong, and X. Liu. Study on flow and heat transfer characteristics of porous media in engine particulate filters based on lattice Boltzmann method. Energies, 12(17), 2019. (Cited on page 12).

[39] I. Ginzburg, L. Roux, and G. Silva. Local boundary reflections in lattice Boltzmann schemes : Spurious boundary layers and their impact on the velocity , diffusion and dispersion. Comptes Rendus Mecanique, 343(10-11):518–532, 2015. (Cited on pages 56 & 96).

[40] H. Grad. On the kinetic theory of rarefied gases. Communications on Pure and Applied Mathematics, 2(4):331–407, dec 1949. (Cited on page 15).

[41] R. Greiner, T. Prill, O. Iliev, B. A. van Setten, and M. Votsmeier. Tomography based simulation of reactive flow at the micro-scale: Particulate filters with wall integrated catalyst. Chemical Engineering Journal, 378, 12 2019. (Cited on page 12).

[42] D. Grunau, S. Chen, and K. Eggert. A lattice Boltzmann model for multiphase fluid flows. Physics of Fluids A, 5(10):2557–2562, 1992. (Cited on page 14).

[43] A. K. Gunstensen, D. H. Rothman, S. Zaleski, and G. Zanetti. Lattice Boltzmann model of immiscible fluids. Physical Review A, 43(8):4320–4327, 1991. (Cited on page 14).

[44] Z. Guo, C. Zheng, and B. Shi. Discrete lattice effects on the forcing term in the lattice Boltzmann method. Physical Review E - Statistical Physics, Plasmas, Fluids, and Related Interdisciplinary Topics, 65(4):6, 2002. (Cited on page 44).

[45] D. Hänel. Molekulare Gasdynamik. 2004. (Cited on pages 26 & 27).

[46] J. Hardy, Y. Pomeau, and O. De Pazzis. Time evolution of a two-dimensional model system. I. Invariant states and time correlation functions. Journal of Mathematical Physics, 14(12):1746–1759, 1973. (Cited on pages 12, 26 & 54).

[47] X. He, S. Chen, and R. Zhang. A Lattice Boltzmann Scheme for Incompressible Multiphase Flow and Its Application in Simulation of Rayleigh-Taylor Instability. Journal of Computational Physics, 152(2):642–663, 1999. (Cited on page 14).

[48] X. He and L. S. Luo. Theory of the lattice Boltzmann method: From the Boltzmann equation to the lattice Boltzmann equation. Physical Review E - Statistical Physics, Plasmas, Fluids, and Related Interdisciplinary Topics, 55(6):6811–6820, 1997. (Cited on page 13).

[49] X. He, X. Shan, and G. D. Doolen. Discrete Boltzmann equation model for nonideal gases. Physical Review E - Statistical Physics, Plasmas, Fluids, and Related Interdisciplinary Topics, 57(1):R13–R16, 1998. (Cited on pages 13 & 14).

[50] F. J. Higuera and J. Jiménez. Boltzmann approach to lattice gas simulations. Epl, 9(7):663–668, 1989. (Cited on page 13).

[51] C. F. Ho, C. Chang, K. H. Lin, and C. A. Lin. Consistent boundary conditions for 2D and 3D lattice boltzmann simulations. CMES - Computer Modeling in Engineering and Sciences, 44(2):137–155, 2009. (Cited on pages 61 & 62).

[52] J. S. Howitt and M. R. Montierth. Cellular ceramic diesel particulate filter, 1981. (Cited on pages 8 & 11).

[53] H. Huang, M. Krafczyk, and X. Lu. Forcing term in single-phase and Shan-Chen-type multiphase lattice Boltzmann models. Physical Review E - Statistical, Nonlinear, and Soft Matter Physics, 84(4):1–15, 2011. (Cited on page 13).

[54] T. Inamuro, N. Konishi, and F. Ogino. Galilean invariant model of the lattice Boltzmann method for multiphase fluid flows using free-energy approach. Computer Physics Communications, 129(1):32–45, 2000. (Cited on page 14).

[55] F. Jacquot, V. Logie, J. F. Brilhac, and P. Gilot. Kinetics of the oxidation of carbon black by NO2 influence of the presence of water and oxygen. Carbon, 40(3):335–343, 2002. (Cited on page 11).

[56] K. Johansen. Multi-catalytic soot filtration in automotive and marine applications. Catalysis Today, 258:2–10, 5 2015. (Cited on page 1).

[57] Q. Kang, P. C. Lichtner, and D. Zhang. An improved lattice boltzmann model for multicomponent reactive transport in porous media at the pore scale. Water Resources Research, 43, 12 2007. (Cited on page 47).

[58] Q. Kang, D. Zhang, S. Chen, and X. He. Lattice Boltzmann simulation of chemical dissolution in porous media. Physical Review E - Statistical Physics, Plasmas, Fluids, and Related Interdisciplinary Topics, 65(3), 2002. (Cited on page 14).

[59] H. Karani and C. Huber. Lattice Boltzmann formulation for conjugate heat transfer in heterogeneous media. Physical Review E - Statistical, Nonlinear, and Soft Matter Physics, 91(2), 2015. (Cited on pages 15, 44, 46 & 89).

[60] J. Kitagawa, T. Hijikata, and S. Yamada. Electric heating regeneration of large wall-flow type DPF. In Proceedings - Society of Automotive Engineers, volume 100, pages 63–71, 1991. (Cited on page 11).

[61] M. Knauer, M. Carrara, D. Rothe, R. Niessner, and N. P. Ivleva. Changes in structure and reactivity of soot during oxidation and gasification by oxygen, studied by micro-Raman spectroscopy and temperature programmed oxidation. Aerosol Science and Technology, 43(1):1–8, 2009. (Cited on page 19).

[62] M. Knauer, M. E. Schuster, D. Sn, R. Schlögl, R. Niessner, and N. P. Ivleva. Soot structure and reactivity analysis by raman microspectroscopy, temperature-programmed oxidation, and high-resolution transmission electron microscopy.

Journal of Physical Chemistry A, 113(50):13871–13880, 2009. (Cited on pages 19, 21 & 120).

[63] J. M. V. A. Koelman. A simple lattice boltzmann scheme for navier-stokes fluid flow. Europhysics Letters, 15(6):603, jul 1991. (Cited on page 13).

[64] A. G. Konstandopoulos and M. Kostoglou. Reciprocating flow regeneration of soot filters. Combustion and Flame, 121(3):488–500, 2000. (Cited on page 11).

[65] A. G. Konstandopoulos, M. Kostoglou, E. Skaperdas, E. Papaioannou, D. Zarvalis, and E. Kladopoulou. Fundamental studies of diesel particulate filters: Transient loading, regeneration and aging. SAE Technical Papers, 109, 2000. (Cited on page 7).

[66] M. Kostoglou, P. Housiada, and A. G. Konstandopoulos. Multi-channel simulation of regeneration in honeycomb monolithic diesel particulate filters. Chemical Engineering Science, 58:3273–3283, 2003. (Cited on page 12).

[67] T. Kruger, H. Kusumaatmaja, A. Kuzmin, O. Shardt, S. Goncalo, and E. M. Viggen. The lattice boltzmann method, principles and practice. Springer International Publishing, 2017. (Cited on pages 26, 27, 31, 34, 35, 36, 38, 57, 58, 84 & 145).

[68] J. Kuba, J. Mitchels, M. Hovorka, P. Erdmann, L. Berka, R. Kirmse, J. König, J. De Bock, B. Goetze, and A. Rigort. Advanced cryo-tomography workflow developments – correlative microscopy, milling automation and cryo-lift-out. Journal of Microscopy, 281(2):112–124, 2021. (Cited on pages 16 & 133).

[69] A. J. Ladd. Numerical Simulations of Particulate Suspensions Via a Discretized Boltzmann Equation. Part 1. Theoretical Foundation. Journal of Fluid Mechanics, 271:285–309, 1994. (Cited on page 57).

[70] A. J. C. Ladd and R. Verberg. Lattice-Boltzmann Simulations of Particle-Fluid Suspensions. Journal of Statistical Physics, 104(September):1191–1251, 2001. (Cited on page 57).

[71] M. Lapuerta, F. Oliva, J. R. Agudelo, and J. P. Stitt. Optimization of Raman spectroscopy parameters for characterizing soot from different diesel fuels. Combustion Science and Technology, 183(11):1203–1220, 2011. (Cited on page 20).

[72] J. Lätt. Hydrodynamic limit of lattice Boltzmann equations. Science, 20(6):124, 2007. (Cited on page 27).

[73] J. Latt, C. Coreixas, and J. Beny. Cross-platform programming model for many-core lattice boltzmann simulations. PLOS ONE, 16(4):e0250306, Apr. 2021. (Cited on page 49).

[74] M. Latva-Kokko and D. H. Rothman. Diffusion properties of gradient-based lattice Boltzmann models of immiscible fluids. Physical Review E - Statistical, Nonlinear, and Soft Matter Physics, 71(5):1–8, 2005. (Cited on page 14).

[75] K. C. Le, T. Pino, V. T. Pham, J. Henriksson, S. Trk, and P. E. Bengtsson. Raman spectroscopy of mini-CAST soot with various fractions of organic compounds: Structural characterization during heating treatment from 25 °C to 1000 °C. Combustion and Flame, 209:291–302, 2019. (Cited on page 20).

[76] T. Lee and P. F. Fischer. Eliminating parasitic currents in the lattice Boltzmann equation method for nonideal gases. Physical Review E - Statistical, Nonlinear, and Soft Matter Physics, 74(4):1–7, 2006. (Cited on page 14).

[77] T. Lee and C. L. Lin. A stable discretization of the lattice Boltzmann equation for simulation of incompressible two-phase flows at high density ratio. Journal of Computational Physics, 206(1):16–47, 2005. (Cited on page 14).

[78] T. Lei, Z. Wang, and K. H. Luo. Study of pore-scale coke combustion in porous media using lattice Boltzmann method. Combustion and Flame, 225:104–119, 2021. (Cited on pages 16, 42, 47, 84, 88 & 136).

[79] C. Li, F. Mao, R. Zhan, and S. Eakle. Durability performance of advanced ceramic material DPFs. SAE Technical Papers, 2007(724), 2007. (Cited on page 2).

[80] L. Li, C. Chen, R. Mei, and J. F. Klausner. Conjugate heat and mass transfer in the lattice Boltzmann equation method. Physical Review E - Statistical, Nonlinear, and Soft Matter Physics, 89(4), apr 2014. (Cited on pages 15, 44, 45, 83, 89 & 92).

[81] S. V. Lishchuk, C. M. Care, and I. Halliday. Lattice Boltzmann algorithm for surface tension with greatly reduced microcurrents. Physical Review E - Statistical Physics, Plasmas, Fluids, and Related Interdisciplinary Topics, 67(3):5, 2003. (Cited on page 14).

[82] C. H. Liu, K. H. Lin, H. C. Mai, and C. A. Lin. Thermal boundary conditions for thermal lattice Boltzmann simulations. Computers and Mathematics with Applications, 59(7):2178–2193, 2010. (Cited on pages 62 & 63).

[83] Y. Liu, J. Xia, K. Wan, L. Vervisch, Z. Wang, H. Zhao, and K. Cen. Simulation of char-pellet combustion and sodium release inside porous char using lattice Boltzmann method. Combustion and Flame, 211:325–336, jan 2020. (Cited on page 16).

[84] J. H. Lu, H. Y. Lei, and C. S. Dai. A simple difference method for lattice Boltzmann algorithm to simulate conjugate heat transfer. International Journal of Heat and Mass Transfer, 114:268–276, 2017. (Cited on page 15).

[85] D. Lycett-Brown and K. H. Luo. Multiphase cascaded lattice Boltzmann method. Computers and Mathematics with Applications, 67(2):350–362, 2014. (Cited on page 13).

[86] A. A. Mailybaev, J. Bruining, and D. Marchesin. Analysis of in situ combustion of oil with pyrolysis and vaporization. Combustion and Flame, 158(6):1097–1108, 2011. (Cited on page 40).

[87] M. J. Mawson and A. J. Revell. Memory transfer optimization for a lattice Boltzmann solver on Kepler architecture nVidia GPUs. Computer Physics Communications, 185(10):2566–2574, 2014. (Cited on page 51).

[88] R. O. McClellan. Health effects of exposure to diesel exhaust particles. Annual Review of Pharmacology and Toxicology, Vol. 27:279–300, 1987. (Cited on page 1).

[89] M. E. McCracken and J. Abraham. Multiple-relaxation-time lattice-Boltzmann model for multiphase flow. Physical Review E - Statistical, Nonlinear, and Soft Matter Physics, 71(3), 2005. (Cited on page 14).

[90] G. R. McNamara and G. Zanetti. Use of the boltzmann equation to simulate lattice-gas automata. Physical Review Letters, 61(20):2332–2335, 1988. (Cited on page 13).

[91] F. Meng, M. Wang, and Z. Li. Lattice Boltzmann simulations of conjugate heat transfer in high-frequency oscillating flows. International Journal of Heat and Fluid Flow, 29(4):1203–1210, aug 2008. (Cited on pages 15 & 47).

[92] T. Mizutani, Y. Watanabe, K. Yuuki, S. Hashimoto, and T. Hamanaka. Soot Regeneration Model for SiC-DPF System Design Reprinted From : Diesel Exhaust Emission Control Modeling. SAE Technical 2004-01-0159, 2004. (Cited on page 12).

[93] A. Mohamad. Lattice Boltzmann Method. Number 5. Springer, London, second edi edition, 2010. (Cited on pages 25, 29 & 31).

[94] S. Mukherjee and J. Abraham. Crown behavior in drop impact on wet walls. Physics of Fluids, 19(5), 2007. (Cited on page 14).

[95] M. P. Orihuela, A. Gómez-Martín, P. Miceli, J. A. Becerra, R. Chacartegui, and D. Fino. Experimental measurement of the filtration efficiency and pressure drop of wall-flow diesel particulate filters (dpf) made of biomorphic silicon carbide using laboratory generated particles. Applied Thermal Engineering, 131:41–53, 2 2018. (Cited on page 8).

[96] V. Palma, P. Ciambelli, E. Meloni, and A. Sin. Catalytic dpf microwave assisted active regeneration. Fuel, 140:50–61, 1 2015. (Cited on page 11).

[97] A. B. Palotas, L. C. Rainey, C. J. Feldermann, A. F. Sarofim, and J. B. Vander Sande. Soot morphology: An application of image analysis in high-resolution transmission electron microscopy. Microscopy Research and Technique, 33(3):266–278, 1996. (Cited on pages 20 & 133).

[98] G. Pareschi, N. Frapolli, S. S. Chikatamarla, and I. V. Karlin. Conjugate heat transfer with the entropic lattice Boltzmann method. Physical Review E, 94(1):1–16, 2016. (Cited on page 15).

[99] J. K. Park, T. H. Nguyen, C. N. Kim, and S. Y. Lee. Simulation of flow in diesel particulate filter system using metal fiber filter media. International Journal of Automotive Technology, 15(3):361–367, 2014. (Cited on page 9).

[100] C. M. Pooley and K. Furtado. Eliminating spurious velocities in the free-energy lattice Boltzmann method. Physical Review E - Statistical, Nonlinear, and Soft Matter Physics, 77(4):1–8, 2008. (Cited on page 14).

[101] A. J. Pyzik and C. G. Li. New design of a ceramic filter for diesel emission control applications. International Journal of Applied Ceramic Technology, 2:440–451, 2005. (Cited on page 9).

[102] Y. H. Qian, D. D'Humières, and P. Lallemand. Lattice bgk models for navier-stokes equation. Europhysics Letters, 17(6):479, feb 1992. (Cited on pages 13 & 26).

[103] RAC. Diesel particulate filters: everything you need to know about DPFs. https://www.rac.co.uk/drive/advice/emissions/diesel-particulate-filters/. Accessed: 2024-01-07. (Cited on pages 8 & 133).

[104] A. Raiolo, C. Stockinger, U. Tuttlies, N. Ivleva, M. Safdari Shadloo, and U. Nieken. Effect of nanostructure and BET surface area on the oxygen reactivity of soot filter cakes. Carbon, –:–, Submitted. (Cited on pages 115, 116, 120 & 121).

[105] C. V. RAMAN and K. S. KRISHNAN. A New Type of Secondary Radiation. Nature, 121(3048):501–502, 1928. (Cited on page 18).

[106] Y. Ren, N. P. Freitag, and N. Mahinpey. A simple kinetic model for coke combustion during an in situ combustion (ISC) process. Journal of Canadian Petroleum Technology, 46(4):47–52, 2007. (Cited on page 99).

[107] Z. D. Ristovski, B. Miljevic, N. C. Surawski, L. Morawska, K. M. Fong, F. Goh, and I. A. Yang. Respiratory health effects of diesel particulate matter. Respirology, 17(2):201–212, 2012. (Cited on page 1).

[108] D. H. Rothman and J. M. Keller. Immiscible cellular-automaton fluids. Journal of Statistical Physics, 52(3-4):1119–1127, 1988. (Cited on page 14).

[109] R. Rubinstein and L. S. Luo. Theory of the lattice Boltzmann equation: Symmetry properties of discrete velocity sets. Physical Review E - Statistical, Nonlinear, and Soft Matter Physics, 77(3):1–11, 2008. (Cited on page 27).

[110] A. Sadezky, H. Muckenhuber, H. Grothe, R. Niessner, and U. Pöschl. Raman microspectroscopy of soot and related carbonaceous materials: Spectral analysis and structural information. Carbon, 43(8):1731–1742, 2005. (Cited on pages 19, 120 & 133).

[111] M. A. Safi and S. Turek. Rising bubble simulations using lattice Boltzmann method coupled with level set interface capturing. Pamm, 14(1):675–676, 2014. (Cited on page 13).

[112] V. D. Sarli and A. D. Benedetto. Modeling and simulation of soot combustion dynamics in a catalytic diesel particulate filter. Chemical Engineering Science, 137:69–78, 12 2015. (Cited on page 12).

[113] M. Sbragaglia, R. Benzi, L. Biferale, S. Succi, K. Sugiyama, and F. Toschi. Generalized lattice Boltzmann method with multirange pseudopotential. Physical Review E - Statistical, Nonlinear, and Soft Matter Physics, 75(2):1–13, 2007. (Cited on page 13).

[114] M. B. Schlaffer. Non-reflecting Boundary Conditions for the Lattice Boltzmann Method; Lehrstuhl für Computation in Engineering. page 216, 2013. (Cited on pages 25, 27 & 145).

[115] T. Schmid and P. Dariz. Raman microspectroscopic imaging of binder remnants in historical mortars reveals processing conditions. Heritage, 2(2):1662–1683, 2019. (Cited on pages 18 & 133).

[116] Seher S. Experimentelle Charakterisierung und Modellierung der Rußoxidation. PhD thesis, University of Stuttgart, 2017. (Cited on pages 3, 10, 112 & 133).

[117] H. J. Seong and A. L. Boehman. Evaluation of Raman parameters using visible Raman microscopy for soot oxidative reactivity. Energy and Fuels, 27(3):1613–1624, 2013. (Cited on page 20).

[118] J. R. Serrano, V. Bermúdez, P. Piqueras, and E. Angiolini. On the impact of DPF downsizing and cellular geometry on filtration efficiency in pre- and post-turbine placement. Journal of Aerosol Science, 113(August):20–35, 2017. (Cited on page 9).

[119] J. R. Serrano, H. Climent, P. Piqueras, and E. Angiolini. Filtration modelling in wall-flow particulate filters of low soot penetration thickness. Energy, 112:883–898, 10 2016. (Cited on pages 8 & 12).

[120] T. SETA and K. OKUI. Effects of Truncation Error of Derivative Approximation for Two-Phase Lattice Boltzmann Method. Journal of Fluid Science and Technology, 2(1):139–151, 2007. (Cited on page 14).

[121] X. Shan and H. Chen. Lattice Boltzmann model for simulating flows with multi phases and componentsShan, X., & Chen, H. (1993). Lattice Boltzmann model for simulating flows with multi phases and components. Physical Review E, 47(3), 1815–1819. https://doi.org/10.1103/PhysRevE. Physical Review E, 47(3):1815–1819, 1993. (Cited on page 13).

[122] X. Shan and H. Chen. Simulation of nonideal gases and liquid-gas phase transitions by the lattice Boltzmann equation. Physical Review E, 49(4), 1994. (Cited on page 13).

[123] Y. Shi, Y. Zhou, Z. Li, Y. Cai, X. Li, Y. He, and J. Fang. Effect of temperature control conditions on DPF regeneration by nonthermal plasma. Chemosphere, 302(April):134787, 2022. (Cited on page 11).

[124] N. Singh, C. J. Rutland, D. E. Foster, K. Narayanaswamy, and Y. He. Investigation into different dpf regeneration strategies based on fuel economy using integrated system simulation. 2009. (Cited on page 12).

[125] Statistisches Bundesamt. Dieselverbrauch - statistisches bundesamt. https://www.destatis.de/DE/Presse/Pressemitteilungen/Zahl-der-Woche/2017/PD17_32_p002.html. Accessed: 2024-01-08. (Cited on page 2).

[126] Statistisches Bundesamt. Fahrleistungen und kraftstoffverbrauch der privaten haushalte mit personenkraftwagen - statistisches bundesamt. https://www.destatis.de/DE/Themen/Gesellschaft-Umwelt/Umwelt/Materialfluesse-Energiefluesse/Tabellen/fahrleistungen-haushalte.html. Accessed: 2024-01-08. (Cited on page 2).

[127] W. Stöber. On the health hazards of particulate diesel engine exhaust emissions. In SAE Technical Papers, volume 96, pages 643–665, 1987. (Cited on page 1).

[128] C. Stockinger, A. Raiolo, A. Hadjadj, U. Nieken, and M. Shadloo. Simulation of Heterogeneous Combustion Reactions in Porous Media for Application in Soot Filter Regeneration Using the Lattice Boltzmann Method. Journal of Computational Physics, –:–, Submitted. (Cited on pages 77 & 98).

[129] C. Stockinger, A. Raiolo, U. Nieken, R. Alamian, A. Hadjadj, and M. Safdari Shadloo. Lattice Boltzmann Simulations of Heterogeneous Combustion Reactions for Application in Porous Media. Engineering Analysis with Boundary Elements, –:–, Under Review. (Cited on pages 77, 95 & 109).

[130] A. Strzelec, T. J. Toops, and C. S. Daw. Oxygen reactivity of devolatilized diesel engine particulates from conventional and biodiesel fuels. Energy and Fuels, 27(7):3944–3951, 2013. (Cited on page 123).

[131] S. Succi. The Lattice Boltzmann Equation for Fluid Dynamics and Beyond. Clarendon Press, Oxford, 2001. (Cited on page 27).

[132] M. R. Swift, E. Orlandini, W. R. Osborn, and J. M. Yeomans. Lattice Boltzmann simulations of liquid-gas and binary fluid systems. Physical Review E - Statistical Physics, Plasmas, Fluids, and Related Interdisciplinary Topics, 54(5):5041–5052, 1996. (Cited on page 13).

[133] K. Tsuneyoshi and K. Yamamoto. A study on the cell structure and the performances of wall-flow diesel particulate filter. Energy, 48(1):492–499, 2012. (Cited on pages 8 & 133).

[134] TUINSTRA F and KOENIG JL. Raman Spectrum of Graphite. Journal of Chemical Physics, 53(3):1126–1130, 1970. (Cited on pages 18, 19, 120 & 133).

[135] Umweltbundesamt Bundesrepublik Deutschland. Grenzwerte für Schadstoffemissionen von PKW. https://www.umweltbundesamt.de/sites/default/files/medien/376/bilder/dateien/tabelle_grenzwerte_fuer_schadstoffemissionen_von_pkw.pdf, 2017. Accessed: 2024-04-08. (Cited on pages 2 & 133).

[136] R. L. Vander Wal, A. Yezerets, N. W. Currier, D. H. Kim, and C. M. Wang. HRTEM Study of diesel soot collected from diesel particulate filters. Carbon, 45(1):70–77, 2007. (Cited on page 20).

[137] A. J. Wagner. The origin of spurious velocities in lattice Boltzmann. International Journal of Modern Physics B, 17(1-2):193–196, 2003. (Cited on page 13).

[138] J. Wang, M. Wang, and Z. Li. A lattice boltzmann algorithm for fluid–solid conjugate heat transfer. International Journal of Thermal Sciences, 46(3):228–234, 2007. (Cited on page 14).

[139] Y. Wang, D. C. Alsmeyer, and R. L. McCreery. Raman spectroscopy of carbon materials: Structural basis of observed spectra. Chemistry of Materials, 2:557–563, 1990. (Cited on page 19).

[140] H. E. Wichmann. Diesel exhaust particles. In Inhalation Toxicology, volume 19, pages 241–244, 2007. (Cited on page 1).

[141] M. Williams and R. Minjares. A technical summary of euro 6/vi vehicle emission standards. International Council for Clean Transportation (ICCT), Washington, DC, accessed July, 10:2017, 2016. (Cited on page 2).

[142] D. A. Wolf-Gladrow. Lattice-Gas Cellular Automata and Lattice Boltzmann Models. Springer Berlin, Heidelberg, 2004. (Cited on page 24).

[143] Q. Xu, W. Long, H. Jiang, C. Zan, J. Huang, X. Chen, and L. Shi. Pore-scale modelling of the coupled thermal and reactive flow at the combustion front during crude oil in-situ combustion. Chemical Engineering Journal, 350(April):776–790, 2018. (Cited on pages 15, 16, 47, 51, 53, 80, 83, 84, 86, 87, 88, 95, 96, 99, 109, 123, 129, 136, 137, 138, 145 & 147).

[144] K. Yamamoto, R. Komiyama, and T. Sakai. Flow and Pressure Variations Through Porous Filter During Soot Filtration and Regeneration. Journal of Thermal Science and Engineering Applications, 12(1):1–6, 2020. (Cited on page 12).

[145] K. Yamamoto and T. Sakai. Simulation of continuously regenerating trap with catalyzed dpf. Catalysis Today, 242:357–362, 3 2015. (Cited on page 16).

[146] K. Yamamoto, S. Satake, H. Yamashita, N. Takada, and M. Misawa. Lattice boltzmann simulation on porous structure and soot accumulation. Mathematics and Computers in Simulation, 72:257–263, 9 2006. (Cited on page 16).

[147] K. Yamamoto and N. Takada. Lb simulation on soot combustion in porous media. Physica A: Statistical Mechanics and its Applications, 362:111–117, 3 2006. (Cited on page 16).

[148] K. Yamamoto, N. Takada, and M. Misawa. Combustion simulation with lattice boltzmann method in a three-dimensional porous structure. Proceedings of the Combustion Institute, 30:1509–1515, 2005. (Cited on page 16).

[149] K. Yamamoto and K. Yamauchi. Numerical simulation of continuously regenerating diesel particulate filter. Proceedings of the Combustion Institute, 34:3083–3090, 2013. (Cited on page 16).

[150] K. Yamamoto, K. Yamauchi, N. Takada, M. Misawa, H. Furutani, and O. Shinozaki. Lattice boltzmann simulation on continuously regenerating diesel filter. Philosophical Transactions of the Royal Society A: Mathematical, Physical and Engineering Sciences, 369:2584–2591, 6 2011. (Cited on page 16).

[151] P. Yuan and L. Schaefer. Equations of state in a lattice Boltzmann model. Physics of Fluids, 18(4), 2006. (Cited on page 13).

[152] D. yuan Wang, J. hong Cao, P. qiang Tan, Z. xin Wang, W. long Li, Z. wei Liu, and J. Wang. Full course evolution characteristics of DPF active regeneration under different inlet HC concentrations. Fuel, 310(PC):122452, 2022. (Cited on page 10).

[153] Z. Zhang, R. Dong, G. Lan, T. Yuan, and D. Tan. Diesel particulate filter regeneration mechanism of modern automobile engines and methods of reducing PM emissions: a review. Environmental Science and Pollution Research, pages 39338–39376, 2023. (Cited on page 11).

[154] H. W. Zheng, C. Shu, and Y. T. Chew. A lattice Boltzmann model for multiphase flows with large density ratio. Journal of Computational Physics, 218(1):353–371, 2006. (Cited on page 14).

[155] D. P. Ziegler. Boundary conditions for lattice Boltzmann simulations. Journal of Statistical Physics, 71(5-6):1171–1177, 1993. (Cited on page 54).

[156] Q. Zou and X. He. On pressure and velocity boundary conditions for the lattice Boltzmann BGK model. Physics of Fluids, 9(6):1591–1596, 1997. (Cited on pages 57 & 61).

[157] K. Zuse. Über den allgemeinen plankalkül als mittel zur formulierung schematisch-kombinativer aufgaben, 1948. (Cited on page 72).